



Pressure-temperature-time evolution of the Variscan high-pressure units of the eastern Massif-Central : geodynamic implications

Luc De Hoÿm de Marien

► To cite this version:

Luc De Hoÿm de Marien. Pressure-temperature-time evolution of the Variscan high-pressure units of the eastern Massif-Central : geodynamic implications. Earth Sciences. Université de Rennes, 2019. English. NNT : 2019REN1B056 . tel-02945844

HAL Id: tel-02945844

<https://theses.hal.science/tel-02945844>

Submitted on 22 Sep 2020

HAL is a multi-disciplinary open access archive for the deposit and dissemination of scientific research documents, whether they are published or not. The documents may come from teaching and research institutions in France or abroad, or from public or private research centers.

L'archive ouverte pluridisciplinaire **HAL**, est destinée au dépôt et à la diffusion de documents scientifiques de niveau recherche, publiés ou non, émanant des établissements d'enseignement et de recherche français ou étrangers, des laboratoires publics ou privés.

THESE DE DOCTORAT DE

L'UNIVERSITE DE RENNES 1
COMUE UNIVERSITE BRETAGNE LOIRE

ECOLE DOCTORALE N° 600
Ecole doctorale Ecologie, Géosciences, Agronomie et Alimentation
Spécialité : Sciences de la Terre et de l'Environnement

Par

LUC DE HOÏM DE MARIEN

Évolution pression-température-temps des unités varisques de haute pression de l'est du Massif Central : implications géodynamiques

Thèse présentée et soutenue à Rennes le 13 décembre 2019
Unité de recherche : Géosciences

Rapporteurs avant soutenance :

Jean-Marc Lardeaux
Pavla Štípská

Professeur (Université de Nice-Sophia-Antipolis)
Maître de conférence (Université de Strasbourg)

Composition du Jury :

Président : Michel Ballèvre

Professeur (Université de Rennes 1)

Examineurs : Jean-Pierre Burg
Jean-Marc Lardeaux
Charlotte Möller
Pavla Štípská

Professeur émérite (ETH Zurich, Suisse)
Professeur (Université de Nice-Sophia-Antipolis)
Professeur (Université de Lund, Suède)
Maître de conférence (Université de Strasbourg)

Dir. de thèse : Florence Cagnard
Pavel Pitra
Jean Van Den Driessche

Ingénieur/chercheur (BRGM, Orléans)
Maître de conférence (Université de Rennes 1)
Professeur (Université de Rennes 1)

Invité(s)

Benjamin Le Bayon
Marc Poujol

Ingénieur/chercheur (BRGM, Orléans)
Maître de conférence (Université de Rennes 1)

Résumé étendu :

Les premiers stades de la formation de la chaîne Paléozoïque varisque en France restent méconnus, que ce soit dans les zones internes ou externes. Dans le Massif Central, les Maures et le Tanneron, caractéristiques des zones internes l'orogène, le stade initial est enregistré par des éclogites caractéristiques d'un métamorphisme de haute-pressure typique des zones de subduction. Le mode d'affleurement des éclogites sous la forme de lentilles dans des migmatites traduit une évolution postérieure en décompression à haute-température. L'âge du métamorphisme de haute-pressure est toutefois mal contraint, plusieurs mécanismes pourraient expliquer les haute-température liées à la décompression et la distinction des déformations associées à l'enfouissement et l'exhumation des éclogites n'a jamais pu être réalisée. Par conséquent, le contexte tectonique de l'exhumation de ces roches ne peut être précisément défini. De la même manière, le métamorphisme varisque dans les Pyrénées, région typique des zones externes de la chaîne varisque, est très largement dominé par une empreinte de basse-pressure et haute-température (BP-HT) ce qui suggère que la croûte continentale était à l'époque soumise à un gradient thermique anormal, particulièrement chaud. Plusieurs évolutions tectoniques pourraient expliquer ce phénomène et certaines études suggèrent qu'un scénario dans lequel la croûte serait préalablement épaissie puis au moins localement amincie soit à favoriser. Toutefois, l'épaississement crustal précoce n'a jamais été clairement démontré. L'objectif de ces travaux est donc d'apporter des contraintes pétrologiques sur les premiers stades de l'évolution métamorphique de la chaîne varisque et ainsi définir l'histoire tectonique qu'ils enregistrent.

La première partie de ce manuscrit est dédiée à l'étude pétrologique des éclogites de La Borie dans le Haut-Allier (Massif Central). Ces éclogites ont fait l'objet d'une étude géochronologique dans les années 80 à l'aide d'une méthode dont on sait désormais qu'elle peut produire des résultats erronés. Nous avons entrepris une étude pétrochronologique pour réévaluer cet âge et définir leur évolution métamorphique. Les méthodes mises en œuvre sont

la modélisation de l'équilibre des phases (pseudosections), et de la datation U-Pb in situ au LA-ICP-MS sur zircons, apatites et rutiles. La signification des âges obtenus est contrainte du point de vue pétrologique par une analyse détaillée des relations texturales en lame mince, la détermination de la nature des micro-inclusions dans les zircons par spectroscopie RAMAN et l'analyse des éléments trace dans le zircon (REE et Ti) et le rutile (Zr).

Le protolithe magmatique de cette roche mafique s'est mis en place à l'Ordovicien (c. 485 Ma) comme en témoigne les cœurs de zircons. Ceux-ci présentent une zonation oscillatoire, un rapport $\text{Th/U} > 0.1$ et des spectres d'éléments de terres rares caractéristiques de zircons cristallisés dans un liquide magmatique. L'évolution métamorphique de cette roche dans le champ des éclogites est d'abord caractérisée par une augmentation de pression et de température ($650\text{ }^{\circ}\text{C} - 20\text{ kbar} \rightarrow 700\text{ }^{\circ}\text{C} - 22.5\text{ kbar}$) puis par une augmentation de température isobare ($875\text{ }^{\circ}\text{C} - 22.5\text{ kbar}$). Cette évolution culmine dans le champ de la fusion partielle, par conséquent, métamorphisme de haute-pression et de haute-température sont étroitement liés dans le Haut-Allier. La fusion partielle est notamment indiquée par la présence de niveaux particulièrement enrichis en grenat. Leur formation implique l'extraction d'un liquide magmatique préalablement produit par l'afflux localisée d'un fluide aqueux. Ce stade est daté du Dévonien (c. 365 Ma), par les zircons qui présentent des textures métamorphiques et un rapport $\text{Th/U} < 0.1$. Les spectres d'éléments de terres rares et les relations d'inclusions avec le grenat, l'omphacite et le rutile confirment leur cristallisation dans le faciès des éclogites. L'analyse détaillée des textures de zircons suggère une évolution complexe comprenant plusieurs évènements de cristallisation et un rééquilibrage final au pic des conditions du métamorphisme indiqué par la quantité de Ti qu'ils contiennent qui permet d'estimer leur température de cristallisation/homogénéisation. La fusion partielle de cette roche a pu faciliter son exhumation marquée par une décompression d'au moins 13.5 kbar associée à un refroidissement modéré ($750\text{--}850\text{ }^{\circ}\text{C}$) qui se traduit par le remplacement partiel des minéraux de haute-pression par des symplectites. Un refroidissement postérieur rapide et plus important entre 350 et $550\text{ }^{\circ}\text{C}$ est indiqué par la fermeture du système U-Pb des apatites à c. 353 Ma et possiblement du rutile. En outre, la préservation d'une zonation prograde dans le grenat malgré

le caractère de haute-température de cette roche traduit la brièveté de l'ensemble de l'évolution métamorphique de cette roche et par conséquent du réchauffement.

La période contemporaine du pic de pression et de l'exhumation de l'échantillon étudié entre 365-360 Ma, est marquée dans le nord du Massif Central par la mise en place d'un bassin d'arrière arc associée à un magmatisme d'origine mantellique. Ces enregistrements traduisent un amincissement de la lithosphère de la plaque située au dessus de la zone de subduction. Cette information suggère que (i) le réchauffement rapide et isobare observée pourrait être expliqué par l'amincissement de la lithosphère de la plaque supérieure et son remplacement par du matériel asthénosphérique chaud et que (ii) un mécanisme d'extension aurait permis l'exhumation des éclogites. Dans ce contexte, les mécanismes à l'œuvre pour l'exhumation des roches de haute-pression du Massif Central seraient comparables à ceux proposés pour la Mer Egée. L'entrée en subduction au Dévonien de lambeaux de croûte continentale morcelée à l'Ordovicien a été démontrée dans le sud du Massif Central. Elle aurait pu entraîner la verticalisation du panneau plongeant et l'amincissement de la lithosphère de la plaque supérieure. La fusion partielle dans la croûte subductée, consécutive au remplacement de la lithosphère « froide » par l'asthénosphère « chaude », aurait facilité la délamination entre la croûte et le manteau lithosphérique subductés. La délamination aurait engendré le recul du panneau plongeant (slab roll-back) et de ce fait, l'exhumation des roches de haute-pression.

La seconde partie de ce manuscrit est dédiée à l'analyse du métamorphisme de plusieurs orthogneiss. Leur protolithe s'est mis en place essentiellement à l'Ordovicien pendant une période d'extension qui a permis l'ouverture de domaines océaniques restreints par la suite refermés pendant l'orogénèse varisque. Les orthogneiss sont donc susceptibles d'avoir enregistré le métamorphisme et les déformations associés aux événements varisques. Si un métamorphisme de haute-pression a été clairement documentée dans certains granites du sud du Massif Central, la subduction de la croûte continentale ailleurs dans les massifs varisques en France reste à démontrer malgré des critères minéralogiques ou la proximité d'éclogites qui la suggèrent. En outre, les roches granitiques sont réputées être de bonnes archives de la

déformation et pourraient contribuer à la reconnaissance des déformations liées à l'enfouissement et l'exhumation des roches de haute-pression varisques. Après une synthèse des indices minéralogiques dans les orthogneiss et les métaгранites, nous en avons réalisé un échantillonnage, à travers les gradients de déformation, largement répartis à l'échelle régionales dans le Massif Central (Limousin, Thaurion, Haut-Allier, Najac, Lévézou, Monts-du-Lyonnais), les Maures et le TANNERON.

Parmi les métaгранites et orthogneiss échantillonnés, les faciès qui préservent des textures métamorphiques sont les moins déformés. Le métamorphisme est exprimé sous la forme de couronnes de biotites autour des grenats, des pseudomorphoses (cordiérite magmatique) et d'enclaves d'origine pélitique. Les couronnes de grenat autour des biotites sont de potentiels indicateurs d'un métamorphisme de haute-pression. Toutefois, dans les cas étudiés, la stabilité du grenat en association avec l'ilménite ou le plagioclase suggère plutôt un métamorphisme dans le faciès des granulites. L'étude des assemblages qui composent les pseudomorphoses et les enclaves a été réalisée au moyen de pseudosections sur les assemblages les plus prometteurs et suggèrent des conditions de formation dans des conditions de moyennes pression et température qui pourraient traduire d'un rééquilibrage tardif. L'étude approfondie des conditions pression et température antérieures pourraient être étudiées à travers d'autres méthodes de thermobarométrie (p.ex. pressions résiduelles des quartz dans les grenats) mais ces démarches n'ont pas été entreprises notamment à cause de limitations liées au matériel étudié (p.ex. absence de quartz dans les grenats, rééquilibrage tardif de ces derniers). L'étude pétrographique à travers les gradients de déformation montre que les couronnes de grenat sont dispersées et résorbées dans les faciès déformés, ce qui traduit le caractère rétro-morphique et tardif de la déformation principale des orthogneiss. Celle-ci est possiblement postérieure à l'évolution tectonique définie à travers l'étude des éclogites. Ainsi, le contexte tectonique de ces déformations reste à préciser.

La troisième de ce manuscrit concerne l'étude de micaschistes varisques de la Zone Axiale des Pyrénées. Ces témoins sont reconnus comme appartenant aux zones externes de la

chaîne Varisque. Les stades tardifs de l'évolution de cette portion sont relativement bien connus et marqués par un métamorphisme de BP-HT, associé à un magmatisme bimodal important daté à c. 300 Ma. Certains critères minéralogiques et structuraux suggèrent une évolution antérieure associée à un épaississement de la croûte, dont l'amincissement consécutif pourrait expliquer le métamorphisme BP-HT. Ceci-dit, cet épaississement crustal n'a jamais été clairement démontré par une étude pétrologique. Aussi, nous avons entrepris cette étude à travers l'analyse de micaschistes du massif du Canigou où la présence de disthène décrit dans la littérature suggère un tel épaississement. Les démarches entreprises comprennent la réalisation de pseudosections et la datation du métamorphisme au LA-ICP-MS par méthode U-(Th)-Pb *in-situ* et en contexte sur monazite et allanites.

Les échantillons représentent une série sédimentaire intrudée à l'Ordovicien par l'orthogneiss du Canigou. L'analyse de ces échantillons suggère une évolution métamorphique postérieure en deux stades syntectoniques respectifs à staurotide (M1) puis andalousite (M2) dont la température est identique (580 °C), mais dont les pressions respectivement de 5.5 et 3 kbar sont différentes. Le stade M1 traduit une augmentation de température d'abord associée à une augmentation de pression (500 °C – 5.5 kbar → 550 °C – 7.5 kbar), puis une décompression jusque dans le champ à staurotide (580°C – 5.5 kbar). L'augmentation de pression est associée à un gradient thermique faible (9 °C/km) et syntectonique comme en témoigne des inclusions sigmoïdales dans le grenat. Ces éléments témoignent de l'épaississement crustal varisque de la Zone Axiale des Pyrénées. L'âge de cet évènement n'a pas pu être estimé malgré notre tentative de datation d'allanites présentes dans le grenat. La roche a ensuite subi une décompression qui peut être expliquée soit par une décompression isotherme puis un refroidissement, soit par un refroidissement et une décompression initiaux auxquels succéderaient un réchauffement. Cette seconde interprétation est favorisée. Elle traduirait d'abord une période d'extension associée à une érosion significative à laquelle succéderait un apport de chaleur, fournie par le manteau et reflété par un magmatisme bimodal largement documenté dans les Pyrénées. Les résultats de datation des monazites indiquent une date de 300 Ma, interprété comme l'âge de l'évènement de BP-HT.

En conclusion, ces résultats apportent des contraintes sur les premiers stades de la formation de la chaîne varisque dans plusieurs de segments en France.

Les éclogites du Haut-Allier, traduisent un stade initial de subduction dont l'âge est ré-évalué au Dévonien (c. 365 Ma). Le caractère régional de haute-température des roches de cette région est illustré par la fusion partielle des éclogites et par conséquent intimement lié au fonctionnement même de la zone de la zone subduction. L'évolution rapide des conditions de pression et de température (réchauffement, décompression et refroidissement) et l'intégration de ces données dans leur contexte régional suggère qu'une évolution tectonique du type « slab roll-back » aurait permis l'exhumation des roches de haute pression.

C'est sans doute à ce stade que certains orthogneiss du Massif Central et du Tanneron ont enregistré un métamorphisme granulitique. La préservation des traces de ce métamorphisme dans les faciès non déformés, qui conservent généralement une texture granitique, et la superposition des déformations sur ces traces dans les faciès d'orthogneiss francs traduit le caractère tardif des déformations. La signification de celle-ci reste à préciser, tout au plus peut-on affirmer qu'elle se produit lors du trajet rétrograde.

La formation de la chaîne varisque s'est poursuivie par un stade de collision continentale et d'épaississement crustal dont les témoins ont été clairement identifiés pour la première fois dans les Pyrénées. L'âge de ce événement reste toutefois à définir précisément. Dans cette région, à la suite de l'épaississement crustal les roches ont vraisemblablement été exhumées et refroidies avant de subir un nouveau réchauffement autour de c. 300 Ma. Ce réchauffement traduirait l'apport dans la croûte de magma en provenance du manteau, ce qui en suggère l'importance sur l'évolution thermique des zones orogéniques.

Extended abstract

This thesis essentially focuses on the tectonometamorphic record of subduction and to a lesser extent of continental collision in the Variscan basement of France. A petrological study using numerical modelling of phase equilibria and petrologically constrained LA-ICP-MS, U-(Th)-Pb dating is performed on eclogites from the Massif Central, metagranites from the Massif Central and the Maures-Tanneron massifs and metapelites from the Variscan Pyrenees.

Re-investigation of the P - T - t path of a previously inferred Silurian eclogite indicates a Devonian age (c. 365 Ma, U/Pb zircon) for the eclogite facies. Subduction of an Ordovician (c. 485 Ma, U/Pb zircon) oceanic crust is recorded by a prograde P - T path (20 kbar, 650°C to 22.5 kbar, 750°C). Subsequent partial melting during isobaric heating (up to ~875°C) testifies to heat and fluid influx to the subducted crust. Melt extraction led to the formation of a garnet-rich residuum. Fast exhumation is shown by a pervasive HT-MP (< 7 kbar; 800°C) overprint and ensuing cooling inferred from the closure of the apatite U/Pb system at c. 353 Ma. Isobaric heating and subsequent fast exhumation point to a switch in the subduction dynamics. Slab steepening at the onset of subduction of continental ribbons and consecutive asthenospheric flow account for the isobaric heating. Partial melting of the subducted crust facilitated slab detachment and induced slab roll back resulting in the exhumation of the subducted crust during a period of extension.

An extensive exploration of several metagranites, some closely associated with eclogites, from different segments of the Variscan belt in France, did not reveal any clear relics of eclogite-facies metamorphism. Relics of probable HP granulite-facies metamorphism are locally preserved in undeformed lenses, whereas the surrounding orthogneisses record a syndeformational, exhumation-related metamorphism, commonly in the amphibolite facies.

A polystage P - T path is determined for metapelites in the Pyrenees (Canigou massif). Initial MP (Barrovian) metamorphism is attributed to crustal thickening. Renewed LP heating after decompression and cooling points to a time lag between continental collision and subsequent magmatism, suggesting advection of heat from a mantle source.

Remerciements

Après ces trois années intenses, je tiens à exprimer ma gratitude à tous ceux qui ont participé à cette thèse ainsi qu'à tous ceux qui ont partagé ce bout de chemin avec moi. Il y a trop de souvenirs qui se bousculent et je ne saurais tous les remémorer et vous nommer, alors, que tous ceux qui se reconnaissent dans les mots qui précèdent se sachent remerciés.

Tout d'abord, mes sincères remerciements à mes encadrants. Merci Florence pour avoir su convaincre le BRGM de financer cette thèse, ta finesse et ton soutien en toute circonstance. Merci Pavel pour toutes les belles choses que tu m'as apprises ainsi que les idées que tu m'as soufflées entre 19 et 20h autour d'un verre et d'une dernière clope avant de filer du labo. Merci Jean pour la liberté dont j'ai bénéficié ces trois ans, tes précieuses réflexions sur le terrain et m'avoir donné en exemple ce que c'est d'être droit dans ses idées.

Viennent ensuite, les non-officiels, mais absolument essentiels pour la réalisation de ce travail. Merci Ben pour ta bonne humeur, ton enthousiasme constant et ton œil aiguisé sur le terrain. Merci Marc et Nathan pour votre participation improvisée, votre investissement dans la mise en place des protocoles d'analyse et votre patience pour l'interprétation des données.

Merci aux personnels administratifs et techniques. Marie-Anne Z. pour m'avoir guidé dans les méandres de l'administratifs. Yann L. et Xavier L.C., merci pour votre amitié et vous être arrangés avec vos plannings tendus lors de mes demandes urgentes et de dernière minute. Merci Francis G., Loïc J. du CMEBA et Jessica L. de la microsonde ouest à l'IFREMER pour votre disponibilité et votre aide.

Merci à tous les permanents du labo pour les riches discussions que nous avons eues. Une mention spéciale pour Philippe B. et Thibault D. pour votre soutien dans la tourmente de la publication de mon premier article de thèse. J'ai un souvenir amusé des instants partagés avec vous – ainsi qu'avec Marc P., Nathan C., Yannick B. et Pierre G. – au Tournebride. J'ai

aussi une pensée émue pour Jean-Pierre B. qui m’a parlé de nombreuses fois de tectonique avec des étoiles dans les yeux. Cindy L., je te remercie ici – en espérant que cette petite distorsion de « place » soit prémonitoire – pour tes encouragements, tes explications et ton amitié !

Je remercie les membres de mon jury, Jean-Marc L. et Pavla S. pour avoir pris le temps de rapporter ma thèse, ainsi que, Michel B., Jean-Pierre B. et Lotta pour avoir accepté d’évaluer ce travail et pour les pistes qu’ils m’ont soufflées suite à la soutenance. Je remercie également Jean-Marc L. pour m’avoir accompagné dans les Monts-du-Lyonnais et fait découvrir les petits bouchons lyonnais. Ce sont d’excellents souvenirs.

Merci aux copains du labo. Père môle : Caro L., Solenn H., Sylvia D.O., Riccardo A., Anne-Morwenn P., Carlos F.G., Louise J., Audrey C., Leny M., Auregan B., Camie M., Céline D., Elhadji G., Jérôme L.B., Alice P., Mathilde M., Diane D., Pierre D., Aurélie W., France P., Julien M. Aurélie G., Sietske B., Ewan C., Martin S., Nataline S., Jan W., et Jessica U pour le plaisir que j’ai eu à discuter, grimper ou me balader avec vous. Merci Camille B. pour ton écoute et tes conseils.

Charline je glisse un moment pour toi ici, entre labo et bistrot, tu peux choisir la place que tu préfères... Merci pour ton amitié et m’avoir beaucoup fait sourire !

C’est plus rigolo en buvant un coup, alors, merci aux copains du troquet, Clément et Sophie, Thibault, Karim, ainsi que mes très bons copains Émie et Pipo, Laura et Alan, Anaïs pour le plaisir de lever le coude en votre compagnie et tout ce qui s’ensuit !

Merci à mon très chouette voisin, kiné et copain Félix ainsi que Landry et Tiff’ pour m’avoir nourri à la fin de ma thèse.

Je remercie aussi les indéboulonnables, ceux qui restent depuis des années. Sylvain, Milena, Thomas, Sam, Kim, Guillaume, Chloé, Miguel, Julia, Arthur, Julien, Constance et Nicolas. Merci pour être passés me voir ou m’avoir accueilli pendant ces trois ans et plus. Votre

amitié durable, la joie de vous voir, les moments partagés et tout ce que vous me faites découvrir me sont très chers.

Et cerise sur le gâteau, merci à Rémi, Alex et Flo, mes trois indéfectibles camarades rennais. Rémi, merci pour ton oreille attentive en toutes circonstances, ton optimisme inaltérable et ton humour. Flo, merci pour ces soirées improvisées à brasser, ton sens du partage et les belles personnes que tu m'as présenté. Alex, merci pour le volley, les balades dans Rennes à 4h du mat' et ta bonne humeur. Gardez la pêche (et l'abricot).

Table of content

Introduction	13
Eclogite facies metamorphism in the Haut-Allier (Massif Central)	22
Variscan eclogite- to granulite-facies metamorphism in the Haut-Allier (French Massif Central): geodynamic implications	28
1. Introduction	31
2. Geological setting	32
3. Petrography and mineral chemistry	34
4. Interpretation of the petrographic observations	39
5. Pseudosections	40
6. Discussion.....	46
7. Conclusion	51
Petrogenetic investigations of garnet-rich layers in eclogites: evidence of partial melting at high pressure?	58
1. Introduction	59
2. Petrography and mineral chemistry of the garnet-rich layer	61
3. Pseudosection	67
4. Discussion.....	71
5. Conclusions	76
Petrologically constrained U-Pb dating of the “La Borie” eclogites	78
1. Introduction	79
2. Analytical methods	80
3. Petrological constraints on zircon, rutile and apatite	85
4. U/Pb results.....	99
5. Discussion.....	111
Petrologic study of French Variscan metagranites	153
1. Mineralogical indicators of HP metamorphism in metagranite.....	157
2. Methods	163
3. A petrologic study of Variscan metagranites	164
4. Discussion and implications of the petrological study of the metagranites	188
Petrologic study of metapelites from the Variscan Pyrenees	192

Two-stage Variscan metamorphism in the Canigou massif: evidence for crustal thickening in the Pyrenees	193
1. Introduction	195
2. Geological setting	197
3. Structural data.....	200
4. Petrography and mineral chemistry	201
5. <i>P–T</i> estimations.....	208
6. Geochronology.....	218
7. Discussion.....	220
8. Conclusions	230
General discussion and conclusions.....	246
References	257

Introduction

Subduction and mountain building

Understanding the formation of mountain belts is a challenge for geologists. Since the development of the plate tectonic theory, the interpretation of mountain belts that involve the convergence between two continents has been dominated by the Himalayan model. In this model, most of the tectonometamorphic evolution is interpreted as the result of the continental collision subsequent to the closure of an oceanic domain. This model has been in particularly invoked to explain the main tectono-metamorphic features of the Variscan French Massif Central (e.g. Matte and Burg, 1981; Brun and Burg, 1982; Matte 1986, 1991; Lardeaux et al. 2014; Fig. 1a).

Recent tectonics models emerge where most of the deformation and metamorphism of the internal zones of some mountain belts is rather controlled by the dynamics of the initial subduction zone itself. An emblematic example is provided by the Aegean belt during the Tertiary (e.g. Brun and Faccenna, 2008; Fig. 1b). The internal zones of the mountain belt result from the subduction and the exhumation of island arcs or parts of the continental margins previously thinned and torn during the opening of the ocean. Later continental collision may superimpose on the early tectonic history resulting in their much more complex tectono-metamorphic evolution compared to the external zones expected to result from crustal thickening driven by the continental collision itself.

This second type of mountain building is characterized among others (i) by the very short time lapse (some Mys) between the peak pressure age and subsequent decompression of the HP rocks and (ii) by the close spatial association between HP and HT rocks. The Variscan belt of Europe, and especially the French Massif Central, appears to present these characteristics, suggesting an Aegean-type model for Variscan tectonics.

Introduction

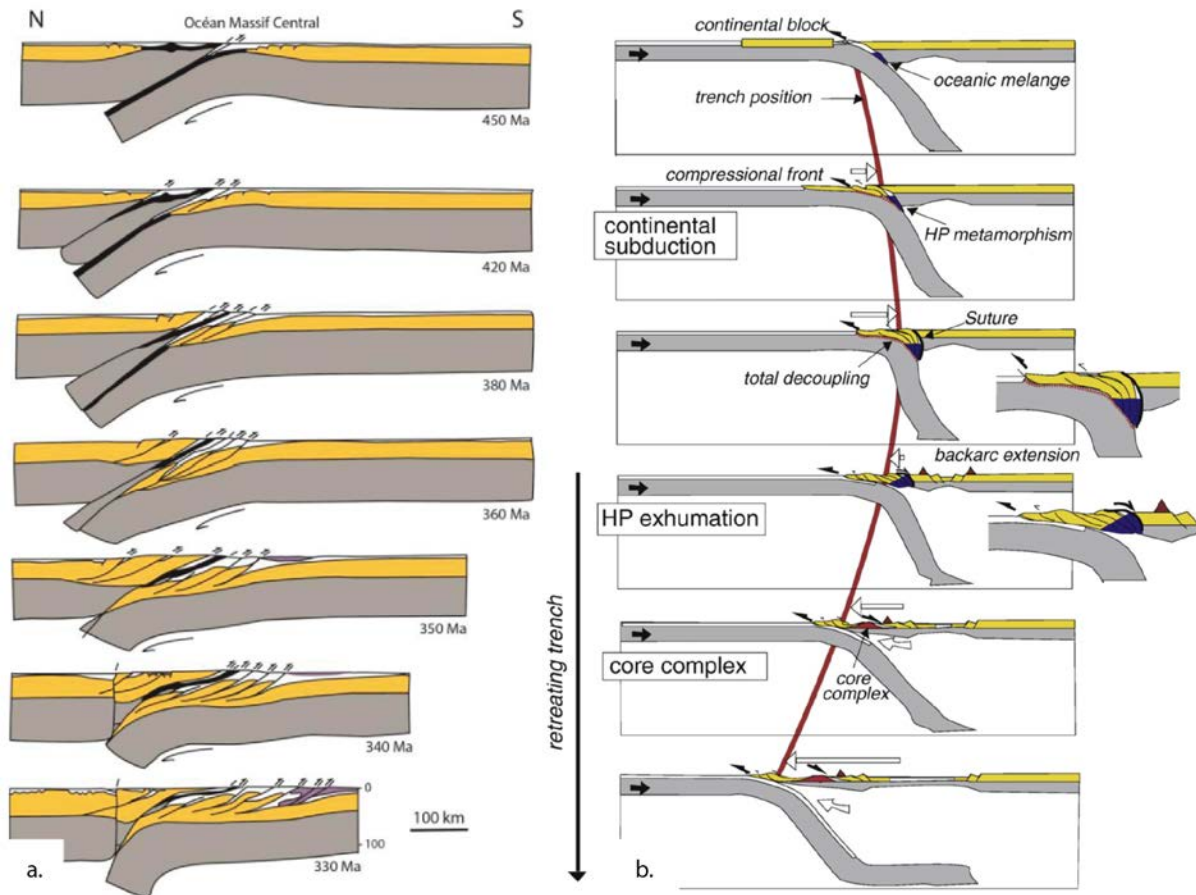


Figure 1: (a) Himalayan type model of continental collision after Matte (1986; modified by Lotout, 2017); (b) slab rollback model for the Aegean after Brun and Faccena, 2008.

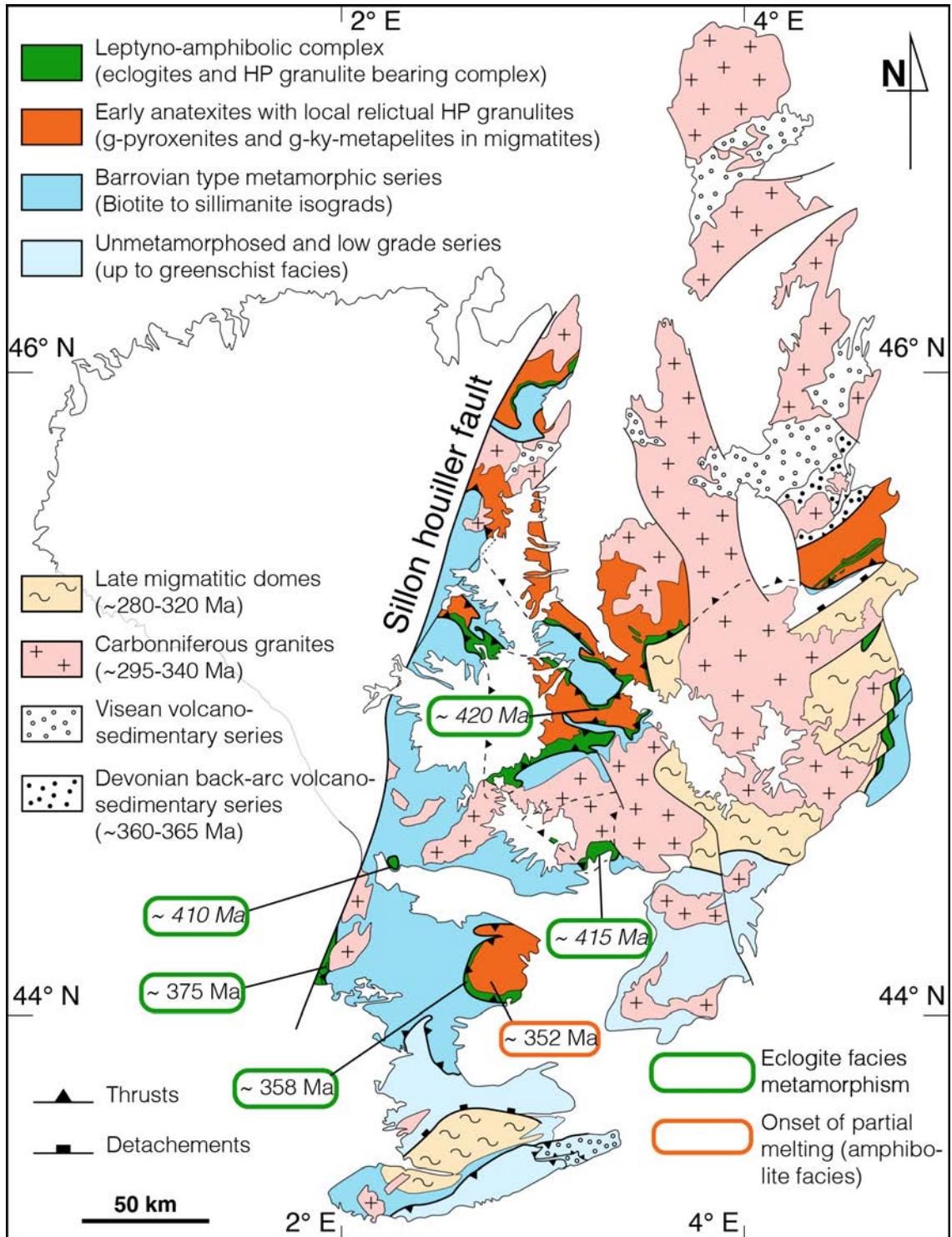
Determine the respective role of burial and exhumation processes in the metamorphic and structural record of rocks and the evolution of processes driving the orogeny through time is then a key in understanding mountain building. What is a sake for geologist is to be able to identify in rocks the structures and the metamorphic record of burial and exhumation process superposed in time and their migration in space.

Research questions

The Massif Central and the Pyrenees are emblematic examples of the internal and external zones of the Variscan orogeny respectively. The ubiquitous evidences of HP metamorphism in the Massif Central and the scarcity of MP pressure evidences in the Pyrenees typify a completely different tectono-metamorphic evolution. Alternatively, both of them are characterized by a widespread migmatization during the orogeny. Accordingly, they may be used to seize the variability of processes at work in the tectono-thermal evolution of an orogen.

The earliest subduction-related Variscan events in the Massif Central are recorded in metabasites occurring in a bimodal magmatic association interpreted as the remnant of a continental margin thinned during a period of rifting in the Ordovician time (e.g. Pin 1990; Briand et al., 1991; Lardeaux, 2014). Subsequent subduction referred to the Eo-Hercynian event is inferred to be of Silurian age (e.g. Faure et al., 1997; Lardeaux, 2014; Lardeaux et al., 2001; Pin and Vielzeuf, 1988; Berger et al., 2010). However, recent re-investigation of the ages of the HP metamorphism in the Armorican Massif points to a later Devonian age for the high-pressure metamorphism and challenges this interpretation (Bosse et al., 2000, 2005). These geochronological studies also indicate that most of the decompression of HP bearing units occurred in a short period of time (~10Ma). Similar results obtained in Najac and Lévézou in the Massif Central also point to a similar age for the HP metamorphism and subsequent fast decompression (< 6 Ma) (Lotout et al., 2017; Lotout et al., submitted; Fig. 2). The Najac and Lévézou were never dated before and the Devonian age for the HP metamorphism remains to be confirmed in other areas.

Introduction



Introduction

Figure 2 (previous page): Synthetic map of the main tectono-metamorphic characteristics of the eastern Massif Central. Contour of the metamorphic units after Burg et al., 1984 and Lardeaux 2014. Metamorphic ages after Paquette et al., 1995; Pin and Lancelot, 1982; Ducrot et al., 1983; Lotout, 2017; in italic: Silurian ages. The early anatexites are characterized by a retrograde (decompression) amphibolite facies metamorphism; the Barrovian type metamorphic series are characterized by a prograde metamorphism the higher grade rocks reach the amphibolite facies. Abbreviations are : g – garnet ;ky – kyanite.

The eclogites are mostly closely associated in space with migmatites recording a subsequent HT amphibolite facies overprint (Fig. 2) that has been interpreted to result from thermal relaxation during continental collision and crustal nappe stacking (e.g. Matte and Burg, 1981; Burg et al., 1984). The amphibolite facies has been explicitly compared to a Barrovian type metamorphism (e.g. Brug, 1977; Nicollet et al., 1983; Burg and Matte, 1981). However, in many areas like the Haut-Allier, the extensive amphibolite facies overprint on eclogite assemblages does not correspond to a prograde, progressive sequence of appearance of index minerals but rather results of a decompression and thus, may not readily be attributed to crustal nappe stacking. In addition, geochronological results in the Lévézou suggest that the eclogites reached the peak pressure conditions (18-23 kbar) at c. 358 Ma before a significant decompression ($P \sim 9$ kbar) by c. 352 Ma and that country rocks underwent partial melting at c. 350 Ma (Lotout, 2017). Partial melting after thermal relaxation would require tens of Myr (e.g. Dewey, 2005; Sonder et al., 1987), consequently, the short span of time between the eclogite facies metamorphism, decompression and partial melting needs to be explained by another mechanism.

The eclogite metamorphism is mostly recorded in metamafic rocks, however, HP assemblages after cordierite have been reported in the Lévézou suggesting that subduction of insular arcs or small continental blocks occurred in the Massif Central (e.g. Lotout, 2017; Lotout et al. 2017). Subduction of insular arcs or small continental blocks is further suggested

Introduction

by eclogites spatially associated with – and maybe enclosed within – orthogneisses (e.g. Thaurion, Vibal, Meuzac, Tullès, Lévêzeu, Picheraie, Tanneron; shown on a map in Chapter 2) or even within late migmatitic domes (Montagne Noire). The orthogneisses are reputedly good markers of continental deformation (e.g. Gapais, 1989) and the possibility to distinguish between several generations of structures (e.g. Pitra et al., 2012) is a chance to unravel the burial-related deformation elusive in the Massif Central (e.g. Faure et al., 2009), and eventually to distinguish these structures from a later overprint by decompression-related structures. In addition, the protoliths of the orthogneisses emplaced during the Orovician rifting and may be found on both sides of the oceanic domain. Accordingly, the strain pattern in the orthogneisses subducted during the Variscan orogeny may allow to distinguish them from those of the overriding plate and may consequently help to determine the exact position of the suture.

The Pyrenees are characterized by a widespread HT-LP metamorphism. In several areas of the Variscan belt, HT-LP metamorphism has been interpreted as consequence of thermal relaxation of a previously thickened crust and subsequent orogenic collapse. However, reports of a higher-pressure metamorphism in the Pyrenees, are scarce and contrasting P – T path proposed. As a consequence, the possible effect of crustal thickening on the subsequent thermal event remains poorly understood.

Structure of the manuscript

The aim of this manuscript is to better constrain the first stages of the Variscan tectonometamorphic events. To do so, we have first focused our study on the re-investigation of eclogites previously interpreted as Silurian eclogites in the Haut-Allier, secondly, we have tried to unravel an eclogite facies metamorphism in the orthogneisses from the Massif Central and the Maures-Tanneron massifs in Provence, a third section is a side study of the earliest metamorphic record of the variscan Pyrenees.

The Chapter I, is dedicated to the study of the subduction dynamic through the re-investigation of the Haut-Allier eclogite and divided in three sections. The section 1, focuses on the geodynamic consequences of the HP granulitic overprint on eclogite facies assemblages of a mafic eclogite studied through phase equilibria modelling (P – T pseudosection). The eclogites hosts garnet-rich layers the origin of which are discussed in terms of primary origin (magmatic layering) or secondary origin (partial melting) in the section 2. The section 3 is dedicated to the U/Pb, LA-ICP-MS geochronological (re)investigation of the zircons, apatites and rutiles of this previously inferred Silurian eclogites. An attempt of textural interpretation of the processes controlling Zr behaviour at HP conditions is proposed in the light of inclusions relationships involving zircon, internal textures and the results of Ti-in-zircon thermometry.

The Chapter II, concern the petrological studies of Ordovician and Cambrian metagranites and orthogneisses of the Massif Central suspected to record a HP metamorphism. These results are ambivalent; however, this study allows a discussion of the significance of the structures preserved by several orthogneiss massifs in the Massif Central.

The Chapter III is dedicated to the results of a side petrologic study of MP metapelites with HT overprint from the Pyrenees. The aim of this study is to constrain the tectono-thermal evolution of the external zones of the Variscan belt.

Introduction

The Chapter IV, is dedicated to the conclusions. The respective implications of each studies are recalled and integrated to briefly discuss (i) the respective implications of the subduction and continental collision on thermal evolution of mountain belts, (ii) the signification of amphibolite facies metamorphism from the internal and external zones of the Pyrenees. A focus is made on the main results provided by the study of mafic eclogites unravelling key elements of the evolution of the subduction zone of the Massif Central. These elements, brought together with first order geological features of the Massif Central are used to draw the outlines of a tectonic model for the exhumation of the HP bearing units of the eastern Massif Central.

Eclogite facies metamorphism in the Haut- Allier (Massif Central)

Introduction to the study of Haut-Allier eclogites

The Haut-Allier region is important for the geology of the French Massif Central for three main historical reasons. First, an association of meta-peridotites, eclogites and mafic and acid granulites has been described in detail for the first time in the Massif Central in this area (Lasnier, 1968; Forestier and Lasnier, 1969; Forestier and Lasnier, 1973). This association was extensively described by Marchand (1974) and Lasnier (1977). Second, one of the first attempts of U/Pb dating on zircon from eclogites of the Massif Central was carried out on an eclogite from this region (La Borie). Third, it is the first place where the juxtaposition of a HP bearing unit over a unit devoid of HP metamorphic rocks was interpreted as a thrust (Burg and Matte, 1978). This led to the now classic interpretation of the Massif Central as a collisional orogen.

The granulites with HP primary assemblages always display a lower pressure overprint and occur as lenses in a host rock displaying LP-HT mineral assemblages. Some mafic amphibolites contain sapphirine that led the above-mentioned pioneers to believe that this series belongs to a Precambrian crust. At that time, and by analogy, Forestier and Lasnier (1969) wrote that: “*La sapphirine est presque un fossile caractéristique des zones précambriennes*”. The granulites were referred to as a granulite-kinzigite-khondalite trilogy that was supposedly characteristic of Precambrian terrains. An alternative interpretation was proposed by Burg and Matte (1978) who suggested a possible Variscan age for the eclogite and granulites facies metamorphism. This interpretation was later supported by a pioneering geochronological study of the La Borie eclogite by Ducrot et al. (1983) confirming a Palaeozoic age for the eclogite. Forestier and Lasnier (1973) proposed that these rocks underwent pressures between 20-30 kbar and Pin and Vielzeuf (1988) determined a peak pressure condition of 20 kbar at a fixed temperature of 800°C using conventional thermobarometry.

Chapter 1 – Introduction

We decided to reinvestigate these eclogites for two reasons. First, Lasnier (1977) proposed an isothermal decompression for the eclogites, suggesting the primary HT character of these rocks. On the other hand, Lardeaux (2014) pointed out an alternative interpretation of post-peak pressure thermal re-equilibration reworking early lower thermal gradient (HP-LT), possibly during the continental collision. This uncertainty results on the lack of well constrained P – T path. The second reason concerns the age of the eclogite facies metamorphism. Similar Silurian ages (e.g. Peucat et al., 1982; Paquette et al., 1985) for the eclogite facies metamorphism in the Armorican Massif was recently reinvestigated and younger 360-380 Ma ages were obtained (Bosse et al., 2000). In the study of Paquette et al., (2017) La Bessenoit eclogites in the Massif Central, was also re-investigated and the previously obtained Silurian age (Paquette et al., 1995) was not confirmed. Similarly, a multimethod geochronological study (U/Pb zircon; Lu/Hf and Sm/Nd garnet) was performed for the first time in the Najac and Lévézou massifs and yielded two, c. 380 Ma and a c. 360 Ma ages for the eclogite facies metamorphism in the southern part of the Massif Central (Lotout et al., 2018, Lotout et al., Submitted). Consequently, the previously published Silurian ages for the HP metamorphism needs to be re-investigated. In order to address these two points, we used a P – T pseudosections and a U/Pb dating of zircon, rutile and apatite approach in order to reinvestigate these eclogites and produce a reliable P – T – t path and constrain their tectonic evolution.

The eclogites are localized SW of La Borie where they occur as hectometric boulders or lenses surrounded by felsic rocks themselves associated with biotite-sillimanite bearing gneisses (Lasnier, 1977). The felsic rocks interpreted as recrystallized rhyolites by Forestier (1961) and as blastomylonites by Burg (1977, 1984). A typical character of these rocks is to display quartz-sillimanite nodules.



Figure I.1: Field photographs of the felsic rocks associated with the mafic rocks. These rocks contain quartz-sillimanite nodules (a), biotite-rich aggregates interpreted as elongated schlieren that mark a fabric (b), biotite-rich with lenticular polycrystalline plagioclase-rich aggregates with diffuse border that may be restite enclaves (c). In the core of the mafic body, numerous amphibolite (likely retrogressed eclogites) elongated and folded lenses are embedded in a felsic (quartz-plagioclase-rich) rock (d).

Lasnier (1977) indicated that the eclogites contain primary kyanite and corundum. They are mostly composed of omphacite (now turned into symplectite), garnet, kyanite and a minor amount of corundum, rutile, quartz, apatite, sulphide, graphite. Kyanite content is variable and may represent up to ~20% of the rock volume. A layering is marked by the alternation of garnet-omphacite and garnet-rich layers ($g > 80\%$).

The sampled eclogites were found in the same context. The sillimanite-quartz nodule bearing rock (Fig. I.1.a) is mostly composed by quartz and feldspar and subordinate biotite. The latter always marks a fabric but quartz and plagioclase are often undeformed and evidence strain

gradients, however, mylonites were never observed. In the less deformed facies, the fabric is often marked by biotite-rich aggregates (Fig. I.1.b). Elongated boudins of amphibolites and rare lenses of biotite-rich gneisses with polycrystalline lenticular aggregates mostly composed of plagioclase with biotite are also present (Fig. I.1.c). The latter display diffuse border with their surroundings. The contact between these rocks and the main mafic body was not directly observed. It is noteworthy that in the middle of the main mafic body, similar rock types (quartz-feldspar-biotite) are present and contain numerous highly ductile lenses of amphibolites that are most likely retrogressed eclogites (Fig. I.1.d).



Figure II.2: Field photographs of the eclogite types. The finer-grained size variety is observed on metric outcrops (a), where a strong layering is marked by the proportion of garnet crystals (b). Coarser-grained eclogites display centimetre sized garnet (pointed end of the hammer represents 2.5 cm) and a layering marked by differences in both garnet size and proportion (c) or the presence of garnet-rich layers with contrasting smaller grains (d; thickness of the layer > 4-5 cm).

Chapter 1 – Introduction

In the main mafic body, the lithologies comprise eclogites variously retrogressed from garnet-rich retrogressed eclogite to amphibolite. Fine grained (mm) eclogites are characterized by a banding marked by the alternation of garnet-rich layers and former clinopyroxene-rich layers (now amphibole-plagioclase bearing symplectites; Fig. I.2.a,b). Similar but coarser-grained eclogites contain garnet porphyroblasts up to 1cm. These eclogites preserve a banding marked by both the garnet proportion and grain size (Fig. I.2.c). This type of eclogite also hosts garnet-rich layers up to several centimetres thick (Fig. I.2.d). The layering is parallel to the preferential orientation of former kyanite (now symplectitic white spots).

The results presented in the next section are focused on the coarser grained eclogites. They display many similarities with those studied by Ducrot et al. (1983). First, the frame of the P – T evolution is set, then, a discussion on the origin of the garnet-rich layer is proposed before the presentation and interpretation of the geochronological U/Pb study.

**Variscan eclogite- to granulite-facies metamorphism in the Haut-
Allier (French Massif Central): geodynamic implications**

Bulletin de la société géologique de France, submitted

Luc de Hoÿm de Marien¹, Pavel Pitra^{1,2}, Florence Cagnard³ and Benjamin Le Bayon³

¹Univ Rennes, CNRS, Géosciences Rennes - UMR 6118, F-35000 Rennes, France

²Česká geologická služba, CZ-118 21 Prague 1, Czech Republic

³Bureau de Recherches Géologiques et Minières – BRGM – 3 avenue Claude Guillemin, BP
36009, 45060 Orléans cedex 2, France

Résumé

Cette étude a pour but de contraindre la dynamique de la zone de subduction varisque du Massif Central Français à travers l'étude des évidences pétrographiques de la transition du faciès des éclogites vers celui des granulites de haute-pressions préservées dans un échantillon d'éclogite basique du Haut-Allier. Trois événements métamorphiques, M1, M2 et M3 chacun caractérisés par des paragenèses à grenat1-omphacite-disthène, grenat2-plagioclase et amphibole-plagioclase sont identifiés et définissent une évolution P - T horaire. Ces événements métamorphiques traduisent la succession des conditions du faciès des éclogites (M1 ; 1 ~20 kbar, 650°C to ~22.5 kbar, 750°C), des granulites de haute-pression (M2 ; 19.5 kbar and 875°C), puis des amphibolites de haute-températures (M3 ; 7 kbar, 750-850°C). L'étude pétrologique de cet échantillon par l'analyse de la zonation du grenat, de la minéralogie des inclusions qu'il contient et de la modélisation des équilibres de phases (pseudosection), suggère que le premier événement métamorphique (M1) est prograde et traduit un enfouissement, puis un réchauffement isobare. La résorption du grenat 1 à laquelle succède la croissance du grenat 2 est interprétée comme le résultat d'une décompression isotherme lors du métamorphisme M2. Le dernier événement métamorphique traduit une forte décompression associée à un refroidissement limité. La préservation d'une importante zonation de croissance du grenat à de telles conditions de températures traduit la brièveté de l'événement thermique et par conséquent, du réchauffement, de la décompression puis du refroidissement qui s'ensuit. Cette évolution des conditions P - T est interprétée comme le résultat de la juxtaposition du manteau asthénosphérique chaud contre les roches de la croûte subductée à laquelle succède une exhumation dominée par le retrait du panneau plongeant (slab roll-back).

Abstract

The eclogite to high-pressure granulite facies transition was studied in a mafic eclogite sample from the Haut-Allier in order to constrain the early Variscan subduction dynamic of the French Massif Central. Three successive metamorphic stages M1, M2 and M3, are characterized by garnet1-omphacite-kyanite, garnet2-plagioclase, amphibole-plagioclase bearing assemblages respectively, and define a clockwise P – T path. These events occurred at eclogite (M1; ~20 kbar, 650°C to ~22.5 kbar, 750°C), high-pressure granulite (M2; 19.5 kbar and 875°C) and high-temperature amphibolite (M3; 7 kbar, 750-850°C) facies conditions respectively. Pseudosection modelling, garnet growth zoning and mineralogy of the inclusions suggest an M1 prograde metamorphism first dominated by burial and then by near isobaric heating. Subsequent garnet 1 resorption, prior to a renewed growth of garnet 2 is interpreted in terms of a decompression during M2. M3 testifies to a strong decompression associated with limited cooling. The preservation of garnet growth zoning indicates the short-lived character of the temperature increase, decompression and cooling cycle. We argue that such P – T evolution records the juxtaposition of the asthenosphere against the subducted crust prior to exhumation driven by slab roll-back.

1. Introduction

The dynamics of the early Variscan high-pressure (HP) event in the French Massif Central is poorly known (e.g. Lardeaux et al., 2014). One of the reasons is that the P – T path followed by the eclogites is most of the time unconstrained except, locally (e.g. Berger et al., 2010; Lardeaux et al., 2001, Lotout et al., 2018). A major characteristic of the HP units of the Massif Central is the overprint of an early eclogite-facies metamorphism by HP granulite assemblages (Forestier et al., 1973). Two types of P – T paths could account for this overprint (Lardeaux et al., 2014). A first possibility is that eclogites reached high-temperatures and were exhumed along a (sub-)isothermal P – T path. Alternatively, initially low- to medium-temperature eclogites reached HP granulite facies through thermal equilibration and the associated temperature increase following a limited pressure decrease. Additionally, a polycyclic evolution has been suggested in the Haut-Allier region (Schulz, 2014). Such polycyclic P – T path would be characterized by an initial loop reaching eclogite facies conditions followed by exhumation to low pressures and by a second loop up to HP granulite facies conditions and renewed exhumation. Resolving the P – T paths actually followed by the eclogites would consequently be a valuable addition in the understanding of the early Variscan evolution of the Massif Central.

In this contribution, we reinvestigate the petrology of samples from the historical locality of La Borie in the Haut-Allier region (Fig. I.1.1). Metamorphosed mafic rocks in the area underwent an eclogite-facies metamorphism (Pin and Vielzeuf, 1988) and a subsequent HP granulite overprint (Forestier et al., 1973). Pseudosection modelling constrain the P – T path for the eclogites and allow us to discuss the geodynamic implications in the light of the deciphered eclogite to HP granulite transition.

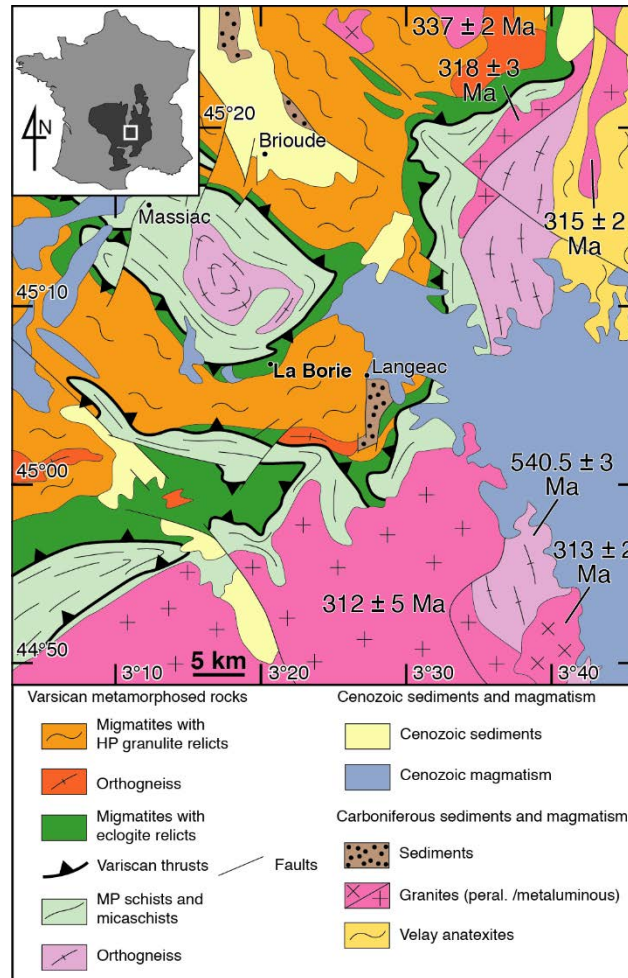


Figure I.1.1: Geological map and localisation of the studied area. The eclogite described in this study has been sampled west of la Borie, in the migmatites with eclogite relicts unit (lat: 45°6'45.29"N; long: 3°19'55.83"E; WGS84).

2. Geological setting

The main tectonic feature of the studied area consists in the juxtaposition of a high-pressure, eclogite-bearing unit, against a lower-pressure unit, devoid of eclogites, interpreted as the result of thrusting during the Variscan collision (Fig. I.1.1; Burg and Matte, 1978). Both units show a high-temperature, sillimanite-bearing, migmatitic regional foliation parallel with the lithological contacts (Burg et al., 1984). The classical interpretation of the structural and petrological data in the area is that the decompression of the eclogites to amphibolite facies

conditions (passing through HP granulite), is coeval with partial melting and thrusting (e.g. Burg and Matte, 1978). On the other hand, based on geochronological and petrological data, it has been proposed that the exhumation of the eclogites predated an independent Early Carboniferous metamorphic cycle related with continental collision and thrusting (Schulz, 2014).

The eclogite free unit, is the so-called Lower Gneiss Unit. This unit is characterized by biotite-sillimanite schists with subordinate garnet-staurolite-kyanite micaschists and migmatites. The metamorphism and partial melting of this unit is considered to result from an inverted metamorphism during thrusting (Burg et al., 1984). Similar peak pressure P – T conditions of ~13 kbar and 700°C have been estimated using conventional thermobarometry in both the biotite-sillimanite gneisses (though without evidence of kyanite relics) and the garnet-staurolite-kyanite micaschists (Schulz et al. 1996). This unit was intruded by an S-type granite dated at c. 542 Ma by LA-ICP-MS U/Pb on zircon (Couzinié et al., 2017), and transformed into an orthogneiss during Variscan tectonics. Undeformed Carboniferous granites intruded this unit at c. 320-310 Ma (LA-ICP-MS U/Pb on zircon, Laurent et al., 2017).

Most of the eclogite bearing unit, the so-called Upper Gneiss Unit, is characterized by garnet-cordierite-sillimanite anatectic gneisses. These gneisses contain relics of eclogites and kyanite-garnet-bearing HP granulites (Forestier et al., 1973). The recorded peak pressure conditions of kyanite-garnet granulite from this unit have been estimated by conventional thermobarometry at around 11 kbar and 700°C (Schulz et al., 1996; Schulz, 2014), and around 8-10 kbar in a garnet-rutile-kyanite bearing paragneiss (Gardien et al., 2011). According to Schulz (2014), the peak of pressure is followed by heating up to 800°C at 11 kbar. The age of this metamorphic event is constrained at c. 360 Ma using Th-U-Pb EPMA dating on monazite (Gardien et al., 2011; Schulz, 2014). The exhumation, down to pressures around 5 kbar, has been estimated at c. 330 Ma using the same method (Schulz, 2014). This unit was intruded by

several granitic bodies between c. 337 and c. 299 Ma (Laurent et al., 2017). The final cooling of the unit is estimated at c. 275 Ma ($^{40}\text{Ar}/^{39}\text{Ar}$ on K-feldspar; Gardien et al., 2011).

The above mentioned eclogites outcrop at the contact between the two units. This contact is marked by a zone containing boudins of mafic and ultramafic rocks, orthogneisses and marbles embedded in felsic gneisses and migmatites (Forestier and Lasnier, 1968; Forestier et al., 1973; Lasnier, 1968). Some of the mafic boudins contain relics of granulitic and eclogitic assemblages and some of the ultramafic boudins are garnet peridotites. The mafic lithologies present the geochemical signature of ocean-floor or back-arc basalts (Giraud, 1984). Conventional barometry on eclogites yielded a peak of pressure around 20 kbar assuming a temperature of 800°C (Pin and Vielzeuf, 1988). The c. 430 Ma date determined by dissolution of a zircon population from a kyanite eclogite sampled west of La Borie (Fig. I.1.1) has been interpreted as the age of this metamorphism (Ducrot et al., 1983). This zone, usually called the Leptyno-amphibolitic complex, is interpreted as a suture zone that was reworked during the continent-continent collision stage of the orogeny (Burg and Matte, 1978; Santallier, 1988).

The high temperature character of Variscan eclogites is major specificity of the Haut-Allier (e.g. Pin and Vielzeuf, 1988) and in a larger extent of the French Massif Central (Lardeaux, 2014). The lack of reliable P – T path led to several interpretation of their metamorphic history resulting in variable tectonic models for the orogeny. Therefore, we sampled an eclogite similar to that described by Ducrot et al. (1983), close to La Borie in the Haut-Allier, in order to specify its metamorphic evolution.

3. Petrography and mineral chemistry

Mineral analyses have been performed with a Cameca SX100 electron microprobe (Microsonde Ouest, IFREMER, Brest-Plouzané, France). Representative analyses of selected minerals are listed in Supplementary material (Table I.1.1 – After the references). Mineral

abbreviations are: amp: amphibole, bi: biotite, chl: chlorite, cpx: clinopyroxene, coe: coesite, ep: epidote, g: garnet, ilm: ilmenite, ksp: potassium feldspar, ky: kyanite, law: lawsonite, mu: muscovite, pl: plagioclase, q: quartz, ru: rutile, ttn: titanite, sp: spinel, sul: sulphide. Mineral endmembers (expressed in mole %) and compositional variables are: $X_{Mg} = Mg/(Mg+Fe)$; $X_{Fe^3} = Fe^{3+}/(Fe^{3+}+Fe^{2+})$; almandine, alm = $Fe/(Fe+Mg+Ca+Mn)$, pyrope, prp = $Mg/(Fe+Mg+Ca+Mn)$, grossular, grs = $Ca/(Fe+Mg+Ca+Mn)$, spessartine, sps = $Mn/(Fe+Mg+Ca+Mn)$; jadeite, jd = $Na/(Na+Ca)$; albite, an = $Ca/(Ca+Na+K)$, anorthite, an = $Ca/(Ca+Na+K)$, pistacite, ps = $Fe^{3+}/(Fe^{3+}+Al-2)$; orthoclase, or = $K/(Ca+Na+K)$; geikielite, gk = $Mg/(Fe^{2+}+Fe^{3+}+Mg+Mn)$; pfu: per formula unit. In addition, the amount of calcium on site B labelled Ca(B) and Na on site A labelled Na(A) in amphibole have been calculated according to the procedure of Leake et al. (1997).

Under the microscope, the studied sample is a strongly retrogressed eclogite composed of garnet porphyroblasts and various fine-grained ($< 25\mu m$) symplectites (Fig. I.1.2a). It also contains minor rutile, ilmenite, apatite and zircon. A foliation is marked by the ellipsoidal shape of the symplectites, whereas the crystals that compose these aggregates are randomly oriented and lack signs of deformation which is illustrated by the preservation of the cor-sp-mu-pl coronitic textures (Fig. I.1.2a).

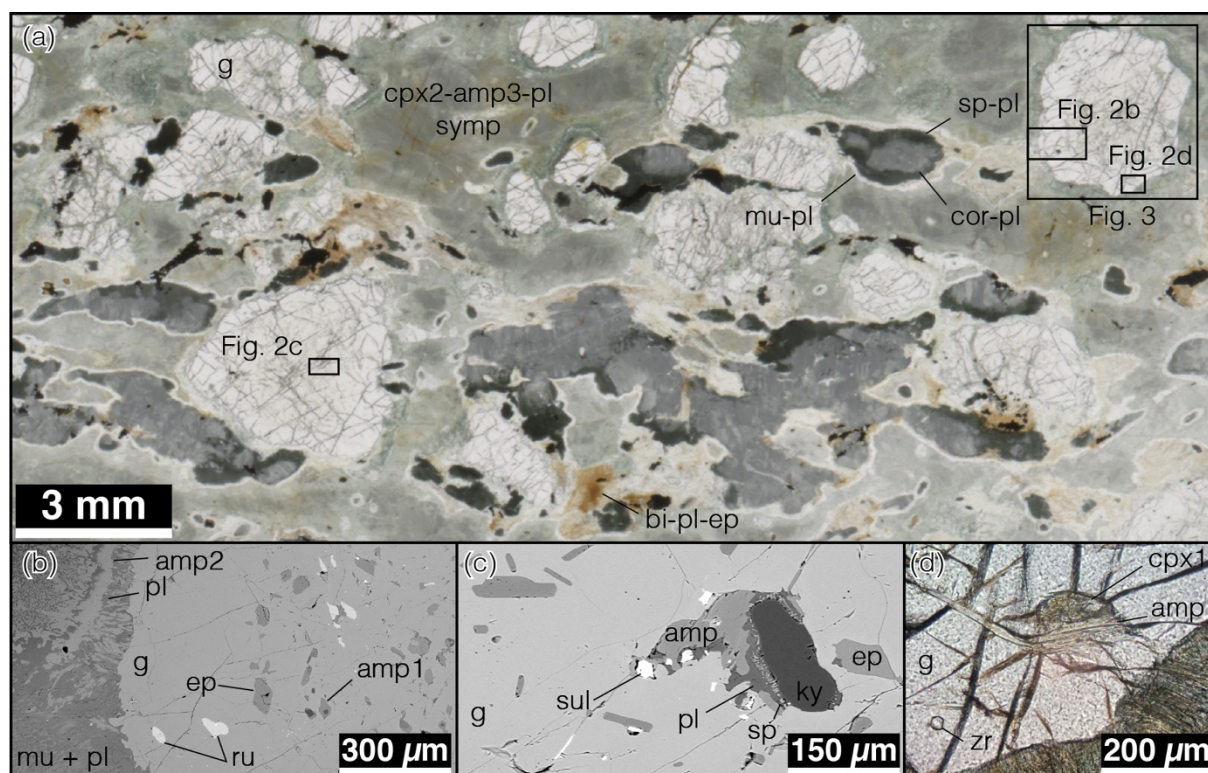


Figure I.1.2: Photomicrograph of a (a) part of thin section of the studied sample and (b, c, d) details of inclusions in garnets. (a) Transmitted light photomicrograph of a part of a thin section made in the studied sample. The sample is characterized by small sized garnets in a matrix composed of various symplectites. The shape of these symplectites (particularly cor-sp-mu-pl) marks a fabric, however, the fine aggregates forming these symplectites are undeformed. (b, c, d): Primary inclusions in garnets: (b) BSE image of multiple inclusions of amphibole and epidote in garnet mantle and inclusion poor rim. Garnet displays irregular edges at the contact with matrix crystals and is surrounded by a corona made of amphibole and plagioclase. (c) BSE image of epidote, amphibole and kyanite in garnet. Amphibole, kyanite and garnet reacted to form a corona of spinel and plagioclase around kyanite. (d) Transmitted light photograph of inclusion of clinopyroxene crystal in garnet

2. Clinopyroxene display an irregular edge with garnet (upper side of the crystal) and is cut by amphibole (lower side of the crystal).

Garnet locally contains inclusions of amphibole, epidote (Fig. I.1.2b), kyanite (Fig. I.1.2c), clinopyroxene (Fig. I.1.2d), phengitic muscovite (mu1; Si = 3.7 pfu; X_{Mg} = 0.6), rutile, quartz and minor zircon. The distribution of the inclusions defines an optical zoning (Fig. I.1.3a, b). Garnet core and mantle contain numerous inclusions of epidote (ep1; ps = 0-0.4) and pargasitic amphibole (amp1; Ca(B) = 1.5–1.8; Na(A) = 0.4-0.6; Al = 2.7-3.1 pfu; Si = 6.0–6.1

pfu; $X_{Mg} = 0.64\text{--}71$). They are small ($<100\text{ }\mu\text{m}$) in the core and significantly larger (up to $200\text{ }\mu\text{m}$) in the mantle. Garnet rim is free of epidote and contains only scarce amphibole (Amp1; $\text{Ca(B)} = 1.74\text{--}1.75$; $\text{Na(A)} = 0.51\text{--}0.6$; $\text{Al} = 3.5\text{--}3.6$ pfu; $\text{Si} = 5.8$ pfu; $X_{Mg} = 0.62\text{--}66$) as well as rutile and zircon. Garnet core, mantle and rim are referred to as garnet 1 (see below). An outer rim, referred to as garnet 2, is characterized by the presence of amphibole (Fig I.1.3b; Amp2; $\text{Ca(B)} = 1.6\text{--}1.7$; $\text{Na(A)} = 0.7$; $\text{Al} = 3.2\text{--}3.5$ pfu; $\text{Si} = 5.7\text{--}5.9$ pfu; $X_{Mg} = 0.76\text{--}82$) and anhedral omphacitic clinopyroxene (Fig. I.1.2b; Cpx1; $\text{jd} = 38\text{--}39$; $X_{Mg} = 0.85\text{--}0.90$).

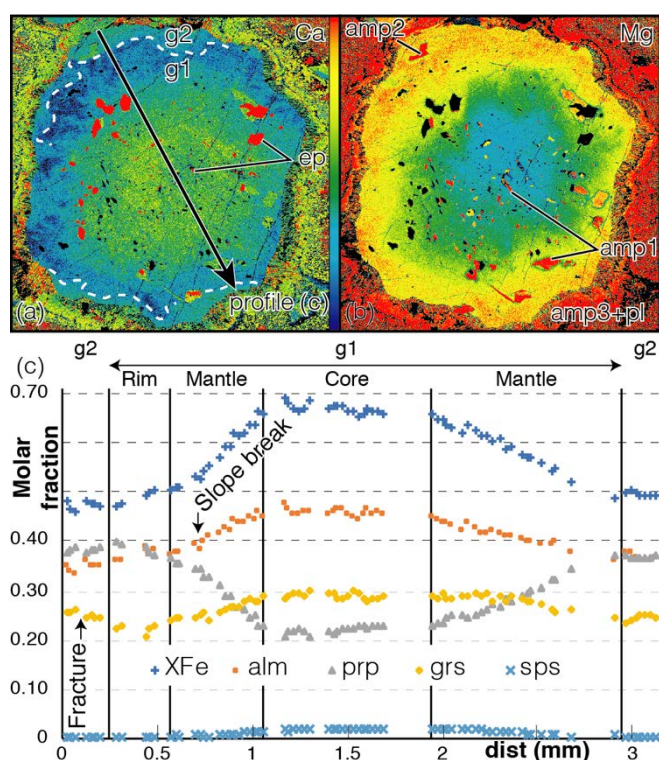


Figure I.1.3: Garnet zoning inclusions pattern and chemical zoning. XRay maps for (a) Mg and (b) Ca contents in garnet. Notice the change of size and amount of inclusions from garnet core, mantle and rim. (c) Chemical zoning profile in garnet.

The optical zoning of garnet defined by the inclusion pattern coincides with the chemical zoning (Fig. I.1.3). Garnet 1 is characterized by a decreasing grossular content and increasing pyrope content. The zoning is weak in the core with a roughly constant grossular (grs28-30)

and spessartine (sps2) contents, slightly increasing pyrope (prp21→23) content and decreasing almandine content (alm47→45). The mantle and the rim are characterized by a stronger zoning that involves further increase of the pyrope content (prp23→38→40) associated with a decrease of the almandine (alm41→38→36), grossular (grs28-30→23→21) and spessartine (sps2→1→1) contents. The highest proportion of pyrope corresponds to the lowest grossular content. It is noteworthy that the slope of the pyrope, grossular and almandine zoning flattens from the outer part of the mantle rimwards (transition marked by an arrow in Fig. I.1.3c). The outer rim (garnet 2) displays a striking inversion of the trend of grossular (grs21→26) and pyrope (prp40→39) contents. The strong gradient of the grossular content corresponds to an irregular boundary that marks the limit between garnet 1 and garnet 2 (Fig. I.1.3a).

Garnet is surrounded by a corona of amphibole and plagioclase, the composition of which is similar to the composition of amphibole and plagioclase of other symplectites in the matrix. The most abundant type of matrix symplectites comprises diopside (cpx2; jd = 0; XMg = 0.85–0.86), amphibole (amp3; pargasite to magnesiohornblende, Ca(B) = 1.7–1.9; Na(A) = 0.2–0.6; Al = 1.1–2.4; Si = 6–7.2 pfu; XMg = 0.75–88), plagioclase (an = 18–35), and minor quartz (Fig. I.1.2a). Another type of symplectites is distinctly Al-rich and zoned. Corundum is present in the inner corona, followed rimwards by spinel (XMg = 0.44–0.52) and muscovite (Si = 3.1 pfu). These minerals are intergrown with plagioclase of a strongly variable composition from anorthite-rich in the inner symplectite to albite-rich in the rim (an = 91 → 20). Kyanite has been observed in the core of these coronitic structures in another similar sample. The third symplectite is K-rich and characterized by biotite, muscovite (Si = 3.0–3.1 pfu), plagioclase (an = 18–82) and minor epidote (Al = 2.6–3.0 pfu). This type of symplectites is associated with anhedral rutile juxtaposed to ilmenite (geikielite up to 19%, pyrophannite <1%), both of them

being locally surrounded by a corona of titanite. Of special interest are scarce anhedral blebs of pure albite in the matrix, surrounded by a corona of diopside.

4. Interpretation of the petrographic observations

These observations can be interpreted in terms of three metamorphic events. The dominant assemblage comprises relatively coarse (several mm) crystals of garnet and three minerals now replaced by symplectites. Diopside-amphibole-plagioclase-quartz symplectites are interpreted as former omphacite, corundum/spinel-plagioclase as former kyanite, and biotite-bearing symplectites as replacing a K-rich mineral (muscovite or K-feldspar). These minerals are also preserved as inclusions in garnet, associated with amphibole, epidote, muscovite, rutile and quartz. Together with the remarkable absence of plagioclase inclusions, this suggests that the dominant metamorphic stage (M1) records eclogite-facies conditions. In detail, the core and mantle of garnet contain abundant inclusions of epidote and amphibole, whereas the rim is epidote-free and contains only rare crystals of amphibole (g1, Fig I.1.3a). The progressive decrease of the proportion of hydrous phases testifies to the prograde character of M1. This is also in agreement with garnet zoning, characterized by a decrease of spessartine and increase of pyrope, typical of prograde growth zoning.

The irregular boundary between the rim and the outer rim of garnet (Fig. I.1.3a), associated with the relatively abrupt increase of grossular, as well as the irregular garnet contour, commonly with convex faces, cutting across the concentric growth zoning, suggest a period of partial resorption of garnet (g1) before a renewed growth (outer rim – g2).

The growth of garnet 2 (with higher grossular, and lower pyrope contents) is characteristic of the second metamorphic stage, M2. This event is also marked by the renewed growth of amphibole (included in garnet 2) and by the resorption of omphacite. Minor rutile and quartz, preserved as inclusions in garnet 2, were also part of the assemblage. The albite

blebs (significantly larger than plagioclase crystals in the symplectites) surrounded by a diopside corona suggest that they are not in equilibrium with the matrix symplectite and could be attributed to the M2 metamorphic stage. This interpretation suggests that M2 records high-pressure granulite-facies conditions.

The M3 event is characterized by the replacement of the large M1 crystals by plagioclase- and diopside-bearing symplectites. They typically develop during decompression of high-pressure rocks, suggesting that M3 occurred at lower pressures. This agrees with the observed relations between rutile, ilmenite and titanite that suggest a sequential growth of ilmenite at the expense of rutile and then titanite at the expense of both rutile and ilmenite.

5. Pseudosections

P-T pseudosections were calculated in the model system MnNCKFMASHTO and NCFSMASHO using Theriak/Domino (de Capitani & Brown, 1987; de Capitani & Petrakakis, 2010) and the thermodynamic data set 6.2 (Holland & Powell, 2011). The solution phases considered in the calculations and the activity-composition models used are amphibole, clinopyroxene, melt (Green et al., 2016); biotite, chlorite, garnet, muscovite (White et al., 2014b); epidote (Holland & Powell, 2011); ilmenite (White et al., 2000; White et al., 2014b); orthopyroxene (White et al., 2014a, 2014b) plagioclase (Holland and Powell, 2003), spinel (White et al., 2002). The mixing models were converted for Theriak/Domino by Doug Tinkham (<http://dtinkham.net/peq.html>).

Bulk compositions used for the calculations were obtained by the area-scan method at SEM-EDS (JSM-7100 F scanning electron microscope, CMEBA, University Rennes 1) on parts of thin sections estimated to approach an equilibration volume and the results checked for robustness. FeO (vs. Fe₂O₃) was set so that the FeO/Fe₂O₃ ratio was equal to that of the bulk rock composition (analysed at the Geochemical and Petrographical Research Center, SARM

laboratory, CNRS-CRPG, Nancy; FeO measured by wet titration) unless otherwise stated. The bulk compositions used are indicated as insets in the diagrams in mole per cent normalized to 100% with the exception of H₂O which is indicated as an additional component.

A first P – T pseudosection (Fig. I.1.4) was calculated for a bulk composition measured on an area comprising garnet with inclusions of epidote, amphibole, omphacite and a proportion of matrix with diopside-amphibole-plagioclase bearing symplectite, Al-rich symplectite K-rich symplectite and albite blebs. The P – T pseudosection was contoured with compositional isopleth for garnet and amphibole in order to investigate the initial prograde metamorphism. In this diagram, epidote is stable below 20.5–24.5 kbar and 750°C. Isopleths corresponding to the composition of garnet core (alm47; prp23; grs28) and the lowest observed value for Al in amphibole (Al = 2.7 pfu) intersect in the field cpx-amp-g-ep-mu-q-ru around 650°C and 20 kbar. Decreasing grossular and almandine content together with an increasing pyrope content is compatible with increasing P – T conditions toward the stability field of kyanite and ultimately the epidote-absent field (cpx-amp-g-mu-ky-q-ru). This field is limited at higher pressures by the amphibole-out line between 650°C at 28 kbar and 750°C at 23 kbar. The flattening of the slope of pyrope, almandine and grossular zoning in the outer mantle suggests a curvature of the P – T path crossing the isopleths at lower angle and, consequently, a higher thermal gradient. Compositional isopleths for garnet 1 rim (alm36; prp40; grs21) intersect in the field cpx-amp-g-mu-ky-q-ru, close to the melt-in line around 22.5 kbar and 750°C. Lower pyrope and almandine, and higher grossular contents are consistent with garnet 2 crystallising in the melt stability field. Since melt incorporates a significant amount of water, and the topology of the pseudosection beyond the solidus is expected to be dependent of the availability of water, another P – T pseudosection has been calculated to investigate the evolution of the rock in this domain.

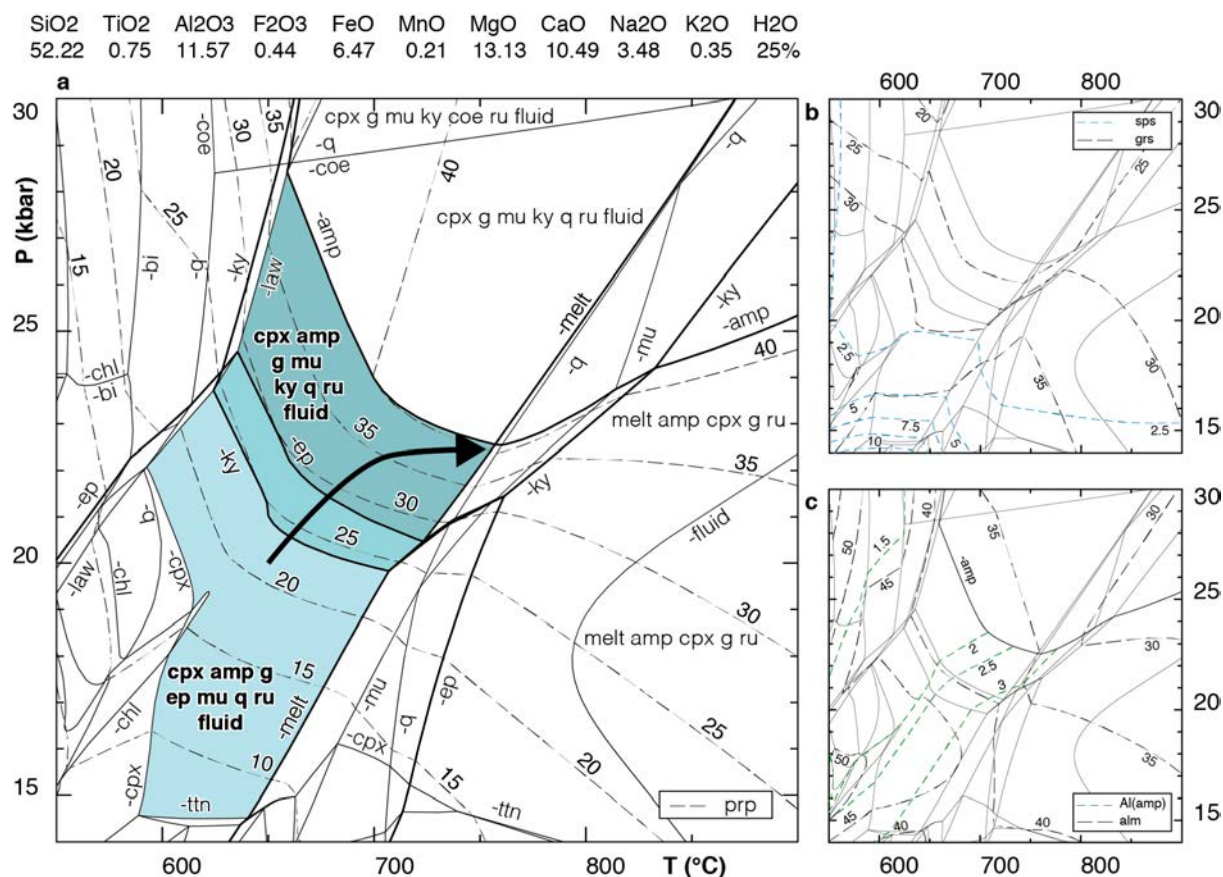


Figure I.1.4: P – T pseudosection calculated in the MnNCKFMASHTO system for a local bulk composition of a part of the sample measured by SEM, and compositional isopleths for garnet: pyrope (a); spessartine, grossular (b); almandine and Al content in amphibole (c). Coloured fields highlight the stability of the M1 assemblage with epidote, epidote-kyanite and kyanite. The arbitrary large amount of H_2O ensures that all the subsolidus assemblages are saturated in aqueous fluid.

In the second P – T pseudosection (Fig. I.1.5), the amount of H_2O is set so that at 750°C and 22.5 kbar, in the field cpx-amp-g-mu-ky-q-ru, the rock is just H_2O -saturated, i.e. contains about 1 volume % of free aqueous fluid. The resulting P – T pseudosection has been contoured with compositional isopleths for garnet and amphibole, as well as modal isopleths for garnet and clinopyroxene. Considering the M2 assemblage, the stability of plagioclase, muscovite or K-feldspar and kyanite is expected in a narrow band from 700°C at 15 kbar to 880°C at 20 kbar. Compositional isopleths corresponding to the composition of garnet 2 (alm36; prp38; grs26)

and amphibole (Al = 2.7 pfu) intersect in the field melt-amp-cpx-g-pl-ky-q-ru-mu/ksp between 850-900°C and 18.5-19.5 kbar.

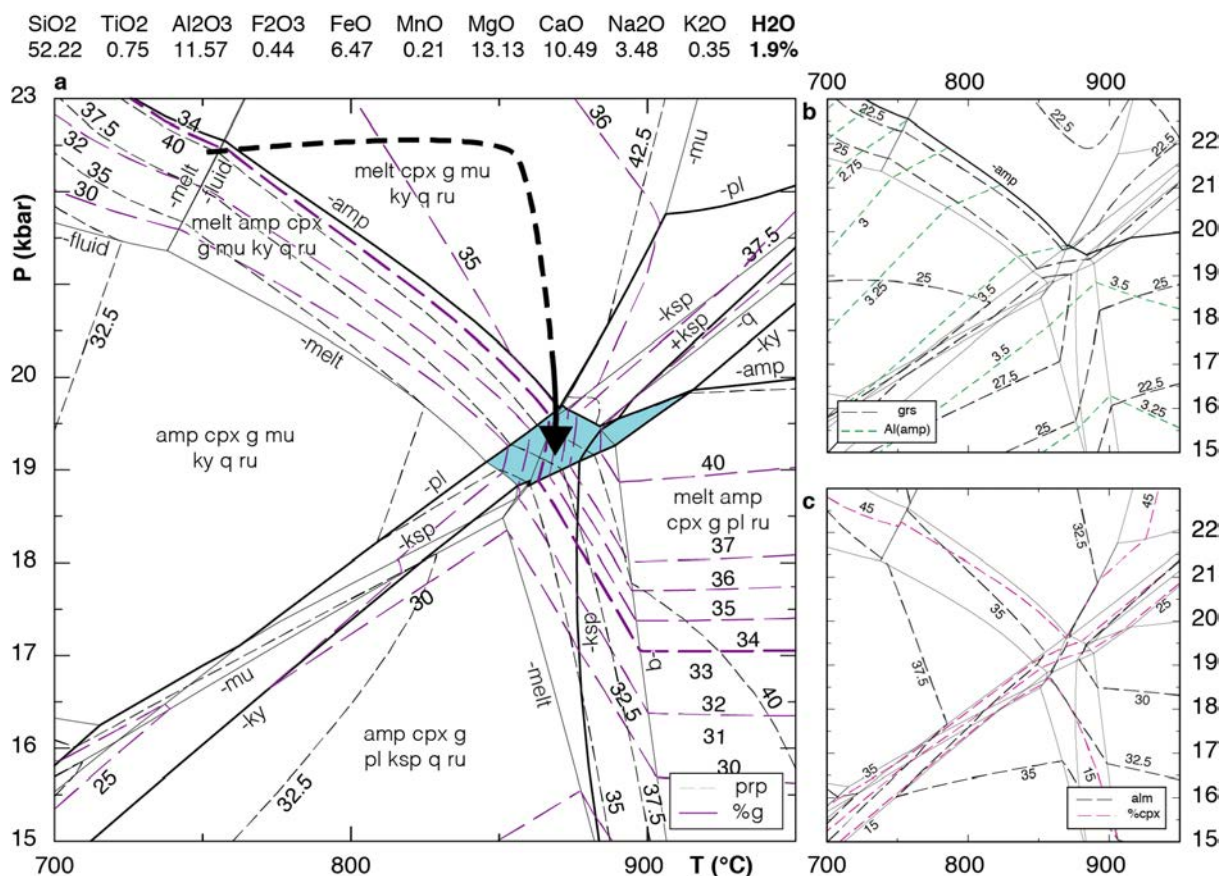


Figure I.1.5: P - T pseudosection for the same bulk composition as Fig.I.1.4 except for a limited amount of H_2O (see text for details). The diagram is contoured with modal isopleths for garnet (a) and clinopyroxene (c), and compositional isopleths for pyrope (a), grossular (b) and almandine (c) content in garnet, and aluminium content in amphibole (b).

However, it must be emphasized that a straight P - T path between the M1 peak conditions (750°C and 22.5 kbar) and the M2 conditions (c. 875°C and 19.5 kbar) could not account for the observations. Indeed, the peak M1 conditions were determined using the composition of the outermost rim of garnet 1. A straight P - T path would only result in decreasing the amount of garnet, so that the observed garnet 1 rim would have been lost during resorption. Garnet 1 must have then been larger before resorption. A likely explanation is that the rock underwent further heating (associated or not with slightly increasing pressure) to account for further increase of

garnet mode and growth of garnet 1. A subsequent decrease of pressure would allow the garnet mode to first decrease in the field melt-cpx-g-mu-ky-q-ru, accounting for the inferred resorption of garnet 1, but subsequently to increase in the plagioclase bearing field resulting in the growth of garnet 2. To account for the growth of garnet 2, the mode of garnet in the granulite-facies metamorphic stage M2 must be higher than the mode of garnet at the peak of M1 (750°C, 22.5 kbar), suggesting that the rock equilibrated at temperature higher than 870°C, in the field melt-amp-cpx-g-pl-ksp-ky-q-ru. This P – T path would also account for the anhedral shape of clinopyroxene at the garnet 1/garnet 2 boundary since clinopyroxene mode is very pressure-sensitive and expected to decrease with decreasing pressure. It also accounts for the renewed growth of amphibole (included in garnet 2).

A final pseudosection (Fig. I.1.6) has been calculated for the bulk composition of a small area of symplectite composed of diopside, amphibole, plagioclase and a small amount of quartz, inferred to mostly be the product of retrogression of former M1-M2 omphacite, in order to investigate the retrograde P – T path and the conditions of the M3 stage. The H₂O amount was arbitrarily fixed as equivalent to the previous P – T pseudosection and the X_{F3} ratio set in agreement with the ferric iron incorporated in omphacite at 19.5 kbar and 875°C (X_{F3} = 0.40). In the resulting diagram, the field corresponding to the observed assemblage (amp-cpx-pl-q) extends from 750°C to 875 °C and 3 kbar to 15 kbar. The observed ranges of composition for Al in amphibole (Al = 1.1-2.4) from the matrix are consistent with an equilibration pressure below 7 kbar in these fields delimiting a temperature range between 750°C and 850°C. Though less constraining, this is also in agreement with the observed Si in amphibole (Si = 6–7.2 pfu), Al in clinopyroxene (Al = 0–0.1 pfu) and albite content of plagioclase (an = 18-35).

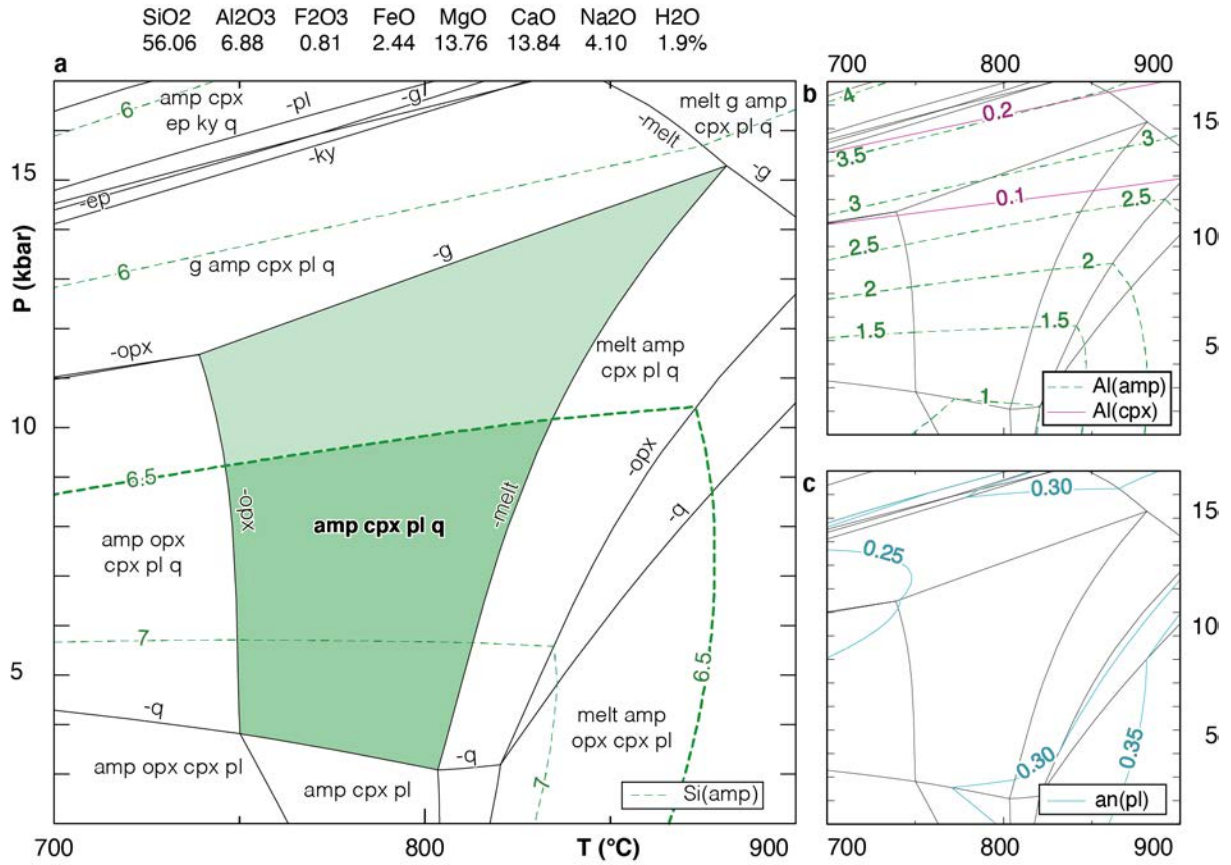


Figure I.1.6: *P–T* pseudosection calculated in the NCFMASHO system for a SEM measured bulk composition measured of a part of the amphibole-clinopyroxene-plagioclase-quartz symplectite from the matrix and compositional isopleth for silicium content in amphibole (a); aluminium content in amphibole and clinopyroxene (b); as well as albite content in plagioclase (c).

6. Discussion

6.1. *P–T evolution*

The metamorphic evolution of the studied sample is defined by three metamorphic stages. The M1 event is characterized by the development of a foliation in a garnet- and omphacite-bearing but plagioclase-free assemblages typical for eclogite-facies metamorphism. The inferred M2 assemblage includes garnet, clinopyroxene and plagioclase that represent a high-pressure granulite-facies metamorphism. The M3 stage is characterized by the widespread replacement of former crystals by diopside-amphibole-plagioclase- and corundum/spinel-plagioclase-bearing symplectites, suggesting an equilibration under HT amphibolite/LP granulite facies conditions. Taken together these events characterize a clockwise *P–T* path.

The M1 metamorphic stage can be traced through the inclusion suite in garnet. The progressive disappearance of hydrated phases – amphibole and epidote – from the core to the rim of garnet typifies prograde metamorphism from ~20 kbar – 650°C to ~22.5 kbar – 750°C, quantified using the compositional zoning of garnet. Further analysis of this growth zoning suggests that this metamorphic stage was initially dominated by burial (pressure increase), followed by heating (temperature increase).

Petrographic observations indicate that a portion of garnet grown during the M1 metamorphism was subsequently partly resorbed (Fig. I.1.7a). This leaves an uncertainty on the peak *P–T* conditions for this metamorphic event. However, two observations can be used to tentatively infer the trend of the missing portion of the *P–T* path: (i) the preserved trend of garnet growth zoning indicates a progressively flattening (dominated by heating) *P–T* path (Fig. I.1.4a), and (ii) the growth of garnet 2 requires either isothermal decompression or heating in the field melt-amp-cpx-g-pl-ksp-ky-q-ru (Fig. I.1.5a); garnet 2 could not have grown during cooling. Accordingly, unless the rock underwent an unusual pressure and temperature

evolution, one can assume that the peak P – T conditions for the M1 event did not significantly exceed 22.5 kbar and 880°C (Fig. I.1.7b).

Textural features suggest that garnet 2 was in equilibrium with plagioclase and amphibole, as well as kyanite, clinopyroxene, quartz and rutile preserved from the M1 stage. In addition, a K-rich mineral was also stable in this assemblage. Pseudosection modelling indicates that garnet mode decreases in the plagioclase free field but increases in a small field with plagioclase (light blue fields in Fig. I.1.5a) through a decrease of pressure, possibly associated with an increase of temperature. This path also accounts for the renewed growth of amphibole and the anhedral shape of clinopyroxene, both observed in garnet 2. The transition from the eclogite to the high-pressure granulite facies therefore results from a decompression associated or not with heating toward 19 kbar, 875°C following the significant temperature increase during M1 (Fig. I.1.7b).

The M3 metamorphism is evidenced by the pervasive replacement of the former high-pressure minerals by symplectites. Pseudosection modelling indicates a strong decompression along a steep retrograde P – T path associated with a slight to moderate cooling to <7 kbar, 750–850°C (Fig. I.1.7b). The shape of retrograde P – T paths is strongly controlled by the exhumation rate (e.g. Rey et al., 2009) suggesting a fast exhumation of this sample. In addition, short time at high temperature and fast cooling subsequent to the exhumation is strongly suggested from the preservation of garnet growth zoning (cf. Caddick et al., 2010).

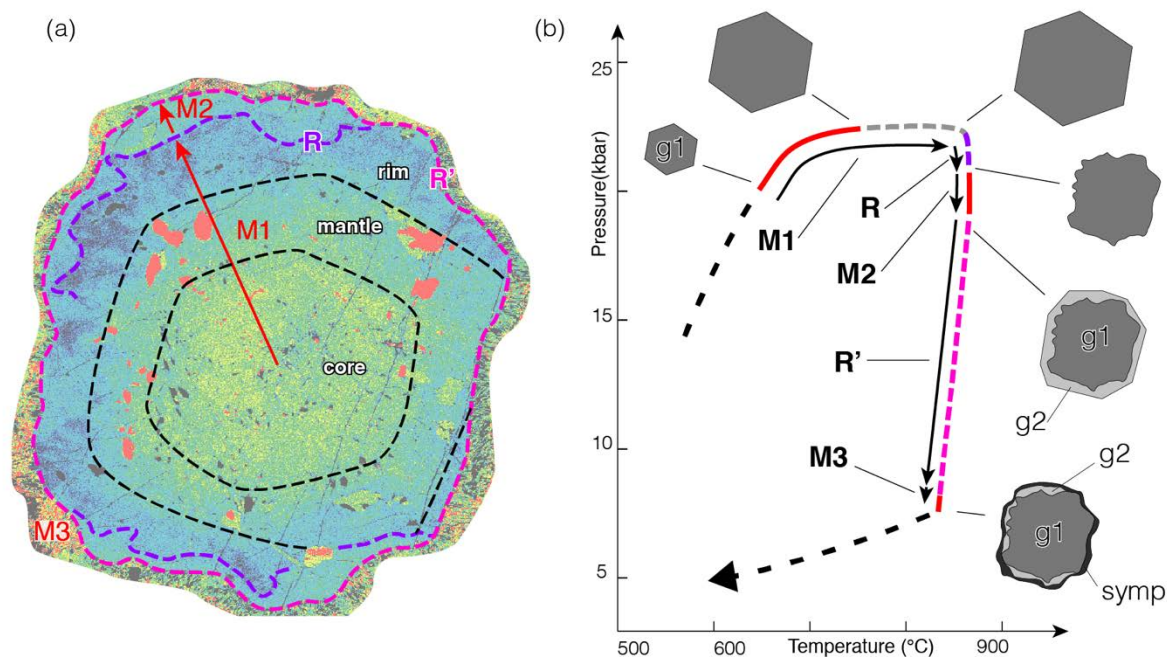


Figure I.1.7: (a) XRay map of calcium content in garnet showing the textural evidences of garnet growth and resorption sequence (same garnet grain as in figure. I.1.3). Concentric zones (core, mantle and rim) can be traced according to the inclusion pattern in garnet 1. Note that the resorption surface (R) is characterized by contrasting Ca content in garnet 1 rim and garnet 2. (R') marks the current contour of garnet. (b) Synthetic P - T path and schematic pictures of the inferred garnet growths and resorptions sequence.

6.2. Regional implications

Our data indicate high-pressure metamorphism, consistent with P conditions estimated in the area (20 kbar assuming a temperature of 800°C; Pin and Vielzeuf, 1988) as well as the discovery of coesite in the Monts-du-Lyonnais area (28 kbar; Lardeaux et al., 2001), and recent petrological works from other parts of the French Massif Central: the Limousin area (~29 kbar; Berger et al., 2010), the Najac massif (15-20 kbar; Lotout et al., 2017), the Lévêzeu massif (18-23 kbar; Lotout et al. submitted) and the Montagne Noire (21 kbar; Bretagne et al. submitted).

Fast exhumation and short residence times at high temperatures are suggested by the shape of the P - T path and the preservation of garnet growth zoning (e.g. Rötzler and Romer, 2001; O'Brien and Rötzler, 2003). Available geochronological data from similar samples of the same area, indicate a *c.* 430 Ma age for the eclogite facies metamorphism (Ducrot et al., 1983).

Subsequent crustal nappe stacking is inferred at *c.* 360 Ma (e.g. Schulz et al., 2014; Gardien et al., 2011). This is difficult to reconcile with the common interpretation of the exhumation of the HP bearing units coeval with continental collision and crustal nappe stacking (e.g. Burg and Matte, 1978). According to this interpretation, the exhumation of such eclogites resulted from a long process acting during several tens of millions of years. Meanwhile, the simple clockwise *P–T* path recorded by our sample does not reflect a polycyclic evolution, as proposed by Schulz (2014). A problematic point remains the evaluation of the HP event age. The age of the so-called eo-variscan subduction event (*c.* 430 Ma) has been recently challenged (Paquette et al., 2017; see further discussion in Lotout et al., 2017). Consequently, the eclogite-facies age of *c.* 430 Ma (Ducrot et al., 1983) has to be considered with caution.

Additionally, the peak temperature conditions indicate that the rock underwent partial melting. Although the detailed study of partial melting evidences is beyond the scope of this study (and is the aim of work in progress), it is noteworthy that kyanite-garnet-epidote bearing leucosomes in eclogites have been interpreted as high-pressure trondhjemites recording the partial melting of their host rocks in the Lévézou and Marvejols massifs, south of the studied area (Nicollet and Leyreloup, 1978). This suggests that conditions in agreement with the partial melting of the eclogites could be rather widespread at the peak *P–T* conditions in eclogites from the French Massif Central.

6.3. *Heat source and exhumation*

The inferred *P–T* path is characterised by strong heating followed by sub-isothermal exhumation. This agrees with published data that infer a LP-HT event following the HP metamorphism (Forestier et al., 1973). The LP-HT assemblages are coeval with the development of the regional foliation (Burg et al., 1984). Preservation of garnet growth zoning suggests that the whole heating/decompression/cooling cycle was short lived according to

diffusion modelling in garnet (Caddick et al., 2010). Taken together, these data indicate a strong heat pulse, shortly followed by decompression resulting in a regional scale syntectonic LP-HT.

Among the mechanisms controlling the thermicity of a steady-state subduction zone (Penniston-Dorland et al., 2015), shear-heating in the subduction channel might account for large scale heating (Gerya et al., 2008). However, only rocks that were juxtaposed with the asthenosphere are modelled to undergo significant temperature increase and reach temperatures comparable to those observed here. Consequently, the modelled strong heating does not result from shear heating but is rather controlled by the proximity of hot material from the asthenosphere. Alternative existing models involving shear heating explain a temperature rise of ~200 C (Duretz et al., 2014; Schmalholz & Duretz, 2015). These studies however focus on the process of nappe formation, which may not explain a synchronous temperature rise at the regional scale.

Dragovic et al. (2015) have documented roughly isobaric heating similar to our results. These authors interpreted this evolution as a consequence of (i) the decoupling of the rock from the subducting slab and its incorporation in a mantle wedge after Gerya et al. (2002) or, (ii) to the passage of the subducting slab to the maximum depth of decoupling of Wada and Wang (2009). The first proposition might not explain a regional HT event. Alternatively, in the second proposition, the heat flow is inferred to be brought by the mantle wedge flowing toward the subducted crust. However, as it stands, this interpretation does not explain the subsequent exhumation of the rocks. On the other hand, the regional HT metamorphism may be explained by the delamination of the lithospheric mantle from the subducted crust allowing heating asthenosphere flow (Brun and Faccena, 2008). Such process is expected to trigger the retreat of the subducting slab, that in turn, provokes the exhumation of the subducted rocks. Accordingly, such process may be invoked to explain the exhumation of the studied sample.

7. Conclusion

The studied sample records three metamorphic stages. M1 is characterized by garnet, omphacite and kyanite, without plagioclase, indicating eclogite-facies metamorphic conditions. The rimward disappearance of epidote and the decreasing proportion of amphibole in garnet 1 indicates a prograde metamorphism from 20 kbar and 650°C to, at least, 22.5 kbar and 750°C. The trend of garnet growth zoning indicates that the prograde path was first dominated by burial and then by heating. M2 is characterized by an association of garnet 2 and plagioclase together with clinopyroxene, typical for the HP granulite-facies metamorphism, that crystallized around 19.5 kbar and 875°C. The M3 stage is characterized by the replacement of former HP minerals by symplectites at <7 kbar and 750-850°C. This overall evolution defines a clockwise P – T path initially dominated by a pressure increase, then a heating and finally by a strong decompression. The relatively short duration of this P – T evolution and the probable subsequent fast cooling are suggested by the preservation of garnet growth zoning.

A strong heating (>200°C) encompasses the peak pressure conditions in eclogite-facies conditions and is followed by a fast exhumation, suggesting that current tectonic models for the French Massif Central may be questioned. Considering the regional character of the HT event and the P – T evolution of HP rocks, we suggest that the heating can be explained by crust-mantle delamination during subduction and the subsequent exhumation by the subsequent retreat of the trench.

Acknowledgments

This work benefited the support of the French geological survey (Bureau de Recherches Géologiques et Minières -BRGM). X. Le Coz is acknowledged for the efficient production of the thin sections. We are grateful for the assistance in SEM observations and EDS analyses of the staff of the CMEBA facility (ScanMAT, University Rennes 1), which received financial support from the Région Bretagne and the European Union (CPER-FEDER 2007-2014). We are also grateful to J. Langlade, for her assistance during the EPMA analysis (Microsonde Ouest, IFRMER, Brest-Plouzané, France).

References

- Berger J, Féménias O, Ohnenstetter D, Bruguier O, Plissart G, et al. 2010. New occurrence of UHP eclogites in Limousin (French Massif Central): Age, tectonic setting and fluid–rock interactions. *Lithos*. 118(3–4):365–82
- Brun J-P, Faccenna C. 2008. Exhumation of high-pressure rocks driven by slab rollback. *Earth and Planetary Science Letters*. 272(1–2):1–7
- Burg JP, Leyreloup A, Marchand J, Matte P. 1984. Inverted metamorphic zonation and large-scale thrusting in the Variscan Belt: an example in the French Massif Central. *Geological Society, London, Special Publications*. 14(1):47–61
- Burg JP, Matte PJ. 1978. A Cross Section through the French Massif Central and the Scope of its Variscan Geodynamic Evolution. *Zeitschrift der Deutschen Geologischen Gesellschaft*. 429–60
- Caddick MJ, Konopásek J, Thompson AB. 2010. Preservation of Garnet Growth Zoning and the Duration of Prograde Metamorphism. *J. Petrology*. 51(11):2327–47
- Couzinié S, Laurent O, Poujol M, Mintrone M, Chelle-Michou C, et al. 2017. Cadomian S-type granites as basement rocks of the Variscan belt (Massif Central, France): Implications for the crustal evolution of the north Gondwana margin. *Lithos*. 286(Supplement C):16–34

- de Capitani C, Brown TH. 1987. The computation of chemical equilibrium in complex systems containing non-ideal solutions. *Geochimica et Cosmochimica Acta*. 51(10):2639–52
- de Capitani C, Petrakakis K. 2010. The computation of equilibrium assemblage diagrams with Theriak/Domino software. *American Mineralogist*. 95(7):1006–16
- Dragovic B, Baxter EF, Caddick MJ. 2015. Pulsed dehydration and garnet growth during subduction revealed by zoned garnet geochronology and thermodynamic modeling, Sifnos, Greece. *Earth and Planetary Science Letters*. 413:111–22
- Ducrot J, Lancelot JR, Marchand J. 1983. Datation U-Pb sur zircons de l'éclogite de La Borie (Haut-Allier, France) et conséquences sur l'évolution ante-hercynienne de l'Europe occidentale. *Earth and Planetary Science Letters*. 62(3):385–94
- Duretz T, Schmalholz SM, Podladchikov YY, Yuen DA. 2014. Physics-controlled thickness of shear zones caused by viscous heating: Implications for crustal shear localization. *Geophysical Research Letters*. 41(14):4904–11
- Forestier FH, Lasnier B. 1969. Découverte de niveaux d'amphibolites à pargasite, anorthite, corindon et saphirine dans les schistes cristallins de la vallée du Haut-Allier. *Contr. Mineral. and Petrol*. 23(3):194–235
- Forestier FH, Lasnier B, Leyreloup A, Marchand J. 1973. Vues nouvelles sur la catazone dans le Massif Central français et le Massif Armoricaïn, de l'affleurement au Moho. *Bulletin de la Société Géologique de France*. S7-XV(5–6):562–78
- Gardien V, Vanderhaeghe O, Arnaud N, Cocherie A, Grange M, Lécuyer C. 2011. Thermal maturation and exhumation of a middle orogenic crust in the Livradois area (French Massif Central). *Bulletin de la Société Géologique de France*. 182(1):5–24
- Gerya TV, Perchuk LL, Burg J-P. 2008. Transient hot channels: Perpetrating and regurgitating ultrahigh-pressure, high-temperature crust–mantle associations in collision belts. *Lithos*. 103(1):236–56
- Gerya TV, Stöckhert B, Perchuk AL. 2002. Exhumation of high-pressure metamorphic rocks in a subduction channel: A numerical simulation. *Tectonics*. 21(6):6-1-6–19
- Giraud A, Marchand J, Dupuy C, Dostal J. 1984. Geochemistry of leptyno-amphibolite complex from Haut Allier (French Massif Central). *Lithos*. 17:203–14

- Green ECR, White RW, Diener JFA, Powell R, Holland TJB, Palin RM. 2016. Activity-composition relations for the calculation of partial melting equilibria in metabasic rocks. *Journal of Metamorphic Geology*. 34(9):845–69
- Holland T, Powell R. 2003. Activity–composition relations for phases in petrological calculations: an asymmetric multicomponent formulation. *Contrib Mineral Petrol*. 145(4):492–501
- Holland TJB, Powell R. 2011. An improved and extended internally consistent thermodynamic dataset for phases of petrological interest, involving a new equation of state for solids. *Journal of Metamorphic Geology*. 29(3):333–83
- Lardeaux JM. 2014. Deciphering orogeny: a metamorphic perspective Examples from European Alpine and Variscan belts. *Bulletin de la Société Géologique de France*. 185(5):281–310
- Lardeaux JM, Ledru P, Daniel I, Duchene S. 2001. The Variscan French Massif Central—a new addition to the ultra-high pressure metamorphic ‘club’: exhumation processes and geodynamic consequences. *Tectonophysics*. 332(1–2):143–67
- Lasnier B. 1968. Decouverte de roches eclogitiques dans le groupe leptyno-amphibolique des Monts du Lyonnais (Massif Central francais). *Bulletin de la Société Géologique de France*. S7-X(2):179–85
- Laurent O, Couzinié S, Zeh A, Vanderhaeghe O, Moyen JF, et al. 2017. Protracted, coeval crust and mantle melting during Variscan late-orogenic evolution: U–Pb dating in the eastern French Massif Central. *Int J Earth Sci (Geol Rundsch)*. 106(2):421–51
- Leake BE, Woolley AR, Arps CES, Birch WD, Gilbert MC, et al. 1997. Nomenclature of amphiboles; Report of the Subcommittee on Amphiboles of the International Mineralogical Association, Commission on New Minerals and Mineral Names. *American Mineralogist*. 82(9–10):1019–37
- Lotout C, Pitra P, Poujol M, Anczkiewicz R, Van Den Driessche J. 2018. Timing and duration of Variscan high-pressure metamorphism in the French Massif Central: A multimethod geochronological study from the Najac Massif. *Lithos*. 308–309:381–94
- Lotout C, Pitra P, Poujol M, Driessche JVD. 2017. Ordovician magmatism in the Lévézou massif (French Massif Central): tectonic and geodynamic implications. *Int J Earth Sci (Geol Rundsch)*. 106(2):501–15

- Nicollet C, Leyreloup A. 1978. Pétrologie des niveaux trondhjémiques de haute pression associés aux éclogites et amphibolites des complexes leptyno-amphiboliques du Massif Central français. *Canadian Journal of Earth Sciences*. 15(5):696–707
- O'Brien PJ, Rötzler J. 2003. High-pressure granulites: formation, recovery of peak conditions and implications for tectonics. *Journal of Metamorphic Geology*. 21(1):3–20
- Paquette JL, Ballèvre M, Peucat JJ, Cornen G. 2017. From opening to subduction of an oceanic domain constrained by LA-ICP-MS U-Pb zircon dating (Variscan belt, Southern Armorican Massif, France). *Lithos*. 294–295:418–37
- Penniston-Dorland SC, Kohn MJ, Manning CE. 2015. The global range of subduction zone thermal structures from exhumed blueschists and eclogites: Rocks are hotter than models. *Earth and Planetary Science Letters*. 428:243–54
- Pin C, Vielzeuf D. 1988. Les granulites de haute-pression d'Europe moyenne temoins d'une subduction eo-hercynienne; implications sur l'origine des groupes leptyno-amphiboliques. *Bulletin de la Société Géologique de France*. IV(1):13–20
- Rötzler J, Romer RL. 2001. P–T–t Evolution of Ultrahigh-Temperature Granulites from the Saxon Granulite Massif, Germany. Part I: Petrology. *J Petrology*. 42(11):1995–2013
- Santallier D, Briand B, Menot RP, Piboule M. 1988. Les complexes leptyno-amphiboliques (CLA): revue critique et suggestions pour un meilleur emploi de ce terme. *Bull Soc Géol Fr*. 1:3–12
- Schmalholz SM, Duretz T. 2015. Shear zone and nappe formation by thermal softening, related stress and temperature evolution, and application to the Alps. *Journal of Metamorphic Geology*. 33(8):887–908
- Schulz B. 2014. Early Carboniferous P–T path from the Upper Gneiss Unit of Haut-Allier (French Massif Central) - reconstructed by geothermobarometry and EMP-Th-U-Pb monazite dating. *J Geosci*. 59(4):327–49
- Schulz B, Triboulet C, Audren C, Feybesse J-L. 1996. Zoned garnets in metapelites and P–T-deformation path interpretation of the Variscan inverted metamorphic sequence of Haut-Allier, French Massif Central. *Zeitschrift der Deutschen Geologischen Gesellschaft*. 249–73
- Wada I, Wang K. 2009. Common depth of slab-mantle decoupling: Reconciling diversity and uniformity of subduction zones. *Geochemistry, Geophysics, Geosystems*. 10(10):

- White RW, Powell R, Clarke GL. 2002. The interpretation of reaction textures in Fe-rich metapelitic granulites of the Musgrave Block, central Australia: constraints from mineral equilibria calculations in the system $K_2O-FeO-MgO-Al_2O_3-SiO_2-H_2O-TiO_2-Fe_2O_3$. *Journal of Metamorphic Geology*. 20(1):41–55
- White RW, Powell R, Holland TJB, Johnson TE, Green ECR. 2014a. New mineral activity–composition relations for thermodynamic calculations in metapelitic systems. *Journal of Metamorphic Geology*. 32(3):261–86
- White RW, Powell R, Holland TJB, Worley BA. 2000. The effect of TiO_2 and Fe_2O_3 on metapelitic assemblages at greenschist and amphibolite facies conditions: mineral equilibria calculations in the system $K_2O-FeO-MgO-Al_2O_3-SiO_2-H_2O-TiO_2-Fe_2O_3$. *Journal of Metamorphic Geology*. 18(5):497–511
- White RW, Powell R, Johnson TE. 2014b. The effect of Mn on mineral stability in metapelites revisited: new a–x relations for manganese-bearing minerals. *Journal of Metamorphic Geology*. 32(8):809–28

Table I.1.1: Table of representative analysis of minerals from the host rock of the sample BR18

Mx. Pos. #Anal.	g C 10p1 - 62	g C-M 10p1- 41	g M-R 10p1- 13	g R 10p1-3	cpx in g 10- 013b	cpx S mtx 12-014	ep in g 7005	amp in g 10-03	amp S mtx 9020	amp g crn 8003	pl S mtx 3007	pl g crn 8002	pl S Al 9001	pl Ab blb 10-09	ilm mtx 3002	mu in g 2052p	mu mtx 4010	sp S Al 9006	sph 3003	bi S K 4019
SiO2	39.01	39.06	39.95	39.78	55.99	55.87	38.77	40.16	49.14	40.63	61.89	55.84	44.52	68.45	0.02	57.09	47.31	0.12	30.04	35.20
TiO2	0.09	0.01	0.03	0.00	0.00	0.00	0.03	0.00	0.41	0.10	0.00	0.00	0.00	0.00	54.40	0.00	0.00	0.00	39.77	1.84
Al2O3	21.93	22.04	22.81	22.57	11.23	1.25	32.28	19.95	7.73	17.87	24.35	28.08	35.64	18.79	0.06	20.26	37.10	62.72	0.99	19.29
Cr2O3	0.00	0.00	0.03	0.01	0.00	0.00	0.00	0.00	0.09	0.04	0.00	0.00	0.00	0.00	0.01	0.00	0.00	0.18	0.00	0.06
NiO	0.02	0.00	0.00	0.00	0.05	0.00	0.00	0.05	0.04	0.04	0.00	0.00	0.00	0.00	0.02	0.09	0.04	0.06	0.00	0.07
MgO	5.90	6.10	10.64	10.46	9.72	15.83	0.03	10.07	17.18	12.78	0.01	0.01	0.01	0.00	3.15	4.18	0.08	11.71	0.08	16.38
FeO	23.09	22.80	19.95	18.47	3.25	5.22	2.45	13.97	9.18	11.74	0.17	0.14	0.00	0.00	42.28	5.03	0.12	25.23	0.24	12.76
MnO	1.10	0.88	0.37	0.36	0.02	0.00	0.08	0.13	0.15	0.19	0.01	0.01	0.00	0.00	0.67	0.07	0.00	0.24	0.01	0.04
CaO	10.35	10.59	7.80	9.75	15.39	21.82	24.54	10.93	11.70	11.41	5.62	9.93	19.14	0.00	0.01	0.18	0.69	0.21	28.74	0.10
P2O5	0.02	0.00	0.00	0.04	0.04	0.00	0.00	0.00	0.01	0.01	0.03	0.04	0.00	0.00	0.03	0.01	0.00	0.03	0.00	0.00
Na2O	0.02	0.05	0.01	0.00	5.82	0.00	0.00	2.55	1.33	2.63	8.55	6.07	0.90	12.76	0.01	0.35	1.00	0.01	0.01	0.86
K2O	0.00	0.00	0.00	0.01	0.00	0.00	0.00	0.17	0.28	0.53	0.12	0.01	0.01	0.00	0.00	10.63	8.87	0.00	0.01	8.47
Sum	101.51	101.54	101.59	101.45	101.52	99.99	98.19	97.98	97.24	97.97	100.77	100.14	100.22	100.00	100.65	97.88	95.22	100.50	99.90	95.07
Si	2.97	2.97	2.96	2.94	1.95	2.03	2.95	5.83	6.99	5.86	2.73	2.51	2.05	3.00	0.00	3.74	3.10	0.00	0.98	2.60
Ti	0.01	0.00	0.00	0.00	0.00	0.00	0.00	0.00	0.04	0.01	0.00	0.00	0.00	0.00	1.00	0.00	0.00	0.00	0.98	0.10
Al	1.97	1.97	1.99	1.97	0.47	0.05	2.90	3.41	1.30	3.04	1.27	1.49	1.94	0.97	0.00	1.56	2.87	1.96	0.04	1.68
Cr	0.00	0.00	0.00	0.00	0.00	0.00	0.00	0.00	0.01	0.00	0.00	0.00	0.00	0.00	0.00	0.00	0.00	0.00	0.00	0.00
Fe3	0.08	0.11	0.10	0.15	0.04	0.00	0.16	0.50	0.43	0.63	0.00	0.00	0.00	0.00	0.00	0.00	0.00	0.03	0.00	0.00
Ni	0.00	0.00	0.00	0.00	0.00	0.00	0.00	0.01	0.00	0.01	0.00	0.00	0.00	0.00	0.00	0.01	0.00	0.00	0.00	0.00
Mg	0.67	0.69	1.17	1.15	0.50	0.86	0.00	2.18	3.64	2.75	0.00	0.00	0.00	0.00	0.12	0.41	0.01	0.46	0.00	1.80
Fe2	1.39	1.34	1.14	1.00	0.06	0.16	0.00	1.20	0.66	0.79	0.01	0.01	0.00	0.00	0.87	0.28	0.01	0.53	0.01	0.79
Mn	0.07	0.06	0.02	0.02	0.00	0.00	0.01	0.02	0.02	0.02	0.00	0.00	0.00	0.00	0.01	0.00	0.00	0.01	0.00	0.00
Ca	0.84	0.86	0.62	0.77	0.57	0.85	2.00	1.70	1.78	1.77	0.27	0.48	0.95	0.00	0.00	0.01	0.05	0.01	1.01	0.01
P	0.00	0.00	0.00	0.00	0.00	0.00	0.00	0.00	0.00	0.00	0.00	0.00	0.00	0.00	0.00	0.00	0.00	0.00	0.00	0.00
Na	0.00	0.01	0.00	0.00	0.41	0.00	0.00	0.72	0.37	0.74	0.73	0.53	0.08	1.09	0.00	0.04	0.13	0.00	0.00	0.12
K	0.00	0.00	0.00	0.00	0.00	0.00	0.00	0.03	0.05	0.10	0.01	0.00	0.00	0.00	0.00	0.89	0.74	0.00	0.00	0.80
OH							1.00	2.00	2.00	2.00						2.00	2.00			2.00
Sum	8.00	8.00	8.00	8.00	4.00	3.95	8.02	17.59	15.30	17.71	5.01	5.01	5.02	5.06	0.00	8.94	8.90	3.00	3.02	7.91
XMg	0.33	0.34	0.51	0.54	0.90	0.84		0.65	0.85	0.78					0.12	0.60		0.47	0.36	0.70
alm/Na(A)	0.47	0.45	0.39	0.34				0.55	0.25	0.61										
prp/ab	0.23	0.23	0.40	0.39							0.73	0.52	0.08	1.00						
grs/an/jd	0.28	0.29	0.21	0.26	0.41	0.00					0.26	0.47	0.92	0.00						
sps/or	0.02	0.02	0.01	0.01							0.01	0.00	0.00	0.00						

Abbreviation: Ab blb – Albite bleb, C – core, g crn – corona around garnet, in g – inclusion in garnet, M – mantle, Mx. Mineral, Pos. – Position, R – rim, S mtx- matrix symplectite, S

Al – Al-rich symplectite after kyanite, S K – K-rich symplectite after muscovite, #Anal. – Analysis number.

**Petrogenetic investigations of garnet-rich layers in eclogites:
evidence of partial melting at high pressure?**

(Article in prep)

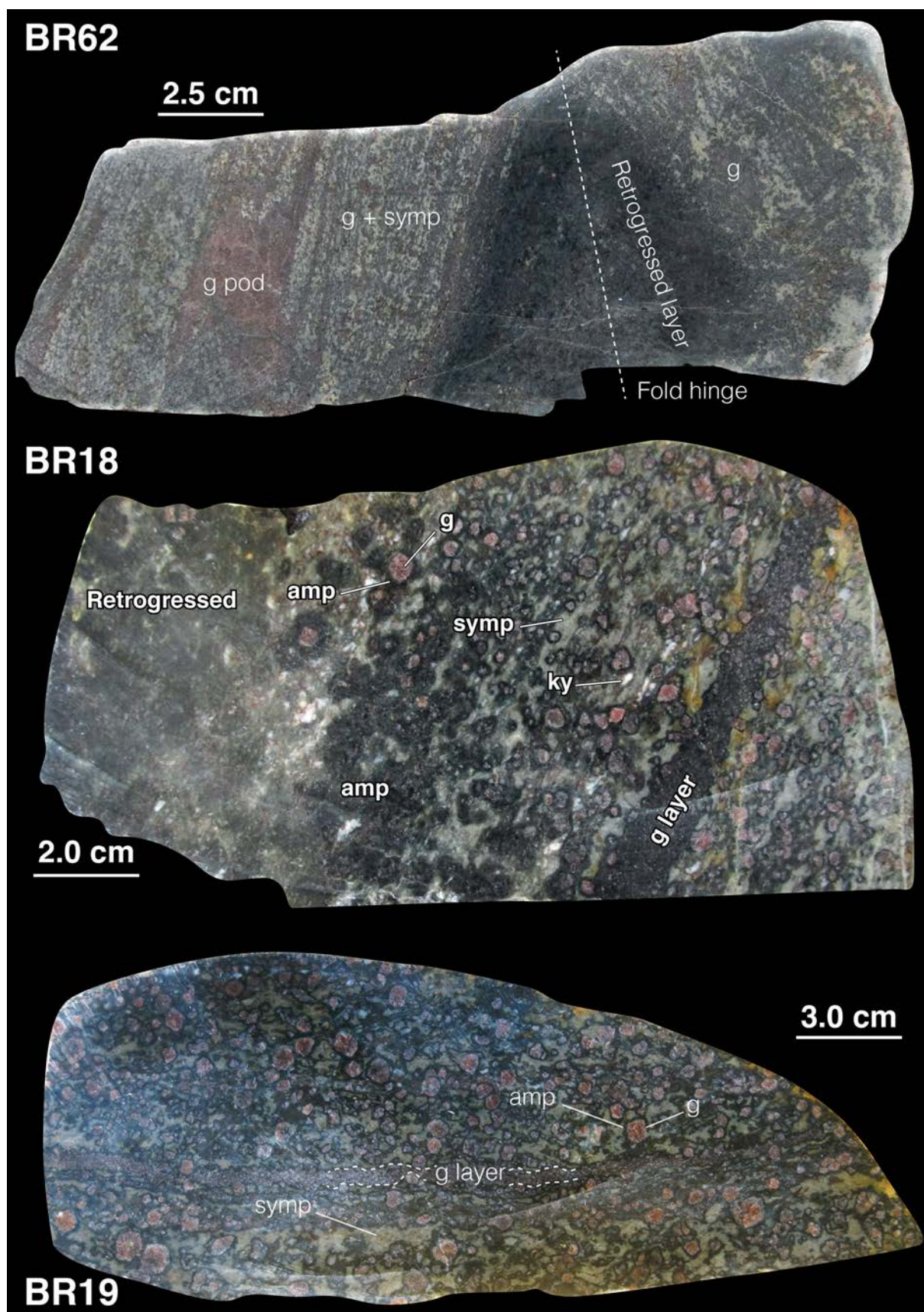
1. Introduction

The studied eclogite contains garnet-rich layers (Fig. I.2.1). Similar layers in mafic granulite facies rocks have been reported worldwide and variably interpreted either in terms of metamorphism of an originally layered cumulate (e.g. Yang et al., 2008; Konzett et al., 2005) or as residuum after partial melting of the protolith (e.g. Yamamoto and Yoshino, 1998; Daczko et al., 2001; Angiboust et al., 2017; Shchipansky et al., 2012; Cao et al., 2019). Whether a garnet-rich layer is the result of the metamorphism of a cumulate inherited from a previous magmatic history, or of the partial melting of the rock during the metamorphism obviously involve various processes with different magmatic, metamorphic and tectonic implications.

The garnet-rich layers in the Haut-Allier have been first reported by Lasnier (1977) but their petrogenetic significance is unknown. The pioneer geochemical study of Giraud (1984) pointed out the cumulate character of some amphibolite with high Al_2O_3 or CaO as well as low TiO_2 and FeO_{tot} interpreted as plagioclase-rich cumulates. On the other hand, trondhjemites associated with eclogites have been reported in the French Massif Central and interpreted as high-pressure melts (Nicollet and Leyreloup, 1978). In addition, temperatures compatible with a suprasolidus evolution of the eclogites are common (Fig. I.2.2). Accordingly, both hypotheses are likely. In the next section, we present the result of a geochemical, petrographic and petrologic study, using phase equilibrium modelling in order to explore both hypotheses.

Figure I.2.1 (next page): Photographs of samples with garnet rich layers. BR62 – Fine-grained layered eclogite (Field photographs Fig. I.2a, b). BR18 and BR19 – Coarser grained eclogite (Field photographs Fig. I.2c, d).

The samples are variously retrogressed.



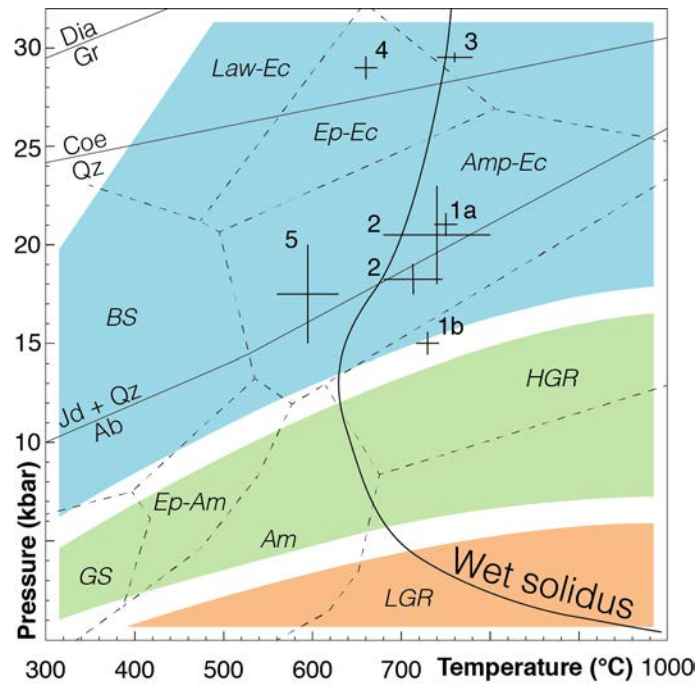
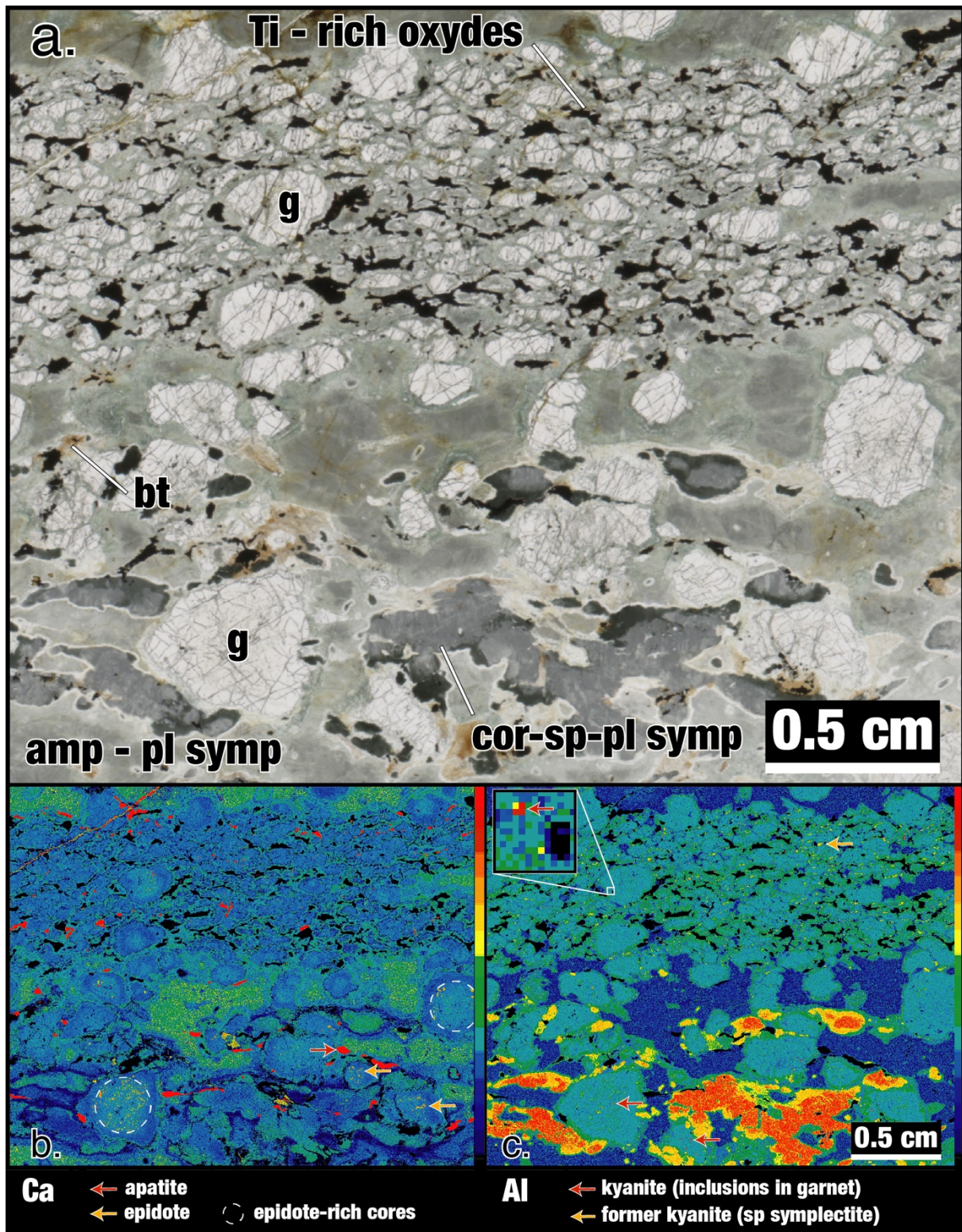


Figure I.2.2: Recent P - T conditions data on eclogite. Montagne Noire: 1a – 21 kbar-750°C (P - T pseudosection) after Bretagne et al. (submitted); 1b – 15 kbar-725°C (P - T pseudosection) after Whitney et al. (2015); Lézou: 2 – 18-23 – 680-800°C and 17.5-19kbar 680-750°C (P - T pseudosection) after Lotout et al. (submitted); Lyonnais: 3 – 29kbar 740-780°C (conventional thermobarometry) after Lardeaux et al. (2001); Limousin: 4 – 29 kbar-660°C (conventional thermobarometry) after Berger et al. (2010); Najac: 5 – 15-20kbar-560-630°C. Subdivision of eclogite-facies and reaction curves diamond = graphite, coesite = quartz and jadeite + quartz = albite from Bundy (1980), Chopin (1984), Holland (1980). Wet solidus for basalt solidus after Lambert and Wyllie (1972). AM, amphibolites facies; Amp-EC, amphibole eclogite facies; BS, blueschist facies; Dry-EC, dry eclogite facies; EA, epidote amphibolites facies; GS, greenschist facies; HGR, high-pressure granulite facies; LGR, low-pressure granulite facies; Lws-EC, lawsonite eclogite facies; Zo-EC zoisite eclogite facies.

2. Petrography and mineral chemistry of the garnet-rich layer

Garnet-rich layers occur within the eclogite (“host rock”) that contains garnet (25-35%), clinopyroxene (50-65%), kyanite (15-5%), rutile (~1%), muscovite/K-feldspar (~1%) as well as a small amount of quartz. Comparatively, the garnet-rich layer is enriched in garnet (~70-

75%) and Ti-rich minerals (rutile and ilmenite; 5-10%), contains less former kyanite (~1-2%) and clinopyroxene (10-20%). It also contains abundant zircon and apatite as accessory minerals.



Chapter I – Section 2

Fig. I.2.3 (previous page): Photomicrograph (a) and X-Ray map for Ca (b) and Al (c). Compare the zoning of the medium grained garnet labelled “g” from the garnet rich layer with the larger garnet from the host rock (see profile in Fig. I.2.4). Most of the smaller garnets in the garnet-rich layer lack a Ca-rich core and have Ca content similar to that of the rim of the medium-sized crystals.

Most of the garnets crystals are small-sized (150µm) but some reaches up (300µm). The larger garnets are characterized by a core with epidote, rutile and amphibole inclusions, a mantle with kyanite and rutile inclusions and a rim free of inclusions. Garnet crystals are surrounded by a corona of amphibole ($X_{\text{Si}} = 5.5\text{-}5.8$; $X_{\text{Mg}} = 0.79\text{-}0.89$) and plagioclase (an50-80) symplectite. The garnet-rich layer also contains to a lesser extent amphibole plagioclase symplectite that does not form coronas around garnet suggesting that it could result from the breakdown of former omphacite. A small amount of spinel-bearing symplectite is also observed and interpreted. Kyanite is included in garnet, consequently, the spinel-bearing symplectites may be the breakdown product of kyanite. Ilmenite commonly surrounds rutile, suggesting a later development at the expense of rutile; rutile is interpreted to have been the only Ti-oxide in equilibrium with the peak-pressure eclogite facies assemblage (g-cpx-ky-mu-q-ru).

The chemical composition of garnet core is similar to that of garnet mantle from the host rock (grs28, prp35, alm36; Fig. I.2.4). The mantle displays a decreasing grossular content (grs20) and increasing pyrope (prp41) and almandine (alm38) contents. The rim is characterized by lower almandine (alm33) and pyrope (prp38) contents associated with a higher grossular (grs26) content.

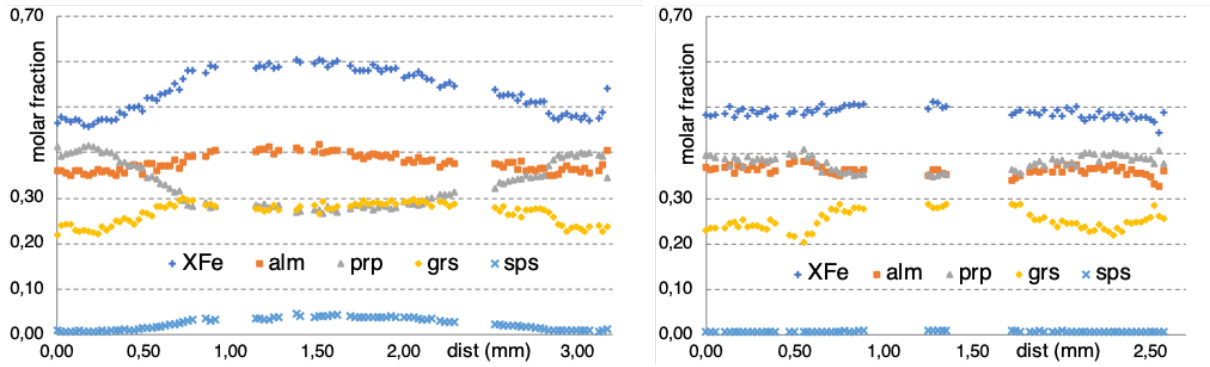


Figure I.2.4: Chemical zoning profile in garnet from the host rock (left) and the garnet-rich layer (b).

Fig. I.2.5 shows the relative major elements depletion and enrichment of the garnet-rich layer relative to the host rock. On the one hand, the garnet-rich layer is depleted in SiO_2 , Al_2O_3 , CaO , Na_2O , K_2O and strongly enriched in TiO_2 , MnO , FeO_{tot} and MgO in the other one. The chemical composition is given in Table I.2.2.

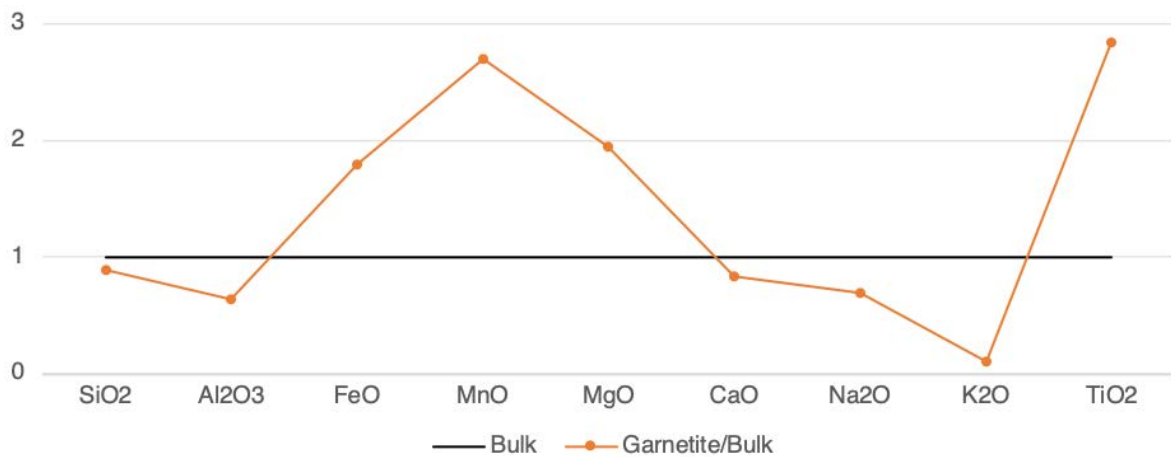


Figure I.2.5: Composition of the garnet-rich layer normalized to the bulk rock composition for comparison. The garnet-rich layer composition is a SEM measured composition obtained on an area of the garnet-rich layer

Chapter I – Section 2

Table I.2.1: Table of representative analysis of minerals from the garnet-rich layer of the sample BR18

Mx Pos. #Anal.	g C 1052	g M 1022	g R 1097	ep in g 1006	amp S mtx 1023	amp g crn 1013	pl S mtx	pl g crn 1017
SiO ₂	39.89	39.91	39.93	38.84	40.52	39.10	55.45	46.77
TiO ₂	0.03	0.00	0.00	0.14	0.13	0.03	0.00	0.00
Al ₂ O ₃	22.44	22.58	22.93	30.32	18.68	22.03	28.78	33.17
Cr ₂ O ₃	0.00	0.00	0.00	0.00	0.00	0.00	0.00	0.00
NiO	0.00	0.00	0.08	0.00	0.00	0.00	0.00	0.03
MgO	9.51	10.94	10.32	0.22	13.29	16.81	0.04	0.62
FeO	18.29	19.17	17.92	4.42	10.77	15.53	0.19	0.78
MnO	0.43	0.39	0.35	0.10	0.13	0.31	0.03	0.03
CaO	10.47	7.56	9.59	24.12	10.96	0.79	10.73	16.29
P ₂ O ₅	0.01	0.07	0.02	0.03	0.02	0.04	0.01	0.02
Na ₂ O	0.00	0.00	0.02	0.00	2.94	3.13	5.77	2.21
K ₂ O	0.01	0.00	0.03	0.00	0.06	0.00	0.01	0.00
Sum	101.08	100.62	101.19	98.20	97.49	97.78	101.00	99.92
Si	3.0	3.0	3.0	3.0	5.8	5.5	2.5	2.2
Ti	0.0	0.0	0.0	0.0	0.0	0.0	0.0	0.0
Al	2.0	2.0	2.0	2.7	3.2	3.7	1.5	1.8
Cr	0.0	0.0	0.0	0.0	0.0	0.0	0.0	0.0
Fe ₃	0.1	0.1	0.1	0.3	0.7	1.0		
Ni	0.0	0.0	0.0	0.0	0.0	0.0	0.0	0.0
Mg	1.1	1.2	1.1	0.0	2.8	3.5	0.0	0.0
Fe ₂	1.1	1.1	1.0		0.6	0.9	0.0	0.0
Mn	0.0	0.0	0.0	0.0	0.0	0.0	0.0	0.0
Ca	0.8	0.6	0.8	2.0	1.7	0.1	0.5	0.8
P	0.0	0.0	0.0	0.0	0.0	0.0	0.0	0.0
Na	0.0	0.0	0.0	0.0	0.8	0.9	0.5	0.2
K	0.0	0.0	0.0	0.0	0.0	0.0	0.0	0.0
OH				1.0	2.0	2.0		
Sum	8.0	8.0	8.0	9.0	15.7	17.6	5.0	5.0
XMg	0.50	0.48	0.47		0.82	0.81		
alm/Na(A)	0.35	0.38	0.35	0.28	0.65	0.57		
prp/ab	0.35	0.41	0.39				0.49	0.20
grs/an/jd	0.28	0.20	0.26				0.51	0.80
sps/or	0.01	0.01	0.01				0.00	0.00

Abbreviation: C – core, g crn – corona around garnet, in g – inclusion in garnet, M – mantle, Mx. Mineral,

Pos. – Position, R – rim, S mtx- matrix symplectite, #Anal. – Analysis number.

Chapter I – Section 2

Table 1.2.2: Bulk composition of the host-rock, garnet-rich layer and modelled melt at 850°C – 22.5 kbar using the with 9.5% H₂O added to the bulk rock composition (see text for details). The bulk host-rock and garnet-rich layer are compositions used for P–T pseudosection calculations. Note that the bulk compositions are normalized to 100% for better comparison.

	Host-rock SEM-measured	Garnet Layer SEM-measured	Modelled Melt 850°C - 22.5 kbar
SiO ₂	48.35	43.26	74.88
Al ₂ O ₃	20.50	13.04	13.16
FeO(tot)	7.42	13.35	0.12
MnO	0.11	0.31	0.00
MgO	7.78	15.18	0.12
CaO	11.09	9.30	2.68
Na ₂ O	2.82	1.96	6.84
K ₂ O	0.97	0.10	2.20
TiO ₂	0.94	2.68	0.00
XMg	0.51	0.53	0.49
A/NK			1.46
A/CNK			1.27

3. Pseudosection

During the pseudosection modelling, we realized two sets of pseudosections. On the one hand, if the garnet-rich layer represents a former cumulate, the P – T evolution inferred from a pseudosection calculated using the bulk composition of the layer (measured over a representative area) should be consistent with the P – T path previously determined for the host rock. On the other hand, if the garnet-rich layer result from the modification (by partial melting) of a protolith similar to the host rock, the same bulk rock composition the variable degree of H_2O added should allow variable degree of partial melting and to reproduce the first order observations (i.e. mode of minerals). Accordingly, P – T and $TX(H_2O)$ pseudosection were constructed to explore these first order considerations.

3.1. Pseudosection investigation of a magmatic origin

In order to investigate the possibility that the garnet rich layers represent an initial heterogeneity of the protolith, a P – T pseudosection has been calculated for a SEM-measured composition analysed over an area that comprises garnet, with inclusions of epidote, amphibole and kyanite with amphibole-plagioclase symplectites as well as rutile and ilmenite. This diagram has been calculated under H_2O -saturated conditions and $Fe^{3+}/(Fe^{3+}+Fe^{2+}) = 12\%$ (i.e. the same as the host rock). In the P – T pseudosection (Fig I.2.6a), epidote is stable with garnet and amphibole below 620°C and 24 kbar. The predicted grossular and pyrope contents of a garnet in equilibrium with epidote would be comprised between 20-30% and 10-25% respectively. The pyrope content observed in garnet core (prp35) with epidote inclusions is not consistent with the modelled garnet in the epidote stability field.

A possibility is that the garnet-rich layer and its host rock were not characterized by the same $Fe^{3+}/(Fe^{3+}+Fe^{2+})$ ratio. Accordingly, a $TX(Fe^{3+})$ pseudosection has been calculated in order to investigate the effect of varying Fe oxidation state (Fig I.2.6b). In this diagram,

calculated at constant pressure (i.e. 20 kbar) the stability of epidote is largely increased toward high temperature with increasing Fe^{3+} . However, the maximum pyrope content predicted remains lower than 25%. Therefore, the results of the P – T pseudosection calculated using the bulk composition of the garnet-rich layer does not faithfully reproduce the observations.

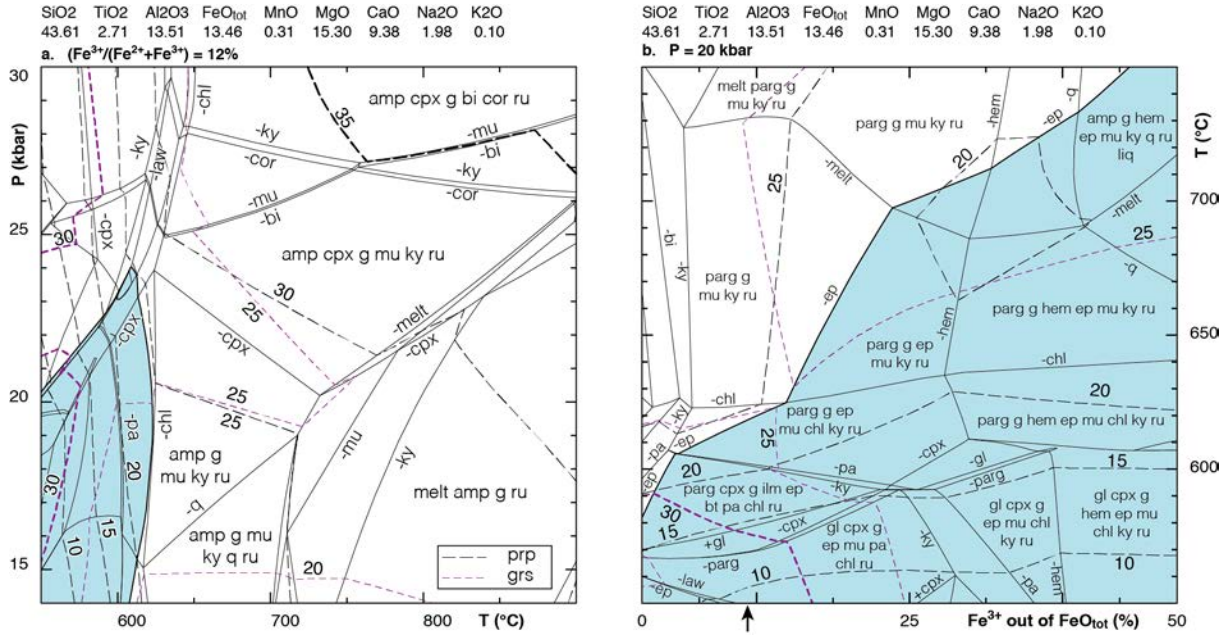


Figure I.2.6: P – T (a) and $TX(\text{Fe}^{3+})$ (b) pseudosections calculated for the SEM measured bulk composition of the garnet-rich layer. The pseudosections are contoured with isopleths for pyrope and grossular content in garnet (same legend for both diagrams). Isopleths for garnet core are shown in bold lines. The epidote field is shown in light blue. The arrow on the x-axis of (b) indicates the Fe^{3+} content used in (a).

3.2. Pseudosection investigation of a metamorphic origin

In order to investigate the possibility that the garnet-rich layers results from the partial melting of the eclogites during the isobaric heating (M1, Fig. I.2.7), a T – $X(\text{H}_2\text{O})$ pseudosection using the bulk composition of the host rock but varying H_2O content has been calculated at 22.5 kbar to investigate the effect of varying H_2O content on the modelled assemblages. In this diagram, quartz, amphibole, muscovite and kyanite disappear toward increasing H_2O content. The inferred peak assemblage for the host rock is observed in the field melt-cpx-g-mu-ky-q-ru

from 770°C to higher than 900°C for a H₂O content ranging ~1-10 mol% (light yellow field in Fig. I.2.7). The inferred assemblage for the garnet-rich layer is modelled in the field melt-cpx-g-ky-ru with higher water content (H₂O ~5-10 mol; deep orange field in Fig. I.2.7) and temperature than 860°C.

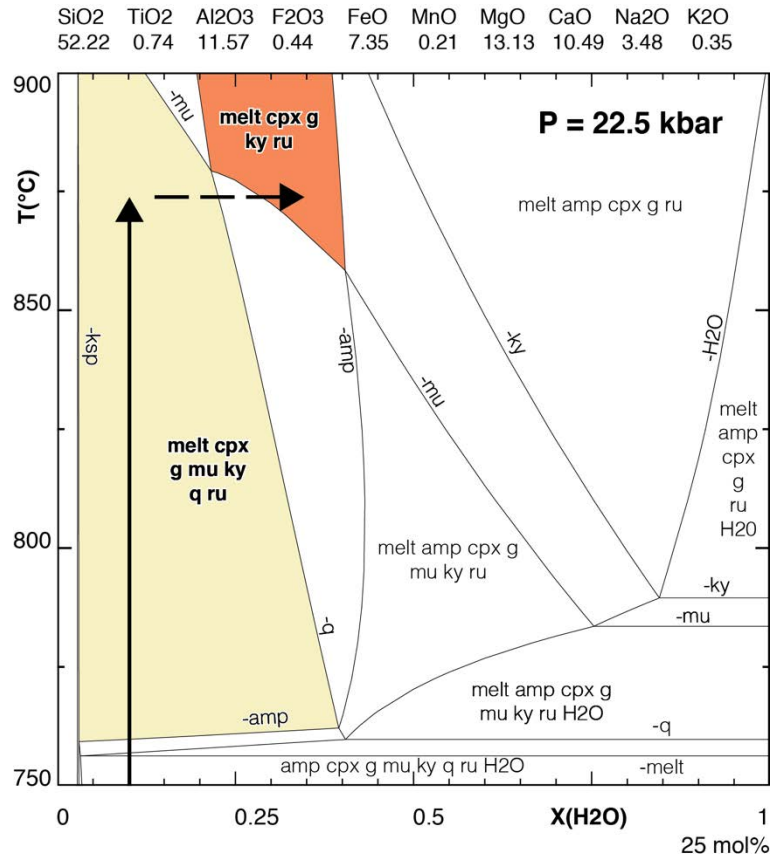


Figure I.2.7: T–X(H₂O) pseudosection for a SEM measured bulk composition of the host rock. The light yellow field represent the assemblage observed in the host rock. The deep orange field represents the inferred assemblage for the garnet-rich layer. The plain arrow indicates the evolution of the host rock during the isobaric heating. The dashed arrow indicates the possible evolution (i.e. partial hydration) of the garnet rich layer at the peak P–T conditions.

According to this result, two P - T pseudosections has been calculated using the estimated H_2O -contents for the garnet-rich layer (~9.5% added H_2O) and the host rock (~2% added H_2O). In the diagram for the garnet-rich layer, the observed assemblage is modelled by the field melt-

cpx-g-ky-ru at temperatures higher than 850°C and pressures above 22 kbar (deep orange field; Fig. I.2.8a). The field melt-cpx-g-mu-ky-q-ru for the host rock (Fig. I.2.8b) has also been reported on the diagram for the garnet-rich layer for easier comparison (light yellow with dashed contours Fig. I.2.8a).

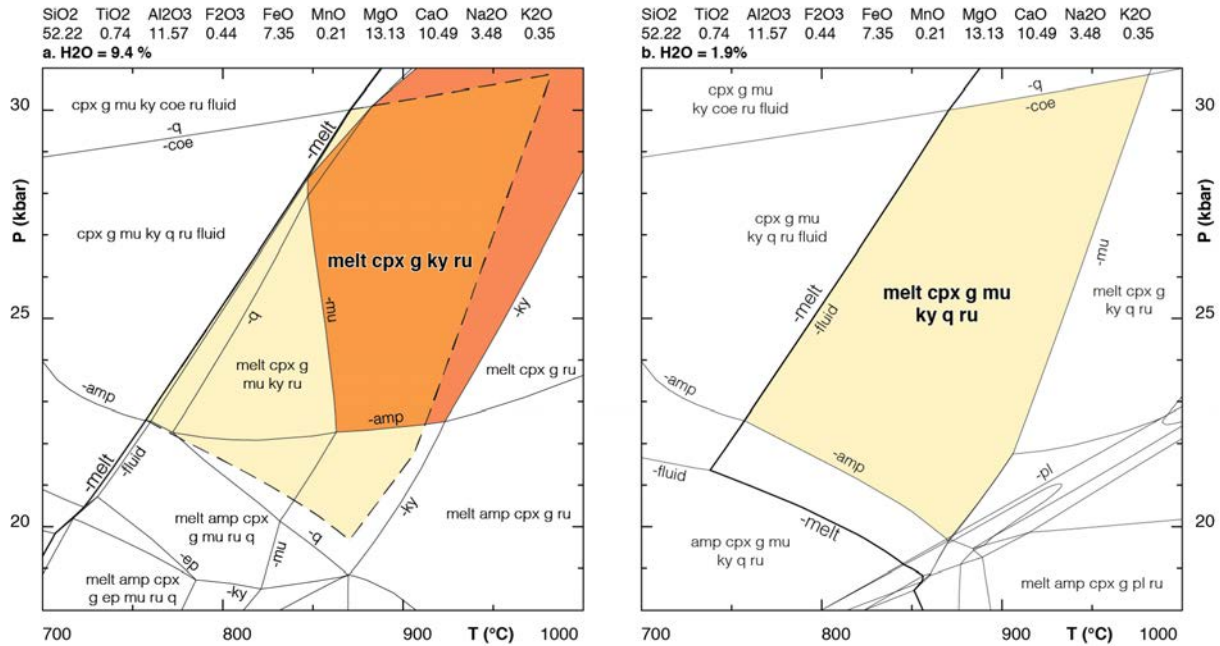


Figure I.2.8: P - T pseudosections for the SEM measured composition of the bulk rock with ~9.5% (a) and ~2% (b) H_2O added. Note that some assemblages are saturated with respect to an aqueous fluid. The deep orange field corresponds to the inferred assemblage of the garnet-rich layer. The light yellow field with dashed contour (a) is a projection of the peak assemblage field for the host rock (b).

In order to investigate the respective effect of temperature, pressure and H_2O contents on mineral assemblages and proportions, three mode boxes have been calculated for the bulk composition of the host rock for either P , T or H_2O variations (Fig. I.2.9). The total mode of solids is normalized to 100%. As a general rule, garnet mode is inversely correlated with the mode of amphibole, kyanite, muscovite/K-feldspar and quartz/coesite. In the temperature varying mode box, the observed assemblage for the garnet-rich layer (melt-cpx-g-ky-ru) is modelled between 870-910°C with 55-60% garnet (Fig. I.2.9a). In the pressure varying diagram, the same assemblage is modelled between 22 to 30 kbar with a maximum garnet mode

of ~55% around 22-23 kbar (Fig. I.2.9b). In the third, water varying mode box, the melt-cpx-g-ky-ru assemblage is modelled between ~6-10 mol H₂O, with a maximum garnet mode between 50-55% (Fig. I.2.9c). The mode boxes indicate that the garnet-rich layers might have formed close to the peak P - T conditions previously estimated (Fig. I.1.7).

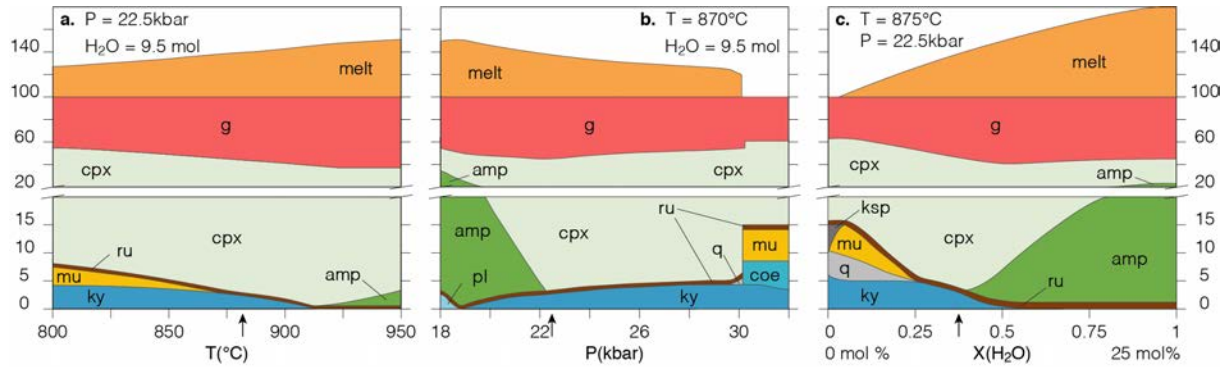


Figure I.2.9: Mode boxes diagrams for varying T (a), P (b) and H_2O (c) content. The arrows indicate the most likely conditions of formation for the garnet-rich layers.

4. Discussion

The main characteristics of the garnet-rich layers are (i) a high mode of garnet and rutile, a low mode of clinopyroxene and kyanite content compared to the host rock, as well as the absence of K-bearing minerals and quartz; (ii) an orientation parallel with the fabric of the host rock; (iii) a depletion of SiO₂, CaO, Na₂O and K₂O and enrichment FeO, MnO, MgO, TiO₂; (iv) a similar zoning and inclusion patterns in the larger garnets of the garnet-rich layer with respect to the garnets in the host rock.

4.1. Origin of the garnet rich layers

In this section, both the possible cumulate or residuum origin for the garnet-rich layers will be discussed. To do so, the discussion will focus successively on a comparison of major element composition of the garnet-rich layer with respect to its host rock, a comparison of

garnet compositions from the host rock and the garnet-rich layer and the results of phase equilibrium modelling.

Garnet-rich layers in metabasic rocks were interpreted as the result of metamorphism of various types of magmatic cumulate layers. Each has specific chemical characteristics. Plagioclase accumulations are characterized by higher Al_2O_3 and CaO contents than their host rock ($\text{Al}_2\text{O}_{3\text{layer}}/\text{Al}_2\text{O}_{3\text{host}} \sim 8$; $\text{CaO}_{\text{layer}}/\text{CaO}_{\text{host}} \sim 9$) (Konzett et al., 2005). Spinel accumulations are characterized by a high CaO content ($\sim 20\%$) and a high CaO/ Al_2O_3 ratio (~ 1.5) due to the extraction of Al-rich spinel (Yang et al., 2008). The studied garnet-rich layers are characterized by a depletion of the Al_2O_3 content compared with the host rock ($\text{Al}_2\text{O}_{3\text{layer}}/\text{Al}_2\text{O}_{3\text{host}} \sim 0.65$) and lower CaO content ($\text{CaO}_{\text{layer}}/\text{CaO}_{\text{host}} = 0.8$) inconsistent with a significant accumulation of plagioclase in the protolith of the studied garnet rich layer. The high Al_2O_3 content of the host rock, does not support a depletion of Al_2O_3 because of spinel accumulation in the garnet-rich layer. On the other hand, our data indicate that garnet-rich layers are characterized by lower SiO_2 , CaO, Na_2O and K_2O contents, but higher FeO, MnO, MgO, TiO_2 contents. Mafic components are concentrated in garnet and Ti in rutile. A possible alternative protolith for the garnet-rich layer would be a former ilmenite cumulate, with significant proportion of pyrophanite and geikilite, that could account for the high TiO_2 , FeO, MnO, MgO content of the layer (this point is discussed in the light of the pseudosection hereafter). On the other hand, the granitoid composition of melt derived from metabasites partial melting is indicated by experiments with composition ranging from andesitic (e.g. Senn and Dunn, 1994) to rhyolitic (e.g. Schmidt et al., 2004). This variability may be attributed to the variable content of K-bearing minerals (mostly phengite at high-pressure) in natural protoliths. The occurrence of biotite-plagioclase \pm quartz \pm K-feldspar bearing polyinclusions or cusped veinlets interpreted as former melt in partially molten mafic eclogite (e.g. Cao et al., 2019, Wang et al., 2014) also suggest a granitoid composition of the melt. The bulk composition of the garnet-rich layer could

therefore be explained by a depletion of incompatible elements due to partial melting and melt extraction.

In addition to the bulk composition of the layer, garnet composition may also indicate a cumulate or a residuum origin for the garnet-rich layer. Garnet crystallized from a plagioclase-rich cumulate contains higher grossular contents than the host-rock ($grs_{host}3-14$; $grs_{layer}10-42$; Konzett et al., 2005). Garnet from initial spinel cumulates is richer in pyrope than that from the host-rock (Yang et al., 2008). On the other hand, garnet from garnet-rich layers in partially melted mafic granulite may share a similar composition with garnet of the host-rock (Palin et al., 2018). Our data indicate similar chemical composition of garnet – the core of garnet forming the layers, corresponds to the mantle of garnet in the host eclogite (Fig. I.2.4). The respective cores of garnets from the garnet rich-layer and the host-rock also display the same zoning and inclusion pattern. These observations strongly suggest that they crystallized from the same material and underwent a similar metamorphic evolution.

The P – T pseudosection calculated for the bulk composition of the garnet-rich layer predicts that epidote is stable at T lower than 620°C , below the temperature inferred for the crystallisation of the garnet core in the host rock (650°C ; Fig. I.2.6). In addition, garnet in equilibrium with epidote is predicted to contain less than 25% pyrope, way below the pyrope content observed ($prp35$). Though garnet might have crystallized at lower P – T conditions because of a different composition, the discrepancy between the observed and modelled composition of garnet at equilibrium with epidote is significant. As a consequence, an unmodified bulk composition hypothesis for the garnet-rich layers, like an ilmenite-rich protolith, is not supported by P – T pseudosection modelling.

The T – $X(\text{H}_2\text{O})$ pseudosection (Fig. I.2.7) shows that the assemblage of both the host rock and the garnet rich layer can be modelled for various H_2O -contents and similar T (870 – 875°C) at given P (22.5kbar). Garnet mode increases with temperature (Fig. I.2.9a) and the

pressure varying mode box (Fig. I.2.9b) shows a maximum garnet mode between 22-23 kbar at 870°C consistent with the inferred P – T path (Fig. I.1.7). The maximum garnet mode modelled is around 50-60%. It reaches 70-75% in the observed assemblage, but this limited discrepancy could be explained by modelling uncertainties including uncertainties in the estimation of the effective bulk composition (e.g. the host rock displays variable kyanite content) and also imperfections in the thermodynamic data and activity–composition relations. Accordingly, partial melting and subsequent melt extraction reproduce the first order observations of the garnet-rich layer.

4.2. Consequences of partial melting on Rutile and Zircon precipitation

The garnet-rich layer contains a large amount of rutile and zircon. In the above calculations, the mode of rutile is not reproduced correctly (observed ~5-10%; modelled ~0.5%) suggesting an enrichment of Ti and also possibly of Zr during the genesis of the garnet-rich layer (i.e. during partial melting). The presence of rutile, zircon or baddeleyite in eclogitic veins and fluid inclusions in omphacite from eclogites indicates that Ti and Zr may be mobilized by an aqueous fluid at high pressure (e.g. Philippot and Selverstone, 1991; Rubatto and Hermann, 2003). Consequently, partial melting might have been triggered by the influx of an aqueous fluid enriched in Zr and Ti. H₂O was incorporated in the melt, whereas Zr and Ti precipitated as zircon and rutile.

The solubility of Ti and Zr in melt vary as a function of the melt composition and tend to decrease the increasing peraluminous character of a melt (e.g. Watson, 1979; Dickinson and Hess, 1985; Gwinn and Hess, 1989). The modelled composition of the melt at 850°C and 22.5 kbar is peraluminous ($A/NK = 1.45$ and $A/CNK = 1.27$; Table I.2.2) suggesting only limited solubility of Zr and Ti. Using the example of Zr solubility in the modelled melt, the partitioning coefficient of Zr between zircon and the melt can be estimated using the zircon saturation

equation of Boehenke et al. (2013). In this equation, Zr solubility in melt increases with increasing temperature and Na, Ca and K content of the melt, but decreases with increasing Al and Si content. Using the modelled composition of the melt and assuming a melting temperature of 850°C the calculated partitioning coefficient suggest a strong partitioning of Zr ($D_{Zr} \sim 1 \times 10^6$) in zircon rather than in the melt. Accordingly, a consequence of partial melting would be the precipitation of dissolved Zr and Ti into rutile and zircon.

4.3. Mechanism and implications of partial melting of the eclogites

Pioneering numerical work suggested that partial melting of subducted oceanic lithosphere may only happen if the subducted oceanic crust is young and hot (e.g. subduction of a mid-oceanic ridge) or if high shear stress is exerted on it (e.g. Peacock 1991 and Peacock et al., 1999). Evidence of a possible partially molten ridge has been discovered in Chilean Patagonia (Angiboust et al., 2017), Iran (Rossetti et al., 2010) and Cuba (García-Casco et al., 2008). They are reported in Fig. I.2.10. High thermal gradient may also account for the partial melting of the Archean eclogites from the Belomorian belt (e.g. Konilov et al., 2011; Shchipansky et al., 2012; Mints et al., 2014; Balagansky et al., 2015). Metasomatism in a subduction-related accretionary complex may also trigger partial melting of a piece of oceanic crust stored in the subduction channel (Sorensen and Barton, 1987). Finally, decompression from (U)HP conditions is shown to be a viable mechanism to trigger partial melting of eclogites (Cao et al., 2019; Wang et al., 2014). Leucosome of a trondhjemitic composition has also been reported in the Western Gneiss Region (Labrousse et al., 2011), suggesting a possible partial melting of a mafic rock at high pressures. Our contribution shows that partial melting of eclogites may happen at peak pressure conditions and proposes a heat influx from the asthenosphere as a mechanism to provide sufficient heat.

Partial melting of eclogites has been proposed in the L  v  zou and Marvejols massifs following the discovery of trondhjemite layers intercalated with eclogites (Nicollet and Leyreloup, 1978) suggesting that partial melting in the Massif Central could be widespread. This is consistent with P – T estimations of many eclogites in the Massif Central (Fig. I.2.2. Partial melting of the continental crust brought to (U)HP conditions has been proposed as a mechanism to trigger the exhumation by mantle delamination and rise of the buoyant crust (Labrousse et al., 2011; 2015). Accordingly, partial melting of the eclogites from the Massif Central may have facilitated slab detachment and subsequent exhumation of the eclogites.

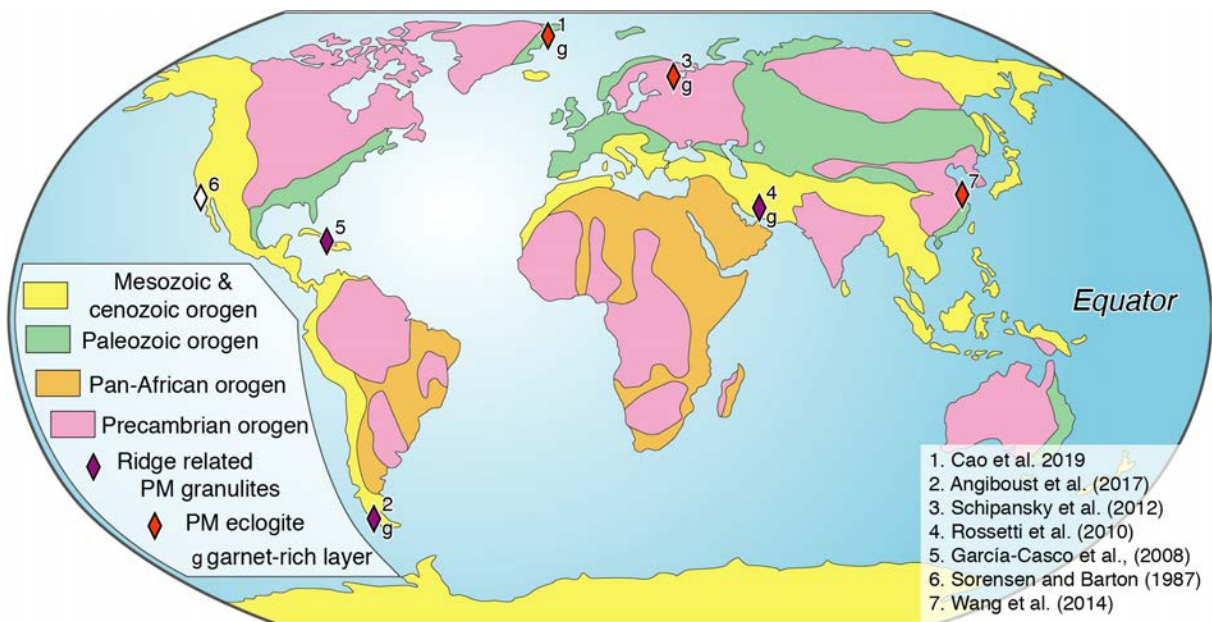


Figure I.2.10: Synthetic map of direct evidence of partially molten (PM) oceanic crust from the literature.

5. Conclusions

The different assemblages and mineral proportions between the garnet-rich layer and the host eclogite has been studied using P – T pseudosections, major element chemistry and comparison between garnet compositions from the garnet-rich layer and the host rock. The results point to a purely metamorphic origin for the garnet-rich layer interpreted as a residuum after partial melting and melt extraction. Localized partial melting was triggered by focused

fluid influx at P – T conditions between 870-915°C and 22-23 kbar. The abundance of zircon and rutile may result from the precipitation of Zr and Ti transported in the aqueous fluid but unable to dissolve in the melt at the onset of partial melting. The apparent absence of melt suggests that it was efficiently extracted to another location.

Partial melting of the eclogite may be widespread at the scale of the Massif Central. It is inferred that the juxtaposition of the hot asthenospheric mantle next to the eclogites conveyed enough heat to reach suprasolidus conditions. Partial melting might have facilitated slab detachment and subsequent exhumation of the eclogites.

Petrologically constrained U-Pb dating of the “La Borie” eclogites

(Article in prep.)

1. Introduction

As previously mentioned in the introductive sections of this manuscript, the Silurian Eo-Hercynian HP event inferred from geochronological results mainly obtained in the 1980s has been challenged in the Armorican Massif (Bosse et al., 2000, 2005). The re-evaluation of the age of the HP metamorphism points to a younger Devonian subduction and to a fast exhumation of the HP units. Similar results have been obtained in the Najac and the Lévézou Massif (Lotout et al., 2018; Lotout et al., Submitted). However, re-evaluation of the inferred Silurian eclogites has not been undertaken yet. Consequently, it remains uncertain whether a Silurian subduction occurred in the Massif Central. Therefore, the aim of our study is to remove this uncertainty and timely constrain the age of the eclogite facies metamorphism and subsequent exhumation.

To do so, we performed U/Pb LA-ICP-MS geochronological study of zircon, rutiles and apatites from samples similar to those of Ducrot et al., (1983). The results are constrained by petrologic observations, Ti-in-zircon and Zr-in-rutile thermometry as well as Raman determination of the micro-inclusions in zircon in order to ensure the interpretation of the geochronological data. The results provide a robust re-evaluation of the age of the eclogite facies metamorphism, brings new constraints on the cooling of the eclogites after a significant decompression (at least 13.5 kbar) and allows a discussion of zircon behaviour at high pressure.

Both samples (BR18 and BR19) display many similarities and the results of the P – T pseudosection for sample BR18 is inferred to apply for BR19 too.

2. Analytical methods

2.1. Mineral separation and U/Pb dating

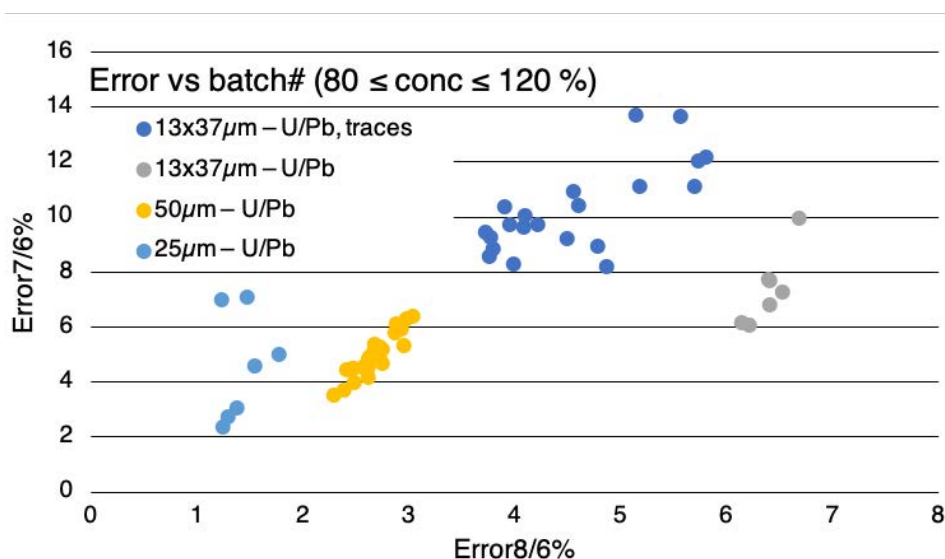
A mineral separation procedure has been applied to concentrate zircon and apatite grains for U-Pb dating using the facilities available at Géosciences Rennes (University of Rennes 1). The samples were crushed and only the powder fraction with a diameter <250 µm was kept. Heavy minerals were first concentrated by Wilfley table, then magnetic minerals were removed with an isodynamic Frantz separator. Heavy minerals were afterwards separated with heavy liquids. Zircon and apatite grains were handpicked under a binocular microscope. The selected minerals were then embedded in epoxy mounts, which were polished on a lap wheel. Separated zircon and apatite grains were imaged by cathodoluminescence (CL) using a Reliotron CL system equipped with a digital colour camera available at Géosciences Rennes. Rutile on thin section were imaged using SEM-BSE (JEOL IT 300 LA EDS scanning electron microscope, CMEBA, University Rennes 1). Thin section imaging of zircon was performed at Clermont-Ferrand using a SEM equipped with a CL system.

U-Pb geochronology of zircon, rutile and apatite grains was conducted by in-situ laser ablation inductively coupled plasma mass spectrometry (LA-ICP-MS) at Géosciences Rennes using a ESI NWR193UC Excimer laser coupled to an Agilent quadrupole 7700x ICP-MS equipped with a dual pumping system to enhance sensitivity. The instrumental conditions are reported in the Table I.3.1. Further information on the zircon dating protocol can be found in Ballouard et al. (2015) and in Pochon et al. (2016) for apatite.

Zircon, apatite and rutile crystals from two eclogite samples were analysed in order to determine the ages of the eclogite facies metamorphism and subsequent cooling history after decompression. Given the variety of minerals analysed and their various morphologies, several sets of analyses with distinct analytical conditions (spot size, repetition rate and fluence) were

performed. For the sake of clarity, only the needed information is given here and a comprehensive summary of the analytical conditions is given in Table I.3.1.

Simultaneous measurements of the U-Pb ratios and trace elements analyses were performed on zircon grains from the eclogite samples during three analytical sessions (BR18: analytical sessions 1 and 2; BR19: analytical session 6) on separated crystals. Analyses were performed with a rectangular ablation spot of $37 \times 14 \mu\text{m}$ in order to analyse thin rims around zircons cores. The results were checked for consistency, given the scatter of the inferred metamorphic dates, two analytical sessions were then performed on the same crystals this time without analysing the trace element contents in order to increase the counting time for both the uranium and lead isotopes and ultimately minimize the error on each individual analysis (BR18: analytical session 3; BR19: analytical session 7; see Fig I.3.1). These two analytical sessions, performed with the same spot size, do not significantly improve the results; therefore, we have focused on metamorphic grains and ablated the crystals with a larger spot diameter of $50 \mu\text{m}$ (analytical session 4). One additional analytical session has been analysed in order to check for a variation of the obtained dates with respect to the textural position of zircon (e.g. differences between zircons from the matrix or included in garnet; BR18: analytical session 5).



Chapter 1 – Section 3

Figure I.3.1 (previous page): Plot of error on individual dates in % (only analyses with $80 < \text{conc} < 120\%$). During the sessions, analysing or not the Trace elements together with the U/Pb and rectangular spot shape did not significantly improve the results (Analytical session 1 & 2 – Trace + U/Pb; Analytical session 3 – U/Pb only). Alternatively, the analytical session with a circular spot shape but equivalent size yielded more precise results (Analytical session 5). The most precise results were obtained when doubling the size of the spot diameter (Analytical sessions 4).

Rutile and apatite from the eclogites samples were also dated. Rutile crystals in different textural positions were analysed directly in thin section with a $50\mu\text{m}$ spot in order to check for any textural control on the obtained dates (BR18 – analytical session 8). Apatite dating was performed on separated grains using a $45\mu\text{m}$ spot diameter (BR18: analytical sessions 9 and 10; BR19: analytical session 11).

Data were corrected for U-Pb and Th-Pb fractionation and for the mass bias by standard bracketing with repeated measurements of the GJ-1 zircon standard (Jackson et al., 2004), Madagascar apatite standard (Thomson et al., 2018) or R10 rutile standard (Luviziotto et al., 2009). Data for trace elements in zircon were corrected using NIST612 glass (Kent et al., 2007). Along with the unknowns, the zircon standards 91500 (1058 ± 2.8 – Hollocher and Ruiz, 1995; Wiedenbeck et al., 2004) and Plešovice (337 ± 0.5 – Sláma et al., 2008) were used as secondary standards during the analyses of analytical sessions 1 to 3 (U-Pb, trace elements) and analytical sessions 4 to 5 (U-Pb) respectively; the apatite standards McClure (523.5 ± 1.5 – Schoene and Bowring, 2006; Thomson et al., 2018) and Durango (31.5 ± 2 – McDowell et al., 2005) and rutile R19 (489.5 ± 1 – Luviziotto et al., 2009) and R632 (496 ± 2 – Axelsson et al., 2018) were also measured to monitor the accuracy of the analyses during apatite and rutile analytical sessions. The produced ages are given in Table I.3.1.

Data reduction was carried out with Iolite (Paton et al., 2011) for zircon. Reproducibility and age uncertainties of reference material Plešovice or 91500 were propagated by quadratic

sum to the analysed zircon grains according to Horstwood et al. (2016). Concordia ages and diagrams were generated using IsoplotR (Vermeesch, 2018). All errors given in Tables I.3.2 to I.3.16 are listed at two sigma.

2.2. Raman spectroscopy

Raman spectroscopy was performed at the Laboratoire Magmas et Volcans (Clermont-Ferrand, France). Raman spectra were obtained using a Renishaw InVia confocal Raman microspectrometer, equipped with a 532 nm diode laser (output power of 200 mW), a Peltier-cooled CCD detector, a motorized XY stage and a Leica DM 2500M optical microscope. Back-scattered geometry allowed to collect the scattered light and a dielectric edge filter to reject reflected laser radiation as well as Rayleigh scatter. Analyses were performed with a varying laser power of ~ 1 to 15 mW depending on the analysed mineral phase, and the slit aperture set to 20 μm in a high confocality setting. A 100x objective and a 2400 l/mm grating were used for the analyses resulting in spatial and spectral resolution of ~1 μm and 1 cm^{-1} respectively. The spectrometer was calibrated on the basis of a Si $520.5 \pm 0.5 \text{ cm}^{-1}$ peak. The spectra were recorded in the aluminosilicate network domain (~ 100 to 1300 cm^{-1} Raman shifts) and, when necessary, in the water domain (~ 3000 to 3800 cm^{-1}), using Wire 4.2 software. Acquisition times varied from 10 to 300 s depending on laser power condition and nature of the analysed mineral phase.

Table I.3.1: Synthetic table of analytical conditions and results obtained on standards.

#Anal. Ses.	Sample	Mx	Spot size	Rep. Rate	Fluence	Type	Analyzed elements	Standard	Expected std age	Std age	MSWD	n
#1	BR18	zrn	37x14µm	4 Hz	6.9 J/cm2	EM	U-Pb, T	91500	1058±2.8	1062±10	0.65	9/12
#2	BR18	zrn	37x14µm	3 Hz	6.7 J/cm2	EM	U-Pb, T	91500	1058±2.8	1062±10	0.65	9/12
#3, 7	BR18 & BR19	zrn	37x14µm	4 Hz	6.7 J/cm2	EM	U-Pb	Plešovice	337±0.5	337±11	0.22	3/3
#4	BR18	zrn	50µm	4 Hz	6.2 J/cm2	EM	U-Pb	Plešovice	337±0.5	340±2	1.2	7/10
#5	BR18	zrn	25µm	4 Hz	6.3 J/cm2	TS	U-Pb	Plešovice	337±0.5	340±2	1.2	7/10
#6	BR19	zrn	37x14µm	3 Hz	6.7 J/cm2	EM	U-Pb, T	91500	1058±2.8	1079±10	1.2	10/14
#8	BR18	ru	50µm	5 Hz	6.15 J/cm2	TS	U-Pb, Zr	R19 R632	489.5±1 496±2	484±9.5 496±5.5	0 2.6	6/6
#9	BR18	apt	45µm	10 Hz	5.1 J/cm2	EM	U-Pb	Durango Mc Clure	31.5±2 523.5±1.5	33±3 528±9	1.2	14/14
#10	BR18	apt	45µm	10 Hz	5.1 J/cm2	EM	U-Pb	Durango Mc Clure	31.5±0.2 523.5±1.5	33±3 528±9	1.2	14/14
#11	BR19	apt	45µm	10 Hz	5.1 J/cm2	EM	U-Pb	Durango Mc Clure	31.5±0.18 523.5±1.5	33±3 528±9	1.2	14/14

Abbreviation: #Anal. Ses. – analytical session, Mx – analysed mineral, Rep rate – repetition rate, EM – epoxy mount, std – standard, TS – thin section, T – trace elements. The bold text indicates specific analytic conditions. Note that 91500 age obtained during the analytical session 6 is to old.

3. Petrological constraints on zircon, rutile and apatite

3.1. Petrological constraints on zircon

Petrography of zircon

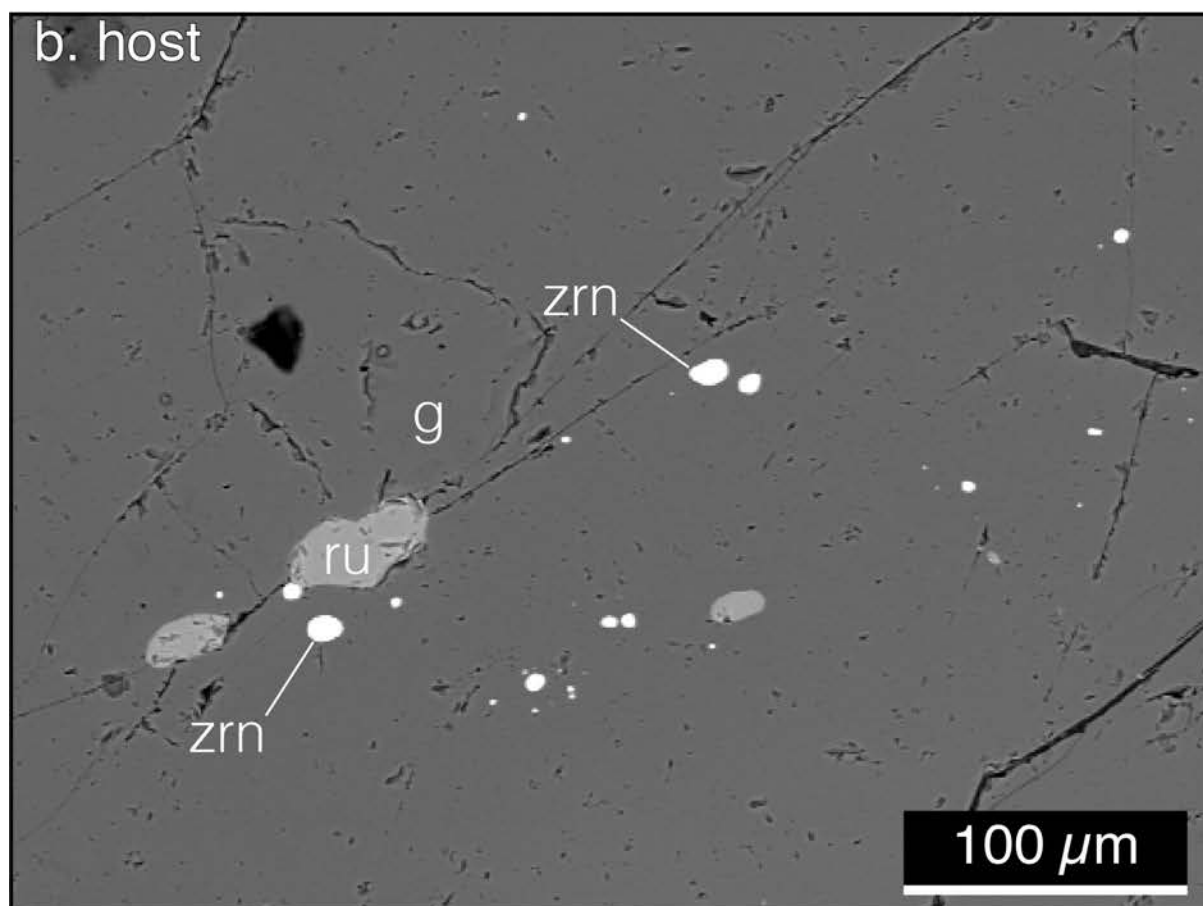
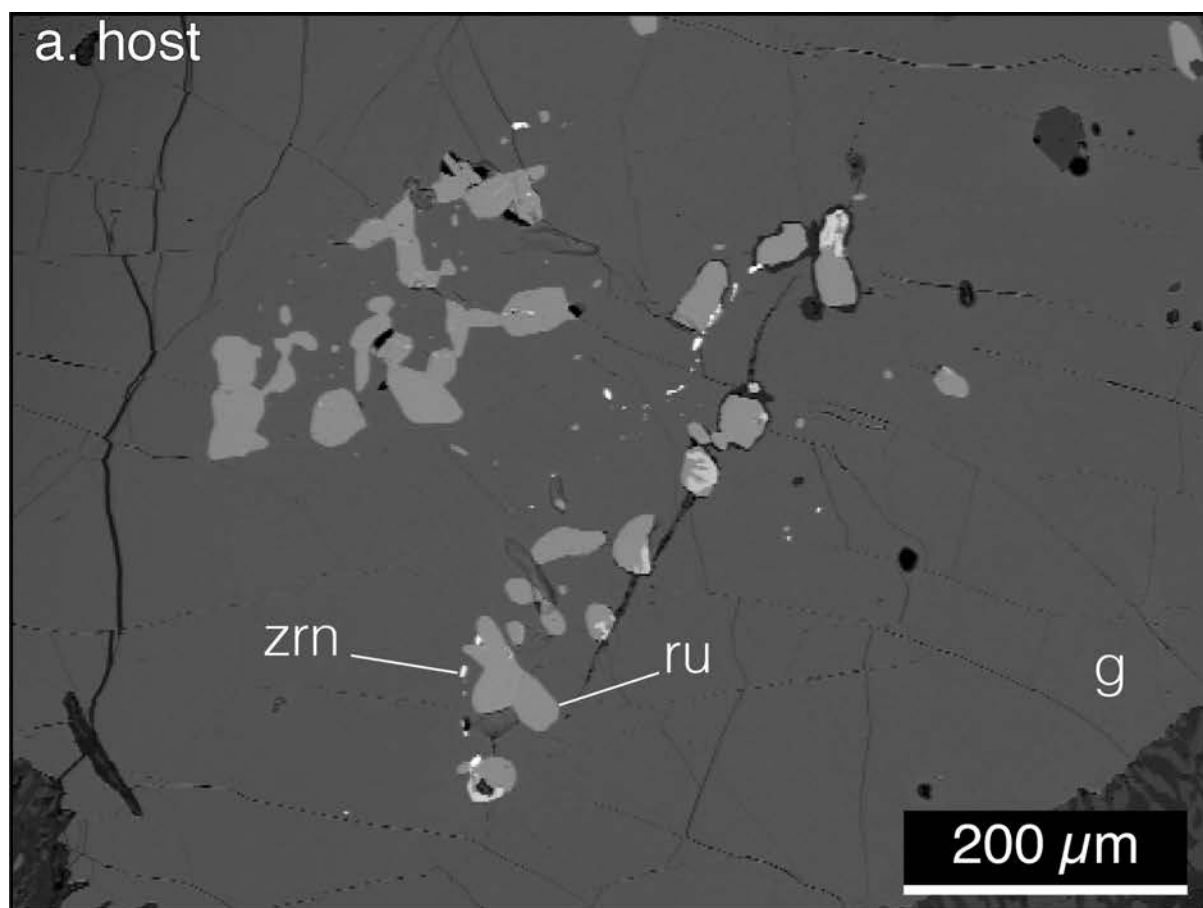
Zircon in samples BR18 and BR19 is common in the host rock and abundant in the garnet-rich layers where most of the largest crystals were found (up to 200 μm). Zircon crystals were observed in several distinct textural positions enclosed or partially enclosed in garnet, in the matrix diopside-amphibole-plagioclase-quartz symplectites, rutile or ilmenite as well as in amphibole-plagioclase corona around garnet (Figs. I.3.2. and I.3.3). Zircon is found in garnet 1 from core to rim as well as in garnet 2 (Fig. I.1.2). In garnet 1, zircon is generally found in small clusters or coronas of tiny rounded crystals close to or around rutile (Fig. I.2.2). On the other hand, single and larger crystals of zircon are found in the matrix and may be associated with rutile (Figs. II.2.3a-d).

Around 250 zircon crystals were hand-picked from each sample. They are stocky to elongated and their size range from 100 to 300 μm . They are either anhedral to subhedral, yellowish, cracked and display a strongly variable inclusion content (Fig. I.3.4A-D); or, anhedral, rounded to elongated, colourless, translucent, without rare cracks and may contain rare small inclusions visible under transmitted light (Fig. I.3.4E-J). Zircon grains from the sample BR18 are predominantly yellowish, inclusion rich and cracked (~75%), on the other hand, those from sample BR19 are in a vast majority translucent (~95%).

Under cathodoluminescence, inclusion rich zircon crystals are dark under CL with oscillatory growth zoning (Fig. I.3.4A,B). Some translucent grains are also dark under CL (Fig. I.3.4C,D). CL-bright rims, lobate zones or patches cut across the oscillatory zoning of the CL-dark zones (Fig. I.3.4A,C). The CL-bright zones form along the edges, cracks and inclusions

within the CL-dark zones. Some crystals are entirely bright under CL (Fig. I.3.4G-J). Their CL colour are comparable to the rims found around the CL-dark zoning. They mostly display flow textures (Fig. I.3.4G,H) and rarely oscillatory (Fig. I.3.4I) or sector (Fig. II. 1.3.J) zoning. The internal textures of zircons observed in thin (BR18) mostly display CL-bright flow textures, sector or patchy zoning.

Figure I.3.2 (next page): BSE images that exemplify the recurrent association of zircon cluster with rutile in the inclusion poor garnet mantle from the host rock. The picture (a) show a chaplet of tiny zircon crystals around rutile. These textures a very similar to those reported by Bingen et al. (2001) and Beckman and Möller (2018) in metamafic rocks and interpreted as a product of ilmenite breakdown. Zircon grains in picture (b) form randomly distributed clusters around rutile.



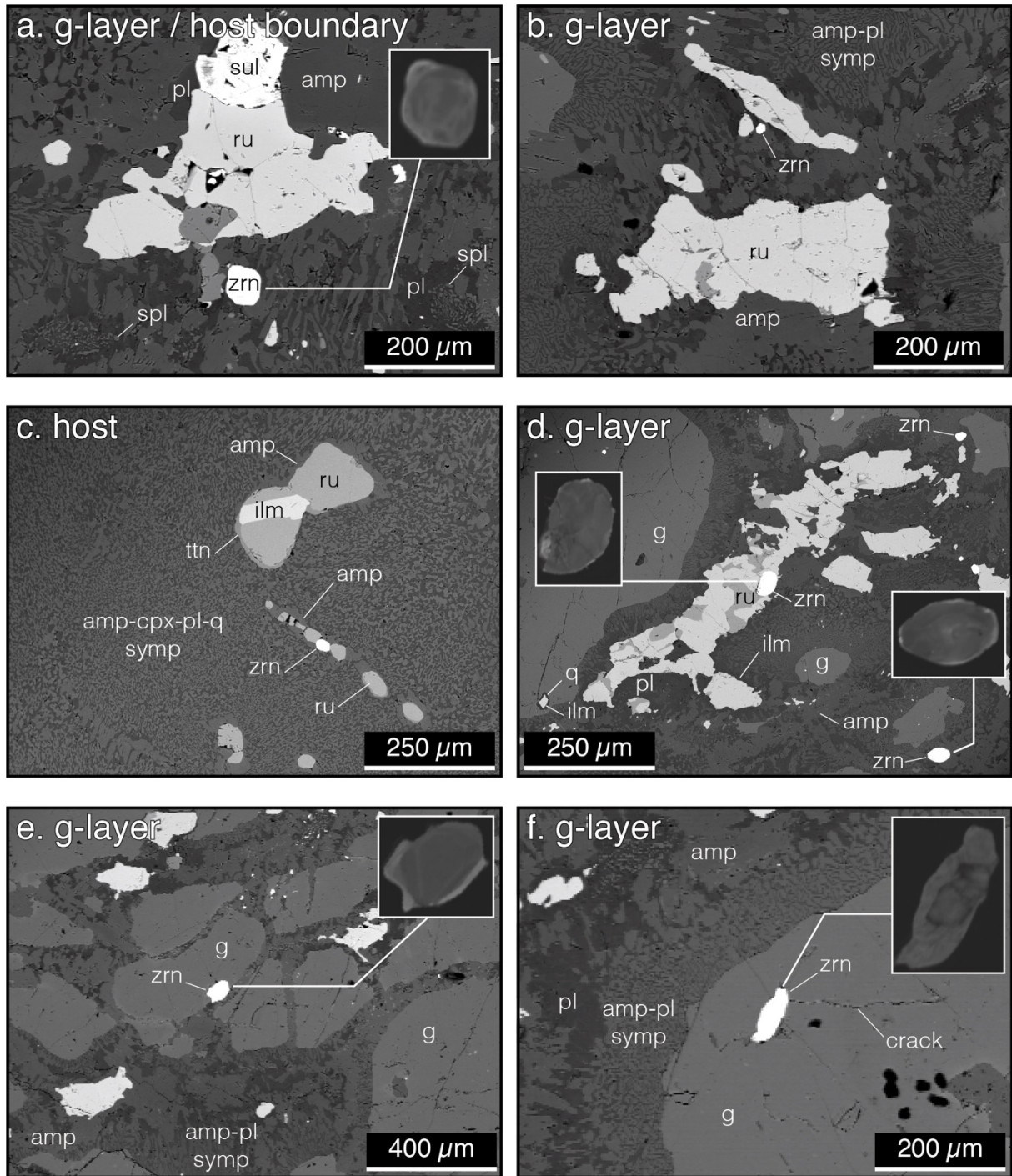


Figure I.3.3: BSE images of zircon crystals associated with rutile (a-d) or enclosed in garnet (e-f), with CL images of these grains. Zircon crystals associated with rutile in the matrix (a-d) tend to be larger than the cluster-forming grains found in garnet (Fig. I.3.2). Zircon crystals in (a) and (d) display a sector zoning pattern and flow textures respectively. All the zircon shown yielded a variscan age except b and c that were not analyzed.

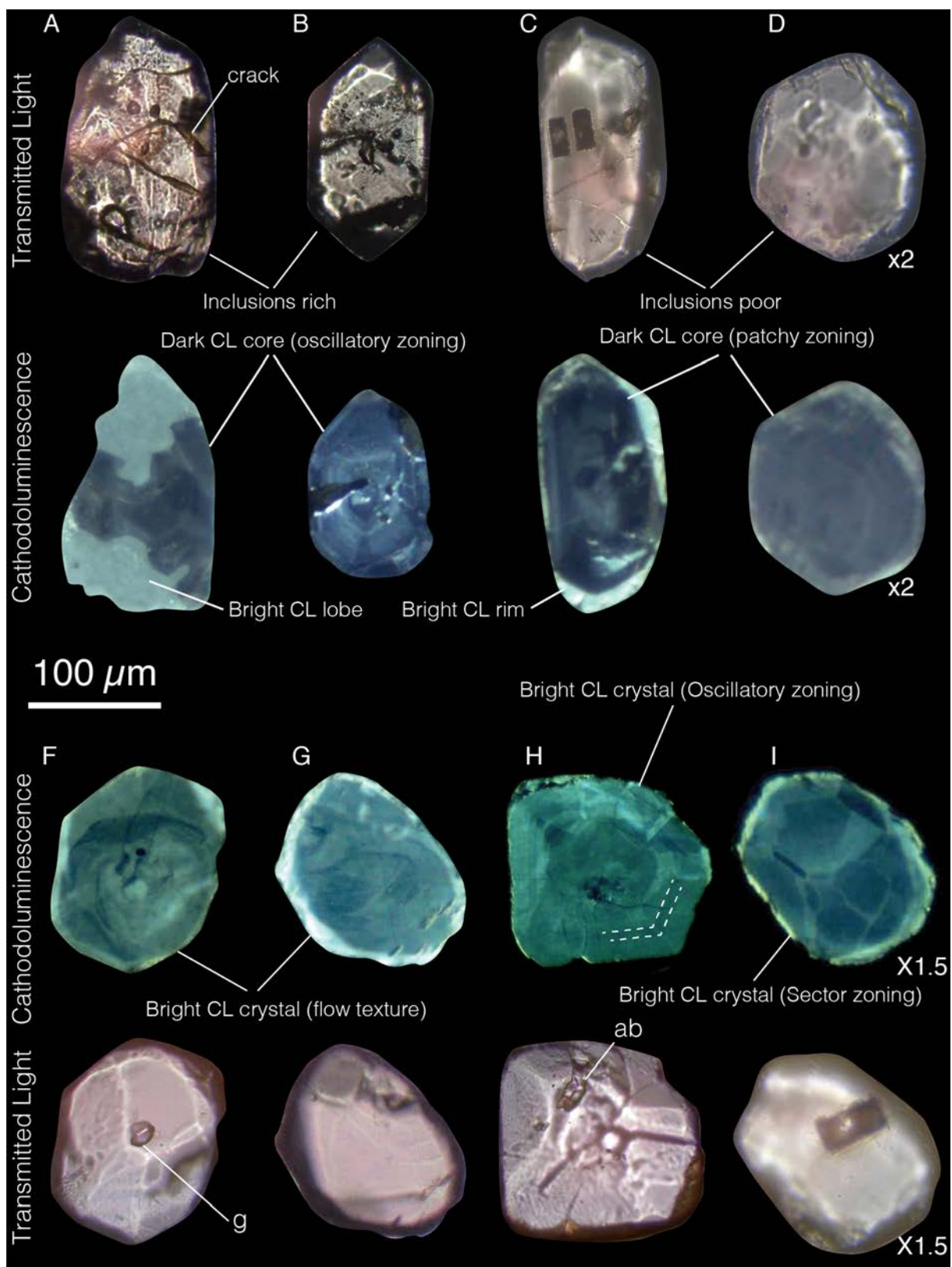


Figure I.3.4 (previous page): Transmitted and cathodoluminescence images of zircon crystals. Zircon grains (A-D) display CL-dark colour and oscillatory zoning faint in (a) and best seen in (b) or patchy zoning (c, d). These CL-dark grains are either inclusion-rich or poor. Note the CL-bright zircon forming lobes within the CL-dark zircon in (A) and the bright rim around (C). Some entire zircons crystals display CL-bright color similar to the CL-bright rim and lobate zircon A and C. The nature of the inclusion in zircons G and I were determined by Raman spectrometry. Zircons G and H display flow textures, zircon I is characterized oscillatory zoning highlighted by the dashed lines in the bottom right tip and also visible in the upper left tip. The zircon J is characterized by sector growth zoning.

Micro-inclusions in zircon Raman spectroscopy

Raman spectroscopy of micro-inclusions in zircon was performed in order to constrain the relative timing of zircon growth with respect to other minerals. Zircon crystals from sample BR19 belong mostly to the CL-bright type of crystals, their internal textures (e.g. flow textures and sector zoning) and chemical characteristics (e.g. REE pattern presented in the next section) strongly suggest a metamorphic origin. Therefore, we have focused Raman investigations on the dated zircon grains from this sample.

Inclusions in these grains are small-sized (max 50 μ m). Most of them were too small to be characterized properly. Nevertheless, twenty-three inclusions have been determined. The most common type of inclusions (n = 13) are round, colourless and translucent with main Raman vibrations at 356.5, 559, and 919 cm^{-1} and secondary vibrations at 637, 860 and 1043 cm^{-1} typical for garnet (Fig I.3.5). A second type of inclusions (n = 5) is brown under transmitted light and subhedral to euhedral, they are characterized by a large main Raman vibration centred around 609 cm^{-1} , with two weak vibrations around 235 and 800 cm^{-1} characteristics for rutile (Fig I.3.6). A yellowish and translucent corona around one of these inclusions is optically visible, this corona is characterized by a main Raman vibration at 609 cm^{-1} similar to that of rutile but also display, weak Raman vibrations at 166, 252, 313 and 355 cm^{-1} that allow the distinction with titanite (Fig I.3.7). Three inclusions of round to elongated, colourless and

translucent crystals display a main vibration at 677 cm^{-1} with weak vibrations between 335 to 412 cm^{-1} and 1010 to 1024 cm^{-1} typical for omphacite (Fig II.3.8). One round and colourless crystal displays a main Raman vibration at 960 cm^{-1} with weak vibrations at 587 , 1045 and 1079 cm^{-1} characteristics for apatite (Fig II.3.9). One small and opaque inclusions display a thin Raman vibration at 224 cm^{-1} and a large vibration at 1328 cm^{-1} which is typical for hematite (Fig II.3.10). In addition, on large colourless and translucent inclusion display only weak Raman vibrations at 479 and 508 cm^{-1} that could be attributed to albite (Fig II.3.11).

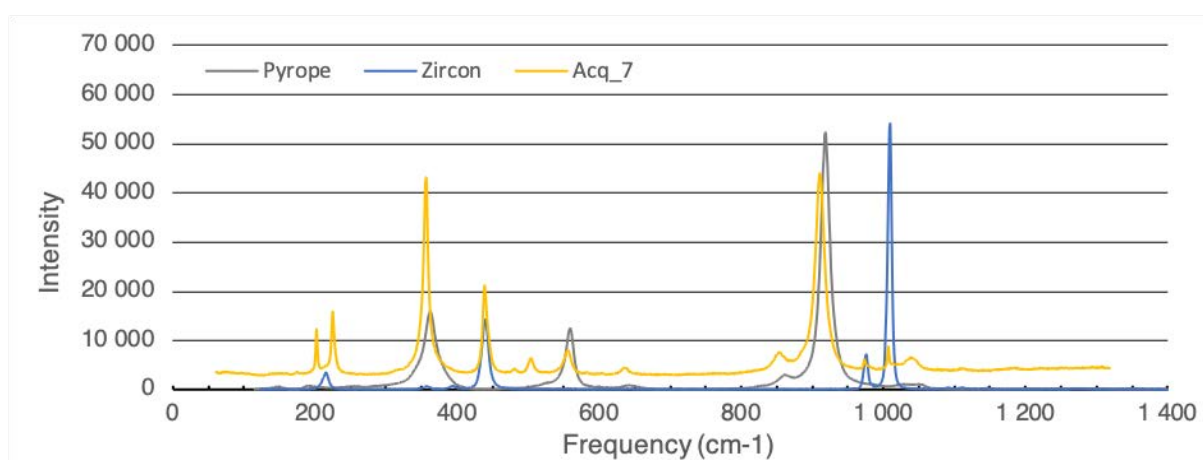


Figure I.3.5: Raman spectra of garnet. Pyrope and zircon spectra are shown for comparison (extracted from the RUFF database – ruff.info).

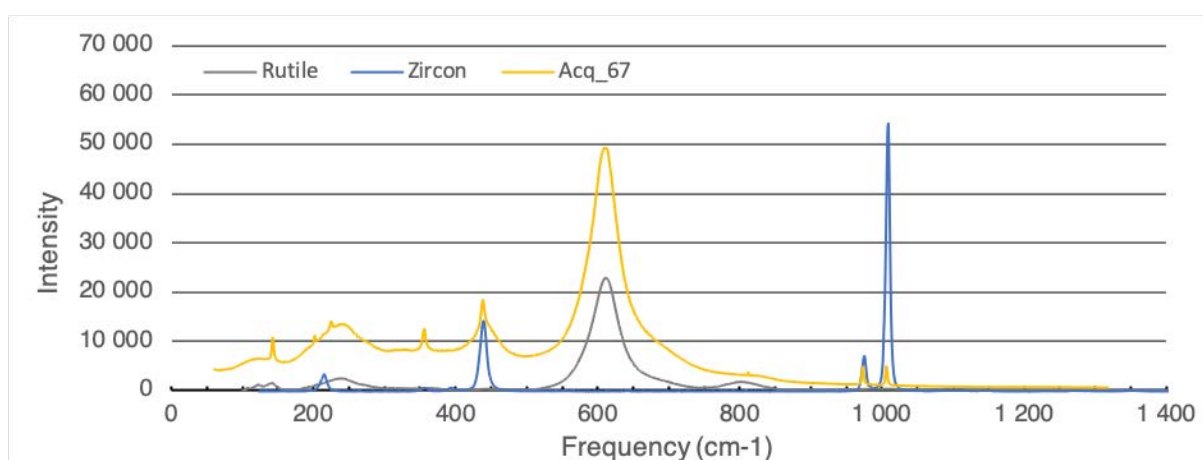


Figure I.3.6: Raman spectra of rutile.

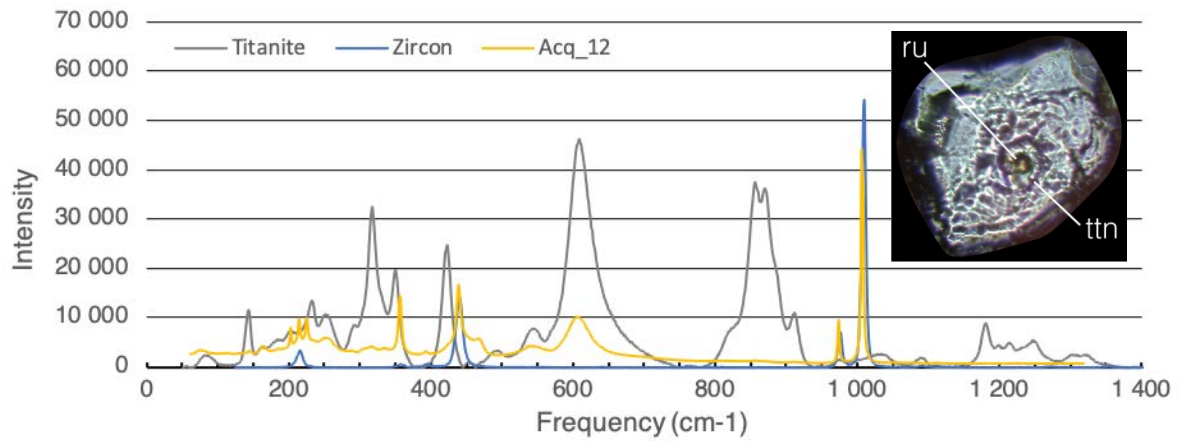


Figure I.3.7: Raman spectra of titanite. Inset: transmitted light photograph of the titanite corona around rutile in zircon. Note the blurry aspect of zircon that could be due to cracks.

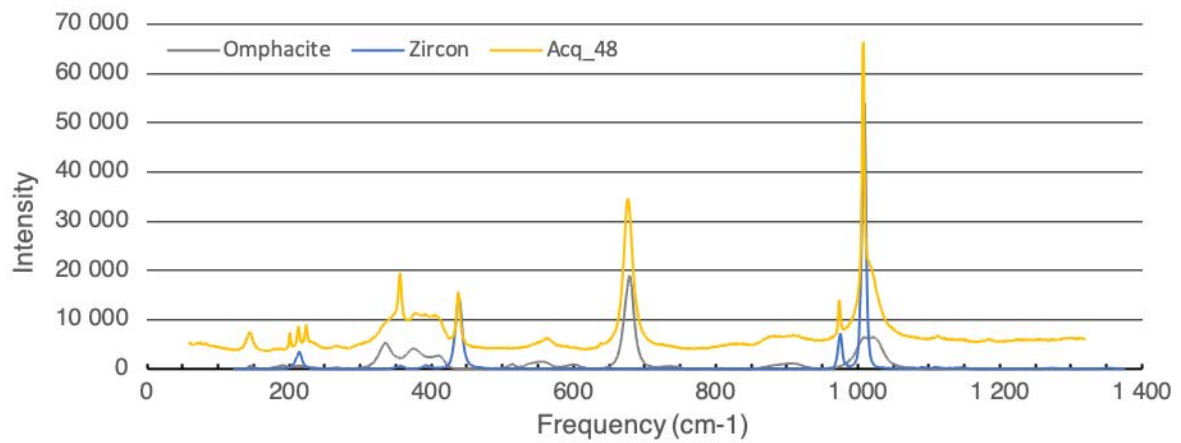


Figure I.3.8: Raman spectra of clinopyroxene.

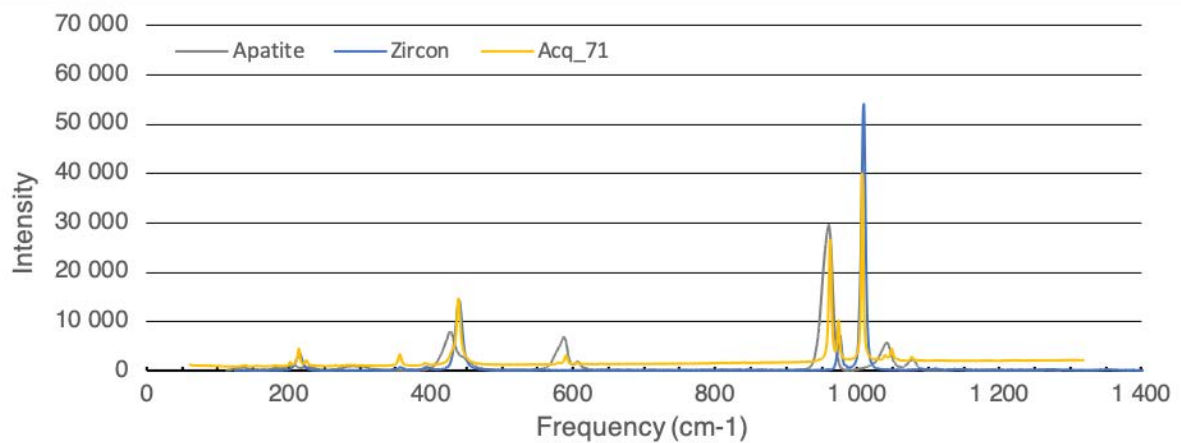


Figure I.3.9 (previous page): Raman spectra of apatite.

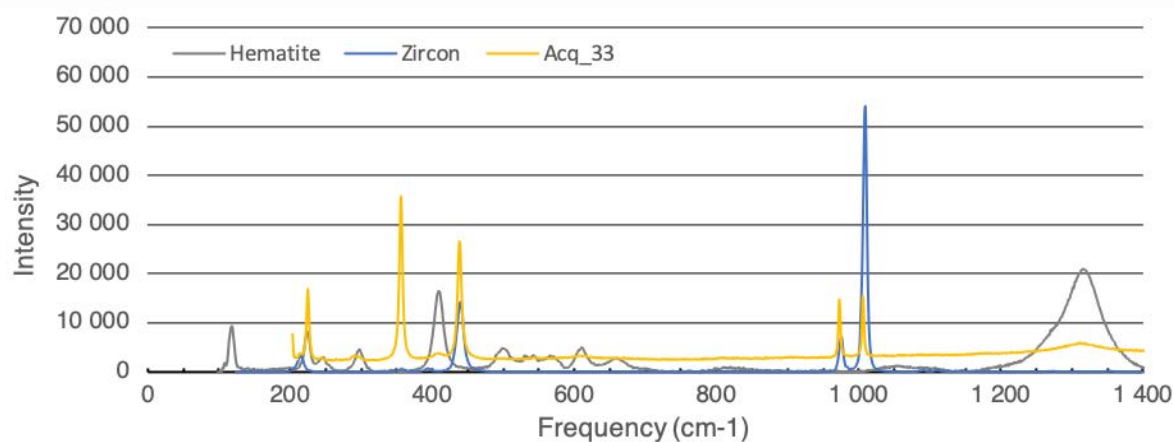


Figure I.3.10: Raman spectra of hematite.

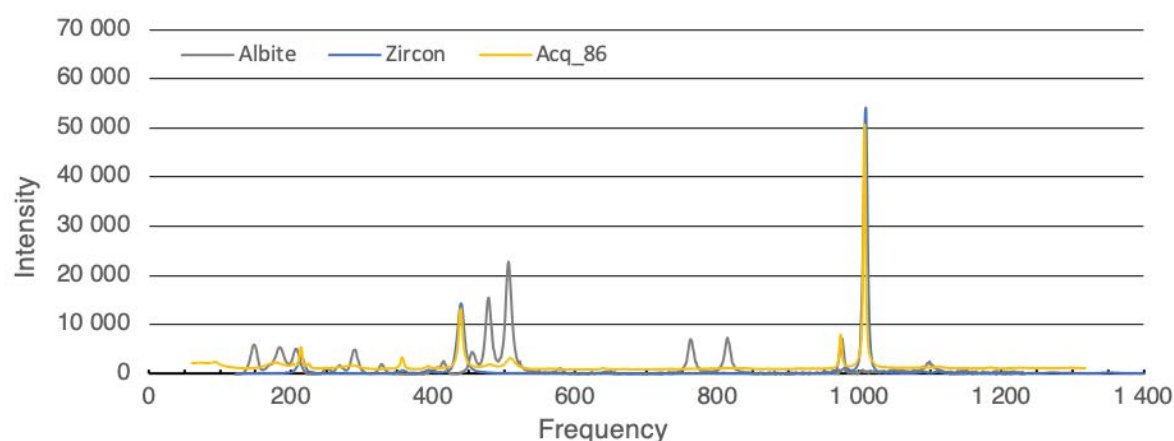


Figure I.3.11: Raman spectra of albite.

Trace elements in zircon

Trace elements measurements, together with U-Pb measurements, were performed on 83 analyses on 36 zircon grains from sample BR18 and 42 spots on 25 zircon crystals from sample BR19. Every different texture found within a given grain was analysed in order to check for their chemical signature. For the sake of clarity, these analyses were screened on the basis of their U-Pb concordance (with $80 \leq \text{concordance} \leq 120\%$) and 66 and 39 analyses for samples

BR18 and BR19 respectively are presented hereafter (note that concordance = $100 \times ((^{207}\text{Pb}/^{235}\text{U})/(^{206}\text{Pb}/^{238}\text{U}))$).

Population 1: CL-dark zircon sectors from sample BR18 display variable uranium (114-556; av: 286) content, Th/U (0.44-2.16; av: 0.77) and REE contents. Normalized to chondrite, the REE patterns are characterized by a negative Eu anomaly ($\text{Eu}/\text{Eu}^* = 3-22$; av: 9; Fig. I.3.12a) and a moderate HREE enrichment ($\text{Lu}/\text{Gd} = 13-31$; av: 20; Fig. I.3.12a). Ti content is variable (3-15; av = 8). Only one zircon from sample BR19 displays similar chemical characteristics ($\text{U} = 132$; $\text{Th}/\text{U} = 1$; $\text{Eu}/\text{Eu}^* = 19$; $\text{Lu}/\text{Gd} = 22$). One CL-dark zircon (BR18) is at variance with the characteristics described above ($\text{U} = 14$; $\text{Th}/\text{U} = 0.02$; no Eu anomaly; $\text{Lu}/\text{Gd} = 2$; Fig. I.3.12b).

Population 2: CL-bright crystals display striking homogeneity in both samples. They are characterized by lower U (BR18: 7-96, av: 34; BR19 – U: 19-99, av: 47.5) and Th/U ratios (BR18 – Th/U: 0.01- 0.1, av: 0.03; BR19 – Th/U: 0.01-0.06, av: 0.02). Their REE patterns do not display any Eu anomaly, though Eu/Eu^* ratio is quite similar to that of CL-dark zircon grains (BR18 – $\text{Eu}/\text{Eu}^* = 0.4-8$, av: 1.5; BR19 – $\text{Eu}/\text{Eu}^* = 2.2-20$, av: 7.6; Fig. I.3.12a), in addition, they show a depletion to a weak enrichment in HREE (BR18 – $\text{Lu}/\text{Gd} = 0.4-8.0$, av: 1.5; BR19 – $\text{Lu}/\text{Gd} = 0.4-2.1$, av: 1.0; Fig. I.3.12a). Their Ti content is less variable (BR18 – $\text{Ti} = 1.8-5.1$, av = 3.2, with one analysis $\text{Ti} = 20$; BR19 – $\text{Ti} = 0.89-7.5$, av = 3.73; with one analysis at 10).

The thin CL-bright rims around CL-dark zircons display heterogeneous chemical characteristics in between the populations 1 and 2 ($\text{U} = 11-307$; $\text{Th}/\text{U} = 0.01-1$; variable Eu anomaly; $\text{Eu}/\text{Eu}^* = 0.04-9.5$; $\text{Gd}/\text{Lu} = 2.6-37.7$; $\text{Ti} = 1.9-8.8$; av = 4.4; with one analysis $\text{Ti} = 2200$). However, it is noteworthy that three of them are characterized by low U content (11-35, av = 21) and Th/U ratio (0.05); no EU anomaly and weak HREE enrichment ($\text{Lu}/\text{Gd} = 3-7$; Fig.

I.3.12b); as well as Ti content (2.7-3.6; av = 3.0) similar to the CL-bright crystals. The isolated patches also display a characteristic in between the two populations.

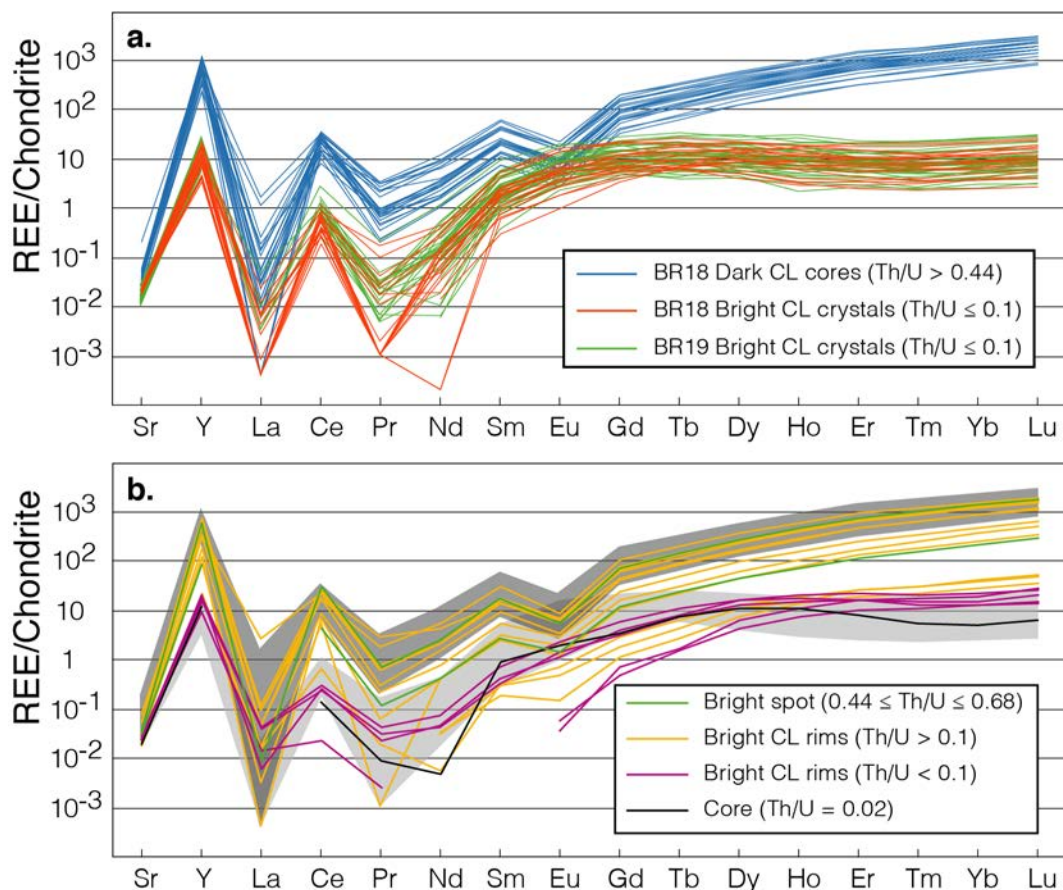


Figure I.3.12: REE spectra for the various textures found within the zircon population. CL-dark zircons and CL-bright crystals form two distinct populations. Alternatively, one core, the overgrowths, and bright patches display mixed signature (interpreted as mixing during the analyses). Some overgrowths display a typical metamorphic signature. The grey shaded area on (b) has been re-drawn from (a). Reference values for chondrite REE content after Barrat et al. (2012).

3.2. Petrography and chemistry of apatite

Apatite occurs rarely as inclusion in garnet but is common in the matrix of both samples (Fig. I.3.13a). It is also found included in zircon crystals in sample BR19 (Fig. I.3.9). In the matrix, apatite occurs as mm-sized aggregates of subhedral crystals ranging from 200 to 500µm

in length. These aggregates are elongated and parallel with the fabric (Fig. I.3.12b,c). Under transmitted light, separated crystals are limpid and may contain small inclusions (Figure I.3.13). Under CL, the crystals are homogeneous but their colour may vary from yellow to purple (Fig I.3.14).

Seventy-two analyses have been performed on 33 crystals from sample BR18 and 40 analyses on 21 crystals for sample BR19. Apatite grains from sample BR18 display Th/U ratios that are similar whatever their CL colour (yellow, Th/U = 0.08-3.32, Av = 0.53; purple, Th/U = 0.08-0.94, Av = 0.49) but the purple crystals tend to be richer in U (yellow, U = 0.15-25.46, Av = 6.60; purple, U = 0.15-83.70, Av = 26.65), particularly two grains (III and XXVII in tables I.3.18 and I.3.19) with higher U content (43 and 73 ppm in average respectively). The apatite crystals from the sample BR19 yield lower U contents in average (U = 1.37). The yellow population display a lower Th/U ratio and contains less U than the purple one (yellow, Th/U = 0.08-0.68, av = 0.22, U = 0.15-2.92, av = 1.02; purple, Th/U = 0.21-0.49, av = 0.34, U = 0.99-3.97, av = 2.31).

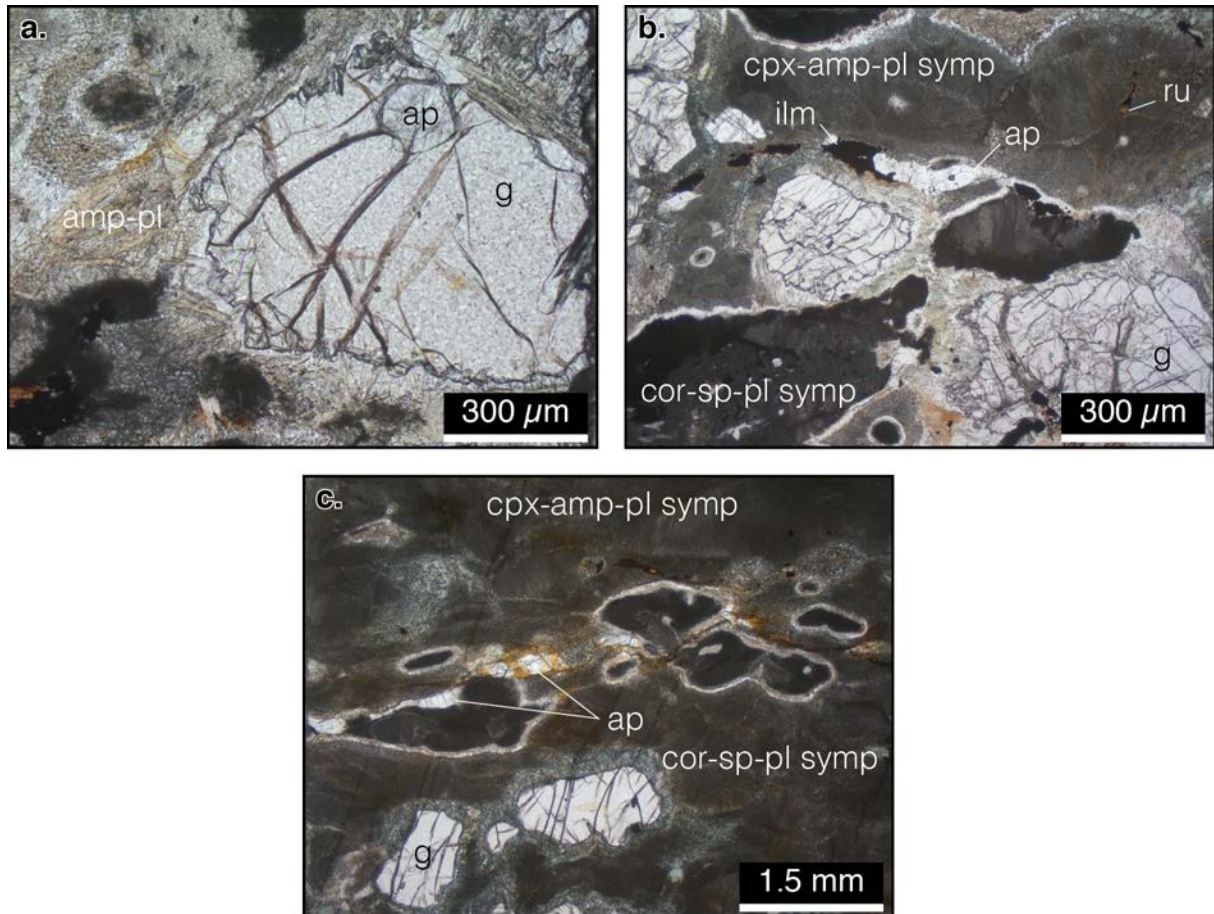


Figure I.3.13: Microphotographs of apatite included in garnet (a), and elongated clusters of apatite in the matrix (b, c).



Figure I.3.14: CL images of apatites.

3.3. Petrography and chemistry of rutile

Rutile is common and found either in the matrix and as inclusion in garnet (Fig. I.3.2). The crystals are anhedral with size ranging from 50 to 250 μm. Forty-two analyses were

performed on 18 grains. U and Pb contents are low (U = 0.03-34.3, av = 2.0; Pb = 0.01-3.3; av = 0.2) whatever their textural positions. Zirconium contents vary from 137 to 362 ppm with an average of 250 ppm.

3.4. Ti-in-zircon and Zr-in-rutile thermometry

In order to constrain the conditions of zircon and rutile crystallization we applied the Zr-in-rutile and Ti-in-zircon thermometry. The application of these methods relies on the equilibrium between quartz, zircon and rutile. In the studied samples, clusters of zircon crystals are observed in garnet around rutile. Zircon grains are also included in rutile and the inverse relationship is demonstrated by petrography and Raman spectroscopy (Figs. I.3.2; I.3.3d; I.3.6). Though rare, quartz is included in garnet. The incorporation of Ti and Zr in zircon and rutile respectively is dependent on temperature but also on pressure. Consequently, we have applied the P dependent calibrations of Hofman et al. (2014) and Tomkins et al. (2007) for zircon and rutile respectively.

The Ti contents for the CL-bright zircon crystals (population 2) is variable at the scale of the whole population (BR18 – Ti = 1.8-5.1, av = 3.2, with one analysis Ti = 20; BR19 – Ti = 0.89-10, av = 3.98), or even within a single grain (e.g. BR19-Zrn-V; Ti 1.95-6.10; Table I.3.14). There is no systematic core-rim enrichment or depletion relationship (e.g. zircons IX – core: 7.5, rim: 4.3 and XIII – core: 2.3, rim: 4.7 in Table I.3.14), nor apparent age versus Ti content relationship. The Ti contents of zircon grains with rutile inclusions are also consistent for the whole population (BR19 – Ti = 2.4-5.4; n = 4). At the scale of this study, Ti thus appears randomly distributed in zircon. Zirconium content in rutile is variable (Ti = 137-362) and there is no correlation between Zr content and the textural position (i.e. included in garnet or in the matrix; Table I.3.17). Note that core-rim relationship is qualitative more than quantitative since the used spot size was 50µm and that the size of most rutile analyzed range from 50 to 200µm.

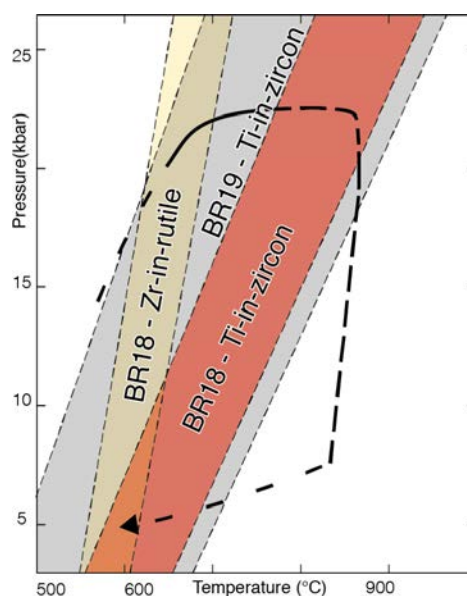


Figure I.3.15: P – T path contoured with the results of Ti-in-zircon and Zr-in-rutile thermometry.

A P – T diagram has been contoured with the minimum and maximum isopleths of the Ti content in zircon and Zr content in rutile (Fig. I.3.15). The thermometry results intersect the P – T path in the prograde and the retrograde parts. Ti-in zircon in the sample BR19 yield a wide range of temperatures between 600 and 850 °C at $P > 19$ kbar and $T < 700^{\circ}\text{C}$ at $P < 6$ kbar. In sample BR18, the range of temperatures is narrower with T 770–862°C at P 20–22.5 kbar and 580–680 at $P = 5$ kbar. Zr-in-rutile indicates T between 622–706°C at $P > 18$ kbar and 570–630°C at $P = 5$ kbar.

4. U/Pb results

4.1. U/Pb results of rutile

Forty-two analyses were performed directly in thin section, on 17 different rutile crystals with distinct textural positions. The high error of most grains allows to use only six analyses (Table I.3.16) on four rutile grains found in the matrix. Plotted in a Tera-Wasserburg concordia diagram, the data are discordant indicating the presence of various amount of common Pb. A

lower intercept date of 348 ± 9 Ma can be calculated (MSWD = 2.1) yielding an initial $^{207}\text{Pb}/^{206}\text{Pb}$ ratio of 0.795 ± 0.108 , in agreement with the Stacey and Kramers (1975) terrestrial Pb evolution model.

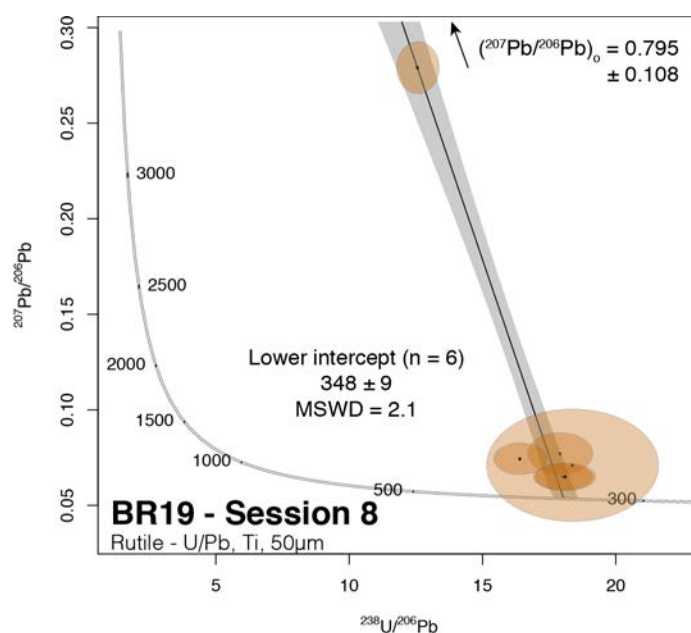


Figure II.3.16: Tera Wasserburg plot of the data obtained on rutile from the sample BR18. Note that two ellipses are almost superposed (the two more concordant).

4.2. U/Pb results of apatite

Seventy-two U-Pb analysis were performed on 32 individual grains from sample BR18 and forty analyses on 21 crystals separated from sample BR19. In a Tera-Wasserburg concordia diagram, the data from both samples plot in a very discordant position indicative of a high proportion of common Pb (Fig. I.3.17). The data for sample BR18 defines a lower intercept date of 353 ± 1 Ma (MSWD = 1.3) with a $^{207}\text{Pb}/^{206}\text{Pb}$ initial value of 0.857 and those from sample BR19 a lower intercept date of 357 ± 9 Ma (MSWD = 1.2) with a $^{207}\text{Pb}/^{206}\text{Pb}$ initial value of 0.856. These $^{207}\text{Pb}/^{206}\text{Pb}$ initial values for both samples are in a good agreement with the Stacey and Kramers (1975) terrestrial Pb evolution model.

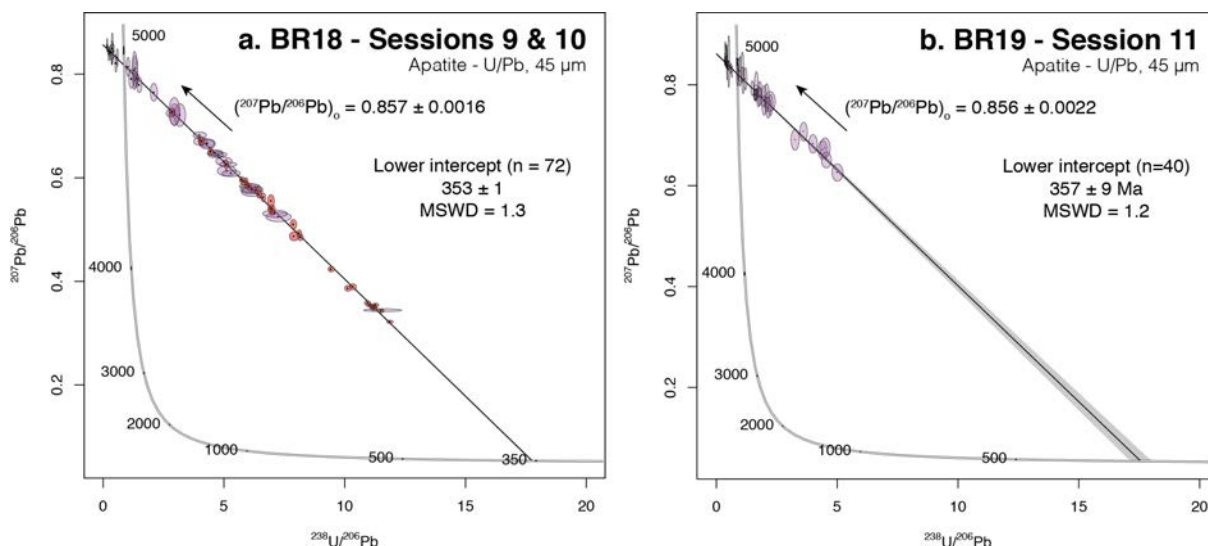


Figure I.3.17: Tera Wasserburg plot of the data obtained on apatite from the sample BR18 (a) and BR19 (b). In both cases, the common lead composition was calculated by Isoplot R.

4.3. U/Pb Zircon

Representative CL images of the analysed zircon grains from samples BR18 and BR19 are shown in Figs I.3.18 and I.3.19 respectively. Eighty-three analyses were performed on 36 grains. A first set of two analytical sessions (1 and 2) was performed on both the CL-dark cores and the CL-bright rims (Fig. I.3.20). Two other analytical sessions were acquired solely on CL-bright separated grains from sample BR18 (analytical sessions 3 to 4; Fig. I.3.21a-c). Moreover, one analytical session (analytical session 5; Fig. I.3.21d-f) was also performed directly in context in thin section. In addition, 50 analyses have been performed on 27 zircon grains for sample BR19 (41 CL-bright crystals and one CL-dark core) during analytical sessions 6 and 7 (Fig. I.3.22a).

The interpretation of the results obtained on zircon is not straightforward. Therefore, this section is organized in several parts with first, a description of the results obtained for the different textures. Then the second part focuses on the discrimination and description of the

different clusters obtained (one on the CL-dark cores and possibly two on the CL-bright crystals). Finally, several dates using various method of calculation are presented and discussed.

The results from analytical sessions 1 and 2 obtained on various textures (CL-dark cores, CL-bright crystals and or rims) are plotted in a Tera-Wasserburg concordia diagram (Fig. I.3.20a). Once the discordant data (>20% of discordancy) are removed, two main clusters can be distinguished at c. 490 and 340 Ma respectively (Fig. I.3.20b) with the exception of two analyses that plot around 700 Ma (red ellipses in Fig. I.3.17a). The position of the discordant data can be attributed to various amount of common Pb and/or Pb loss.

Most of the analyses performed on the CL dark cores are concordant and cluster around 490 Ma (Fig. I.3.20b). The CL-bright analyses plot in a concordant to discordant position and cluster around 340 Ma (Fig. I.3.20b). In addition, one ellipse obtained on a CL-bright crystal display a $^{206}\text{Pb}/^{238}\text{U}$ apparent age older than the main cluster (bold ellipse, Fig. I.3.20b). The core with $\text{Th}/\text{U} < 0.1$ yields an apparent $^{206}\text{Pb}/^{238}\text{U}$ age of 424 ± 24 Ma. The two bright patches in CL-dark cores yield two apparent $^{206}\text{Pb}/^{238}\text{U}$ ages of 502 ± 18 Ma and 400 ± 24 Ma (Fig. I.3.20c). The CL-bright rims around CL-dark zircon cores are characterized by either $\text{Th}/\text{U} > 0.1$ or $\text{Th}/\text{U} < 0.1$ and clusters around 490 or 340 Ma (Fig. I.3.20d). The rims, bright patches and the low Th/U core yield ambiguous results that will be discussed later. However, a clearer pattern emerges from the CL dark cores and CL-bright crystals.

The results obtained on the CL-dark zircons scatter between c. 500 Ma up to 390 Ma. This is best shown in a KDE diagram (Fig. I.3.20e) that display an asymmetric distribution of the $^{238}\text{U}/^{206}\text{Pb}$ dates with a maximum frequency of the ages between 490-505 Ma and a scattering toward younger dates, suggesting that they underwent lead loss. However, most of the data remain concordant, and allow to calculate a concordia date of 485 ± 3 (MSWD = 1.6) using 20 out of the 25 analyses discarding the youngest analyses (i.e. suspected of lead loss).

The results on CL-bright crystals during each sessions are shown in specific Tera-Wasserburg concordia diagrams (BR18: Figs. I.3.21 and BR19: Figs. I.3.22a,b). All the data are plotted in two KDE diagrams, after a common lead correction following the Stacy and Kramer two stage isotope model implemented in IsoplotR (Fig. I.3.22c,d). These plots show that the data cluster is scattered with $^{206}\text{Pb}/^{238}\text{U}$ apparent ages ranging between ~280-360 Ma indicating lead loss. The data obtained during the analytical sessions 4 and 5 (Fig. I.3.21c,d) both display aligned discordant ellipses. This pattern is characteristic for a common lead incorporation at the time of zircon crystallization.

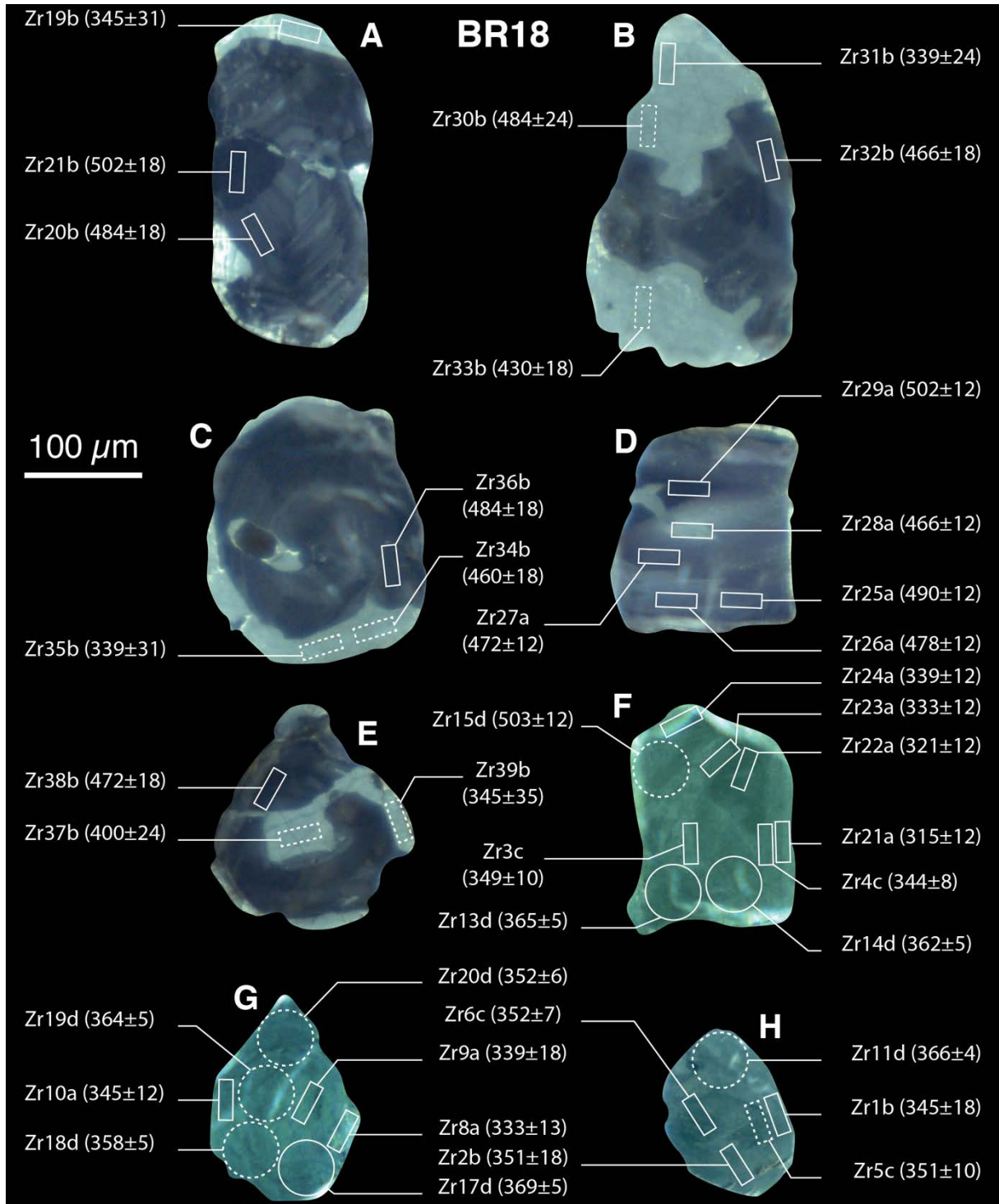


Figure 1.3.18: Representative CL images of zircon crystals from sample BR18. The position of the spots is shown. Dashed lines spots indicate either discordant analyses (conc < 80%) or overgrowth yielding “magmatic” dates. The CL colour has been modified to enhance contrast of the metamorphic zircon. Note the “bright patch” in zircon E.

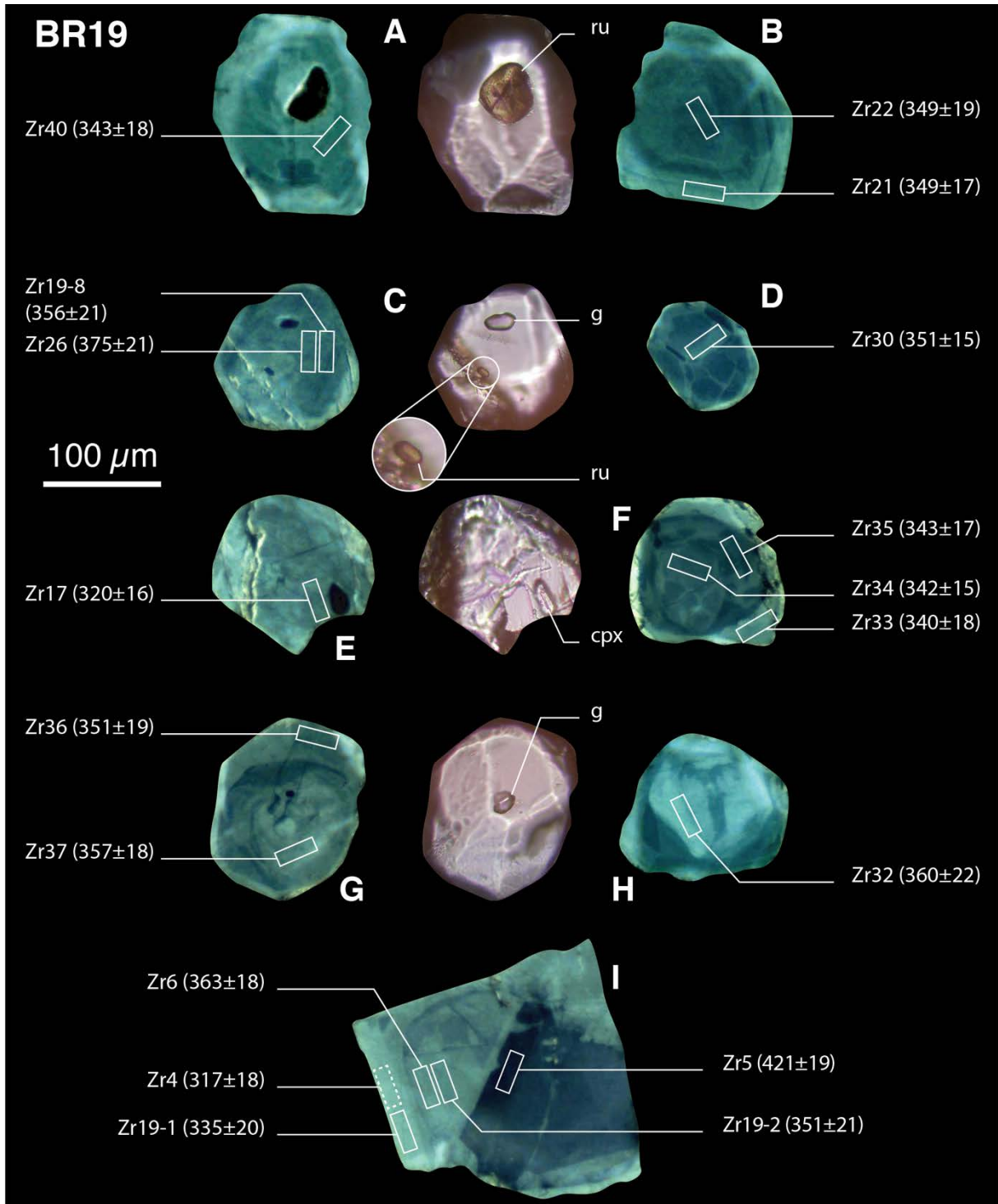


Figure I.3.19: Representative CL images of zircon grains from the sample BR19. The position of the spots is shown. Dashed lines spots indicate either discordant analyses (conc < 80%). The CL colour has been modified to enhance contrast of the metamorphic zircon. Note the oscillatory growth zoning of the zircon B, the overgrowth over zircon F and the flow textures in zircon grains G and H. The analysis Zr 5 on zircon I is the only one performed on CL dark zircon in this sample.

Chapter 1 – Section 3

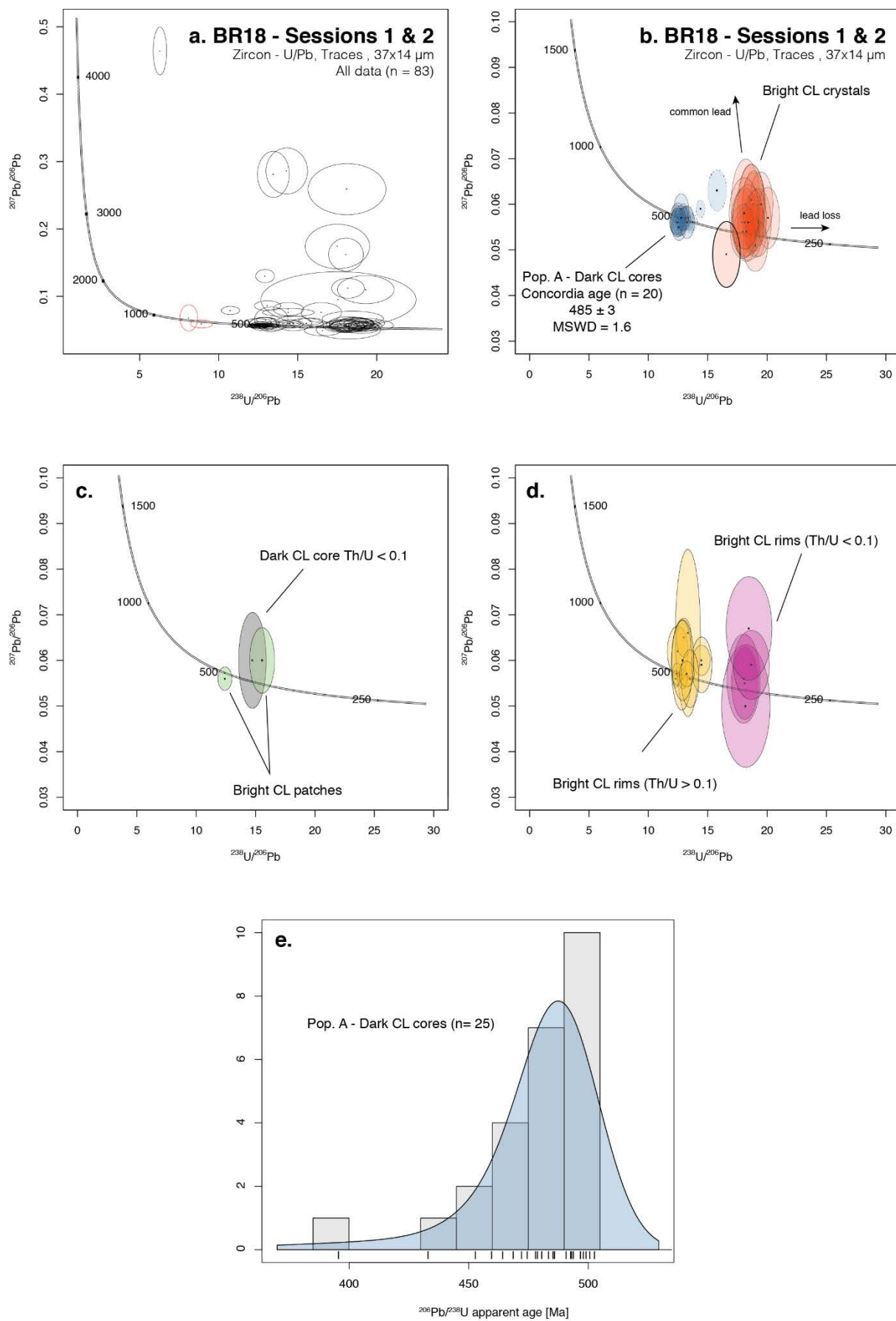
Legend for the Figures II.4.17 to II.4.19 by order of apparition in the next three pages.

Figure I.3.20: Plots of the U/Pb data obtained during the analytical sessions 1 & 2. Tera-Wasserburg concordia diagram with all the data (a); data with $120 < \text{conc} < 80$ (b-d) and KDE diagram for the CL-dark cores (e). A concordia age for the CL-dark cores has been calculated using the plain ellipses (a). Note the bimodal distribution of the CL-bright rims apparent ages and the asymmetric distribution of CL-dark cores apparent ages.

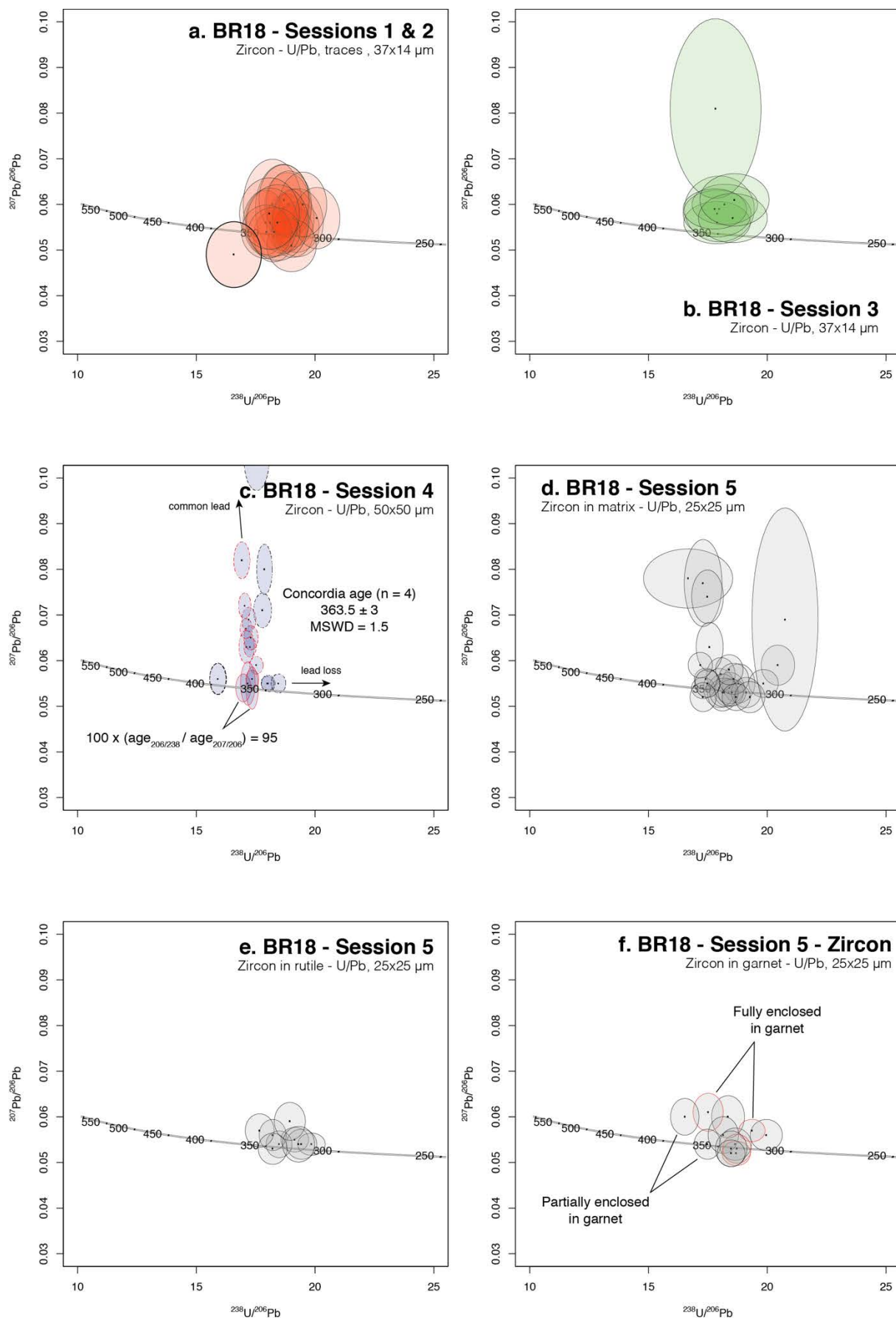
Figure I.3.21: Tera-Wasserbug concordia diagrams for the data obtained on CL-bright zircon grains from sample BR18. Note that most of the data are discordant (best seen on plots c and d). Also, the data are scattered (best seen on plots a, d, e and f). Bold line ellipses in (a) and (c) plot away from the main population. The four plain ellipses in (c) were used to calculate a concordia age. The four red ellipses in (f) were obtained on zircon crystals fully enclosed in garnet (although these garnet grains contain numerous cracks).

Figure I.3.22: Tera-Wasserbug concordia diagrams for the data obtained on sample BR19 (a, b) and KDE plots of the $^{206}\text{Pb}/^{238}\text{U}$ apparent ages of metamorphic zircon after a Stacey and Kramer common lead correction (BR18: c; BR19: d). An asymmetric distribution of the data is best seen on the KDE for analytical session 3, analytical sessions 1-5 and analytical session 6. Note that the bold or dashed ellipses of the plot (a) are not shown on the KDE diagram (e). Note that the dashed ellipse in (a) correspond to the analysis of a CL-dark core (analyse Zr5 in Fig. I.3.16). This is the only analysis of CL-dark core performed on sample BR19 because of the rarity of such zircon.

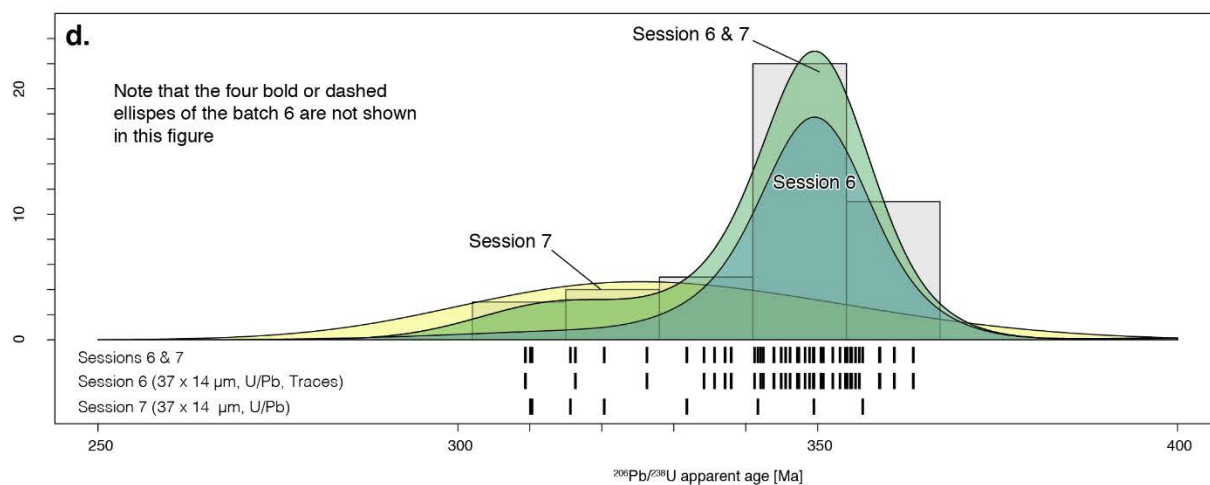
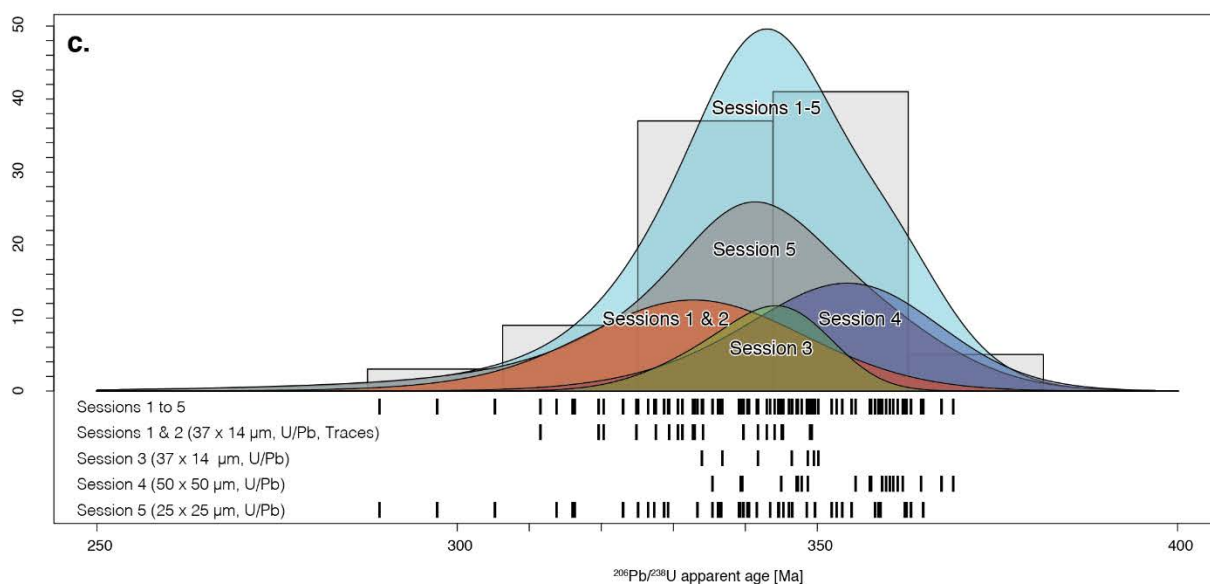
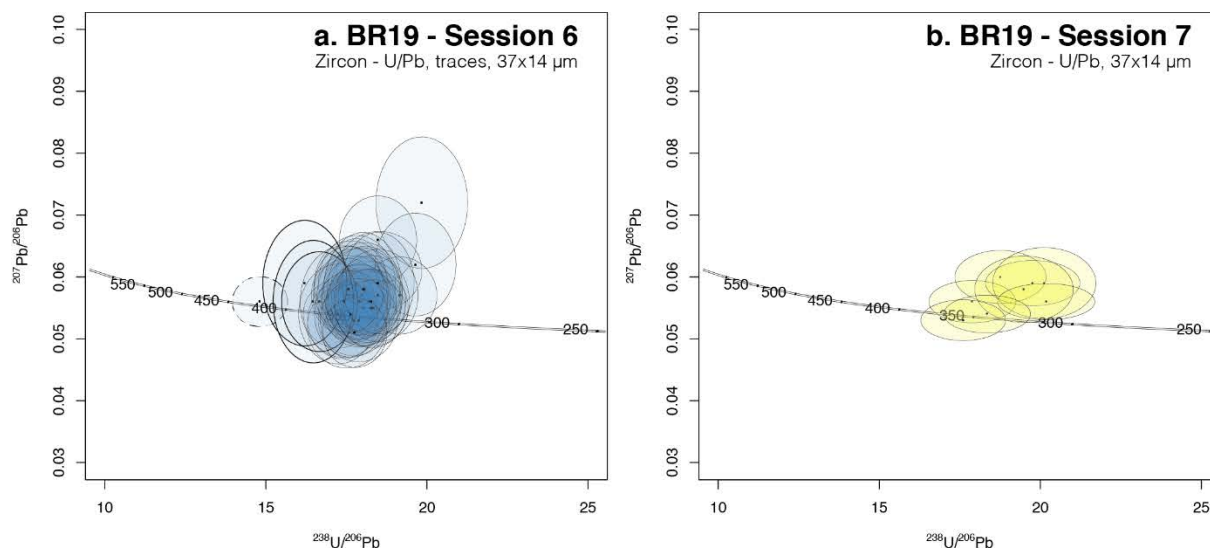
Chapter 1 – Section 3



Chapter 1 – Section 3



Chapter 1 – Section 3



In Fig. I.3.22.c the red ellipses are concordant to discordant. They define an alignment pointing toward two ellipses with a $^{238}\text{U}/^{206}\text{Pb}$ apparent age of ~ 365 Ma. The black dashed ellipses display a younger $^{238}\text{U}/^{206}\text{Pb}$ apparent age suggestive for lead loss. On the other hand, the signification of the bold dashed ellipse with an $^{238}\text{U}/^{206}\text{Pb}$ apparent ages ~ 385 Ma is surprising. Indeed, it is hardly conceivable that the red ellipses lost a significant amount of Pb, otherwise, they would not align. This suggest that the bold dashed ellipse belong to another age population. Several ellipses with similar $^{238}\text{U}/^{206}\text{Pb}$ apparent ages from different analytical session are shown in bold in the Figs. I.3.21a,c and I.3.22a. Plotted in a Tera Wasserburg (Fig. I.3.23), these analyses allow to calculate a concordia age of 389 ± 6.5 Ma (MSWD = 1.4).

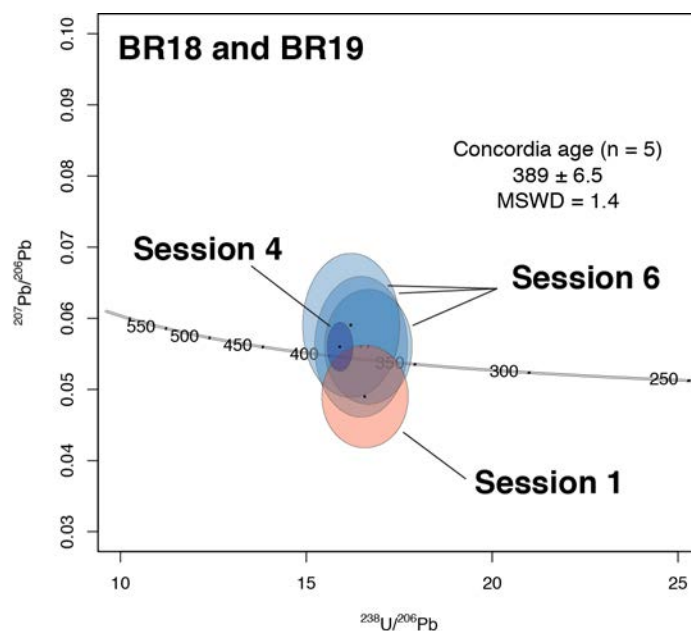


Figure I.3.23: Tera Wasserburg concordia diagram of the “old cluster” obtained on CL-bright crystals.

The well-defined alignment of data obtained during analytical session 4 (Figs. I.3.21c and I.3.26). allow to calculate a concordia date of 363.5 ± 3 Ma ($n = 4$; MSWD = 1.5; Fig. I.3.21c).

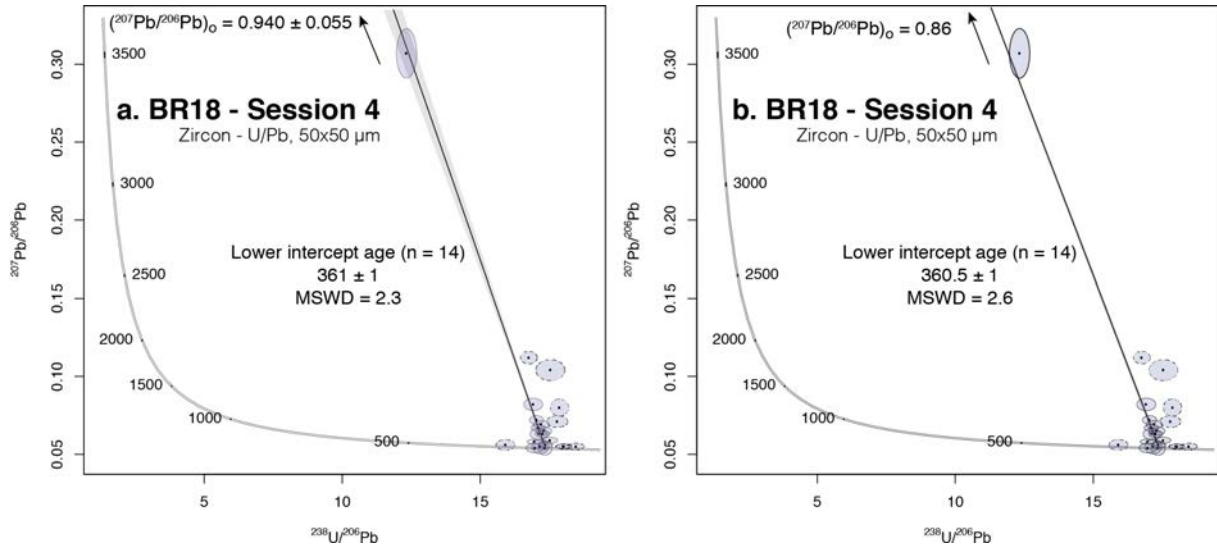


Figure I.3.26: Tera Wasserburg concordia diagrams and calculated lower intercept ages for the data obtained during analytical session 4. Initial common Pb composition is unanchored in (a) and anchored to the common Pb composition of 0.86 (365 Ma) in (b).

5. Discussion

A special focus on zircon crystallization has been undertaken. Indeed, zircon might form along diverse portions of the P – T path (e.g. Rubatto and Hermann, 2007). Zircon may crystallize either by crossing Zr-releasing metamorphic reactions (e.g. Bingen et al., 2001; Kohn, 2015; Beckman and Möller, 2018) or by recrystallisation (e.g. Schaltegger et al., 1999). The later may occur with or without implication of a fluid phase (Geisler et al., 2007). Possibly various zircon forming processes may be recorded by internal texture, chemical characteristics and textural position of zircon crystals. Identifying Zr sources and understanding zircon dissolution-recrystallization process are keys in the understanding of zircon crystallization during HP metamorphism. First, the interpretation of zircon dating will be confronted to the results of Ducrot et al. (1983). Second, a general consideration on zircon crystallization at high pressure will be proposed based on the interpretation of internal textures and textural relationship of zircon with other minerals.

5.1. *Zr-in-rutile and Ti-in-zircon thermometry results*

First of all, it is important to recall that the incorporation of Zr and Ti in rutile and zircon, respectively, depends on the equilibrium of zircon, rutile and quartz (Watson and Harrison, 2005). Evidence of zircon growth at high pressure is further discussed in the following sections. However, the close relationship between zircon and rutile in garnet (Fig. I.3.2) and the observation of rutile in zircon (Fig. I.3.19A,B) and *vice versa* (Fig. I.3.3d) strongly suggest a period of coeval growth. Quartz is also included in garnet suggesting that the prerequisite to the use of these thermometers are fulfilled.

Because the incorporation of Zr in rutile and Ti in zircon reflect an equilibrium, Ti-in-zircon and Zr-in-rutile thermometer could be expected to record similar temperatures. The results of thermometry in rutile and zircon from sample BR18 intersect at low pressure (Fig. I.3.15) but an equilibration of the metamorphic zircons at low pressure can be ruled out because garnet and rutile typically crystallize at high temperature in mafic rocks. On the other hand, the thermometry results do not intersect at high pressure... During the analyses of rutiles, the large ablation spots (~50µm) and the small size of rutile crystals (~100µm) did not allowed to investigate the core to rim repartition of Zr-in-rutile with a high resolution. A possible explanation for the apparent discrepancy between the temperature estimated using these two thermometers would be that zircon equilibrated with rutile rims at peak P - T conditions and that their core inherited and retained a lower Zr content. This interpretation is consistent with the results of Taylor-Jones et al. (2015) who proposed that the volume diffusion in rutile is slow and that only the rims of rutile might be available to equilibrate with zircon, even at relatively high-temperature. According to the same authors, the size of the rutile rim at the equilibrium with zircon calculated for a cooling of 8°C/Ma of a 100µm size rutile (in the range of size of the analysed rutiles) would be ~15µm. In the studied case, rutile is not expected to equilibrate with zircon during cooling but rather during increasing temperature. However, the preservation

of garnet growth zoning suggests a short-lived thermal event that could explain only limited equilibration of zircon with rutile edges. Accordingly, the temperature indicated by Zr-in-rutile thermometry are interpreted as the crystallization temperature of rutile and those of Ti-in-zircon thermometry as later (i.e. higher) crystallization or equilibration temperature.

5.2. Discussion of U/Pb results

In the framework of evolving P – T conditions during subduction the timing of successive metamorphic events might be recorded by various datable minerals and isotopic couples. Accordingly, the use of zircon, apatite and rutile are expected to give different time constraints on the P – T path. On the one hand, zircon and rutile U/Pb dating yielded scattered results (~280–360 $^{206}\text{Pb}/^{238}\text{U}$ apparent age) and imprecise results respectively. On the other hand, apatite is remarkably homogeneous from an isotopic point of view. Therefore, the results of the zircon and rutile dating will be discussed in the light of the interpretation of the apatite U/Pb results.

Apatite dating

Seventy-two analyses have been performed over 33 separated crystals of the sample BR18 and 40 analyses over 21 separated crystals of the sample BR19. The analyses obtained on samples BR18 & BR19 yielded two dates, similar within the uncertainty, of 353 ± 1 Ma (MSWD = 1.3) and 357 ± 9 Ma (MSWD = 1.2) with $^{207}\text{Pb}/^{206}\text{Pb}$ initial values of $(^{207}\text{Pb}/^{206}\text{Pb})_0 = 0.857 \pm 0.0016$ and $(^{207}\text{Pb}/^{206}\text{Pb})_0 = 0.856 \pm 0.0022$, respectively, in a good agreement with the Stacey and Kramers (1975) terrestrial Pb evolution model.

Apatite is systematically observed included in garnet, in eclogitic zircon or in the matrix, forming elongated cluster conformably oriented with the eclogitic fabric, thus, it is inferred to belong to the peak assemblage. The dates obtained on apatite are similar to a wide range of dates obtained on zircon, the latter even yielded some apparently younger results. In the first hand, apatite closure temperature is estimated between 375 and 550°C (Cherniak et al., 1991;

Chamberlain and Bowring, 2001; Harrison et al., 2002; Cochrane et al., 2014). On the other hand, Villa (1998, 2010) suggested that the concept of closing temperature estimated during experiments is not relevant under most geological conditions. Accordingly, we have to consider the possibility that the 353 ± 1 Ma and 357 ± 9 Ma dates obtained on apatite may not be cooling ages.

The first order observation to interpret the apatite date is that the samples are pervasively retrogressed (Figs. I.2.1 and I.2.3). The retrogression of clinopyroxene involved fluids since it is replaced by amphibole. The use of apatite as a tracer for hydrothermal alteration explicitly rely on its reactivity to fluids (e.g. Harlov, 2015 and references therein). Therefore, it is unlikely that fluids retrogressing the matrix did not affect the apatite grains as well. Given, the analysed population of 54 grains (BR18: 33 crystals; BR19: 21 crystals) display a remarkable isotopic homogeneity at the scale of the whole population and CL colours at the scale of a single grain, it is likely that the apatites have re-equilibrated after retrogression, possibly by recrystallization, erasing the probable effect of fluids alteration. According to the P – T pseudosection modelling, the retrogression of clinopyroxene occurred at high-temperature (750–825°C) and pressures lower than 7 kbar. Therefore, apatite might have re-equilibrated during cooling after the decompression. Thus, the lower intercept dates of 353 ± 1 Ma and 357 ± 9 Ma is a cooling age (i.e. after the decompression and retrogression).

Rutile dating

Forty-two analyses were performed directly in thin section, on 17 different rutile crystals with distinct textural positions. However, most of the rutile analysed display very low U and Pb contents and consequently resulted in unexploitable results. As a consequence, only six analyses performed on four rutile grains from the matrix contained sufficient U and Pb to obtain a lower intercept date of 348 ± 9 Ma date (MSWD = 2.1; Fig. I.3.16). The closure temperature

of 600°C has been estimated for rutile crystals of ~100µm (in the range of the analysed crystals; Cherniak, 2000). This date is similar within the incertitude to the cooling age of apatite and is interpreted as a cooling age as well.

Zircon dating

A total of 213 analyses were performed on 92 zircon grains. Among them, 30 were carried on magmatic cores and 183 on zircon crystals with metamorphic textures including 50 analyses performed in context (i.e. in thin section). Trace elements were measured during all the analyses of magmatic cores and 95 analyses out of the 133 performed on separated grains with metamorphic textures. The 38 analyses without trace element estimation were performed on grains already characterized by trace element analyses. U/Pb analyses allow to distinguish three group of ages. The older cluster (~485 Ma) was obtained on CL-dark cores and the two other clusters (~390Ma and ~360-290Ma) were obtained on metamorphic rims or crystals.

CL-dark cores

During the dating of the CL-dark cores, all but two analyses yielded consistent results yielding early Ordovician $^{206}\text{Pb}/^{238}\text{U}$ apparent ages. The two inconsistent analyses display a late Silurian $^{206}\text{Pb}/^{238}\text{U}$ apparent ages and different REE spectra. The first one (Zr12b, batch 2, Table I.3.3) yielded a $^{206}\text{Pb}/^{238}\text{U}$ apparent age of 424 ± 24 Ma (concordance = 97) and a flat REE pattern ($\text{Lu}/\text{Gd} = 0.23$) and no Eu/Eu^* anomaly (0.002) along with a low Th/U ratio of 0.02. The other yielded a $^{206}\text{Pb}/^{238}\text{U}$ apparent age of 421 ± 19 Ma (concordance = 99, Zr5a, batch 6 – Table I.3.12), a $\text{Th}/\text{U} = 0.1$ as well as a weak negative Eu/Eu^* anomaly (18.8) and enrichment in HREE ($\text{Lu}/\text{Gd} = 22$). These analyses yielded similar U/Pb results but contrasting REE pattern, therefore they are not reproducible. Accordingly, it is likely that they result from a mixed analysis of a CL-dark core and a CL-bright patch below the surface of the crystal and thus unseen.

Though not decisive, the oscillatory zoning (Figs. I.3.4AB and I.3.14A) of the CL-dark cores and their low Th/U (0.44-2.16; av: 0.77) suggest a magmatic origin (e.g. Corfu, 2003; Rubatto 2002 and discussion in Harley et al., 2007). The negative Eu anomaly ($\text{Eu}/\text{Eu}^* = 3\text{-}22$; av: 9; Fig. I.3.12) of these zircons may indicate equilibrium with plagioclase and the moderate HREE enrichment ($\text{Lu}/\text{Gd} = 13\text{-}31$; av: 20) the absence of garnet during their crystallization (Rubatto, 2002). Therefore, the lower Ordovician concordia date of 485 ± 3 Ma (MSWD = 1.6) obtained on this population is interpreted as the crystallization age of the protolith.

CL-bright rims, patches and crystals

The CL-bright colours are observed in rims around CL-dark cores or entire crystals with various textures reported in metamorphic rocks (rims around primary cores: e.g. Liermann et al., 2007; flow texture: and sector zoning: e.g. Vavra et al., 1996; oscillatory zoning: Gebauer et al., 1997), suggesting a metamorphic origin. Though entire CL-bright crystals yielded consistent REE spectra and variscan $^{206}\text{Pb}/^{238}\text{U}$ apparent ages, the CL-bright rims and patches yielded ambiguous results.

The CL-bright patches and thin rims cut through the oscillatory zoning of the CL-dark cores (e.g. Figs. I.3.4A,C and I.3.18E) demonstrating their secondary origin. Most of the thin CL-bright rims around CL-dark zircons display heterogeneous chemical characteristics in between the CL-dark cores and CL-bright crystals having a strongly varying U content ($\text{U} = 11\text{-}307$), Th/U (0.01-1), Eu anomaly ($\text{Eu}/\text{Eu}^* = 0.04\text{-}9.5$), HREE enrichment ($\text{Gd}/\text{Lu} = 2.6\text{-}37.7$). Three of them (Zr3b,5b,19b), on the other hand, are characterized by low U content (11-35, av = 21) and Th/U ratio (0.05); no EU anomaly and weak HREE enrichment ($\text{Lu}/\text{Gd} = 3\text{-}7$) similar to the CL-bright crystals. The two isolated patches analysed also display a characteristic in between the two populations. CL colours being controlled by the trace element content of zircon

(Nasdala et al., 2003), the mixed signal in between the CL-bright rims and the CL-dark cores is interpreted as melange during the analyses.

As mentioned above, the CL-bright crystals display textures reported in metamorphic rocks. They are also characterized by a low Th/U ratio (BR18 – Th/U: 0.01- 0.1, av: 0.03; BR19 – Th/U: 0.01-0.06, av: 0.02) suggesting a metamorphic origin. Though Eu/Eu* ratio is quite similar to that of CL-dark zircon grains (BR18 – Eu/Eu* = 0.4-8, av: 1.5; BR19 – Eu/Eu* = 2.2-20, av: 7.6), their REE patterns (Fig. I.3.12) do not display any Eu anomaly but a depletion to a weak enrichment in HREE (BR18 – Lu/Gd = 0.4-8.0, av: 1.5; BR19 – Lu/Gd = 0.4-2.1, av: 1.0), respectively suggesting that they crystallized in the absence of plagioclase but presence of garnet. In thin section, zircon is included in garnet and rutile (Figs. I.3.2, I.3.3 and the inverse relationship is demonstrated on separated crystals by Raman spectroscopy (Figs. I.3.4, I.3.5, I.3.6). In addition, omphacite is also included in zircon (Fig. I.3.8). The presence of zircon in eclogitic garnet and garnet in zircon strongly suggest a coeval period of growth during the eclogite facies metamorphism.

The identification of a possible plagioclase in CL-bright crystal (most likely albite; Figs. I.3.4I and I.3.11) in one zircon in sample BR19 (Zircon XVIII in Tables I.3.11 and I.3.12) could argue against this interpretation. This zircon is perfectly concordant (concordance = 100) with a $^{206}\text{Pb}/^{238}\text{U}$ apparent age of 364 Ma. It displays a low U content (34 ppm) and Th/U ratio (0.02), no negative Eu/Eu* anomaly and a slight depletion in HREE (Gd/Lu = 0.8; in Tables I.3.11 and I.3.12). It is oscillatory zoned suggesting that it could have grown in a melt (e.g. Corfu, 2003) or, alternatively, from a fluid at high-pressure (Gebauer et al., 1997). Plagioclase is stable close to the peak *P–T* conditions during the M2 metamorphism in the melt stability field (Fig. I.1.5) suggesting that zircon and plagioclase might have grown together during M2. If this is taken to be true, the absence of negative Eu/Eu* anomaly of this zircon is surprising and might have consequences for the interpretation of the REE spectra of zircons. It must be noted that a low

plagioclase content is expected during M2; therefore, plagioclase would not be able to uptake a significant amount of Eu and could explain the absence of negative Eu/Eu* anomaly. Alternatively, zircon preferentially incorporate Eu^{3+} in its crystal lattice while plagioclase takes up divalent Eu, thus, Eu content of zircon might not be affected by the co-stability with plagioclase (Kohn, 2016). An alternative interpretation based on the shape of this inclusion is possible. The inclusion is elongated, having a “zig-zag” tubular shape different from others inclusions (i.e. garnet, rutile or clinopyroxene) that are shorter and sometimes faceted (Fig. I.3.19C,G). The inclusion also displays a brown termination (Fig. I.3.4I) suggesting that it could be polycrystalline, and possibly a melt inclusion. Alternatively, the shape of the inclusion could also point to fracture filling. Further investigation of this inclusion remains necessary to conclude. The first step would be to obtain a better Raman spectrum of the inclusion and determine whether the inclusion is polycrystalline or not. However, the Ti-in-zircon temperature recorded by this zircon ($\text{Ti} = 2.30 \pm 1.10$; $T = 810 \pm 50^\circ\text{C}$ at 22.5 kbar) is in better agreement with a crystallization during the isobaric heating (M1; Fig. I.1.7).

The preservation of titanite (inset in Fig. II.4.7) in the same population of CL-bright zircon is also surprising. This zircon (zircon VI; Table I.3.12 and I.3.15) display a 356 Ma $^{206}\text{Pb}/^{238}\text{U}$ apparent age (concordance = 95), no Eu/Eu* anomaly (6.3) and a depletion in HREE ($\text{Lu/Gd} = 6.5$). It is noteworthy that titanite (pale yellow) forms a corona around a brown inclusion of rutile. Also, the blurry aspect of this zircon suggest that it is cracked. Accordingly, this titanite inclusions is inferred to be a secondary inclusion.

What is highlighted in this discussion is that the CL-bright zircon formed at high pressure, during the eclogite facies and/or at the beginning of the granulite facies. These CL-bright zircons yielded a main cluster between ~360-290 Ma and a few analyses at ~390 Ma.

The main cluster of analyses obtained on metamorphic zircon yield scattered results between c. 365-280 Ma. This scatter is interpreted as lead loss since most of the analyses yield

apparent ages younger than the ~353 Ma age obtained on apatite and interpreted as a cooling age after decompression (Figs. II.4.17a and I.3.22c,d). The scatter of the $^{206}\text{Pb}/^{238}\text{U}$ apparent ages obtained on zircon enclosed in garnet (i.e. that is expected to prevent lead loss) can be attributed to the pervasive fracturing of garnet (e.g. Fig. I.3.3f). The REE spectra with no Eu/Eu* anomaly but a depletion to a slight enrichment in HREE, obtained during the analyses of these zircons suggest a crystallization in the eclogite facies. The observation of one plagioclase or melt inclusion in one zircon with a $^{206}\text{Pb}/^{238}\text{U}$ apparent age of 364 Ma strongly constrain the interpretation of this date as a crystallization or recrystallization age (this point is discussed in the next section) close to the peak P – T conditions, either during the isobaric heating of M1 or M2 (Fig. I.1.7). The best estimation of this age is probably the concordia age of 363.5 ± 3 Ma (MSWD = 1.5) obtained using four concordant analyses of the analytical session 4. A lower intercept age calculated in a Tera Wasserburg diagram using discordant analyses of the same batch yield a 361 ± 1 Ma (MSWD = 2.3; $n = 14$) date similar within the uncertainty comforting the concordia age, however, this age must be considered as a minimum age because of the lead loss underwent by these zircons. However, the preserved alignment on Fig. I.3.21c suggest that lead loss was limited, otherwise, the ellipses would be strongly dispersed. Therefore, the estimated age is most likely very close to the actual age of the eclogite facies metamorphism. This age of c. 363 Ma is also very similar to those obtained by Lotout et al. (submitted) for the eclogite metamorphism in the Lévézou.

The ~390 Ma $^{206}\text{Pb}/^{238}\text{U}$ apparent age cluster was calculated using only 5 analyses from three analytical sessions (Zr42b, analytical session 2, Table I.3.3; Zr8d, batch 4, Table I.3.9; Zr20a,25a,26a, batch 6, Table I.3.12) measured on both samples (Fig. I.3.23). Repeated measurement on the same grain does not allow to reproduce the ~390 Ma $^{206}\text{Pb}/^{238}\text{U}$ apparent ages (Fig. I.3.19C), however, given the recurrence of analyses yielding ~390 Ma $^{206}\text{Pb}/^{238}\text{U}$ they must be discussed in more details.

These analyses were obtained on zircons with flow textures or patchy zoning, without Eu/Eu* anomaly but a depletion to limited enrichment in HREE and containing small inclusions of garnet, omphacite, rutile, all being consistent with a growth in the eclogite facies. The internal textures of the zircons and the small-sized inclusions suggest that they could have grown at the beginning of the eclogite facies metamorphism (this point is discussed further in the next section). The oldest age obtained on eclogitic zircon during this study is 389 ± 6.5 Ma and the youngest, 363.5 ± 3 Ma. The later age is a minimum age, approaching the actual age of the eclogite facies metamorphism. The time of span between the oldest and the youngest zircon indicate a maximum duration of the eclogite facies metamorphism between 16 and 35 Ma pointing to a slow subduction. However, they are at odd with the preservation of the garnet growth zoning that suggest a short period of time at high temperature and with the results of Lotout et al. (2017) indicating a shorter duration of the eclogite facies metamorphism (i.e. 6 ± 4.5 Ma). Since the $^{206}\text{Pb}/^{238}\text{U}$ ratio during the analyses that remained stable, there is no analytical reason to discard these ages. Accordingly, these results could be interpreted in two different way (i) these ages are geologically meaningful and reflect a slow subduction or (ii) these ages reflect a constant mixing with an inherited core. Accordingly, these results should be reproduced before being considered as a strong constrain for any tectonic model.

5.3. Implication for the Silurian dates obtained on eclogites of the French Variscan belt

Our geochronological results contribute to the reevaluation of the age of the HP metamorphism. In this section results obtained by Ducrot et al., (1983) in the Haut-Allier are discussed in detail before enlarging this discussion to the other Silurian dates obtained on eclogites from the French Variscan belt.

Ducrot et al. (1983) performed ID-TIMS U-Pb dating using a population of zircon grains extracted from eclogites that were sampled in the same locality than the studied eclogites. The dated grains were described as rounded, translucent, colourless or with faint yellow coloration. The internal textures of these grains were not imaged prior to dissolution. The results are significantly but not strongly discordant having $^{206}\text{Pb}/^{238}\text{U}$ apparent ages ranging from ~390 to 415 Ma and yield an upper intercept of $432 \pm 20 - 10$ Ma and a meaningless lower intercept date of $109 \pm 125/-133$ Ma (Fig. II.4.27).

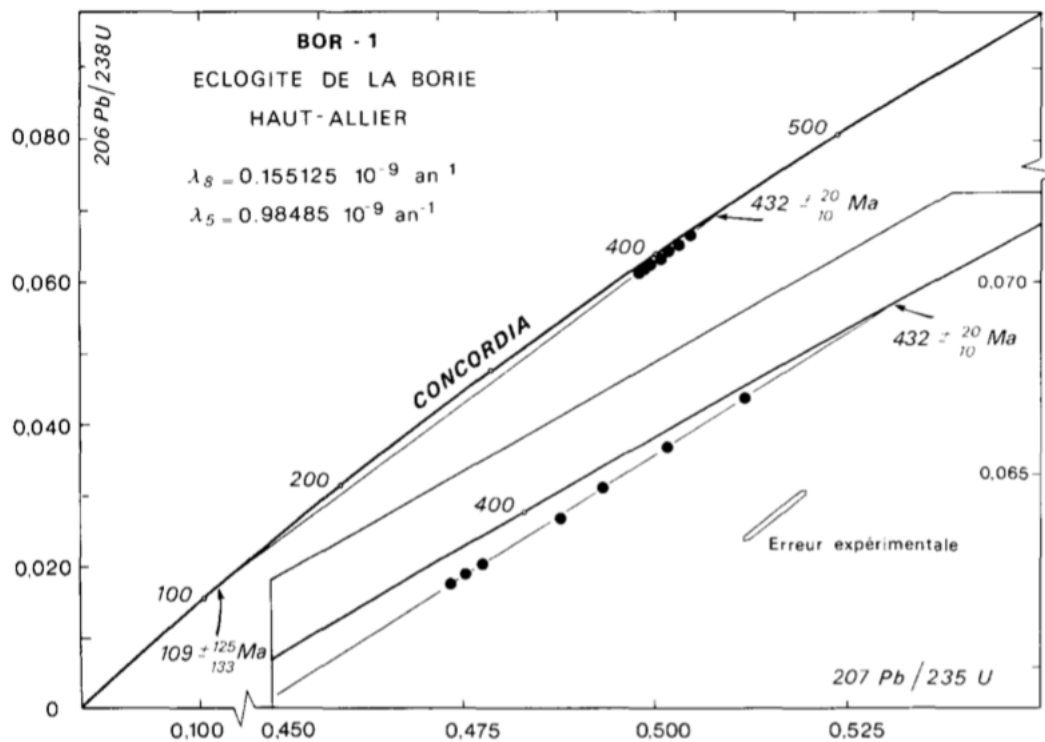


Figure I.3.27: Wetherill concordia diagram from Ducrot et al. (1983).

Our observations show that most magmatic zircon grains contain cracks and inclusions and must have been discarded by Ducrot et al. (1983). However, rare inclusion-free, translucent and colourless zircon crystals with CL-dark colours and magmatic textures have been observed (Fig. I.3.4C, D) suggesting that some mixing of the metamorphic and magmatic with respective

ages of ~365 and ~480 Ma, is possible. Paquette et al. (2017) recently re-investigated la Bessenoit eclogite and suggested that a previously obtained silurian upper intercept age (Paquette et al., 1995) was probably overinterpreted. Because the Silurian age is not reproduced and the likely mixing between zircons with contrasting evolutions, the upper-intercept age obtained by dissolution of zircon population obtained by Ducrot et al., (1983) was most likely overinterpreted too.

Similar Silurian ages were also inferred for several other eclogites in the Massif Central: La Bessenoit (Sm/Nd on garnet and upper intercept U/Pb dissolution of zircon population; Paquette et al., 1995), Marvejols (upper intercept, U/Pb dissolution of zircon population; Pin and Lancelot, 1982), and La Roche Abeille eclogite in the Limousin (U/Pb zircon In-Situ LA-ICP-MS; Berger 2010). As previously mentioned, zircons from la Bessenoit eclogite were reinvestigated by Paquette et al. (2017) and the Silurian age was not reproduced. Dissolution of zircon populations may result in mixing zircons with different, possibly complex histories, and Paquette et al. (2017) concluded that the Silurian upper intercept date resulted from an overinterpretation of the data. A similar conclusion is proposed for the La Borie eclogite (Haut-Allier) and envisioned for the Marvejols area. The Sm/Nd age obtained on garnet from two samples of the Bessenoit area is discussed in detail by Lotout et al. (2018). They concluded that the garnet of one of the samples may have been contaminated by inclusions and that this age should be considered with caution until further reinvestigations. The last Silurian age (412 ± 6 ; $n = 3$) was obtained by Berger et al. (2010) by U/Pb In-Situ LA-ICP-MS dating on zircons from La Roche Abeille eclogite in the Limousin. It is noteworthy that they also obtained a 382 ± 7 ($n = 3$) date that they attributed to retrogression. These dates are not petrologically constrained and were interpreted owing to their similarity with previously published ages of the metamorphism. Because several studies in the Armorican Massif and the Massif Central (Bosse et al., 2000; Paquette et al., 2017; Lotout et al., 2018; Lotout, 2017) and our results cast doubts

on the geological meaning of the Silurian ages, the interpretation of the Silurian age of the HP metamorphism must be taken with care and the age the HP metamorphism of this eclogite may be best seen at c. 360-380 Ma.

5.4. Implications for the Haut-Allier area

Schulz (2014) performed a geochronological study on monazites from a pelitic granulite in the Haut-Allier and inferred a 360 Ma age for the peak P – T conditions. Based on the inferred 420 Ma results of U/Pb dating of the eclogites by Ducrot et al. (1983), the author proposed a polycyclic tectonometamorphic scenario where two independent orogenic cycles led to the formation of the eclogites at c. 420 Ma and the HP granulites at c. 360 Ma. Our results show that the age of the HP granulite and the eclogite are very similar and that a single orogenic event led to the formation of both rock types.

The analysed zircons are characterized by lead loss. Consequently, some zircons display a $^{206}\text{Pb}/^{238}\text{U}$ apparent age as young as 290 Ma, post-dating the closure of the apatites. Many zircons underwent a limited but significant lead loss, which is attributed to a late thermal pulse or a continuous HT regime. The inferred P – T path suggests a simple clockwise P – T loop and may not record this late event. Alternatively, Nicollet et al. (1993) proposed that a late thermal pulse may be recorded in coronitic gabbro from the Haut-Allier. Their conclusions are not unequivocal, however, and two scenarios were proposed suggesting that further investigation is needed. Though a metamorphic record of a late thermal pulse is still to be established with confidence, the emplacement of granite from c. 340 to 290 Ma in the neighbourhood (Laurent et al., 2017) suggests either a subsequent later thermal pulse separated by a time lag or a continuously high-thermal regime that lasted for several tens of Myr.

5.5. Tectonic implication of the upper Devonian age of the eclogite facies metamorphism

Once the previously proposed Silurian age for the eclogite facies metamorphism is discarded, two Devonian periods of HP metamorphism are revealed.

A first group of ages at c. 380 Ma is recognised in the Armorican Massif, the western and eastern Massif Central. In the Armorican Massif, garnet pyroxenites yielded c. 380 Ma (Peucat et al., 1982). In the Limousin area (western Massif Central; west of the Sillon Houiller Fault in Fig. I.3.28), two HP units may be distinguished, only one of them has been dated at 380 Ma. The Najac eclogite yielded a similar age for the eclogite facies metamorphism (Lotout et al., 2018). The only available geochronological data for the exhumation of the c. 380 Ma eclogites was obtained in the Najac massif on apatite and yielded 369 ± 13 Ma. The scarcity of the data and the large uncertainty does not allow to discuss the exhumation stage of these eclogites.

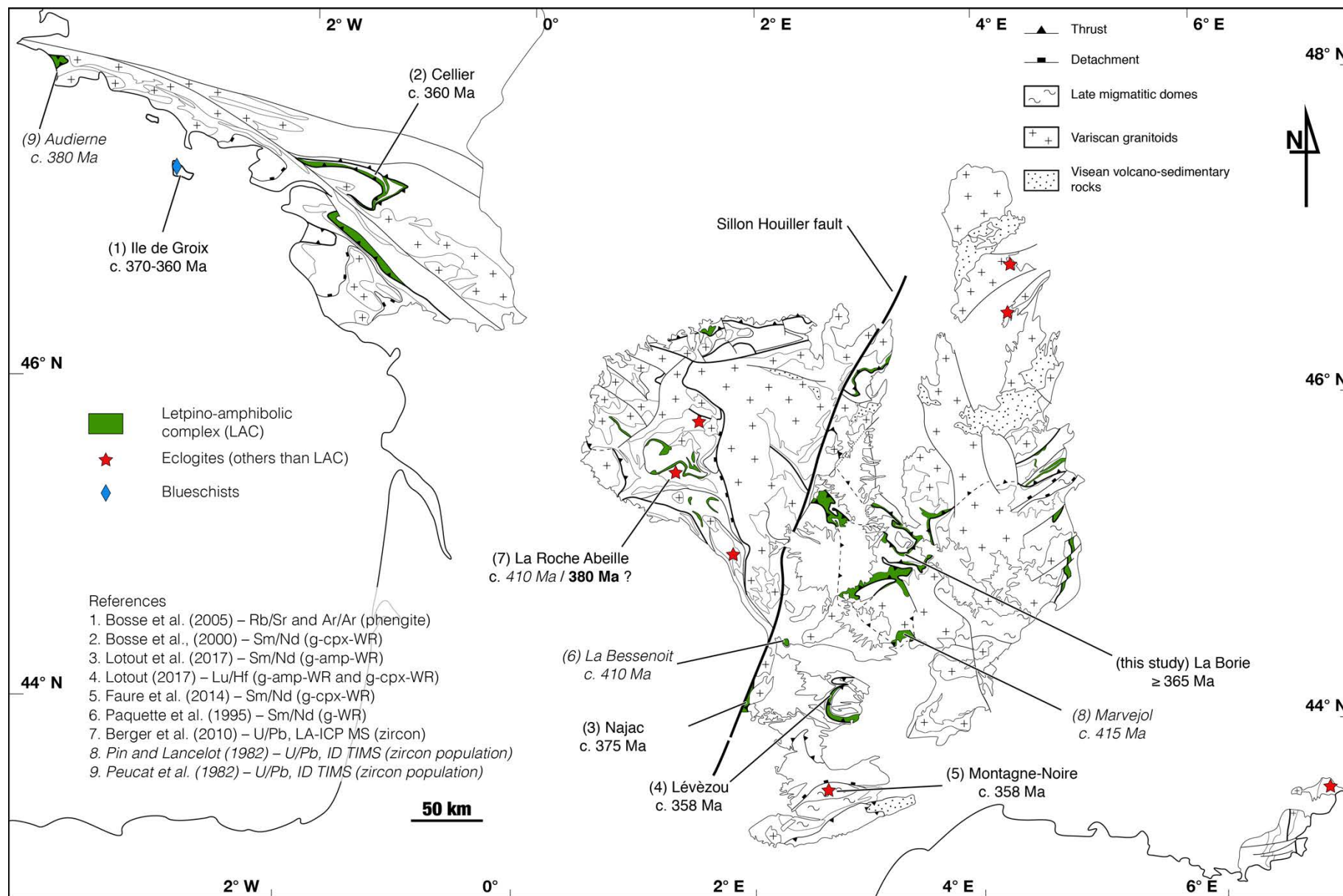
A second group of ages for the HP metamorphism of 370-360 Ma is recognized in the Armorican Massif and the eastern Massif Central (east of the Sillon Houiller Fault in Fig. I.3.28). In the Armorican Massif, these ages were obtained on blueschists and eclogites (Bosse et al., 2000 and Bosse et al., 2005). In the eastern Massif Central, these ages were obtained on eclogites (Faure et al., 2014; Lotout, 2017; this study). Ar/Ar dating of phengite in the Armorican Massif (Bosse et al., 2000 and Bosse et al., 2005) and U/Pb dating of apatite in the Massif Central (Lotout, 2017; this study) suggest that these eclogites were exhumed by 355-350 Ma.

Within the uncertainty, the age of the exhumation obtained on apatite (369 ± 13 Ma) from the eclogites of the Najac area (HP age: 380 Ma, Lotout et al., 2017) is relatively close to the ages obtained on apatite from the Lévézou (351.8 ± 2.8 Ma; Lotout, 2017) and the Haut-

Allier (353 ± 1 and 357 ± 9 Ma; this study). Because of this large uncertainty, it is impossible to determine whether the exhumation of these eclogites was coeval or episodic.

It remains that the exhumation at 355-350 Ma of the 370-360 Ma HP rocks is remarkably homogeneous across the Armorican Massif and the Massif Central. These HP rocks are distributed over a distance of ~1000 km suggesting a lithospheric scale event at the origin of their exhumation. The exhumation between 370-350 Ma is coeval with the opening of the Brévenne basin, strongly suggesting a link between these two events. Accordingly, crust-mantle delamination and the retreat of the subduction trench may lead to coeval extension in the upper plate and exhumation of the eclogites as proposed for the Aegean Sea (Brun and Faccena, 2008; Tirel et al., 2013).

Figure I.3.28 (next page): Updated map of the available geochronological data for the HP metamorphism in the Massif Central and Armorican Massif.



5.6. *Zircon behaviour at high-pressure*

The observation of zircon in distinct textural positions, together with the inclusions it contains, the internal texture it displays and the Ti-in-zircon thermometry results allow some considerations of zircon behaviour during metamorphism. Indeed, the observation of various internal textures of zircons implies that several processes were at work during zircon crystallization. Three different zircon types, formed by different processes occurring at different moments of the PT evolution of the eclogite can be distinguished (Fig. I.3.29).

Metamorphic zircon crystallized during the prograde subsolidus evolution.

Zircon with flow textures displays highly curved bands that suggest the modification of previous crystals (Fig. I.3.19G, H). These flow textures resemble, to some extent, those reported by Vavra et al. (1996) and interpreted as a “penetrative migration of impurity components within the crystal lattice”. In the studied samples, zircons with flow textures contain small sized inclusions of garnet, clinopyroxene and rutile (Fig. I.3.19A, C, E, G) and have a Ti content (1.80-4.90 ppm; bold rows in Table I.3.14) consistent with a high temperature (min: 762 °C at 20 kbar; max: 919 °C at 22.5 kbar) of equilibration with rutile, during the isobaric heating M1 or M2 (Fig. I.1.7). Because the grain size in metamorphic rocks is expected to increase with increasing temperature the inclusions would not have been trapped at these temperatures. Therefore, small sized inclusions in zircon, high Ti-in-zircon temperature and apparently modified zoning suggests that these zircons crystallized at the beginning of the eclogite facies and subsequently re-equilibrated by solid state recrystallization allowing for the survival of the inclusions.

Garnet 1 contains tiny (a few μm) inclusions of zircon forming small clusters next to or surrounding rutile (Fig. I.3.2). A close relationship between zircon and rutile has been reported by Lasnier (1977) in the “La Borie” eclogites (see his Picture 69). Coronitic textures of zircons

around rutile have been interpreted as the result of magmatic ilmenite breakdown during prograde metamorphism releasing Zr and Ti, and ultimately resulting in the crystallization of zircon and rutile (Bingen et al., 2001; Beckman and Möller, 2018). The same reaction might explain the small zircons clusters associated with rutile and preserved in garnet. These zircon crystals occur both in garnet 1 core and rim and would have crystallized during the prograde part of the PT evolution (M1; Fig. I.3.7), possibly at the entrance into the eclogite facies.

Eclogitic zircon recrystallized by dissolution-precipitation at peak subsolidus conditions.

Rutile grains from the matrix, are not associated with the clusters mentioned above, but rather with single larger zircon crystals (up to 50µm). One of such crystals displays sector zoning (Fig. I.3.3a-c) typical for high grade metamorphism (e.g. Corfu, 2003), and yield a perfectly concordant $^{206}\text{Pb}/^{238}\text{U}$ apparent age of 359 ± 8 Ma (concordance = 100; Zr19 – Table I.3.10, shown in Fig. I.3.3a). These crystals likely formed by dissolution and precipitation of the tiny zircon crystals observed as inclusions in garnet (type 2 above). Cannibalism of the tiny zircons is the most likely source of Zr for the larger zircons. They would have grown during the isobaric heating, or the retrogression (Fig. I.1.7). Trace element analyses have unfortunately not been performed on these crystals, but they display textures and ages similar to the zircon crystals enclosed in garnet and the CL-bright crystals characterized by “eclogitic” REE spectra (Fig. I.3.12a). Accordingly, the growth of this zircon is bracketed between the growth of garnet 1 rims and the significant decompression of M3, that is during the M1 isobaric heating or during M2 (Fig. I.1.7).

The CL-bright rims and patches cutting across the CL-dark cores suggest that the cores have been resorbed by dissolution and that the CL-bright rims crystallized afterward (e.g. Liermann et al., 2007) an aqueous fluid was inferred to act as a solvent. Alternatively,

dissolution and recrystallization of zircon could also occur in a magmatic setting (e.g. Corfu, 2013). It is therefore likely that these overgrowths formed by dissolution-precipitation close to the peak P – T conditions. In the simplest case, precipitation and the crystallisation of the rims took place at the same site, and Zr was not transported.

Zircons crystallized during eclogite-facies incipient partial melting.

The oscillatory zoned CL-bright crystals (Fig. I.3.4I and I.3.19B), could have grown either from a melt or from a fluid at high pressure as proposed by Gebauer et al. (1997). The Ti content (2.30 ± 1.10 ppm) of the oscillatory zoned crystals is in better agreement with a crystallization from a melt during M1 ($810 \pm 50^\circ\text{C}$ at 22.5 kbar). Partial melting occurred in the garnet-rich layer during the M1 isobaric heating (Fig. I.1.7) and was triggered by the influx of probably Zr- and Ti-enriched aqueous fluid. The crystallisation of the oscillatory zoned zircon rims could be related to this event.

Eclogitic zircons production mechanisms

The evidenced mechanisms at work for the crystallization of the observed zircons are either, crystallization from a melt, by dissolution-precipitation and solid-state recrystallization. These mechanisms may involve precipitation at the site of dissolution or redistribution of Zr. The inferred source of Zr for the crystallization of these eclogitic zircons are either ilmenite breakdown during prograde metamorphism and mainly the zircon itself that might recrystallize at the site of dissolution (i.e. rims around magmatic cores) or after limited transport (i.e. large zircons close to rutile in the matrix) or even by solid-state recrystallization (i.e. flow textures zircons). Although zircon is often referred as unreactant with respect to fluids (e.g. Cherniak and Watson, 2001), the mobility of Zr during a HP event is evidenced by zircon bearing eclogitic veins (Rubatto and Hermann, 2003) and baddeleyite from fluid inclusions in omphacite (Philippot and Selverstone, 1991). Liermann et al. (2002) also discussed the

solubility of zircon in HP facies rocks. Accordingly, the redistribution of Zr by zircon dissolution-recrystallization during the HP metamorphism is likely. On the one hand rutile and garnet should balance the Zr release of plagioclase and hornblende breakdown during the prograde P – T path of a hydrous MORB (Kohn et al., 2015). On the other hand, zircon may take up more than 95% of the bulk Zr (Rubatto and Hermann, 2003). Accordingly, if the protolith contains enough zircon to saturate garnet and rutile at peak P – T conditions, the redistribution of Zr by dissolution-recrystallization of former zircon is expected to be the most efficient process to produce an eclogitic zircon.

Figure I.3.29 (next page): Schematic evolution of zircon growth during the inferred rock evolution. 1. Magmatic zircons and ilmenite; 2-4. Zircons grown at subsolidus conditions during the eclogite facies metamorphism; 2. Coeval growth of garnet and zircons at the onset of the eclogite facies metamorphism; 3. Crystallization of rutile with small grained cluster of zircons at the vicinity of the magmatic ilmenite; 4. Growth of garnet, preserving the small grained zircons clusters around rutile and Zr migration from zircons cluster in the matrix resulting in zircons grain coarsening. 5. Zircons grown or modified at peak P – T conditions (i.e. magmatic and eclogitic conditions). Note that all zircons crystallized at peak P – T conditions may not be attributed to a “magmatic crystallization”.

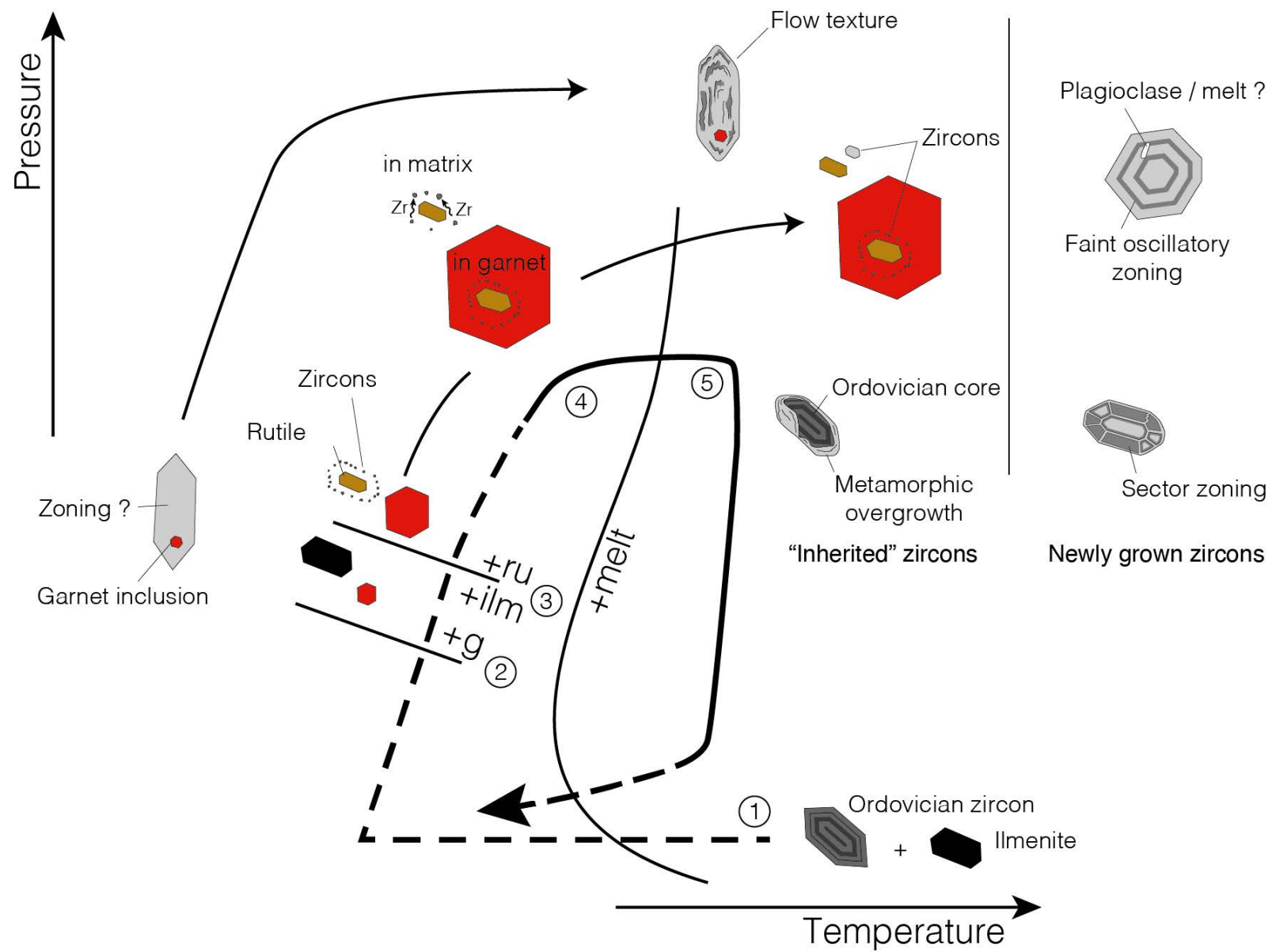


Table I.3.2: U/Pb data of zircons obtained during the analytical session 1 (BR18). BC – bright CL crystals, BR – bright CL rims, BS – bright CL spots, DC – dark CL cores. Italic rows indicate analyses performed on metamorphic zircons but yield a magmatic age.

Table I.3.3: U/Pb data of zircons obtained during the analytical session 2 (BR18). BC – bright CL crystals, BR – bright CL rims, BS – bright CL spots, DC – dark CL cores.

Table I.3.4: REE data of zircons obtained during the analytical session 1 (BR18). BC – bright CL crystals, BR – bright CL rims, BS – bright CL spots, DC – dark CL cores. Bold row indicates the analyse forming the ~390 Ma $^{206}\text{Pb}/^{238}\text{U}$ apparent ages cluster.

Table I.3.5: REE data of zircons obtained during the analytical session 2 (BR18). BC – bright CL crystals, BR – bright CL rims, BS – bright CL spots, DC – dark CL cores.

BR18 - An. Session 1			Content (ppm)				Tera Wasserburg plot				Wetherill plot					Ages (Ma)						Conc.
Label	Crystal	Texture	U	Th	Pb	Th/U	$^{238}\text{Pb}/^{206}\text{Pb}$	2s abs	$\text{Pb}^{207}/\text{Pb}^{206}$	2s abs	$\text{Pb}^{207}/\text{U}^{235}$	2s abs	$\text{Pb}^{206}/\text{U}^{238}$	2s abs	rho	$\text{Pb}^{207}/\text{U}^{235}$	2s abs	$\text{Pb}^{206}/\text{U}^{238}$	2s abs	$\text{Pb}^{207}/\text{Pb}^{206}$	2s abs	
Zr2a	I	DC	323	227	243	0.70	13.5	0.309	0.056	0.0019	0.59	0.022	0.074	0.0017	0.61	472	14	460	12	451	79	97
Zr3a	I	DC	231	129	148	0.56	12.9	0.284	0.058	0.0018	0.64	0.021	0.077	0.0017	0.66	503	13	478	12	529	76	95
Zr4a	II	DC	556	1202	1317	2.16	13.0	0.332	0.056	0.0016	0.62	0.020	0.077	0.0020	0.78	490	13	478	12	451	79	98
Zr5a	II	DC	333	454	535	1.36	12.8	0.279	0.055	0.0015	0.62	0.019	0.078	0.0017	0.70	492	12	484	12	411	81	98
Zr6a	II	BR	202	196	237	0.97	12.9	0.299	0.056	0.0018	0.61	0.021	0.078	0.0018	0.66	482	13	484	12	451	79	100
Zr7a	III	BC	32	0.3	1	0.01	19.2	0.766	0.055	0.0045	0.38	0.029	0.052	0.0021	0.51	326	21	327	12	411	204	100
Zr8a	IV	BC	27	0.4	2	0.01	18.8	0.770	0.060	0.0057	0.42	0.036	0.053	0.0022	0.47	353	26	333	12	603	216	94
Zr9a	IV	BC	18	0.3	1	0.02	18.7	0.960	0.059	0.0080	0.39	0.045	0.054	0.0028	0.44	334	33	339	18	566	296	101
Zr10a	IV	BC	32	0.4	1	0.01	18.2	0.693	0.053	0.0046	0.39	0.034	0.055	0.0021	0.43	337	25	345	12	328	214	103
Zr11a	V	BC	27	0.5	1	0.02	18.8	0.699	0.056	0.0052	0.40	0.037	0.053	0.0020	0.40	342	27	333	12	451	198	97
Zr12a	V	BC	14	0.2	1	0.01	18.2	1.01	0.060	0.0081	0.44	0.054	0.055	0.0031	0.45	367	38	345	18	603	288	94
Zr13a	VI	BC	28	0.4	1	0.01	17.9	0.700	0.056	0.0058	0.43	0.043	0.056	0.0022	0.39	363	31	351	12	451	238	97
Zr14a	VI	BC	32	1	1	0.02	19.1	0.720	0.057	0.0052	0.40	0.035	0.052	0.0020	0.43	340	25	327	12	491	193	96
Zr15a	VI	BC	32	1	1	0.02	19.0	0.717	0.054	0.0046	0.40	0.033	0.053	0.0020	0.45	338	24	333	12	370	208	98
Zr16a	VII	BS	29	3	18	0.12	18.1	0.900	0.162	0.0201	1.22	0.161	0.055	0.0028	0.38	810	74	345	18	2476	208	43
Zr17a	VII	BR	34	12	23	0.35	13.1	0.682	0.086	0.0063	0.82	0.067	0.076	0.0040	0.64	605	37	472	24	1337	135	78
Zr18a	VII	DC	374	255	276	0.68	14.4	0.308	0.059	0.0016	0.57	0.019	0.070	0.0015	0.64	459	12	436	6	566	74	95
Zr19a	VIII	BC	22	0.4	1	0.02	18.9	0.776	0.060	0.0060	0.44	0.042	0.053	0.0022	0.42	368	30	333	12	603	216	90
Zr20a	VIII	BC	21	0.3	1	0.01	19.3	0.877	0.056	0.0061	0.39	0.038	0.052	0.0024	0.46	332	28	327	12	451	238	98
Zr21a	IX	BC	31	1	2	0.03	20.1	0.794	0.057	0.0055	0.39	0.033	0.050	0.0020	0.46	332	24	315	12	491	232	95
Zr22a	IX	BC	29	1	1	0.02	19.5	0.824	0.060	0.0058	0.41	0.035	0.051	0.0022	0.49	350	25	321	12	603	216	92
Zr23a	IX	BC	24	0.5	1	0.02	19.0	0.855	0.051	0.0047	0.38	0.035	0.053	0.0024	0.48	326	26	333	12	240	226	102
Zr24a	IX	BC	23	0.3	1	0.01	18.7	0.861	0.061	0.0063	0.44	0.043	0.054	0.0025	0.47	369	30	339	12	638	212	92
Zr25a	X	DC	414	288	337	0.70	12.6	0.258	0.057	0.0014	0.61	0.017	0.079	0.0016	0.75	481	11	490	12	491	39	102
Zr26a	X	DC	239	104	117	0.44	13.0	0.287	0.057	0.0018	0.58	0.020	0.077	0.0017	0.64	467	13	478	12	491	77	102
Zr27a	X	DC	217	182	203	0.84	13.1	0.306	0.057	0.0020	0.58	0.020	0.076	0.0018	0.67	462	13	472	12	491	77	102
Zr28a	X	DC	152	96	105	0.63	13.4	0.319	0.057	0.0022	0.56	0.023	0.075	0.0018	0.58	454	15	466	12	491	77	103
Zr29a	X	DC	346	182	221	0.53	12.3	0.275	0.058	0.0016	0.63	0.020	0.081	0.0018	0.69	495		502	12	529	76	101
Zr30a	XI	BR	96	55	67	0.57	12.5	0.712	0.062	0.0045	0.66	0.063	0.080	0.0046	0.59	515	39	496	30	673	138	96
Zr31a	XII	BR	551	71	502	0.13	12.9	0.488	0.130	0.0076	1.40	0.075	0.077	0.0029	0.71	890	32	478	18	2097	108	54
Zr32a	XII	DC	304	197	261	0.65	12.3	0.248	0.056	0.0015	0.63	0.020	0.081	0.0016	0.62	497	12	502	12	451	79	101
Zr33a	XII	DC	207	142	181	0.69	12.4	0.306	0.057	0.0020	0.63	0.023	0.081	0.0020	0.67	495	14	502	12	491	77	101
Zr34a	XIII	BR	17	2	27	0.10	8.11	0.462	0.068	0.0160	1.14	0.190	0.123	0.0070	0.34	773	90	748	40	868	488	97
Zr35a	XIII	BR	21	2	23	0.08	8.91	0.572	0.059	0.0046	0.86	0.075	0.112	0.0072	0.74	632	41	684	41	566	185	108
Zr36a	XIV	DC	426	349	421	0.82	12.8	0.281	0.057	0.0016	0.61	0.019	0.078	0.0017	0.69	485	12	484	12	491	77	100
Zr37a	XV	BR	104	69	117	0.67	10.7	0.475	0.079	0.0047	1.00	0.067	0.093	0.0041	0.66	705	34	573	24	1171	125	81
Zr38a	XV	DC	429	289	300	0.67	13.7	0.317	0.056	0.0015	0.56	0.016	0.073	0.0017	0.78	448	10	454	12	451	40	101
Zr39a	XVI	DC	440	248	275	0.56	13.2	0.309	0.057	0.0022	0.59	0.025	0.076	0.0018	0.56	472	16	472	12	491	77	100
Zr40a	XVI	BR	16	3	26	0.17	14.3	1.07	0.286	0.0282	2.59	0.242	0.070	0.0053	0.80	1298	68	436	30	3395	152	34
Zr41a	XVII	BR	34	5	65	0.14	13.5	0.827	0.281	0.0282	2.98	0.372	0.074	0.0046	0.49	1403	95	460	30	3368	156	33
Zr42a	XVII	BR	49	4	20	0.09	18.2	0.848	0.112	0.0121	0.82	0.092	0.055	0.0026	0.42	609	51	345	18	1831	194	57

BR18 - An. Session 2			Content (ppm)				Tera Wasserburg plot				Wetherill plot					Ages (Ma)						Conc.
Label	Crystal	Texture	U	Th	Pb	Th/U	U^{238}/Pb^{206}	2s abs	Pb^{207}/Pb^{206}	2s abs	Pb^{207}/U^{235}	2s abs	Pb^{206}/U^{238}	2s abs	rho	Pb^{207}/U^{235}	2s abs	Pb^{206}/U^{238}	2s abs	Pb^{207}/Pb^{206}	2s abs	
Zr1b	XVIII	BC	32	1	1	0.02	18.12	0.94	0.056	0.0062	0.42	0.045	0.055	0.0029	0.48	358	32	345	18	451	238	97
Zr2b	XVIII	BC	38	1	1	0.02	17.95	0.86	0.054	0.0048	0.41	0.034	0.056	0.0027	0.57	349	24	351	18	370	208	101
Zr3b	XIX	BR	13	0.1	1	0.01	18.02	1.15	0.056	0.0080	0.41	0.059	0.056	0.0035	0.44	349	42	351	24	451	318	101
Zr4b	XIX	DC	342	218	262	0.64	12.38	0.48	0.056	0.0022	0.63	0.026	0.081	0.0031	0.93	494	16	502	18	451	79	102
Zr5b	XX	BR	35	2	2	0.05	18.12	0.91	0.055	0.0065	0.41	0.048	0.055	0.0028	0.43	352	34	345	18	411	284	98
Zr6b	XX	DC	114	96	91	0.84	15.80	0.65	0.063	0.0037	0.55	0.038	0.063	0.0026	0.60	446	25	394	18	707	135	88
Zr7b	XXI	BR	21	3	6	0.13	16.50	1.05	0.076	0.0120	0.63	0.090	0.061	0.0039	0.44	495	56	382	24	1094	316	77
Zr8b	XXI	BR	19	3	12	0.17	17.51	1.67	0.174	0.0271	1.22	0.310	0.057	0.0054	0.37	810	142	357	30	2596	258	44
Zr9b	XXII	BR	16	1	109	0.08	6.28	0.35	0.464	0.0285	10.34	0.780	0.159	0.0089	0.74	2466	70	951	50	4130	93	39
Zr10b	XXII	BR	242	149	171	0.62	12.99	0.51	0.065	0.0035	0.68	0.041	0.077	0.0030	0.65	528	25	478	18	773	97	91
Zr11b	XXII	DC	265	182	204	0.69	12.56	0.48	0.057	0.0022	0.61	0.026	0.080	0.0030	0.89	486	16	496	18	491	77	102
Zr12b	XXIII	DC	14	0.2	1	0.02	14.73	0.95	0.060	0.0086	0.54	0.071	0.068	0.0044	0.49	438	47	424	24	603	324	97
Zr13b	XXIII	BR	25	5	12	0.22	14.41	0.78	0.081	0.0077	0.76	0.072	0.069	0.0038	0.57	572	42	430	24	1221	194	75
Zr14b	XXIII	BR	208	121	144	0.58	14.41	1.34	0.076	0.0053	0.71	0.130	0.069	0.0064	0.50	544	77	430	36	1094	132	79
Zr15b	XXIV	BS	441	299	353	0.68	12.41	0.48	0.056	0.0021	0.62	0.026	0.081	0.0031	0.91	487	16	502	18	451	79	103
Zr16b	XXV	BC	58	6	5	0.10	18.28	0.89	0.054	0.0044	0.40	0.034	0.055	0.0027	0.56	340	25	345	18	370	167	101
Zr17b	XXVI	BC	24	2	2	0.06	18.42	1.07	0.056	0.0068	0.38	0.052	0.054	0.0032	0.42	324	38	339	18	451	278	105
Zr18b	XXVI	BC	27	0.3	1	0.01	18.08	1.03	0.058	0.0064	0.42	0.046	0.055	0.0032	0.51	353	33	345	18	529	226	98
Zr19b	XXVII	BR	17	0.2	1	0.01	18.21	1.67	0.050	0.0110	0.36	0.078	0.055	0.0050	0.42	312	58	345	31	194	512	111
Zr20b	XXVII	DC	426	384	454	0.90	12.77	0.51	0.059	0.0027	0.63	0.032	0.078	0.0031	0.78	494	20	484	18	566	111	98
Zr21b	XXVII	DC	243	172	206	0.71	12.42	0.48	0.056	0.0025	0.63	0.030	0.081	0.0031	0.81	493	19	502	18	451	79	102
Zr22b	XXVIII	DC	201	165	211	0.82	12.64	0.48	0.056	0.0024	0.60	0.027	0.079	0.0030	0.85	479	17	490	18	451	79	102
Zr23b	XXVIII	DC	171	120	143	0.70	12.48	0.49	0.057	0.0027	0.62	0.032	0.080	0.0031	0.76	492	20	496	18	491	116	101
Zr24b	XXVIII	DC	245	162	207	0.66	12.45	0.47	0.056	0.0022	0.62	0.027	0.080	0.0030	0.86	488	17	496	18	451	79	102
Zr25b	XXIX	BR	10	1	1	0.07	13.33	0.86	0.066	0.0150	0.63	0.082	0.075	0.0049	0.50	496	51	466	30	805	476	94
Zr26b	XXIX	BR	218	193	215	0.89	14.49	0.59	0.060	0.0027	0.58	0.028	0.069	0.0028	0.84	461	18	430	18	603	108	93
Zr27b	XXIX	DC	184	143	168	0.78	12.48	0.49	0.056	0.0026	0.61	0.031	0.080	0.0031	0.77	485	20	496	18	451	119	102
Zr28b	XXX	BR	16	1	6	0.08	17.57	4.02	0.095	0.0340	0.74	1.200	0.057	0.0130	0.14	562	700	357	79	1527	674	64
Zr29b	XXX	DC	175	123	147	0.70	12.58	0.49	0.055	0.0024	0.61	0.029	0.080	0.0031	0.83	484	18	496	18	411	81	103
Zr30b	XXXI	BR	15	3	4	0.20	12.82	0.72	0.059	0.0081	0.60	0.058	0.078	0.0044	0.58	477	37	484	24	566	296	101
Zr31b	XXXI	BR	17	1	1	0.05	18.69	1.24	0.059	0.0062	0.44	0.051	0.054	0.0035	0.57	369	36	339	24	566	222	92
Zr32b	XXXI	DC	118	85	102	0.72	13.26	0.51	0.056	0.0029	0.59	0.030	0.075	0.0029	0.76	468	19	466	18	451	119	100
Zr33b	XXXI	BR	67	40	42	0.59	14.49	0.71	0.059	0.0050	0.55	0.043	0.069	0.0034	0.63	442	28	430	18	566	185	97
Zr34b	XXXII	BR	141	88	97	0.62	13.51	0.62	0.056	0.0052	0.58	0.044	0.074	0.0034	0.61	462	28	460	18	451	198	100
Zr35b	XXXII	BR	11	1	2	0.05	18.48	1.58	0.067	0.0093	0.44	0.073	0.054	0.0046	0.52	372	51	339	31	837	280	91
Zr36b	XXXII	DC	293	296	339	1.01	12.79	0.48	0.057	0.0022	0.61	0.026	0.078	0.0029	0.87	480	16	484	18	491	77	101
Zr37b	XXXIII	BS	50	22	26	0.45	15.55	0.86	0.060	0.0059	0.52	0.048	0.064	0.0036	0.60	428	32	400	24	603	216	93
Zr38b	XXXIII	DC	186	145	166	0.78	13.23	0.51	0.057	0.0023	0.59	0.026	0.076	0.0029	0.87	470	17	472	18	491	77	100
Zr39b	XXXIII	BR	12	1	16	0.09	18.12	2.01	0.259	0.0312	1.77	0.321	0.055	0.0061	0.61	1035	118	345	37	3240	189	33
Zr40b	XXXIV	BR	21	4	9	0.18	12.90	0.76	0.060	0.0072	0.60	0.059	0.078	0.0046	0.59	475	38	484	30	603	252	102
Zr41b	XXXIV	BR	16	0.3	5	0.02	19.31	1.47	0.110	0.0170	0.90	0.200	0.052	0.0039	0.34	652	107	327	25	1799	282	50
Zr42b	XXXV	BC	23	2	2	0.10	16.58	0.95	0.049	0.0059	0.39	0.042	0.060	0.0035	0.53	335	31	376	18	147	288	112

Label	Crystal	Texture	Sr	Y	La	Ce	Pr	Nd	Sm	Eu	Gd	Tb	Dy	Ho	Er	Tm	Yb	Lu
Zr2a	I	DC	0.308	1261	0.014	15.8	0.214	3.20	5.96	0.868	26.2	8.40	108	36.8	170	34.7	292	55.7
Zr3a	I	DC	0.257	893	bdl	13.2	0.040	0.782	2.15	0.359	13.1	4.73	69.0	25.5	125	27.0	238	46.8
Zr4a	II	DC	0.264	554	0.27	12.9	0.215	1.80	2.90	0.368	12.8	3.91	48.7	16.7	74.7	15.4	131	24.9
Zr5a	II	DC	0.210	360	bdl	8.50	0.022	0.514	1.19	0.219	7.07	2.37	30.9	11.4	53.7	11.9	107	21.9
Zr6a	II	BR	0.222	199	bdl	4.38	bdl	0.202	0.521	0.124	3.58	1.18	16.2	6.15	30.0	6.88	63.6	13.5
Zr7a	III	BC	0.164	16.0	bdl	0.115	bdl	bdl	0.098	0.112	0.878	0.255	2.32	0.528	1.41	0.205	1.45	0.259
Zr8a	IV	BC	0.167	13.9	bdl	0.163	bdl	bdl	0.162	0.160	1.14	0.284	2.30	0.428	1.02	0.165	1.03	0.196
Zr9a	IV	BC	0.184	13.6	bdl	0.325	bdl	0.034	0.279	0.368	1.93	0.382	2.48	0.428	1.26	0.194	1.49	0.316
Zr10a	IV	BC	0.152	13.4	bdl	0.181	bdl	0.017	0.110	0.114	0.979	0.275	2.28	0.442	1.16	0.181	1.15	0.221
Zr11a	V	BC	0.191	6.42	bdl	0.444	bdl	0.065	0.326	0.303	1.59	0.258	1.38	0.191	0.440	0.064	0.432	0.067
Zr12a	V	BC	0.183	11.6	bdl	0.250	bdl	0.025	0.185	0.236	1.39	0.295	1.84	0.369	0.966	0.164	1.25	0.244
Zr13a	VI	BC	0.161	29.3	bdl	0.170	bdl	0.047	0.189	0.213	1.50	0.488	4.50	0.988	2.62	0.361	2.63	0.422
Zr14a	VI	BC	0.158	26.8	bdl	0.422	bdl	0.127	0.71	0.835	4.93	1.01	6.09	0.881	1.76	0.241	1.60	0.274
Zr15a	VI	BC	0.145	11.5	bdl	0.370	bdl	0.060	0.24	0.289	1.87	0.381	2.45	0.360	0.748	0.102	0.654	0.101
Zr16a	VII	BS	0.359	41.6	0.492	2.09	0.380	2.90	1.26	0.222	2.19	0.422	4.68	1.32	4.70	0.731	5.00	0.907
Zr17a	VII	BR	0.496	63.0	0.404	2.53	0.306	2.48	1.69	0.167	3.39	0.617	6.20	2.01	7.90	1.63	13.0	2.81
Zr18a	VII	DC	1.560	1162	0.390	20.7	0.291	2.95	3.91	0.528	20.2	6.97	91.7	33.9	157	33.5	291.2	55.6
Zr19a	VIII	BC	0.160	21.6	bdl	0.263	bdl	0.020	0.430	0.431	2.67	0.569	3.75	0.683	1.78	0.282	2.06	0.356
Zr20a	VIII	BC	0.157	15.8	bdl	0.235	bdl	0.050	0.349	0.368	2.40	0.485	2.79	0.504	1.38	0.214	1.65	0.266
Zr21a	IX	BC	0.171	17.6	bdl	0.568	bdl	0.15	0.860	1.02	4.96	0.780	3.54	0.537	1.64	0.304	2.57	0.485
Zr22a	IX	BC	0.183	5.74	bdl	0.491	bdl	0.069	0.367	0.302	1.47	0.248	1.06	0.167	0.499	0.084	0.718	0.147
Zr23a	IX	BC	0.166	7.76	bdl	0.449	bdl	0.077	0.294	0.385	2.04	0.352	1.62	0.241	0.637	0.107	0.875	0.167
Zr24a	IX	BC	0.164	6.99	bdl	0.358	bdl	0.045	0.190	0.237	1.15	0.239	1.35	0.208	0.576	0.093	0.637	0.120
Zr25a	X	DC	0.242	1109	bdl	8.22	0.064	1.27	3.53	0.586	23.6	7.53	92.6	32.8	147	29.6	254	46.1
Zr26a	X	DC	0.171	508	bdl	5.97	0.018	0.509	1.16	0.154	8.06	2.97	39.0	15.3	75.0	16.6	152	29.8
Zr27a	X	DC	0.269	1208	bdl	8.91	0.194	3.63	6.38	0.865	31.1	9.31	107	35.7	156	30.6	266	47.9
Zr28a	X	DC	0.282	852	bdl	7.15	0.076	1.67	3.76	0.581	21.1	6.48	76.3	25.2	108	21.6	190	35.3
Zr29a	X	DC	0.356	1605	0.033	9.44	0.298	4.45	6.87	1.03	40.7	12.4	147	48.1	207	40.8	352	65.5
Zr30a	XI	BR	0.225	153	bdl	3.44	bdl	0.198	0.400	0.078	2.38	0.902	12.0	4.71	23.8	5.0	44.6	9.1
Zr31a	XII	BR	18.6	237	47.6	215	30.7	174	24.9	35.6	16.3	1.68	16.0	6.37	38.9	11.3	135	36.4
Zr32a	XII	DC	0.271	814	bdl	17.2	0.076	1.01	2.30	0.379	13.3	4.70	63.0	23.4	111	23.9	210	40.5
Zr33a	XII	DC	0.269	876	0.023	13.7	0.058	1.07	2.65	0.419	14.7	5.20	68.7	25.6	119	25.3	223	42.7
Zr34a	XIII	BR	0.228	27.6	0.056	0.370	0.024	0.097	0.051	0.016	0.273	0.14	2.26	0.880	3.51	0.651	4.55	0.783
Zr35a	XIII	BR	0.164	24.9	bdl	0.102	bdl	0.027	0.019	0.031	0.257	0.13	2.06	0.707	2.93	0.505	4.22	0.731
Zr36a	XIV	DC	0.330	1578	0.026	18.3	0.30	4.23	6.89	1.00	30.7	10.2	127.6	46.2	210	43.0	366	69.0
Zr37a	XV	BR	0.534	134.0	0.512	3.31	0.18	0.940	0.79	0.158	3.28	0.98	12.4	4.29	20.4	4.2	35.8	6.8
Zr38a	XV	DC	0.269	994.0	bdl	19.0	0.080	1.67	3.45	0.543	18.5	6.35	80.0	29.1	136	28.7	252	48.6
Zr39a	XVI	DC	0.259	797.0	bdl	16.9	0.059	0.820	1.97	0.313	12.8	4.76	62.1	23.3	111	23.4	205	40.0
Zr40a	XVI	BR	1.94	23.7	0.411	1.17	0.095	0.760	0.460	0.144	0.840	0.186	2.12	0.754	2.78	0.490	4.16	0.763
Zr41a	XVII	BR	1.54	27.6	1.08	2.43	0.260	1.44	0.450	0.524	0.860	0.240	2.61	0.850	3.44	0.669	4.92	0.972
Zr42a	XVII	BR	3.00	24.8	0.380	1.09	0.154	0.910	0.290	0.077	0.454	0.153	2.03	0.727	3.09	0.545	4.70	0.970

Label	Crystal	Texture	Sr	Y	La	Ce	Pr	Nd	Sm	Eu	Gd	Tb	Dy	Ho	Er	Tm	Yb	Lu
Zr1b	XVIII	BC	0.180	19.9	bdl	0.201	bdl	bdl	0.123	0.176	1.29	0.366	3.04	0.632	1.74	0.232	1.55	0.271
Zr2b	XVIII	BC	0.157	32.4	bdl	0.219	bdl	0.029	0.284	0.338	2.58	0.715	5.46	1.10	2.55	0.33	2.18	0.357
Zr3b	XIX	BR	0.199	16.0	bdl	0.014	bdl	bdl	bdl	bdl	0.103	0.060	1.16	0.439	1.84	0.304	2.31	0.372
Zr4b	XIX	DC	0.292	814	bdl	19.7	0.031	0.797	1.98	0.286	12.8	4.66	62.4	23.5	113	24.4	212	42.1
Zr5b	XX	BR	0.196	31.6	0.011	0.186	bdl	0.035	0.113	0.139	1.24	0.428	4.49	1.05	2.89	0.356	2.3	0.382
Zr6b	XX	DC	0.276	379	0.045	4.75	0.072	0.840	1.66	0.390	8.50	2.71	32.9	11.9	55.1	11.6	101	20.05
Zr7b	XXI	BR	0.374	34.5	0.083	0.216	0.024	0.145	0.066	0.041	0.350	0.204	3.14	1.054	4.05	0.665	4.69	0.785
Zr8b	XXI	BR	2.99	31.6	1.18	3.34	0.255	1.19	0.243	0.083	0.390	0.177	2.20	0.862	3.91	0.89	6.8	1.53
Zr9b	XXII	BR	0.269	24.7	1.79	5.21	0.707	3.87	1.39	0.226	1.57	0.274	2.69	0.785	2.66	0.416	2.97	0.505
Zr10b	XXII	BR	0.651	568	0.649	13.9	0.278	2.03	2.19	0.348	10.1	3.56	45.9	17.2	80.8	17.2	150	29.2
Zr11b	XXII	DC	0.305	811	bdl	16.3	0.053	1.06	2.10	0.343	13.3	4.80	62.5	23.4	112	23.7	206	40.53
Zr12b	XXIII	DC	0.155	18.4	bdl	0.081	bdl	bdl	0.138	0.120	0.700	0.272	2.86	0.606	1.37	0.139	0.854	0.161
Zr13b	XXIII	BR	0.710	39.2	0.244	1.15	0.131	0.720	0.168	0.145	0.546	0.216	3.25	1.12	4.88	0.923	7.35	1.404
Zr14b	XXIII	BR	0.363	315	1.06	7.81	0.370	2.10	1.15	0.557	5.57	1.98	26.3	10.1	49.3	10.5	90.2	18.5
Zr15b	XXIV	BS	0.274	943	bdl	19.0	0.065	1.14	2.80	0.330	15.5	5.48	71.9	26.9	129	27.2	237	45.4
Zr16b	XXV	BC	0.199	22.9	bdl	0.546	0.017	0.21	0.394	0.413	2.66	0.600	4.15	0.775	1.97	0.298	1.92	0.35
Zr17b	XXVI	BC	0.184	30.9	bdl	0.162	bdl	bdl	0.048	0.061	0.720	0.275	3.46	1.05	3.62	0.550	3.84	0.685
Zr18b	XXVI	BC	0.188	35.8	bdl	0.248	bdl	0.065	0.404	0.481	3.05	0.772	6.18	1.12	3.17	0.479	3.61	0.609
Zr19b	XXVII	BR	0.229	23.4	bdl	0.014	bdl	bdl	bdl	bdl	0.160	0.064	1.76	0.682	2.86	0.495	3.3	0.721
Zr20b	XXVII	DC	0.440	1859	0.061	20.9	0.308	5.51	9.35	1.290	41.3	12.68	155	53.5	247	48.9	407	76.7
Zr21b	XXVII	DC	0.262	969	bdl	15.4	0.060	1.39	3.10	0.472	17.6	5.93	75.9	27.79	134	27.7	245	48.3
Zr22b	XXVIII	DC	0.381	1376	bdl	15.6	0.159	3.14	6.68	1.037	32.06	9.89	120	40.18	181	35.4	292	54.1
Zr23b	XXVIII	DC	0.300	921	bdl	12.5	0.071	1.50	3.56	0.493	18.3	6.24	77.9	27.7	127	25.7	215	41.2
Zr24b	XXVIII	DC	0.262	816	bdl	15.2	0.079	1.30	2.87	0.425	15.38	5.15	66.7	24.3	115	24.1	209	40.4
Zr25b	XXIX	BR	0.152	26.5	bdl	0.190	bdl	0.016	0.031	0.009	0.250	0.105	2.01	0.830	3.29	0.596	5.14	0.95
Zr26b	XXIX	BR	0.453	1200	0.022	11.2	0.178	2.67	5.02	0.558	23.1	7.70	97.0	36.1	164	32.7	271	51.3
Zr27b	XXIX	DC	0.315	1054	0.013	15.4	0.087	1.62	3.57	0.522	19.6	6.72	85.4	32.3	151	31.5	276	54.1
Zr28b	XXX	BR	0.217	25.5	1.81	4.30	0.460	1.90	0.320	0.076	0.400	0.168	2.12	0.728	2.96	0.605	4.23	0.716
Zr29b	XXX	DC	0.378	1242	bdl	15.0	0.091	1.35	3.15	0.488	20.23	7.33	96.5	36.09	173	35.7	312	60
Zr30b	XXXI	BR	0.173	33.9	bdl	0.29	bdl	0.015	0.050	0.030	0.400	0.172	3.01	0.870	4.44	0.85	7.2	1.4
Zr31b	XXXI	BR	0.197	34.8	bdl	0.16	bdl	0.022	0.068	0.070	0.850	0.324	4.39	1.21	3.79	0.562	3.8	0.697
Zr32b	XXXI	DC	0.316	614	bdl	11.1	0.043	0.74	1.71	0.249	11.1	4.23	53	20.07	96.0	19.5	176	34.4
Zr33b	XXXI	BR	0.231	291	bdl	5.35	0.020	0.37	0.860	0.178	5.41	1.86	25.4	9.44	44.8	9.33	83.6	16.7
Zr34b	XXXII	BR	0.294	511	bdl	11.2	0.029	0.75	1.52	0.210	8.96	3.2	43.6	16.7	79.5	17.2	152	30.4
Zr35b	XXXII	BR	0.188	27.3	0.010	0.16	0.003	0.020	0.054	0.088	0.680	0.288	3.38	0.889	2.75	0.41	2.59	0.515
Zr36b	XXXII	DC	0.404	1736	0.035	20.4	0.241	4.42	8.85	1.08	36.1	11.84	146.7	51.2	235	47	388	75.6
Zr37b	XXXIII	BS	0.242	131	bdl	2.62	0.011	0.192	0.430	0.083	2.43	0.89	11.9	4.27	19.7	4.01	36.5	7.3
Zr38b	XXXIII	DC	0.216	899	0.011	17.1	0.066	1.20	2.89	0.436	16.44	5.58	71.6	26.1	119	25.6	224	44
Zr39b	XXXIII	BR	1.00	18.9	0.34	1.58	0.128	0.830	0.368	0.676	0.650	0.175	1.98	0.582	1.82	0.35	2.28	0.505
Zr40b	XXXIV	BR	0.141	35.4	bdl	0.401	bdl	bdl	0.052	0.044	0.610	0.246	3.33	1.11	4.49	0.83	7.01	1.31
Zr41b	XXXIV	BR	0.314	15.3	0.036	0.289	bdl	0.049	0.090	0.149	0.840	0.238	1.94	0.444	1.43	0.199	1.63	0.301
Zr42b	XXXV	BC	0.160	20.0	bdl	0.697	bdl	0.185	0.890	0.850	4.430	0.863	4.23	0.643	1.67	0.278	2.26	0.452

Table I.3.6: Table of Ti content of zircon obtained during the analytical session 1 (BR18).

BR18 - An. Session 1				Content (ppm)		T (°C)
Label	Crystal	Texture		Ti	2s abs	at 20 kbar
Zr7a	III	BC	Rim	3.35	0.580	813
Zr8a	IV	BC	Rim	3.52	0.520	818
Zr9a	IV	BC	Core	2.69	0.480	795
Zr10a	IV	BC	Rim	3.42	0.510	815
Zr11a	V	BC	Core	2.34	0.510	783
Zr12a	V	BC	Core	1.80	0.420	762
Zr13a	VI	BC	Core	5.10	0.660	851
Zr14a	VI	BC	Core	5.05	0.560	850
Zr15a	VI	BC	Core	2.79	0.480	798
Zr19a	VIII	BC	Core	3.20	0.530	809
Zr20a	VIII	BC	Core	3.02	0.440	804
Zr21a	IX	BC	Rim	3.37	0.540	814
Zr22a	IX	BC	Rim	2.74	0.510	796
Zr23a	IX	BC	Rim	1.92	0.390	767
Zr24a	IX	BC	Rim	2.41	0.420	786

BC – bright CL crystals, BR – bright CL rims, BS – bright CL spots, DC – dark CL cores.

Table I.3.7: Table of Ti content of zircon obtained during the analytical session 2 (BR18).

BR18 - An. Session 2				Content (ppm)		T (°C)
Label	Crystal	Texture		Ti	2s abs	at 20 kbar
Zr1b	XVIII	BC	Rim	3.81	0.530	824
Zr2b	XVIII	BC	Rim	4.16	0.530	832
Zr3b	XIX	BR		4.58	0.840	841
Zr5b	XX	BR		3.63	0.600	820
Zr16b	XXV	BC		20.0	1.20	992
Zr17b	XXVI	BC	Rim	2.09	0.550	774
Zr18b	XXVI	BC	Core	2.48	0.480	788
Zr19b	XXVII	BR		1.94	0.960	768
Zr31b	XXXI	BR		2.69	0.740	795
Zr35b	XXXII	BR		2.78	0.670	797
Zr42b	XXXV	BC	Core	4.84	0.680	846

Abbreviations: BC – bright CL crystals, BR – bright CL rims, BS – bright CL spots, DC – dark CL cores.

Table I.3.8: U/Pb data of zircons obtained during the analytical session 3 (BR18). BC – bright CL crystals, BR – bright CL rims, BS – bright CL spots, DC – dark CL cores.

Table I.3.9: U/Pb data of zircons obtained during the analytical session 4 (BR18). Same legend. Bold row indicates analyse forming the ~390 Ma $^{206}\text{Pb}/^{238}\text{U}$ apparent ages cluster.

Table I.3.10: U/Pb data of zircons obtained during the analytical session 5 (BR18). G – included or partially included in garnet, M – in the matrix, R – included or partially included in garnet. Italic row indicates analyses with extremely high error (not used).

Table I.3.11: U/Pb data of zircons obtained during the analytical session 5 (BR18). Same legend.

BR18 - An. Session 3			Content (ppm)				Tera Wasserburg plot				Wetherill plot					Ages (Ma)						
Label	Crystal	Texture	U	Th	Pb	Th/U	U^{238}/Pb^{206}	2s abs	Pb^{207}/Pb^{206}	2s abs	Pb^{207}/U^{235}	2s abs	Pb^{206}/U^{238}	2s abs	rho	Pb^{207}/U^{235}	2s abs	Pb^{206}/U^{238}	2s abs	Pb^{207}/Pb^{206}	2s abs	Conc.
Zr1c	V	BC	23	1	1	0.02	17.9	1.15	0.056	0.0038	0.411	0.031	0.056	0.0036	0.86	364	29	351	22	451	159	96
Zr2c	V	BC	14	0.2	1	0.01	18.0	1.20	0.059	0.0059	0.400	0.038	0.056	0.0037	0.70	379	38	349	23	566	222	92
Zr3c	IX	BC	21	0.4	1	0.02	17.9	1.17	0.058	0.0042	0.407	0.030	0.056	0.0037	0.90	375	30	351	22	529	151	93
Zr4c	IX	BC	29	1	1	0.04	18.2	1.13	0.060	0.0036	0.430	0.028	0.055	0.0034	0.95	380	29	345	21	603	144	91
Zr5c	XXVIII	BC	39	1	5	0.02	17.8	1.57	0.081	0.016	0.625	0.350	0.056	0.0049	0.16	494	85	352	30	1221	388	71
Zr6c	XXVIII	BC	33	0.4	1	0.01	17.8	1.09	0.059	0.0036	0.424	0.028	0.056	0.0035	0.93	382	29	353	21	566	148	92
Zr7c	XXVI	BC	21	0.2	0.1	0.01	18.6	1.19	0.057	0.0044	0.387	0.030	0.054	0.0034	0.81	359	29	338	21	491	155	94
Zr8c	XXVI	BC	20	0.3	1	0.01	18.6	1.19	0.061	0.0047	0.418	0.033	0.054	0.0034	0.82	378	33	337	21	638	176	89

BR18 - An. Session 4			Content (ppm)				Tera Wasserburg plot				Wetherill plot					Ages (Ma)						
Label	Crystal	Texture	U	Th	Pb	Th/U	U^{238}/Pb^{206}	2s abs	Pb^{207}/Pb^{206}	2s abs	Pb^{207}/U^{235}	2s abs	Pb^{206}/U^{238}	2s abs	rho	Pb^{207}/U^{235}	2s abs	Pb^{206}/U^{238}	2s abs	Pb^{207}/Pb^{206}	2s abs	Conc.
Zr1d	XXXVI	BC	24	0.4	1	0.02	17.4	0.214	0.054	0.0038	0.431	0.039	0.058	0.00070	0.13	364	28	361	4	378	158	99
Zr2d	XXVI	BC	20	1	9	0.03	16.8	0.253	0.112	0.0033	0.913	0.037	0.060	0.00089	0.37	659	20	374	5	1830	53	57
Zr3d	XXVI	BC	25	1	1	0.03	17.4	0.224	0.056	0.0016	0.442	0.012	0.058	0.00073	0.47	372	8	361	4	463	63	97
Zr4d	XXVI	BC	31	1	1	0.02	18.0	0.234	0.055	0.0015	0.425	0.012	0.055	0.00072	0.46	360	9	348	4	419	61	97
Zr5d	XXVI	BC	35	1	1	0.02	18.0	0.224	0.055	0.0013	0.425	0.010	0.056	0.00069	0.53	360	7	349	4	419	53	97
Zr6d	XXVI	BC	26	0.3	0	0.01	18.5	0.254	0.055	0.0017	0.415	0.015	0.054	0.00075	0.38	352	11	340	5	427	68	97
Zr7d	XXV	BC	29	2	2	0.06	17.0	0.224	0.058	0.0014	0.469	0.012	0.059	0.00076	0.50	390	8	369	5	514	53	95
Zr8d	XXVI	BC	10	0.1	0.4	0.01	15.9	0.283	0.056	0.0028	0.478	0.023	0.063	0.0011	0.37	397	16	393	7	447	111	99
Zr9d	XXXVII	BC	21	0	1	0.01	17.1	0.263	0.063	0.0030	0.502	0.028	0.058	0.00091	0.28	413	19	366	5	721	100	89
Zr10d	XXXVII	BC	7	0	2	0.003	17.5	0.432	0.104	0.0055	0.794	0.075	0.057	0.0014	0.26	593	42	357	9	1699	97	60
Zr11d	XVIII	BC	26	0	3	0.02	17.1	0.214	0.067	0.0018	0.543	0.014	0.058	0.00073	0.48	440	9	366	4	849	56	83
Zr12d	IX	BC	21	1	3	0.03	17.0	0.214	0.072	0.0023	0.576	0.018	0.059	0.00074	0.40	462	12	368	4	971	66	80
Zr13d	IX	BC	23	1	1	0.03	17.2	0.253	0.055	0.0039	0.439	0.049	0.058	0.00086	0.13	370	35	365	5	411	159	99
Zr14d	IX	BC	19	1	2	0.05	17.3	0.244	0.065	0.0022	0.522	0.019	0.058	0.00081	0.38	426	13	362	5	780	71	85
Zr15d	IX	BC	24	1	61	0.02	12.3	0.301	0.307	0.0130	3.350	0.210	0.081	0.0020	0.39	1493	49	503	12	3505	65	34
Zr16d	V	BC	15	0.3	3	0.02	16.9	0.283	0.082	0.0033	0.664	0.045	0.059	0.0010	0.25	517	27	370	6	1235	79	72
Zr17d	IV	BC	14	0.3	1	0.02	17.0	0.263	0.054	0.0025	0.447	0.022	0.059	0.00091	0.31	375	15	369	5	387	103	98
Zr18d	IV	BC	20	0.4	1	0.02	17.5	0.234	0.059	0.0016	0.461	0.012	0.057	0.00075	0.50	385	8	358	5	562	59	93
Zr19d	IV	BC	18	0.4	2	0.02	17.2	0.243	0.069	0.0022	0.545	0.017	0.058	0.00082	0.45	442	11	364	5	907	65	82
Zr20d	IV	BC	14	0.1	2	0.01	17.8	0.313	0.071	0.0031	0.541	0.042	0.056	0.0010	0.23	439	28	352	6	951	90	80
Zr21d	III	BC	22	0.4	4	0.02	17.9	0.273	0.080	0.0045	0.611	0.042	0.056	0.00086	0.22	484	26	351	5	1206	110	72
Zr22d	III	BC	29	0.4	2	0.01	17.3	0.214	0.063	0.0018	0.499	0.014	0.058	0.00071	0.44	411	9	363	4	701	61	88

BR18 - An. Session 5			Content (ppm)				Tera Wasserburg plot				Wetherill plot					Ages (Ma)						
Label	Texture	Pos.	U	Th	Pb	Th/U	U ²³⁸ /Pb ²⁰⁶	2s abs	Pb ²⁰⁷ /Pb ²⁰⁶	2s abs	Pb ²⁰⁷ /U ²³⁵	2s abs	Pb ²⁰⁶ /U ²³⁸	2s abs	rho	Pb ²⁰⁷ /U ²³⁵	2s abs	Pb ²⁰⁶ /U ²³⁸	2s abs	Pb ²⁰⁷ /Pb ²⁰⁶	2s abs	Conc.
Zr1	BC	M	35	0.5	4	0.01	16.7	1.54	0.078	0.0053	0.579	0.043	0.060	0.0055	1.24	464	27	376	33	1138	133	81
Zr2	BC	M	13	1	1	0.06	17.3	0.650	0.077	0.0078	0.440	0.034	0.058	0.0022	0.49	370	23	362	13	1107	204	98
Zr3	BC	M	54	1	1	0.02	18.4	0.505	0.053	0.0025	0.382	0.021	0.054	0.0015	0.50	329	15	341	9	324	103	104
Zr4	BC	M	75	2	2	0.03	18.8	0.560	0.055	0.0035	0.390	0.027	0.053	0.0016	0.44	334	19	334	9	403	139	100
Zr5	BC	M	31	0.4	1	0.01	18.0	0.546	0.054	0.0035	0.378	0.024	0.056	0.0017	0.48	326	17	349	10	378	141	107
Zr6	BC	M	37	0.2	0.3	0.01	18.4	0.507	0.054	0.0028	0.379	0.020	0.054	0.0015	0.53	326	14	341	9	349	114	104
Zr7	BC	M	27	0.4	1	0.01	18.1	0.522	0.053	0.0033	0.386	0.023	0.055	0.0016	0.49	331	16	346	9	345	136	105
Zr8	BC	M	30	0.3	0.4	0.01	18.1	0.488	0.057	0.0030	0.417	0.022	0.055	0.0015	0.51	354	15	348	9	498	112	98
Zr9	BC	M	28	0.3	1	0.01	20.4	0.578	0.059	0.0036	0.386	0.023	0.049	0.0014	0.48	331	16	308	8	574	129	93
Zr10	BC	G	38	0.3	1	0.01	20.0	0.553	0.056	0.0028	0.377	0.019	0.050	0.0014	0.55	325	13	315	8	459	107	97
Zr11	BC	R	64	1	1	0.01	19.1	0.477	0.055	0.0022	0.389	0.017	0.052	0.0013	0.57	334	12	328	7	399	86	98
Zr12	BC	R	70	4	3	0.06	19.8	0.474	0.054	0.0020	0.369	0.015	0.050	0.0012	0.58	319	10	317	7	353	80	99
Zr13	BC	M	47	0.5	1	0.01	19.8	0.510	0.055	0.0025	0.376	0.019	0.050	0.0013	0.51	324	13	317	7	395	99	98
Zr14	BC	R	40	0.3	0.4	0.01	18.5	0.447	0.054	0.0024	0.386	0.018	0.054	0.0013	0.52	331	12	340	7	358	97	102
Zr15	BC	R	31	0.4	1	0.01	18.2	0.466	0.056	0.0028	0.411	0.020	0.055	0.0014	0.53	350	14	345	8	459	107	99
Zr16	BC	R	46	0.4	0.4	0.01	19.4	0.525	0.054	0.0027	0.382	0.019	0.051	0.0014	0.55	329	13	324	8	374	108	98
Zr17	BC	G	72	0.4	2	0.01	18.3	0.567	0.060	0.0038	0.432	0.025	0.055	0.0017	0.54	365	17	342	10	592	134	94
Zr18	BC	G	31	0.5	1	0.02	17.5	0.519	0.061	0.0034	0.461	0.026	0.057	0.0017	0.53	385	17	358	10	624	117	93
Zr19	BC	M	79	1	0.4	0.01	17.3	0.396	0.054	0.0019	0.428	0.017	0.058	0.0013	0.57	362	11	362	7	358	76	100
Zr20	BC	G	40	0.3	3	0.01	17.5	0.460	0.054	0.0027	0.413	0.021	0.057	0.0015	0.52	351	14	359	9	387	107	102
Zr21	BC	G	32	0.3	0.3	0.01	18.1	0.524	0.056	0.0033	0.404	0.024	0.055	0.0016	0.49	345	17	346	9	455	127	100
Zr22	BC	M	47	1	2	0.03	17.5	0.432	0.055	0.0025	0.428	0.020	0.057	0.0014	0.53	362	14	359	8	411	98	99
Zr23	BC	M	57	1	1	0.01	18.2	0.495	0.053	0.0026	0.401	0.021	0.055	0.0015	0.52	342	15	345	9	324	107	101
Zr24	BC	R	27	1	0.4	0.02	17.7	0.498	0.057	0.0030	0.421	0.022	0.057	0.0016	0.54	357	15	355	9	502	111	99
Zr25	BC	R	37	0.4	1	0.01	18.9	0.534	0.059	0.0034	0.412	0.025	0.053	0.0015	0.47	350	17	332	9	574	121	95

BR18 - An. Session 5			Content (ppm)				Tera Wasserburg plot				Wetherill plot					Ages (Ma)						
Label	Texture	Pos.	U	Th	Pb	Th/U	U ²³⁸ /Pb ²⁰⁶	2s abs	Pb ²⁰⁷ /Pb ²⁰⁶	2s abs	Pb ²⁰⁷ /U ²³⁵	2s abs	Pb ²⁰⁶ /U ²³⁸	2s abs	rho	Pb ²⁰⁷ /U ²³⁵	2s abs	Pb ²⁰⁶ /U ²³⁸	2s abs	Pb ²⁰⁷ /Pb ²⁰⁶	2s abs	Conc.
Zr26	BC	R	35	0.2	0.5	0.01	18.3	0.533	0.180	0.0041	0.407	0.025	0.055	0.0016	0.48	347	17	343	9	2652	32	99
Zr27	BC	R	28	0.3	0.4	0.01	18.2	0.497	0.053	0.0028	0.387	0.021	0.055	0.0015	0.51	332	15	345	9	306	117	104
Zr28	BC	R	42	1	1	0.01	19.3	0.554	0.054	0.0032	0.377	0.022	0.052	0.0015	0.50	325	15	326	9	387	128	100
Zr29	BC	M	45	1	1	0.02	19.1	0.509	0.053	0.0027	0.379	0.020	0.052	0.0014	0.51	326	14	329	8	319	112	101
Zr30	BC	M	41	1	1	0.01	18.8	0.730	0.057	0.270	0.406	0.053	0.053	0.0021	0.30	346	38	334	12	487	10474	97
Zr31	BC	M	50	1	1	0.02	18.5	0.480	0.053	0.0024	0.393	0.019	0.054	0.0014	0.54	337	13	339	8	336	98	101
Zr32	BC	G	40	0.3	0.4	0.01	18.6	0.516	0.056	0.0028	0.394	0.021	0.054	0.0015	0.52	337	15	338	9	431	108	100
Zr33	BC	G	34	0.4	1	0.01	18.7	0.552	0.054	0.0029	0.396	0.021	0.054	0.0016	0.56	339	15	337	9	358	118	99
Zr34	BC	G	82	3	4	0.04	19.4	0.452	0.057	0.0020	0.415	0.017	0.052	0.0012	0.56	352	11	325	7	491	74	92
Zr35	BC	G	72	3	3	0.04	18.7	0.489	0.052	0.0022	0.403	0.019	0.053	0.0014	0.55	344	13	336	8	289	92	98
Zr36	BC	G	96	5	5	0.05	18.7	0.489	0.052	0.0024	0.401	0.021	0.054	0.0014	0.50	342	15	336	8	302	100	98
Zr37	BC	M	56	1	1	0.01	19.3	0.517	0.052	0.0028	0.387	0.021	0.052	0.0014	0.50	332	15	326	8	267	120	98
Zr38	BC	G	41	0.4	0.4	0.01	18.7	0.490	0.053	0.0026	0.412	0.021	0.053	0.0014	0.52	350	14	335	8	336	106	96
Zr39	BC	G	33	0.4	0.4	0.01	18.5	0.543	0.053	0.0032	0.414	0.025	0.054	0.0016	0.49	352	17	340	9	332	132	97
Zr40	BC	M	44	1	0.5	0.01	18.4	0.475	0.058	0.0027	0.439	0.022	0.054	0.0014	0.51	370	15	341	8	514	99	92
Zr41	BC	G	54	1	1	0.01	18.5	0.478	0.052	0.0024	0.399	0.019	0.054	0.0014	0.54	341	13	340	8	302	100	100
Zr42	BC	M	69	1	1	0.01	17.4	0.401	0.056	0.0019	0.422	0.016	0.057	0.0013	0.60	357	11	360	7	467	71	101
Zr43	BC	M	38	1	4	0.02	17.5	0.546	0.074	0.0048	0.517	0.035	0.057	0.0018	0.46	423	23	359	10	1035	129	85
Zr44	BC	M	57	1	2	0.01	17.5	0.432	0.055	0.0025	0.387	0.019	0.057	0.0014	0.51	332	13	359	8	411	98	108
Zr45	BC	M	9	0.1	5	0.01	15.3	0.903	-5.600	-8.200	1.07	0.098	0.065	0.0039	0.64	737	48	408	23	0	450364	55
Zr46	BC	M	41	0.3	0.4	0.01	17.3	0.451	0.052	0.0026	0.367	0.019	0.058	0.0015	0.51	317	13	362	9	284	110	114
Zr47	BC	M	77	2	7	0.03	17.6	0.464	0.063	0.0044	0.432	0.036	0.057	0.0015	0.32	365	25	357	9	690	147	98
Zr48	BC	M	54	3	4	0.05	17.2	0.418	0.059	0.0023	0.435	0.018	0.058	0.0014	0.58	367	12	365	8	548	82	99
Zr49	BC	G	26	0.3	2	0.01	16.5	0.491	0.060	0.0033	0.448	0.024	0.061	0.0018	0.56	376	16	379	10	588	116	101
Zr50	BC	M	29	0.4	2	0.01	20.7	1.14	0.069	0.020	0.374	0.049	0.048	0.0026	0.42	323	36	303	16	898	598	94

Table I.3.12: U/Pb data of zircons obtained during the analytical session 6 (BR19). BC – bright CL crystals, BR – bright CL rims, BS – bright CL spots, DC – dark CL core. Italic row indicates analyses with extremely high error (not used). Bold rows indicates the analyses forming the ~390 Ma $^{206}\text{Pb}/^{238}\text{U}$ apparent ages cluster.

Table I.3.13: REE data of zircons obtained during the analytical session 6 (BR19). BC – bright CL crystals, BR – bright CL rims, BS – bright CL spots, DC – dark CL core.

BR19 – An. Session 6			Content (ppm)				Tera Wasserburg plot				Wetherill plot					Ages (Ma)						
Label	Crystal	Texture	U	Th	Pb	Th/U	U ²³⁸ /Pb ²⁰⁶	2s abs	Pb ²⁰⁷ /Pb ²⁰⁶	2s abs	Pb ²⁰⁷ /U ²³⁵	2s abs	Pb ²⁰⁶ /U ²³⁸	2s abs	rho	Pb ²⁰⁷ /U ²³⁵	2s abs	Pb ²⁰⁶ /U ²³⁸	2s abs	Pb ²⁰⁷ /Pb ²⁰⁶	2s abs	Conc.
Zr1a	I	BC	51	1	2	0.02	17.8	0.817	0.058	0.0067	0.426	0.053	0.056	0.0026	0.37	377	41	352	16	529	264	94
Zr2a	I	BC	44	1	1	0.02	17.8	0.975	0.059	0.0063	0.437	0.047	0.056	0.0031	0.51	382	37	352	19	566	222	92
Zr3a	II	BC	55	1	1	0.01	17.5	0.885	0.057	0.0049	0.433	0.043	0.057	0.0029	0.51	376	32	357	18	491	193	95
Zr4a	III	BC	46	0.4	3	0.01	19.8	1.16	0.072	0.0087	0.458	0.051	0.050	0.0030	0.53	412	47	317	18	985	254	77
Zr5a	III	DC	132	131	139	1.00	14.8	0.701	0.056	0.0033	0.518	0.038	0.068	0.0032	0.64	426	25	421	19	451	119	99
Zr6a	III	BC	64	2	2	0.03	17.2	0.884	0.054	0.0045	0.424	0.039	0.058	0.0030	0.56	364	32	363	18	370	208	100
Zr7a	IV	BC	38	1	1	0.02	17.4	0.899	0.053	0.0051	0.409	0.042	0.058	0.0030	0.51	356	32	360	18	328	214	101
Zr8a	V	BC	43	0.5	1	0.01	17.5	1.00	0.052	0.0055	0.378	0.041	0.057	0.0033	0.53	348	38	358	20	284	264	103
Zr9a	V	BC	55	3	4	0.06	18.5	1.08	0.061	0.0052	0.430	0.042	0.054	0.0032	0.60	380	32	339	19	638	176	89
Zr10a	VI	BC	52	1	2	0.02	17.6	0.982	0.057	0.0054	0.421	0.044	0.057	0.0032	0.54	375	33	356	19	491	193	95
Zr11a	VII	BC	41	0.4	1	0.01	17.6	0.924	0.059	0.0056	0.444	0.046	0.057	0.0030	0.51	385	37	356	18	566	222	92
Zr12a	VIII	BC	65	1	2	0.02	18.2	0.852	0.056	0.0043	0.428	0.039	0.055	0.0026	0.52	359	26	345	16	451	159	96
Zr13a	VIII	BC	49	2	2	0.03	18.0	0.964	0.055	0.0050	0.431	0.043	0.056	0.0030	0.54	357	32	348	18	411	204	98
Zr14a	IX	BC	60	1	2	0.02	17.9	0.860	0.056	0.0049	0.425	0.041	0.056	0.0027	0.50	364	31	350	16	451	198	96
Zr15a	IX	BC	50	1	2	0.01	18.5	0.980	0.066	0.0058	0.472	0.046	0.054	0.0029	0.55	406	35	340	18	805	190	84
Zr16a	IX	BC	61	1	1	0.01	19.2	0.943	0.057	0.0051	0.398	0.040	0.052	0.0026	0.49	349	30	328	16	491	193	94
Zr17a	X	BC	48	1	1	0.01	19.6	1.03	0.062	0.0068	0.411	0.044	0.051	0.0027	0.49	367	38	320	16	673	242	87
Zr18a	XI	BC	45	1	1	0.02	18.1	0.875	0.058	0.0057	0.431	0.047	0.055	0.0027	0.45	372	36	347	16	529	226	93
Zr19a	XII	BC	41	1	1	0.02	18.2	0.949	0.056	0.0054	0.410	0.040	0.055	0.0029	0.54	359	31	345	18	451	198	96
Zr20a	XII	BC	21	0.4	1	0.02	16.2	1.07	0.059	0.0083	0.462	0.062	0.062	0.0041	0.49	413	51	386	25	566	296	93
Zr21a	XIII	BC	60	1	1	0.01	18.0	0.894	0.056	0.0044	0.424	0.039	0.056	0.0028	0.54	363	27	349	17	451	159	96
Zr22a	XIII	BC	32	0.3	1	0.01	18.0	1.02	0.057	0.0063	0.416	0.046	0.056	0.0032	0.52	368	37	349	19	491	232	95
Zr23a	XIV	BC	53	1	1	0.01	17.7	0.903	0.053	0.0047	0.398	0.037	0.056	0.0029	0.55	350	32	354	18	328	214	101
Zr24a	XV	BC	4	0.1	0.3	0.03	17.6	2.34	-17.00	-14.00	0.490	0.150	0.057	0.0075	0.43							
Zr25a	XVI	BC	32	1	1	0.03	16.5	1.02	0.056	0.0081	0.439	0.056	0.061	0.0038	0.49	390	50	380	23	451	318	97
Zr26a	XVII	BC	30	1	1	0.03	16.7	0.964	0.056	0.0066	0.453	0.058	0.060	0.0035	0.45	386	44	376	21	451	278	97
Zr27a	XVIII	BC	34	1	1	0.02	17.2	1.00	0.054	0.0066	0.419	0.051	0.058	0.0034	0.48	364	43	364	21	370	292	100
Zr28a	XIX	BC	37	0.4	1	0.01	17.7	0.934	0.057	0.0062	0.416	0.047	0.056	0.0030	0.47	372	37	354	18	491	232	95
Zr29a	XIX	BC	64	1	2	0.01	17.9	0.950	0.056	0.0060	0.420	0.047	0.056	0.0030	0.48	364	37	351	18	451	238	96
Zr30a	XX	BC	89	1	2	0.01	17.9	0.795	0.056	0.0050	0.428	0.042	0.056	0.0025	0.45	364	31	351	15	451	198	96
Zr31a	XXI	BC	38	0.4	0.2	0.01	18.0	0.996	0.058	0.0075	0.424	0.053	0.056	0.0031	0.45	373	46	348	19	529	302	93
Zr32a	XXII	BC	33	0.4	1	0.01	17.4	1.11	0.056	0.0074	0.420	0.056	0.057	0.0037	0.48	372	44	360	22	451	278	97
Zr33a	XXIII	BC	43	0.4	2	0.01	18.5	1.01	0.057	0.0061	0.421	0.048	0.054	0.0030	0.48	360	36	340	18	491	232	94
Zr34a	XXIII	BC	99	2	2	0.02	18.3	0.802	0.055	0.0037	0.404	0.031	0.055	0.0024	0.57	351	25	342	15	411	163	97
Zr35a	XXIII	BC	79	1	1	0.01	18.3	0.926	0.055	0.0051	0.398	0.041	0.055	0.0028	0.50	352	31	343	17	411	204	97
Zr36a	XXIV	BC	38	0.5	1	0.01	17.9	0.982	0.053	0.0055	0.395	0.042	0.056	0.0031	0.52	348	37	351	19	328	256	101
Zr37a	XXIV	BC	39	1	1	0.02	17.6	0.888	0.058	0.0057	0.436	0.043	0.057	0.0029	0.51	381	37	357	18	529	226	94
Zr38a	XXV	BC	40	1	1	0.02	17.6	0.924	0.054	0.0057	0.402	0.045	0.057	0.0030	0.47	358	37	356	18	370	250	99
Zr39a	XXV	BC	39	1	1	0.02	18.1	0.935	0.058	0.0062	0.427	0.046	0.055	0.0029	0.48	372	36	348	18	529	226	93
Zr40a	XXVI	BC	42	1	1	0.02	18.3	0.959	0.056	0.0061	0.406	0.043	0.055	0.0029	0.50	358	36	343	18	451	238	96
Zr41a	XXVII	BC	48	1	1	0.01	18.5	0.913	0.059	0.0067	0.405	0.045	0.054	0.0027	0.45	370	40	340	16	566	258	92
Zr42a	XXVII	BC	51	1	1	0.03	17.8	0.815	0.051	0.0046	0.388	0.038	0.056	0.0026	0.47	339	31	353	16	240	226	104

Label	Crystal	Texture	Sr	Y	La	Ce	Pr	Nd	Sm	Eu	Gd	Tb	Dy	Ho	Er	Tm	Yb	Lu
Zr1a	I	BC	0.156	42.2	0.0008	0.752	0.002	0.227	0.860	1.06	5.72	1.29	6.98	1.73	3.93	0.571	4.14	0.681
Zr2a	I	BC	0.155	11.4	bdl	0.659	bdl	0.024	0.289	0.206	1.58	0.345	1.86	0.468	0.940	0.102	0.950	0.146
Zr3a	II	BC	0.117	19.6	bdl	0.693	bdl	0.083	0.630	0.719	3.81	0.818	4.16	0.849	1.38	0.186	1.37	0.204
Zr4a	III	BC	0.481	47.0	bdl	0.448	0.001	0.105	0.990	0.832	4.74	1.18	7.19	1.82	4.22	0.643	4.60	0.836
Zr5a	III	DC	0.136	534	0.0088	8.48	0.104	1.84	3.16	1.10	13.3	4.42	46.5	22.1	84.1	18.5	171	34.6
Zr6a	III	BC	0.121	38.8	bdl	1.03	0.002	0.254	0.820	0.808	4.26	1.060	6.16	1.53	3.12	0.490	3.53	0.578
Zr7a	IV	BC	0.093	9.53	bdl	0.720	bdl	0.061	0.600	0.516	1.93	0.289	1.83	0.235	0.689	0.110	0.920	0.144
Zr8a	V	BC	0.110	12.4	bdl	0.380	bdl	0.021	0.127	0.184	1.14	0.210	1.67	0.290	1.07	0.156	1.12	0.186
Zr9a	V	BC	0.153	23.6	0.0023	1.69	0.020	0.550	1.42	1.17	3.89	0.438	3.52	0.533	2.37	0.398	3.18	0.545
Zr10a	VI	BC	0.138	6.49	bdl	0.869	0.002	0.026	0.186	0.369	1.30	0.179	1.16	0.125	0.428	0.067	0.429	0.080
Zr11a	VII	BC	0.093	18.3	bdl	0.427	0.003	0.057	0.317	0.497	2.97	0.522	3.75	0.516	1.39	0.204	1.53	0.288
Zr12a	VIII	BC	0.122	27.9	0.0008	0.593	0.003	0.183	0.670	0.673	4.07	0.714	5.08	0.729	2.17	0.322	2.54	0.367
Zr13a	VIII	BC	0.108	11.5	bdl	0.501	0.003	0.063	0.340	0.312	1.90	0.337	2.02	0.394	0.890	0.128	0.880	0.128
Zr14a	IX	BC	0.124	16.3	bdl	0.594	0.002	0.071	0.410	0.363	1.79	0.390	2.55	0.553	1.43	0.180	1.44	0.201
Zr15a	IX	BC	0.212	16.7	bdl	0.321	bdl	0.042	0.241	0.281	1.69	0.357	2.66	0.573	1.44	0.206	1.52	0.265
Zr16a	IX	BC	0.108	19.6	bdl	0.389	0.001	0.030	0.226	0.281	1.68	0.413	2.90	0.653	1.75	0.271	1.75	0.290
Zr17a	X	BC	0.163	27.4	0.0008	0.295	bdl	0.055	0.350	0.509	2.92	0.763	5.21	1.05	2.23	0.265	1.73	0.312
Zr18a	XI	BC	0.091	25.2	bdl	0.647	0.003	0.075	0.780	0.540	3.09	0.652	4.34	0.831	2.17	0.355	2.41	0.465
Zr19a	XII	BC	0.192	15.3	bdl	0.391	bdl	0.048	0.126	0.256	1.49	0.297	2.48	0.416	1.38	0.176	1.56	0.207
Zr20a	XII	BC	0.085	16.2	bdl	0.339	bdl	0.0027	0.200	0.320	1.80	0.421	3.03	0.502	1.25	0.218	1.44	0.287
Zr21a	XIII	BC	0.103	43.3	0.0014	0.492	0.001	0.147	0.820	0.812	4.81	1.08	7.74	1.27	3.47	0.598	4.35	0.743
Zr22a	XIII	BC	0.165	6.68	bdl	0.443	bdl	0.038	0.247	0.264	1.34	0.243	1.31	0.194	0.486	0.064	0.500	0.074
Zr23a	XIV	BC	0.103	12.8	bdl	0.526	bdl	0.040	0.330	0.377	1.72	0.337	2.09	0.357	0.970	0.137	0.830	0.147
Zr24a	XV	BC	0.151	10.0	bdl	0.055	bdl	0.0048	0.068	0.077	0.341	0.121	1.30	0.317	0.747	0.079	0.419	0.054
Zr25a	XVI	BC	0.113	10.7	bdl	0.742	0.004	0.090	0.397	0.487	2.45	0.342	1.81	0.351	0.880	0.141	1.20	0.219
Zr26a	XVII	BC	0.088	18.9	bdl	0.584	0.003	0.083	0.460	0.478	2.41	0.498	3.18	0.622	1.74	0.197	1.55	0.259
Zr27a	XVIII	BC	0.127	6.88	bdl	0.521	bdl	0.053	0.141	0.168	1.05	0.146	1.01	0.183	0.582	0.068	0.640	0.098
Zr28a	XIX	BC	0.093	9.38	bdl	0.412	0.002	0.0048	0.188	0.220	1.28	0.222	1.44	0.256	0.740	0.093	0.720	0.136
Zr29a	XIX	BC	0.206	15.5	0.0112	0.571	bdl	0.046	0.235	0.334	1.33	0.332	2.10	0.507	1.43	0.217	1.38	0.274
Zr30a	XX	BC	0.105	36.6	bdl	0.685	bdl	0.132	0.620	0.648	3.11	0.657	4.95	1.19	3.53	0.590	4.54	0.727
Zr31a	XXI	BC	0.086	13.8	bdl	0.355	bdl	0.017	0.150	0.208	1.29	0.326	2.02	0.417	1.22	0.182	1.34	0.213
Zr32a	XXII	BC	0.114	24.9	bdl	0.314	0.002	0.056	0.380	0.599	3.68	0.775	5.44	1.01	1.76	0.193	1.40	0.234
Zr33a	XXIII	BC	0.120	10.8	bdl	0.174	0.001	0.0029	0.057	0.131	0.84	0.201	1.39	0.349	0.870	0.183	1.31	0.215
Zr34a	XXIII	BC	0.103	8.57	bdl	0.725	bdl	0.042	0.350	0.264	1.16	0.230	1.45	0.276	0.720	0.094	0.690	0.105
Zr35a	XXIII	BC	0.077	14.1	bdl	0.542	bdl	0.0084	0.294	0.310	1.41	0.320	2.15	0.519	1.18	0.135	1.29	0.196
Zr36a	XXIV	BC	0.136	11.4	bdl	0.379	bdl	bdl	0.109	0.163	0.990	0.163	1.74	0.346	1.09	0.168	1.08	0.199
Zr37a	XXIV	BC	0.100	16.6	bdl	0.476	0.001	0.066	0.290	0.488	2.52	0.512	3.01	0.512	1.27	0.159	1.02	0.156
Zr38a	XXV	BC	0.091	17.2	bdl	0.641	0.002	0.076	0.440	0.469	2.14	0.444	3.00	0.518	1.55	0.241	1.78	0.289
Zr39a	XXV	BC	0.158	25.0	bdl	0.404	bdl	0.005	0.270	0.326	2.23	0.500	4.08	0.791	2.50	0.362	2.67	0.460
Zr40a	XXVI	BC	0.118	15.0	bdl	0.655	bdl	0.112	0.420	0.346	1.63	0.385	2.30	0.493	1.29	0.194	1.48	0.231
Zr41a	XXVII	BC	0.097	19.3	bdl	0.444	bdl	0.026	0.258	0.346	2.17	0.492	3.21	0.608	1.61	0.198	1.67	0.279
Zr42a	XXVII	BC	0.083	12.2	bdl	0.917	bdl	0.184	0.790	0.795	3.15	0.461	2.48	0.400	1.01	0.141	1.09	0.171

Table I.3.14: Table of Ti content of zircon obtained during the analytical session 6 (BR19). *Italic row an analysis with very high Ti content interpreted as an outlier. Bold rows indicate zircons with flow textures and containing small sized inclusions.*

Label	BR19 – An. Session 6			Content (ppm)		T (°C) at 20 kbar
	Crystal	Texture		Ti	2s abs	
Zr1a	I	BC	Rim	3.90	1.30	826
Zr2a	I	BC	Core	4.60	1.40	841
Zr3a	II	BC	Core	4.80	1.40	845
<i>Zr4a</i>	<i>III</i>	<i>BC</i>	<i>Rim</i>	<i>16.2</i>	<i>3.60</i>	<i>968</i>
Zr5a	III	DC	Core	7.70	1.90	890
Zr6a	III	BC	Core	10.0	1.90	916
Zr7a	IV	BC	Core	3.40	1.20	815
Zr8a	V	BC	Rim	3.60	1.10	819
Zr9a	V	BC	Core	4.40	1.30	837
Zr10a	VI	BC	Rim	2.60	1.10	792
Zr11a	VII	BC	Rim	3.20	1.00	809
Zr12a	VIII	BC	Rim	4.90	1.20	847
Zr13a	VIII	BC	Rim	2.90	1.10	801
Zr14a	IX	BC	Core	7.50	1.90	887
Zr15a	IX	BC	Rim	4.30	1.20	835
Zr16a	IX	BC	Rim	3.70	1.20	822
Zr17a	X	BC	Rim	5.90	1.50	864
Zr18a	XI	BC	Rim	4.70	1.80	843
Zr19a	XII	BC	Rim	3.70	1.40	822
Zr20a	XII	BC	Core	3.20	1.10	809
Zr21a	XIII	BC	Rim	4.70	1.30	843
Zr22a	XIII	BC	Core	2.30	1.00	782
Zr23a	XIV	BC	Core	3.70	1.50	822
<i>Zr24a</i>	<i>XV</i>	<i>BC</i>	<i>Core</i>	<i>2.70</i>	<i>1.10</i>	<i>795</i>
Zr25a	XVI	BC	Rim	5.00	1.50	849
Zr26a	XVII	BC	Core	5.40	1.50	856
Zr27a	XVIII	BC	Rim	2.30	1.10	782
Zr28a	XIX	BC	Rim	0.89	0.580	710
Zr29a	XIX	BC	Core	4.90	1.50	847
Zr30a	XX	BC	Core	5.50	1.40	858
Zr31a	XXI	BC	Rim	2.10	1.10	775
Zr32a	XXII	BC	Core	2.80	1.10	798
Zr33a	XXIII	BC	Rim	1.95	0.940	769
Zr34a	XXIII	BC	Core	3.00	1.30	804
Zr35a	XXIII	BC	Core	6.10	1.70	867
Zr36a	XXIV	BC	Rim	1.80	1.00	762
Zr37a	XXIV	BC	Rim	1.80	0.850	762
Zr38a	XXV	BC	Rim	4.50	1.60	839
Zr39a	XXV	BC	Core	2.60	1.10	792
Zr40a	XXVI	BC	Core	2.40	1.10	785
Zr41a	XXVII	BC	Rim	3.90	1.20	826
Zr42a	XXVII	BC	Core	2.70	1.10	795

Table I.3.15: U/Pb data of zircons obtained during the analytical session 7 (BR19).

BR19 – An. Session 7			Content (ppm)				Tera Wasserburg plot				Wetherill plot					Ages (Ma)						Conc.
Label	Crystal	Texture	U	Th	Pb	Th/U	U^{238}/Pb^{206}	2s abs	Pb^{207}/Pb^{206}	2s abs	Pb^{207}/U^{235}	2s abs	Pb^{206}/U^{238}	2s abs	rho	Pb^{207}/U^{235}	2s abs	Pb^{206}/U^{238}	2s abs	Pb^{207}/Pb^{206}	2s abs	
Zr1b	II	BC	54	0.5	2	0.01	18.8	1.16	0.060	0.0035	0.435	0.029	0.053	0.0033	0.926	371	28	335	20	603	144	90
Zr2b	II	BC	39	1	1	0.03	17.9	1.10	0.056	0.0028	0.427	0.026	0.056	0.0034	1.01	364	25	351	21	451	119	96
Zr3b	XII	BC	50	1	1	0.02	19.8	1.20	0.059	0.0030	0.400	0.024	0.051	0.0031	1.01	350	23	318	19	566	111	91
Zr4b	XII	BC	19	0.4	0.4	0.02	20.1	1.31	0.059	0.0047	0.371	0.029	0.050	0.0032	0.822	345	31	313	20	566	185	91
Zr5b	XII	BC	24	1	1	0.04	19.5	1.25	0.058	0.0044	0.382	0.029	0.051	0.0033	0.831	349	28	323	20	529	151	92
Zr6b	XVI	BC	64	2	2	0.03	20.2	1.23	0.056	0.0024	0.374	0.021	0.050	0.0030	1.09	329	20	312	19	451	79	95
Zr7b	XVI	BC	51	1	1	0.03	18.3	1.10	0.054	0.0025	0.401	0.022	0.055	0.0033	1.08	346	21	342	20	370	83	99
Zr8b	XVII	BC	48	1	1	0.02	17.6	1.08	0.053	0.0027	0.405	0.024	0.057	0.0035	1.03	352	25	356	21	328	128	101

Abbreviations: BC – bright CL crystals, BR – bright CL rims, BS – bright CL spots, DC – dark CL cores

Table I.3.16: U/Pb data of rutiles obtained during the analytical session 8 (BR19).

Table I.3.17: Zr in rutile data obtained during the analytical session 8 (BR19). g – Included in garnet; mtx – in the matrix.

Table I.3.18: U/Pb data of apatite obtained during the analytical session 9 (BR18).

Table I.3.19: U/Pb data of apatite obtained during the analytical session 10 (BR18).

Table I.3.20: U/Pb data of apatite obtained during the analytical session 11 (BR19).

BR18 – An. Session 8		Content (ppm)		Tera Wasserburg plot				Age (Ma)	
Label	Crystal	U	Pb	U^{238}/Pb^{206}	2s abs	Pb^{207}/Pb^{206}	2s abs	Pb^{207}/Pb^{206}	2s abs
Ru1	I	6.996	0.0394	18.0	0.909	0.065	0.006	260	160
Ru2	I	5.07	0.0272	17.9	1.00	0.077	0.009	200	180
Ru3	I	9.21	0.097	18.4	2.64	0.071	0.024	470	210
Ru4	I	2.222	0.14	15.1	1.04	0.090	0.140		
Ru5	II	0.931	0.0271	16.4	1.54	-0.080	0.370		
Ru6	III	0.273	0.0148	13.7	2.25	-2.800	1.100		
Ru7	III	0.1848	0.0171	12.3	2.74	-2.800	1.400		
Ru8	III	0.1849	0.0218	12.8	2.63	-3.500	1.300		
Ru9	IV	0.2362	0.119	8.62	1.34	-5.300	1.600		
Ru10	IV	0.1979	0.031	11.9	2.55	-3.000	1.400		
Ru11	IV	0.1999	0.027	11.9	2.13	-4.200	1.500		
Ru12	V	0.1098	0.047	12.7	6.25	-2.800	2.700		
Ru13	VI	0.454	0.046	15.2	1.84	-2.500	1.100		
Ru14	VI	0.2125	0.048	12.7	2.24	-2.100	1.200		
Ru15	VI	0.2089	0.049	12.2	2.53	-2.400	1.400		
Ru16	VI	0.1925	0.058	11.8	2.21	-2.700	1.500		
Ru17	VII	0.2221	0.099	15.2	3.44	-3.000	1.600		
Ru18	VII	0.0952	0.05	8.62	6.09	-5.200	4.400		
Ru19	VIII	0.852	0.035	19.2	1.87	-0.410	0.590		
Ru20	VIII	0.698	0.035	17.3	1.74	-3.000	1.300		
Ru21	VIII	0.1006	0.014	11.4	6.33	-8.900	7.600		
Ru22	VIII	0.469	0.032	14.2	1.58	-0.510	0.720		
Ru23	VIII	0.1282	0.38	3.40	0.602	-7.000	3.100		
Ru24	VIII	0.643	0.46	10.6	0.960	-8.000	2.500		
Ru25	IX	34.34	0.114	5.29	0.207	0.077	0.002		
Ru26	IX	0.1661	0.125	9.52	1.72	-10.300	3.200		
Ru27	IX	0.1673	0.05	12.7	2.56	-8.900	2.500		
Ru28	X	0.2287	0.223	8.47	1.22	-14.300	3.400		
Ru29	X	5.356	0.043	18.1	0.919	0.065	0.006	220	160
Ru30	X	8.3	3.29	12.6	0.649	0.279	0.011	3269	58
Ru31	XI	0.0951	0.886	14.1	8.33	1.100	3.300		
Ru32	XII	5.7	0.053	16.4	0.809	0.074	0.007	420	160
Ru33	XII	0.0912	0.0149	9.71	7.26	-11.000	11.000		
Ru34	XII	0.143	0.434	2.00	0.355	-11.200	8.800		
Ru35	XIII	0.283	0.0501	14.5	2.11	-16.500	3.800		
Ru36	XIV	0.354	0.048	13.9	1.90	-14.600	3.900		
Ru37	XIV	0.223	0.11	5.99	1.11	-28.900	7.300		
Ru38	XV	0.1476	0.089	2.13	0.770	-23.400	8.500		
Ru39	XVI	0.1371	0.05	2.94	1.21	-4.100	6.400		
Ru40	XVII	0.1197	0.043	2.94	1.04	-18.000	12.000		
Ru41	XVII	0.1423	0.0203	11.1	3.09	-11.500	6.100		
Ru42	XVIII	0.1006	0.0377	7.35	3.84	-17.000	14.000		

BR18 - An. Session 8			Content (ppm)		T (°C)
Label	Crystal	Texture	Ti	2s abs	at 20 kbar
Ru1	I	mtx	237	2.3	673
Ru2	I	mtx	214	2.1	665
Ru3	I	mtx	211	2.2	664
Ru4	I	mtx	253	2.6	678
Ru5	II	mtx	189	2.2	655
Ru6	III	mtx	294	2.8	691
Ru7	III	mtx	285	2.7	688
Ru8	III	mtx	291	2.7	690
Ru9	IV	g	325	3.4	700
Ru10	IV	g	309	3.1	695
Ru11	IV	g	322	3.4	699
Ru12	V	mtx	231	2.1	671
Ru13	VI	mtx	355	4.1	707
Ru14	VI	mtx	252	3	678
Ru15	VI	mtx	295	4.3	691
Ru16	VI	mtx	270	2.7	684
Ru17	VII	mtx	277	2.5	686
Ru18	VII	mtx	236	2.4	673
Ru19	VIII	mtx	223	2.1	668
Ru20	VIII	mtx	218	2.1	666
Ru21	VIII	mtx	167	1.6	646
Ru22	VIII	mtx	181	1.9	652
Ru23	VIII	mtx	171	1.7	648
Ru24	VIII	mtx	158	1.8	642
Ru25	IX	g	258	2.9	680
Ru26	IX	g	273	3.2	685
Ru27	IX	g	294	3.2	691
Ru28	X	mtx	194	2.3	657
Ru29	X	mtx	217	2.3	666
Ru30	X	mtx	137	1.4	631
Ru31	XI	mtx	193	2.2	657
Ru32	XII	mtx	223	3.1	668
Ru33	XII	mtx	176	2.6	650
Ru34	XII	mtx	183	3.3	653
Ru35	XIII	mtx	200	2.3	659
Ru36	XIV	g	329	3.4	701
Ru37	XIV	g	355	5	707
Ru38	XV	g	328	4.1	700
Ru39	XVI	g	284	3.4	688
Ru40	XVII	g	263	3.1	682
Ru41	XVII	g	281	2.9	687
Ru42	XVIII	g	362	4.3	709

BR18 – An. Session 9			Content (ppm)		Tera Wasserburg plot				Age (Ma)	
Label	Crystal	CL	U	Pb	U^{238}/Pb^{206}	2s abs	Pb^{207}/Pb^{206}	2s abs	Pb^{207}/Pb^{206}	2s abs
Apt1a	I	P	0.4	4	0.432	0.026	0.844	0.012	4997	11
Apt2a	I	P	0.2	4	0.242	0.019	0.840	0.012	4991	11
Apt3a	I	P	0.1	4	0.175	0.012	0.856	0.011	5017	10
Apt4a	II	Y	1	2	1.36	0.082	0.790	0.012	4903	12
Apt5a	III	P	84	15	11.6	0.643	0.344	0.0022	3681	6
Apt6a	IV	P	0.2	3	0.322	0.020	0.842	0.012	4994	11
Apt7a	V	Y	7	9	2.82	0.167	0.725	0.0064	4780	8
Apt8a	VI	Y	0.3	2	0.589	0.034	0.832	0.014	4977	13
Apt9a	VI	Y	0.2	2	0.534	0.034	0.821	0.014	4958	13
Apt10a	VII	Y	1	1	2.96	0.175	0.722	0.017	4775	18
Apt11a	VII	Y	1	1	3.18	0.192	0.721	0.018	4773	19
Apt12a	VIII	Y	7	3	6.16	0.349	0.573	0.0075	4441	11
Apt13a	VIII	Y	4	3	4.32	0.262	0.665	0.0080	4657	10
Apt14a	IX	P	2	5	1.37	0.091	0.792	0.0086	4907	9
Apt15a	X	P	17	8	6.12	0.355	0.579	0.0080	4455	11
Apt16a	XI	Y	15	5	7.27	0.428	0.525	0.0076	4311	12
Apt17a	XI	Y	9	6	5.12	0.315	0.613	0.0083	4539	11
Apt18a	XII	Y	0.5	2	1.18	0.092	0.791	0.015	4905	14
Apt19a	XIII	P	0.5	13	0.173	0.010	0.852	0.0055	5010	7
Apt20a	XIV	Y	0.1	1	0.368	0.030	0.841	0.019	4992	17
Apt21a	XIV	Y	0.1	1	0.382	0.029	0.849	0.025	5006	22
Apt22a	XV	P	8	7	4.03	0.227	0.670	0.0064	4668	8
Apt23a	XV	P	9	7	4.66	0.261	0.645	0.0054	4612	8
Apt24a	XVI	Y	1	2	2.10	0.119	0.765	0.014	4857	14
Apt25a	XVII	Y	25	12	6.06	0.341	0.584	0.004	4468	6
Apt26a	XVIII	P	18	11	5.01	0.276	0.632	0.007	4582	9
Apt27a	XIX	Y	0.3	1	1.33	0.082	0.811	0.020	4941	18
Apt28a	XX	P	21	14	4.79	0.275	0.645	0.0038	4613	6
Apt29a	XX	P	24	14	5.17	0.294	0.626	0.0037	4568	6
Apt30a	XXI	Y	10	8	4.32	0.242	0.666	0.0060	4659	8
Apt31a	XXI	Y	9	8	4.00	0.224	0.682	0.0053	4693	7
Apt32a	XXI	Y	12	8	4.63	0.258	0.648	0.0047	4619	7
Apt33a	XXII	P	23	10	6.19	0.356	0.577	0.0053	4451	8
Apt34a	XXIII	P	0.4	6	0.249	0.015	0.844	0.0077	4996	8
Apt35a	XXIV	Y	0.4	1	1.04	0.061	0.814	0.015	4946	14
Apt36a	XXV	P	0.4	1	1.31	0.085	0.807	0.030	4934	27
Apt37a	XXVI	P	1	1	2.95	0.183	0.728	0.022	4786	22
Apt38a	XXII	P	28	10	7.12	0.415	0.531	0.006	4328	9
Apt39a	XXIII	P	22	11	5.30	0.309	0.608	0.0051	4528	8
Apt40a	XXIV	Y	1	2	1.50	0.088	0.779	0.012	4883	12

Abbreviation: P – Purple CL colour, Y – Yellow CL colour.

BR18 – An. Session 10			Content (ppm)		Tera Wasserburg plot				Age (Ma)	
Label	Crystal	CL	U	Pb	U^{238}/Pb^{206}	2s abs	Pb^{207}/Pb^{206}	2s abs	Pb^{207}/Pb^{206}	2s abs
Apt1b	III	P	72	13	11.2	0.107	0.351	0.0030	3710	8
Apt2b	III	P	61	11	11.2	0.112	0.348	0.0032	3696	8
Apt3b	III	P	65	11	11.2	0.104	0.351	0.0030	3712	8
Apt4b	III	P	70	12	11.0	0.101	0.354	0.0029	3723	7
Apt5b	III	P	75	13	11.5	0.108	0.343	0.0030	3676	8
Apt6b	III	P	77	12	11.9	0.110	0.322	0.0027	3578	8
Apt7b	III	P	77	14	11.3	0.104	0.354	0.0031	3725	8
Apt8b	XXV	P	20	8	6.99	0.083	0.534	0.0052	4337	8
Apt9b	XXV	P	16	8	5.94	0.067	0.587	0.0059	4475	9
Apt10b	XXV	P	19	8	6.45	0.075	0.568	0.0062	4428	9
Apt11b	XXV	P	20	8	6.92	0.081	0.540	0.0061	4354	9
Apt12b	XXVI	P	20	10	6.34	0.068	0.576	0.0057	4448	9
Apt13b	XXVI	P	18	10	5.73	0.059	0.596	0.0058	4497	8
Apt14b	XXVI	P	18	9	5.92	0.067	0.593	0.0059	4490	9
Apt15b	XXVII	P	38	7	10.1	0.113	0.387	0.0046	3857	10
Apt16b	XXVII	P	48	8	10.9	0.105	0.358	0.0036	3742	9
Apt17b	XXVII	P	43	8	10.3	0.118	0.390	0.0047	3868	10
Apt18b	XXVII	P	41	9	9.44	0.107	0.424	0.0043	3994	9
Apt19b	XXVII	P	29	9	7.91	0.156	0.487	0.0072	4202	12
Apt20b	XXII	P	29	9	8.17	0.093	0.485	0.0052	4196	9
Apt21b	XXII	P	18	9	5.82	0.071	0.593	0.0059	4490	9
Apt22b	XXII	P	18	9	6.05	0.073	0.583	0.0060	4465	9
Apt23b	XI	P	13	6	6.64	0.079	0.562	0.0069	4412	10
Apt24b	XI	P	9	6	5.10	0.060	0.626	0.0079	4569	10
Apt25b	XXVII	P	21	6	8.12	0.086	0.493	0.0054	4219	9
Apt26b	XXVII	P	17	7	7.02	0.084	0.540	0.0062	4353	10
Apt27b	XXVII	P	20	6	7.88	0.112	0.510	0.0076	4270	12
Apt28b	XXVIII	P	20	14	4.46	0.085	0.651	0.0061	4625	8
Apt29b	XXVIII	Y	12	15	2.87	0.070	0.727	0.0065	4784	8
Apt30b	XXVIII	Y	17	14	4.01	0.058	0.672	0.0061	4670	8
Apt31b	XXVIII	Y	17	14	4.08	0.078	0.671	0.0068	4669	9
Apt32b	XI	Y	14	6	6.95	0.116	0.555	0.0100	4394	14

Abbreviation: P – Purple CL colour, Y – Yellow CL colour.

BR19 - An. Session 11			Content (ppm)		Tera Wasserburg plot				Age (Ma)	
Label	Crystal	CL	U	Pb	U^{238}/Pb^{206}	2s abs	Pb^{207}/Pb^{206}	2s abs	Pb^{207}/Pb^{206}	2s abs
Apt1	I	P	2	13	0.514	0.018	0.839	0.0076	4988	8
Apt2	I	P	2	17	0.441	0.015	0.840	0.0068	4990	8
Apt3	I	P	2	17	0.399	0.014	0.845	0.0069	4999	8
Apt4	I	P	1	15	0.350	0.012	0.848	0.0078	5004	8
Apt5	II	Y	0.1	1	0.513	0.034	0.846	0.042	5001	36
Apt6	III	Y	0.5	2	1.20	0.049	0.812	0.018	4942	17
Apt7	IV	Y	2	2	4.40	0.157	0.671	0.015	4669	17
Apt8	IV	Y	2	2	4.00	0.146	0.683	0.015	4695	17
Apt9	V	P	1	9	0.478	0.017	0.838	0.0091	4986	9
Apt10	V	P	1	9	0.640	0.025	0.826	0.0097	4967	10
Apt11	VI	Y	0.5	1	1.66	0.069	0.799	0.022	4919	20
Apt12	VII	Y	0.3	1	1.08	0.046	0.834	0.025	4980	22
Apt13	VIII	Y	1	2	1.80	0.065	0.788	0.015	4900	14
Apt14	IX	Y	0.2	2	0.417	0.017	0.857	0.019	5019	17
Apt15	IX	Y	0.2	2	0.419	0.019	0.856	0.019	5017	17
Apt16	IX	Y	0.2	2	0.449	0.019	0.834	0.02	4980	18
Apt17	X	Y	1	3	0.885	0.034	0.820	0.018	4956	16
Apt18	X	Y	1	2	0.917	0.036	0.830	0.018	4974	16
Apt19	XI	Y	0.2	2	0.370	0.016	0.861	0.02	5026	17
Apt20	XII	Y	0.3	1	0.980	0.040	0.827	0.024	4968	21
Apt21	XII	Y	0.4	1	1.11	0.045	0.808	0.021	4935	19
Apt22	XIII	Y	0.5	1	2.08	0.087	0.774	0.023	4874	22
Apt23	XIII	Y	1	1	1.98	0.082	0.769	0.024	4865	23
Apt24	XIV	P	3	8	1.65	0.054	0.782	0.0091	4888	10
Apt25	XIV	P	3	8	1.63	0.056	0.779	0.0095	4883	10
Apt26	XIV	P	3	8	1.61	0.054	0.779	0.0084	4883	9
Apt27	XIV	P	4	8	1.96	0.073	0.768	0.0092	4862	10
Apt28	XIV	P	3	7	1.62	0.058	0.781	0.0090	4886	10
Apt29	XV	Y	1	2	2.22	0.178	0.767	0.016	4861	16
Apt30	XV	Y	1	2	2.23	0.080	0.760	0.017	4848	17
Apt31	XVI	Y	1	2	1.74	0.064	0.777	0.017	4880	16
Apt32	XVII	Y	1	2	1.79	0.064	0.777	0.015	4880	15
Apt33	XVIII	Y	2	2	4.55	0.166	0.651	0.013	4626	15
Apt34	XVIII	Y	2	2	4.50	0.172	0.675	0.016	4678	18
Apt35	XVIII	Y	3	2	5.01	0.186	0.626	0.014	4569	17
Apt36	XVIII	Y	1	9	0.591	0.021	0.833	0.0084	4978	9
Apt37	XVIII	Y	1	1	3.26	0.138	0.691	0.017	4712	18
Apt38	XIX	Y	1	2	2.15	0.083	0.755	0.017	4839	17
Apt39	XX	Y	2	2	3.61	0.130	0.707	0.015	4744	16
Apt40	XXI	Y	1	3	1.49	0.053	0.793	0.012	4909	12

Abbreviation: P – Purple CL colour, Y – Yellow CL colour.

Petrologic study of French Variscan metagranites

Introduction to the petrologic study of metagranites

The high-grade terrains of the French Variscan basement are composed, among others by a bimodal alkaline to calc-alkaline magmatic suite (now metamorphosed - orthogneiss and their effusive equivalent locally called porphyroids) emplaced during the Cambrian-Ordovician period of crustal thinning and oceanisation (c. 490-450 Ma; e.g. Ballèvre et al., 2002, 2012; Paquette et al., 2017; Solá et al., 2008; Crowley et al., 2002). Subsequent subduction, exhumation and continental collision (e.g. Burg and Matte, 1978; Matte, 1991; Santallier et al., 1988; Ledru, 1989) resulted in a polystage deformation and metamorphism during the Variscan orogeny. Although felsic orthogneisses are reputed relatively unreactive during metamorphism (e.g. Peterman et al., 2009; Schertl and O'Brien, 2013), the recent discovery of HP garnet-kyanite-phengite-rutile assemblage (15-17 kbar) after cordierite in an Ordovician metagranite in the Lévézou massif suggests that the continental crust recorded the initial subduction stage (Lotout, 2017). Accordingly, other Ordovician orthogneisses should have recorded the Variscan polystage deformation and metamorphic events. Heterogeneous deformation and strain gradients characteristic of deformed granitoids should then allow to identify the different mineral assemblages and the relative orientation of the different generation of structures.

Given the tectonic setting of their emplacement, the orthogneisses must have been intrusive in the continental margins on both sides of the nascent oceanic domain. One of these margins was subsequently subducted while the other only underwent substantial deformation during the continent-continent collision (Figure V.1.1). Accordingly, the strain pattern of the orthogneisses in the upper and lower plates should be different and it should be possible to distinguish them and identify the suture.

The aim of the study was to provide a map of the subducted portions of continental lithosphere based on the petrology of the orthogneiss. This cartography was a prerequisite to

Chapter II

the following study of the deformation of the orthogneiss in order to distinguish the deformations associated with the burial and the exhumation of the subducted continental margin. To tackle these problems, the first step was to identify the mineralogical markers that could hint a possible HP metamorphism in the orthogneiss. This work was followed by a synthesis of the lineations and shear senses observed in the orthogneisses.

Chapter II

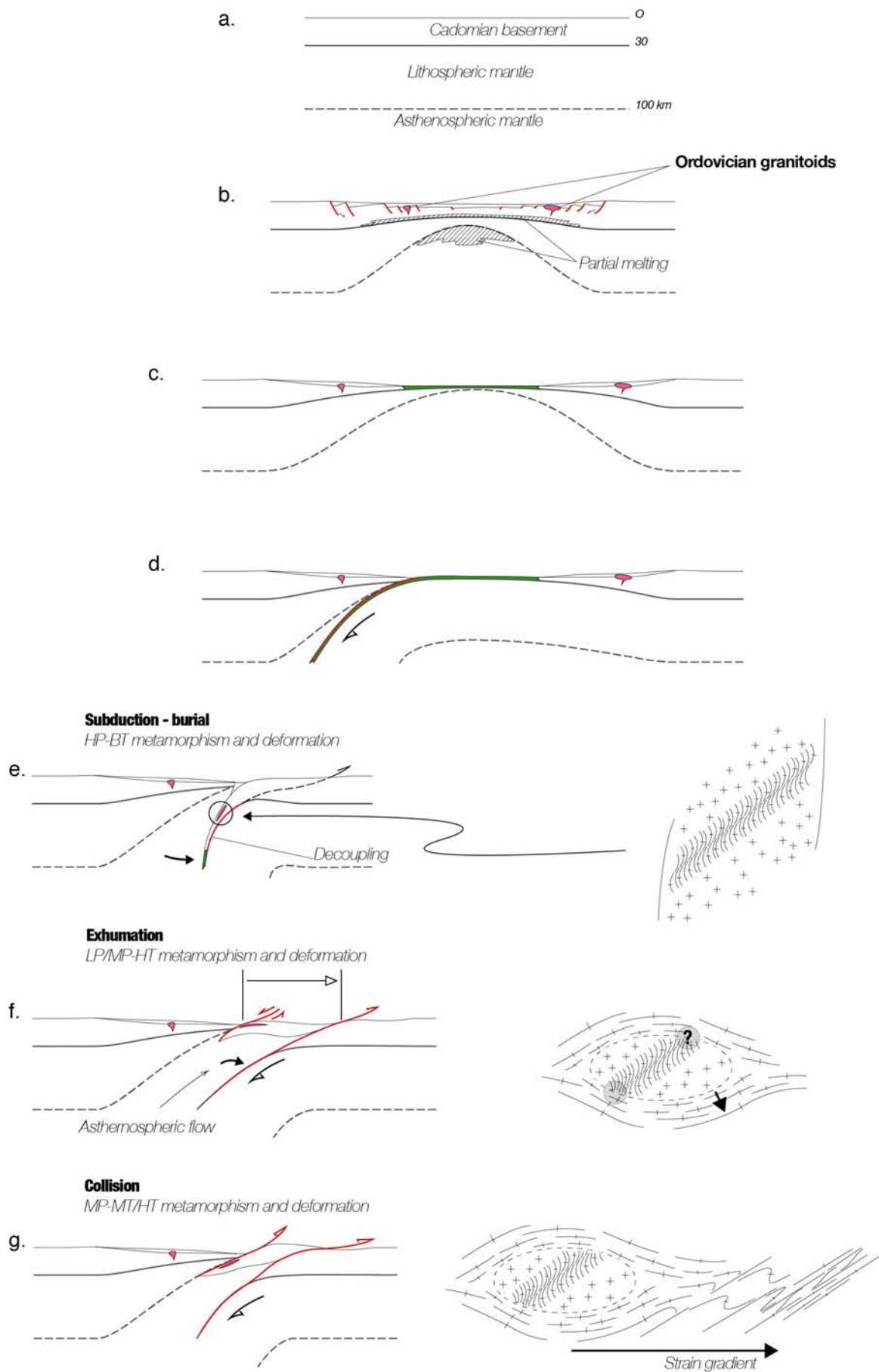


Figure II.1: Schematic drawing of a possible deformation scenario of the Ordovician orthogneisses. The initial setting assumes a normal thickness crust and lithosphere (a), subsequent thinning of the lithosphere triggers partial melting of the asthenospheric mantle and crust with the emplacement of ordovician plutons (b). Continued extension resulted in the opening of an oceanic domain (c) that was subsequently subducted (d). Owing to heterogeneous deformation, the subducted continental crust may localise the deformation or preserve lenses that evidence each step of the deformation and metamorphic history from burial (e) to exhumation (f) that might have been reworked later (g) during the continental collision. These several steps of deformation might be identified in some specific area in the field.

1. Mineralogical indicators of HP metamorphism in metagranite

HP metagranites are characterized by the destabilization of plagioclase and biotite, commonly marked by the development of garnet coronae (e.g. Compagnoni and Mafféo, 1973; Oberhänsli et al., 1985; Biino and Compagnoni, 1992; Marco et al., 1999; Bruno et al., 2001). Plagioclase, K-feldspar and biotite breakdown ultimately results in jadeite-zoisite-quartz/coesite±garnet, phengite+quartz/coesite and garnet-(Ti-bearing) phengite±rutile assemblages respectively (Compagnoni and Mafféo, 1973; Biino and Compagnoni, 1992). Magmatic ilmenite destabilizes into rutile (Biino et al., 1992) and release iron, likely incorporated by garnet. As a general rule, the destabilization of plagioclase produces a grossular-rich garnet (e.g. Proyer, 2003). Grossular-rich garnet-phengite-albite-K feldspar-quartz-biotite-titanite assemblage metastable with respect to jadeite was inferred to record pressures around 20 kbar (Chopin et al., 2012). Garnet-kyanite-phengite-quartz pseudomorphs after cordierite may show pressures higher than 15 kbar (Lotout, 2017), although in this particular case garnet is mostly almandine- rather than grossular-rich. In many cases these HP

Chapter II

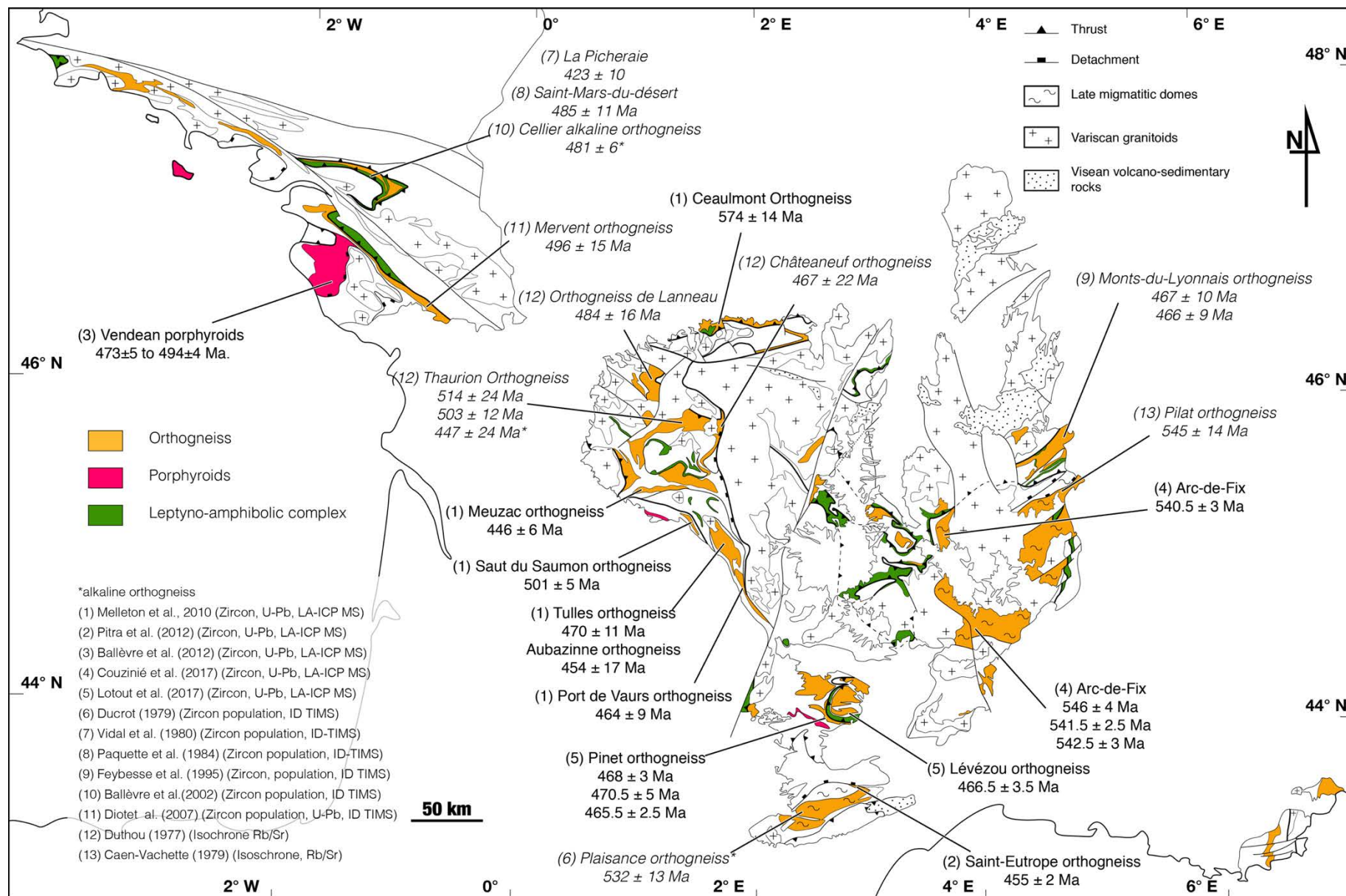
metagranites display a “magmatic” texture (Compagnoni and Mafféo, 1973; Oubrahim et al., 1985; Lotout et al., 2017), but the higher metamorphic grade may be recorded in the most deformed facies (Chopin et al., 2012). Therefore, these criteria were used to target the most relevant sites to conduct a petrological study. Four maps were realized, showing: a synthesis with radiometric data (Fig. V.1.2), potential mineralogical indicators of HP metamorphism (Fig. V.1.3), trends of stretching lineations (Fig. V.1.4), and shear sense criteria (Fig. V.1.5).

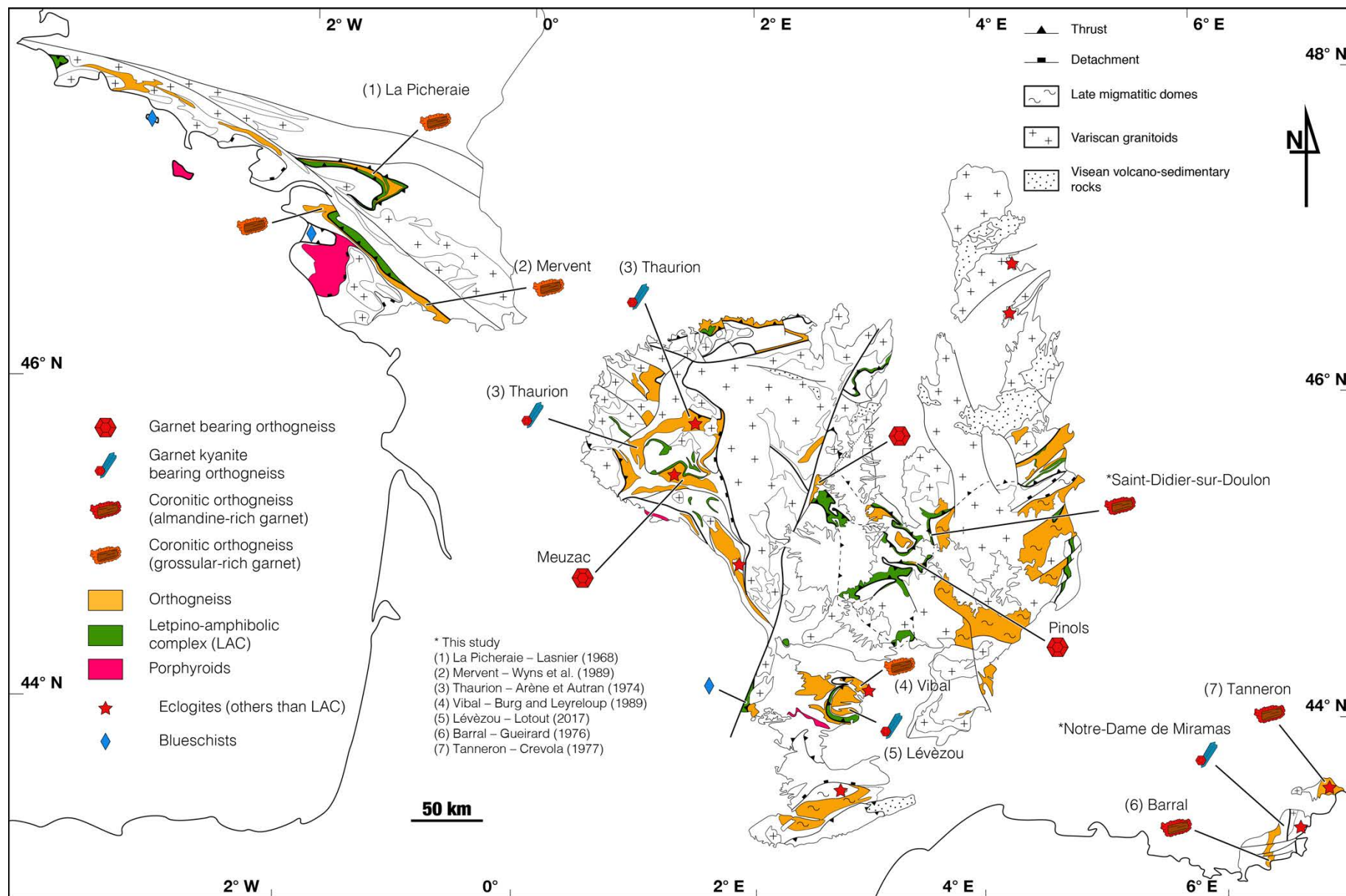
Figure II.2: Synthetic map of the available radiometric data obtained on the orthogneisses. Two generation of Cambrian and Ordovician orthogneisses can be distinguished. Regular refer to In-Situ LA-ICP MS studies and italic to dissolution of zircon population or Rb/Sr isochrone studies.

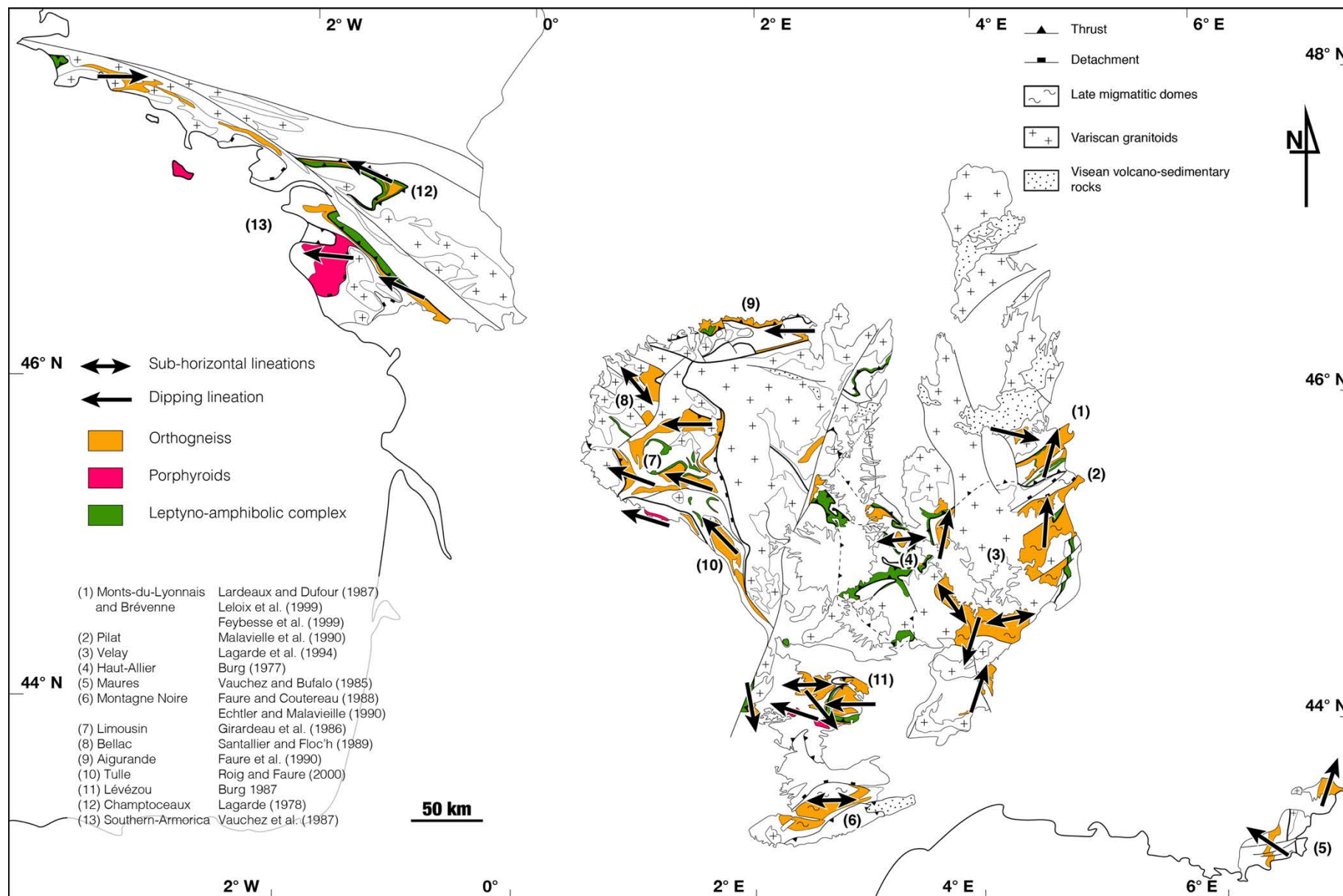
Figure II.3: Synthetic map of potential HP mineralogic indicator in the orthogneiss.

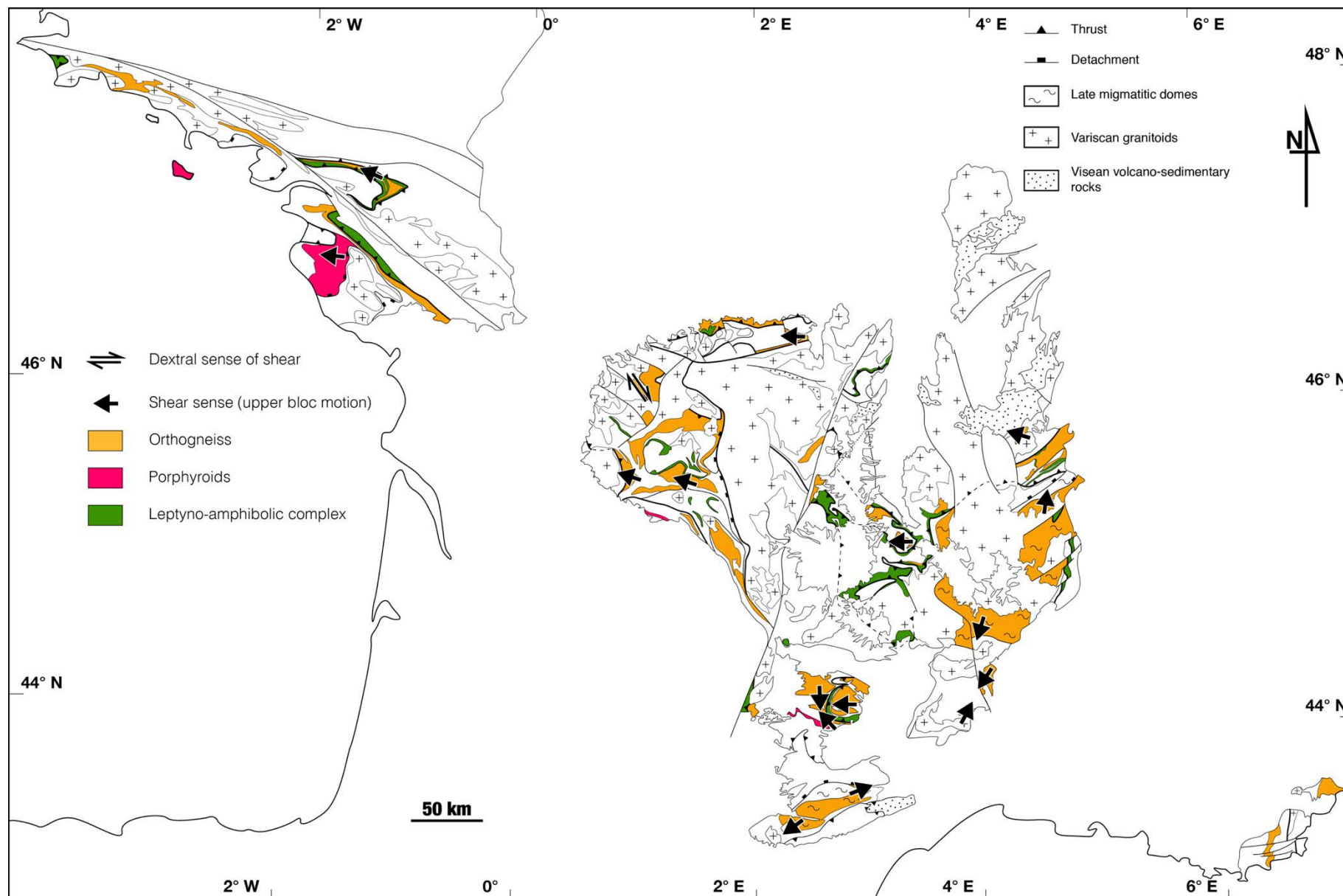
Figure II.4: Synthetic map of the lineation trend in the orthogneisses – data compilation from the literature and the 1/50 000 geological maps (BRGM).

Figure II.5: Synthetic map of the shear sense in the orthogneiss – data compilation from the literature and the 1/50 000 geological maps (BRGM).









In the literature, four metagranite massifs with garnet coronae around biotite were reported (Barral – Maures massif, Tanneron, Vibal – Lévézou massif, La Picheraie – Champtoceaux massif, Mervent – Essarts; Fig. II.2) and an orthogneiss with garnet corona around biotite was also discovered by us in the leptyno-amphibolic complex of the Haut-Allier. Two orthogneisses with garnet-kyanite aggregates were described (Lévézou, Thaurion; Fig. II.2) and we discovered one more in the Maures massif (Notre-Dame de Miramas).

2. Methods

P–T pseudosections were calculated in the model system MnNCKFMASHT using Theriak/Domino (de Capitani & Brown, 1987; de Capitani & Petrakakis, 2010) and the thermodynamic data set 5.5 (Holland & Powell, 1998); updated November 2003; translation for Theriak/Domino by Tinkham, 2012 – <http://dtinkham.net/peq.html>). The solution phases considered in the calculations, and the activity-composition models used are amphibole (Diener & Powell, 2012), chlorite (Le Bayon et al., 2006; based on Holland et al., 1998), chloritoid, cordierite, epidote, staurolite (Holland & Powell, 1998), garnet, biotite, ilmenite, hematite (White et al., 2005), magnetite (White et al., 2000), plagioclase (Holland & Powell, 2003); muscovite, paragonite (Coggon & Holland, 2002) and margarite (margarite-paragonite mixing on sites, neglecting muscovite, $W(\text{ma}, \text{pa}) = 14.5 \text{ kJ}$ (AX notes, Powell & Holland, 2002), DQF for paragonite set to 5 kJ to fit natural data of Höck, 1974 and Feenstra, 1996).

Mineral analyses and bulk compositions used for the calculations were obtained by the area-scan method at SEM-EDS (JSM-7100 F scanning electron microscope, CMEBA, University Rennes 1) on part of the thin section. Mineral abbreviations are: ab: albite; and: andalusite; bi: biotite, cd: cordierite, ctd: chloritoid, g: garnet, ilm: ilmenite, ksp: potassium feldspar, ky: kyanite, mic: microcline; mu: muscovite, pl: plagioclase, q: quartz, ru: rutile, san: sanidine; sill: sillimanite. Mineral endmembers (expressed in mole %) and compositional variables are: $X_{\text{Mg}} = \text{Mg}/(\text{Fe}+\text{Mg})$, almandine,

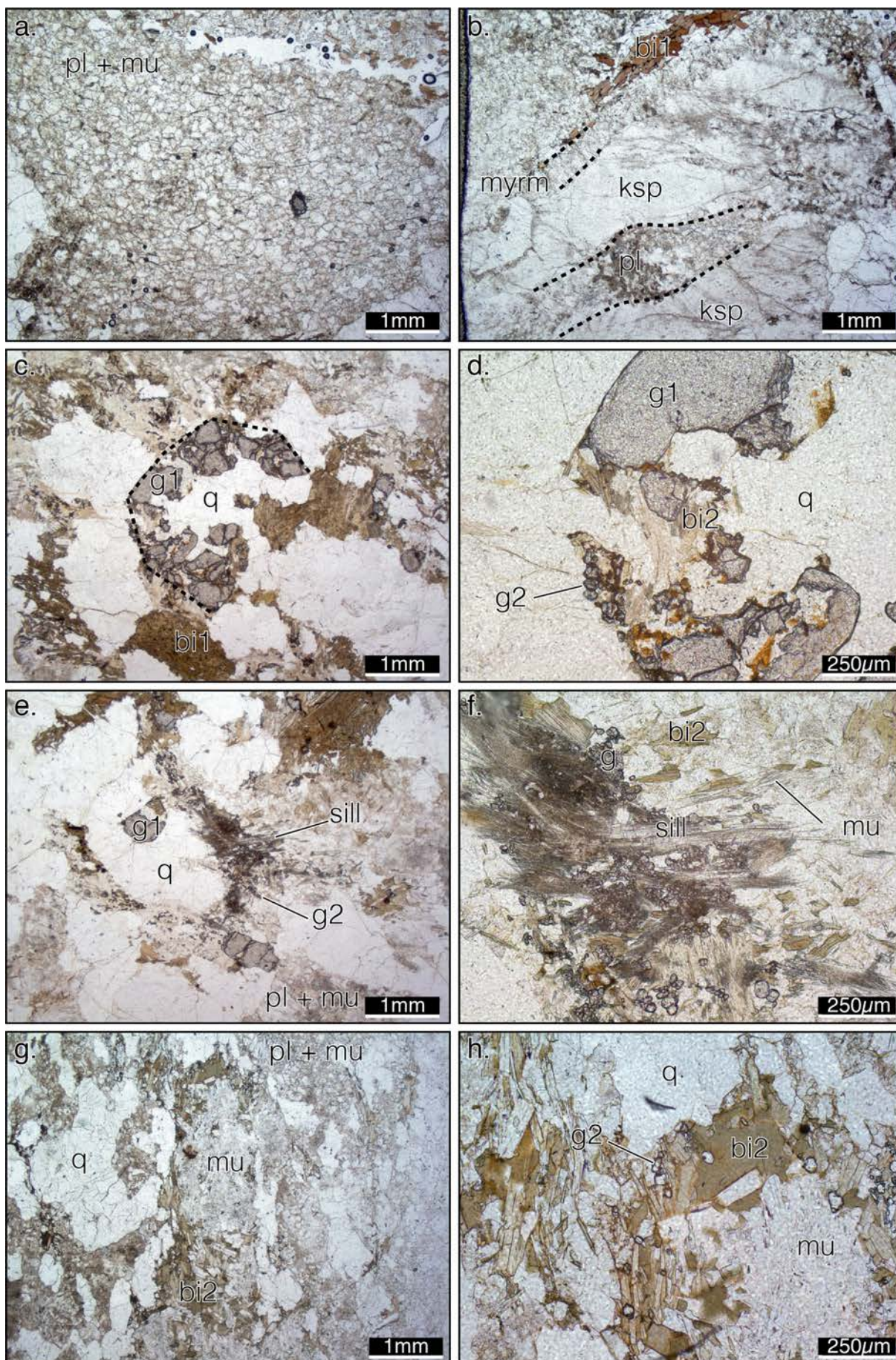
alm = $\text{Fe}/(\text{Fe}+\text{Mg}+\text{Ca}+\text{Mn})$, pyrope, prp = $\text{Mg}/(\text{Fe}+\text{Mg}+\text{Ca}+\text{Mn})$, grossular, grs = $\text{Ca}/(\text{Fe}+\text{Mg}+\text{Ca}+\text{Mn})$, spessartine, sps = $\text{Mn}/(\text{Fe}+\text{Mg}+\text{Ca}+\text{Mn})$, anorthite, An = $\text{Ca}/(\text{Ca}+\text{Na}+\text{K})$.

3. A petrologic study of Variscan metagranites

During this study of the granitoids metamorphosed during the Variscan orogeny, I sampled the massifs of Maures (Barral, Notre Dame de Miramas), Tanneron, Lévézou, Najac, Rodez, Monts-du-Lyonnais, Pilat, Haut-Allier (Mercoeur, Pinols and isolated lenses in the leptyno-amphibolitic complex), Limousin (Meuzac, Thaurion), and Mervent (Fig. II.2). The aim of this sampling was to find the less and most deformed orthogneisses looking for metamorphic evidences. Among them, orthogneisses of the Maures, Tanneron, Thaurion, as well as one isolated lens in the leptyno-amphibolitic complex in the Haut-Allier displayed metamorphic textures.

3.1. *Thaurion metagranite*

The Thaurion metagranite, emplaced during the Cambrian (c. 510 Ma; Duthou, 1977) is spatially associated with an eclogite massif (Sauviat-sur-Vigès). The emplacement of the mafic protolith is dated at 496 ± 25 Ma by zircon population dissolution (Gebauer et al., 1981). A regional HT metamorphism increases from north to south where it reaches partial melting (Arène and Autran, 1978). The metagranite/orthogneiss is variably deformed. The kyanite-garnet-muscovite-biotite aggregates are described in undeformed porphyritic facies (Arène and Autran, 1978). Twenty-three samples of variably deformed metagranite and orthogneiss were sampled in order to find and study the kyanite-garnet-muscovite-biotite aggregates.



Chapter II

Figure II.6 (previous page): Photomicrographs of thin sections of the Thaurion metagranite. Plagioclase and muscovite aggregate with granoblastic texture (a). K-feldspar rimmed by myrmekite and cut across by a small sized plagioclase with granoblastic texture (b). Garnet 1 embedded in quartz (c). Garnet 2 and light biotite 2 around with garnet 1 (d). Xenomorphic garnet 1(e) in quartz surrounded by sillimanite, garnet 2, muscovite, and green biotite 2 aggregate (e, f). muscovite aggregate rimmed by green biotite 2 and garnet (g, h).

Petrography

The less deformed metagranite samples are coarse grained (mm to cm) and porphyritic with K-feldspar up to 3 cm long. Under the microscope, plagioclase, associated with muscovite, forms fine grained (25 μm) polycrystalline aggregate with granoblastic texture (Fig. II.6a). K-feldspar displays a rim of myrmekite and planar aggregates of plagioclase cutting through the crystals (Fig. II.6b). Garnet (g1) forms anhedral crystals, locally included in quartz (Fig. II.6c,d). The overall shape of garnet 1 fragments shown in Fig. II.6c suggests that they belong to a same, strongly resorbed crystal. Brown biotite (bi1) forms millimetric laths contrasting with smaller (100 μm) crystals of green biotite associated with xenomorphic garnet 1. Smaller euhedral garnets (g2) are spatially associated with garnet 1 (Fig. II.6d). Garnet 2 is almandine- and spessartine-rich ($\text{XMg} = 0.1$, alm57, prp7, grs2, sps35). Fine-grained aggregates of garnet 2, biotite 2, muscovite and sillimanite are common in the matrix (Fig. II.6e,f). Other mica-rich aggregates are mostly composed of muscovite with a discontinuous rim of green biotite 2 and garnet 2 (Fig. II.6g,h).

Interpretation

The isotropic aspect of the rock suggests that a magmatic texture is preserved. The magmatic assemblage was likely quartz-plagioclase-K feldspar-biotite. The highly resorbed garnet 1 is generally not surrounded by a thick corona of biotite typical for garnet retrogression at subsolidus conditions but is rather embedded in quartz. This suggests that it may represent a xenocrystal likely resorbed during the magmatic stage (i.e. during the granite emplacement).

The fine-grained granoblastic aggregates of plagioclase are interpreted as recrystallized magmatic plagioclase. The myrmekite rim and planar aggregates of plagioclase surrounding and cutting across K feldspar also suggests a limited recrystallization. Garnet 2 is associated with biotite 2, around garnet 1 and mica-rich aggregate. The first type is mostly composed of muscovite with a limited amount of biotite 2 and garnet 2. Because muscovite is predominant in these aggregates, they could have formed after a magmatic muscovite. The second type of aggregate is composed of muscovite, biotite 2, garnet 2 and sillimanite and is consequently Al, Fe and Mg-rich and could be a pseudomorphs after cordierite.

It is noteworthy that green biotite associated with muscovite have been reported in the high-pressure metagranite of the Lévézou (Lotout, 2017) and in HP felsic granulites (Nahodilová et al., 2014) where they are interpreted as exsolutions from phengitic muscovite. However, garnet 2 is very rich in spessartine, typical for low P – T conditions garnet and could be reequilibrated after higher-pressure metamorphism. In addition, sillimanite is characteristic for MP-LP and HT metamorphic context and rutile was not observed. The sampled metagranite are probably retrogressed equivalent of the garnet-kyanite-muscovite-biotite bearing metagranite of Arène and Autran (1978), however, this promising assemblage was never observed among the 23 samples. In addition, the observed metamorphic garnets are retrogressed and small as well the inclusions they may contain preventing the use of quartz-in-garnet barometry. Furthermore, the only inferred metamorphic aggregates at the equilibrium is rather poor and contains retrogressed garnet, thus not being a propitious target for a P – T pseudosection investigation. Therefore, I have decided not to pursue this study.

3.2. *The Maures-Tanneron Massifs*

The Maures and Tanneron massifs are Variscan massifs separated by the Permian volcano-sedimentary Esterel massif (Fig. II.7). The Maures massifs is characterized by roughly west-east increasing MP-MT metamorphic gradient (biotite, to kyanite/sillimanite isograds) perpendicular to

the vertical a N-S to NE-SW trending foliation. The higher-grade rocks underwent partial melting to the east. The Tanneron massif is likely an equivalent to the eastern migmatitic Maures massifs. The migmatites host eclogite boudins that are mostly recognized to the East of the Joyeuse fault (JGF in Fig. II.7). The Joyeuse-Grimaud (Maures-Tanneron) and La Moure faults are bounded by carboniferous deposits. In addition, The Joyeuse-Grimaud fault borders the Plan de la tour granite.

In the area, two coronitic metagranitoids were reported, (i) the Barral metagranite (Gueirard, 1976) and (ii) the Tanneron orthogneiss (Crévolat, 1977). In addition, we have sampled one more coronitic metagranite with garnet-kyanite bearing xenolith (Notre Dame de Miramas). I did not find any mention of it in the literature.

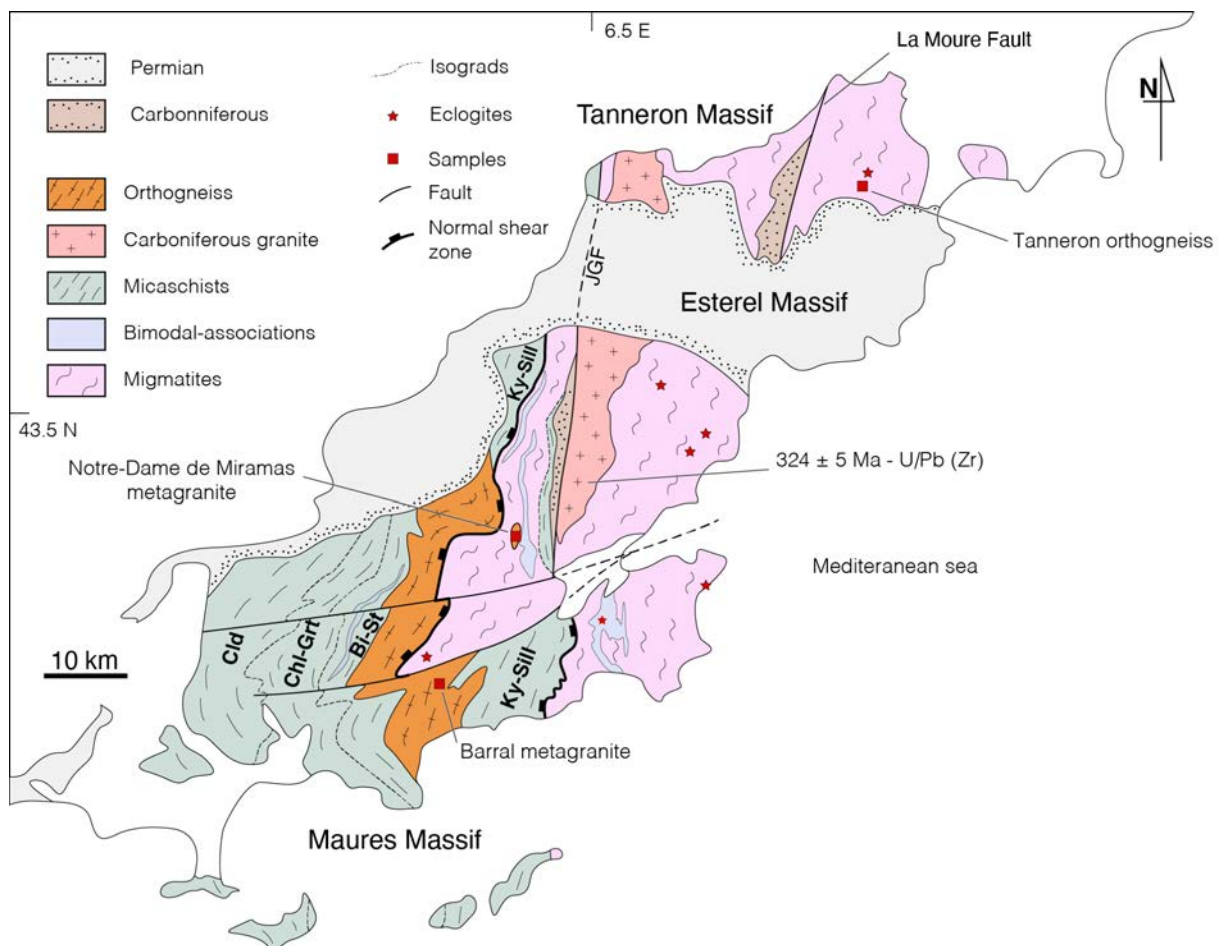


Figure II.7: Structural and metamorphic map of the Maures-Tanneron-Esterel massifs (modified after Schneider et al., 2014, Rolland et al., 2009 and references herein; U/Pb data after Moussavou, 1998).

The Tanneron orthogneiss

The Tanneron orthogneiss is associated with eclogites (Fig. II.7). Undeformed and non migmatitic lenses occur in a variably deformed and migmatized series (Crévoila, 1977). A geochemical study revealed that the undeformed, deformed and migmatized terms of the series evolved independently from an initially homogeneous peraluminous granite (Le Floc'h, comm. pers.). It is inferred by Le Floc'h that heterogeneous deformation lead to focused pathway for fluids and ultimately to localized partial melting.

Petrology of the undeformed Tanneron orthogneiss

The samples display an inherited porphyritic magmatic texture with large crystals of orthopyroxene, K feldspar, plagioclase and quartz (~1-5 mm) in a fine-grained matrix of quartz and plagioclase (~10 μm ; Fig. II.8a). The phenocrysts are rounded to angular and display sharp edges. Graphic intergrowth of quartz and K-feldspar are present (Fig. II.8b). The oscillatory zoning of plagioclase is locally truncated suggesting that the phenocrysts are fragments of originally larger crystals.

The fine-grained quartz-plagioclase matrix displays a granoblastic texture. Orthopyroxene, locally associated with ilmenite, is surrounded by a corona of small sized garnet and quartz (Fig. II.8c). Atolls garnet are also observed around fine-grained biotite-quartz-plagioclase assemblages lacking orthopyroxene. The atoll garnets contain μm sized inclusions of quartz, ilmenite, and biotite (identified using a SEM). Garnet is also present in the core of fine-grained aggregates composed of garnet-muscovite-biotite-quartz-plagioclase and an aluminium silicate (Fig. II.8d). Atoll garnet has the same composition than garnet in the mica-bearing fine-grained aggregate ($\sim\text{XMg} = 0.24$, alm72, prp23, grs2 and sps2).

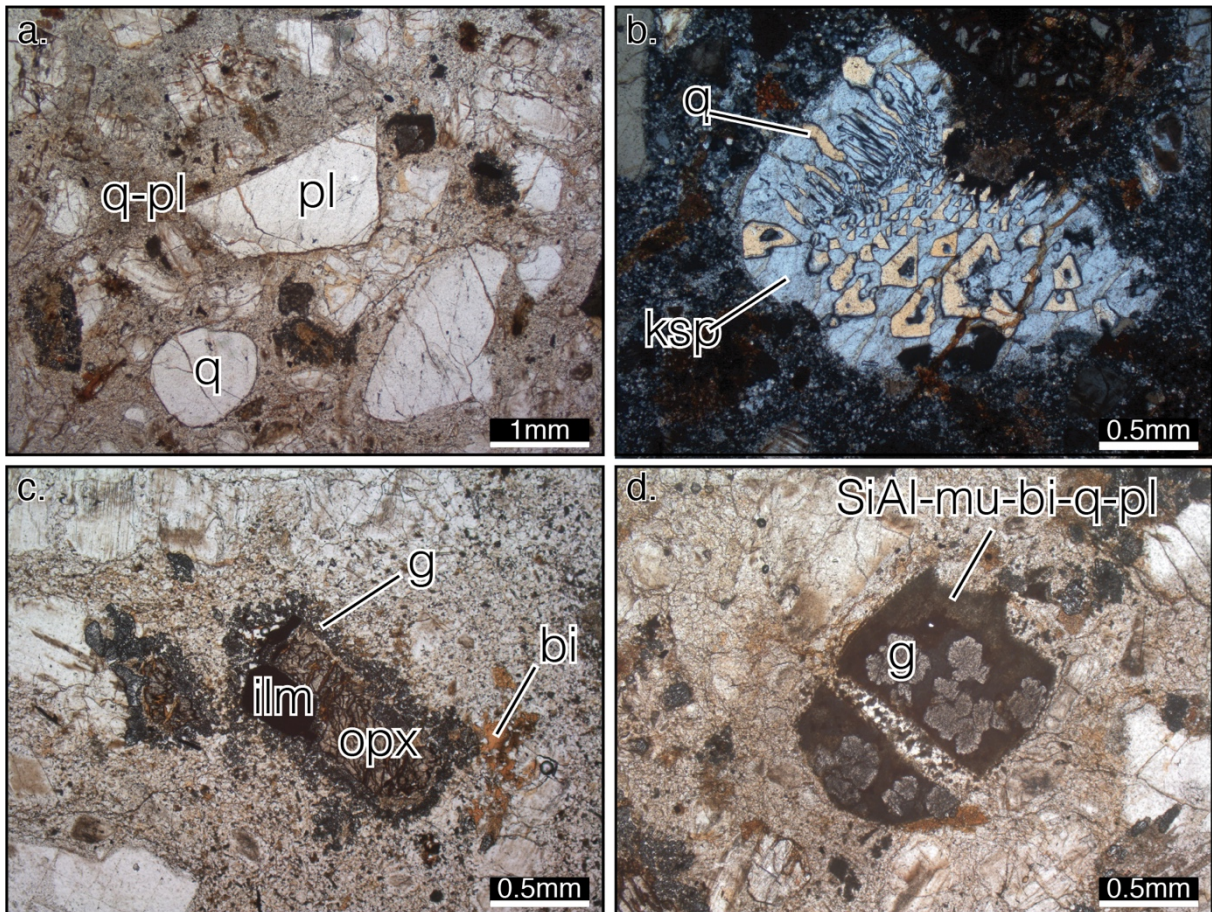


Figure II.8: The samples display a bimodal grain size with large phenocrysts, sometimes broken (pl) in a fine grained granoblastic matrix (a). K-feldspar and quartz graphic intergrowth are present (b). Orthopyroxene is surrounded by a corona of garnet (c). Garnet-bearing fine-grained aggregates are likely pseudomorphs after cordierite (d).

Interpretation

The inferred magmatic assemblage is orthopyroxene-K feldspar-plagioclase-quartz and possibly biotite and cordierite. The bimodal distribution of grain size and the angular (i.e. possibly broken during the rapid ascent of the magma) shape of the phenocrysts indicates a subvolcanic or volcanic setting for the emplacement of the protolith.

The fine-grained granoblastic texture point to a recrystallization of the matrix. The garnet corona around orthopyroxene could point to the destabilization of orthopyroxene during increasing

pressure conditions. The presence of plagioclase included in garnet points to a granulite-facies metamorphism.

The garnet-Al silicate-muscovite-biotite-quartz-plagioclase aggregates may represent pseudomorphs after cordierite. The Aluminium silicate forms thin prisms, but has not been identified and could be either kyanite or sillimanite. Garnet-plagioclase-bearing assemblage also suggest a granulite facies imprint. Garnet is an almandine-pyropite solid solution without significant grossular content suggesting that the anorthite component of plagioclase did not dissolve in garnet suggesting a limited pressure granulitic overprint. In addition, the magmatic plagioclase phenocrysts lack any sign of destabilization and confirm the plagioclase stability during metamorphism.

The garnet-Al silicate-muscovite-biotite-quartz-plagioclase aggregates are likely in local equilibrium and an estimation of P – T conditions could be performed using P – T pseudosection approach. The pressure conditions could also be estimated independently using quartz-in-garnet Raman barometry. I have not undertaken these analyses since the inferred stability of plagioclase precludes equilibration in the eclogite facies, which was what we were looking for.

Barral metagranite

The Barral metagranite outcrops in the south-western Maures. Although the contact cannot be followed continuously, the surrounding orthogneisses appear less deformed toward the contact with the granite. The regional metamorphism is dominated by a Barrovian gradient marked by the progressive appearance of biotite, garnet, staurolite and kyanite/sillimanite from west to east. The presence of garnet-sapphirine-spinel-quartz bearing assemblages typical for granulite facies metamorphism (Gueirard, 1976) in the Barral orthogneiss is thus an anomaly in the regional metamorphism. We wondered whether the granulitic event was predated by a higher-pressure, possibly eclogitic event.

Petrography

The metagranite is isotropic and contains millimetre-sized brown biotite (bi1), K-feldspar, plagioclase, quartz and millimetric garnet- and mica-rich aggregates dispersed in the matrix. In addition, the metagranite displays numerous larger rounded or angular aggregates with various mineralogy (Figure II.9).

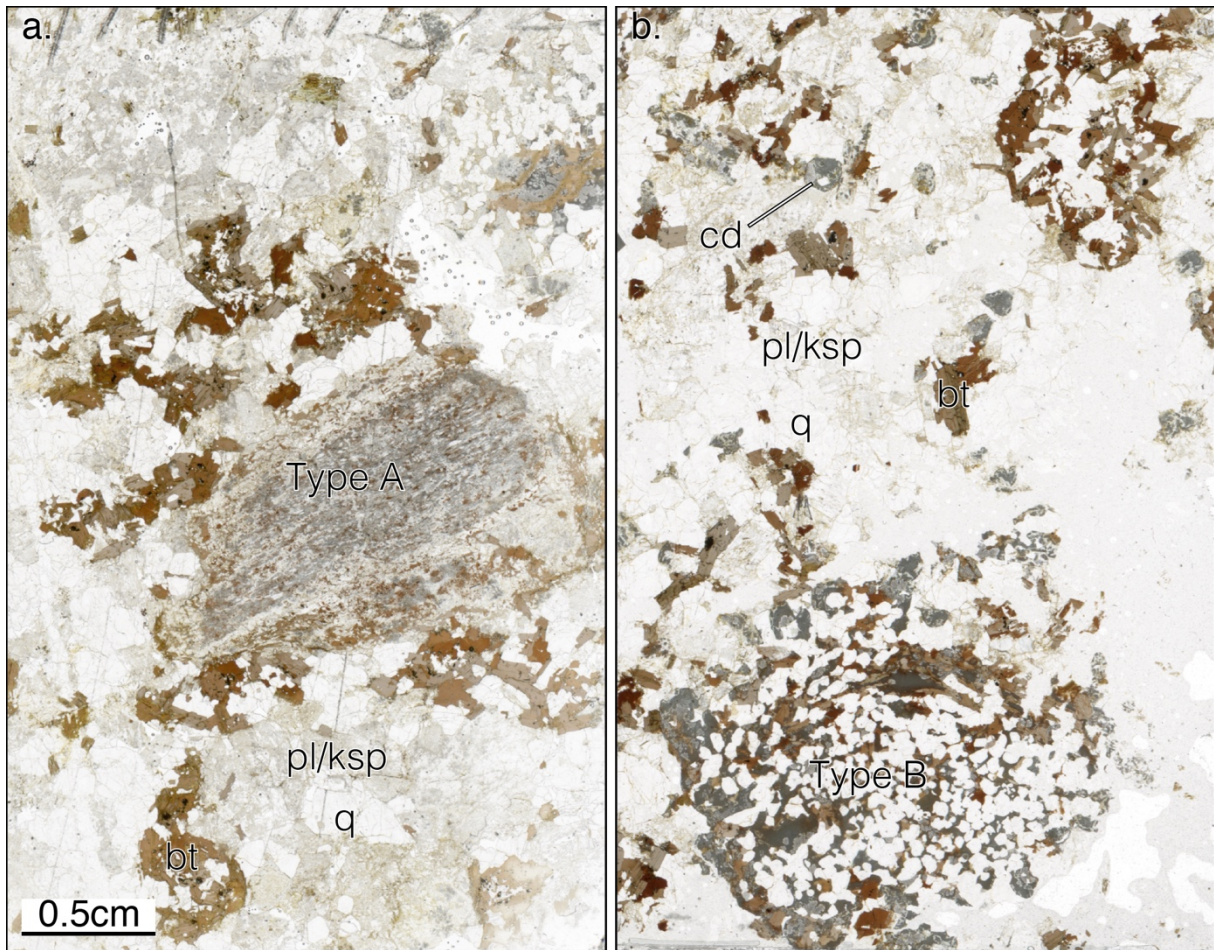


Figure II.9: The samples display a magmatic texture and various mineral aggregates, possibly representing xenoliths: (a) rich in biotite, sillimanite, and garnet or (b) quartz-rich. and minor brown biotite 1 with interstitial fine-grained assemblages of biotite 2-muscovite-plagioclase-aluminium silicate.

In the metagranite itself, plagioclase cores contain variable amounts of fine-grained muscovite, K feldspar and minor green biotite (bi2) (Fig. II.10a,b). When plagioclase is in contact with biotite 1,

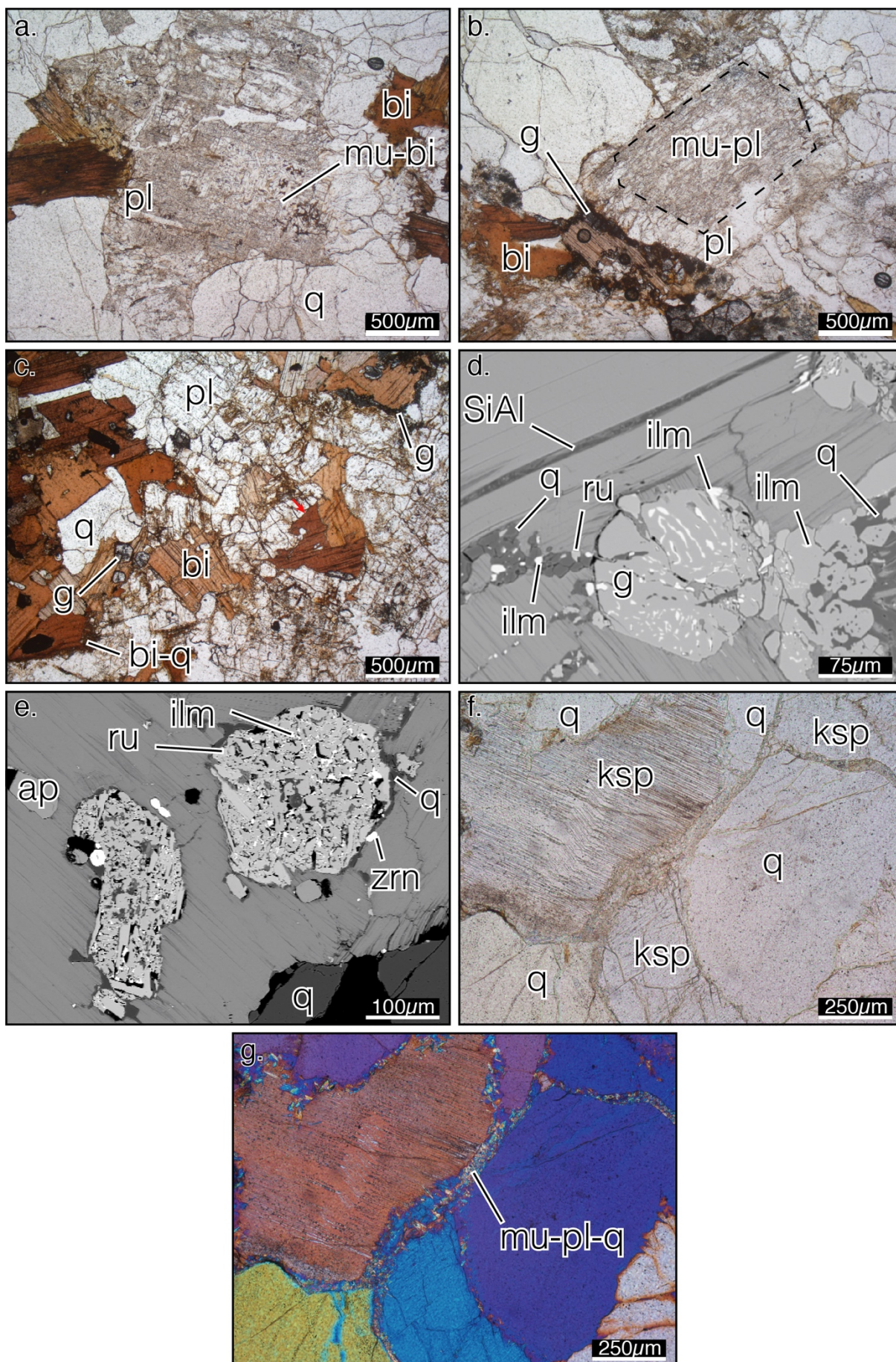
Chapter II

a rim of garnet or fine-intergrowth of quartz and biotite 2 or K-feldspar and ilmenite might be present or the contact may be sharp suggesting local reaction (red arrow in Fig. II.10c). Quartz from the matrix displays sharp contact with plagioclase and with the biotite 1 (Fig. II.10c), though the later is locally marked by chaplets of ilmenite crystals. Biotite 1 contains aggregates of quartz, rutile and ilmenite (Fig. II.10d). Garnet in contact with biotite 1 contains inclusions of ilmenite (Fig. II.10d). Biotite 1 also contains large inclusions of rutile (200 μ m; Fig. II.10e). The contact between rutile and biotite 1 is rimmed by quartz. A fine-grained aggregate of muscovite, plagioclase and quartz is found when quartz and K feldspar are in contact (Fig. II.10f,g).

The matrix contains numerous fine-grained aggregates of muscovite and green biotite 2 (Fig. II.11a). Some of these aggregates have a prismatic shape, and contain garnet (Fig. II.11b). Additionally, they may also contain dark very fine-grained aggregates of aluminium silicates (Fig. II.11c). When these aggregates are in contact with biotite 1, garnet is found at the aggregate/biotite boundary (Fig. II.11c).

The metagranite also displays various mineral aggregates, sometimes having diffuse borders, with strikingly different mineral assemblage. One of these aggregates (type A) displays an angular shape, contains fine-grained (10 to 50 μ m) brown biotite 1-garnet-sillimanite-plagioclase-muscovite (Figure II.12a) and is zoned. The inner zone is characterized by a large amount of sillimanite, biotite and garnet. The outer zone has a larger amount of muscovite.

Figure II.10 (next page): Textures in the Barral metagranite. Plagioclase cores are variously rempaced, mostly by biotite (a, b). Plagioclase in contact with garnet may or may not display garnet coronas (a, b, c). Bioite might have recrystallized in a fine-grained aggregate of biotite and quartz (c). The red arrow in (c) points to a rectilinear contact between biotite and plagioclase. (d) Garnet forming coronas around biotite contains ilmenite. Biotite quartz-ilmenite-rutile aggregates. (e) Biotite contains rutile. The contact between biotite and rutile is punctuated by quartz. A fine-grained aggregate of muscovite-plagioclase-quartz is found between quartz and K feldspar (plane-polarized transmitted light: f; crossed polars with a lambda plate: g).



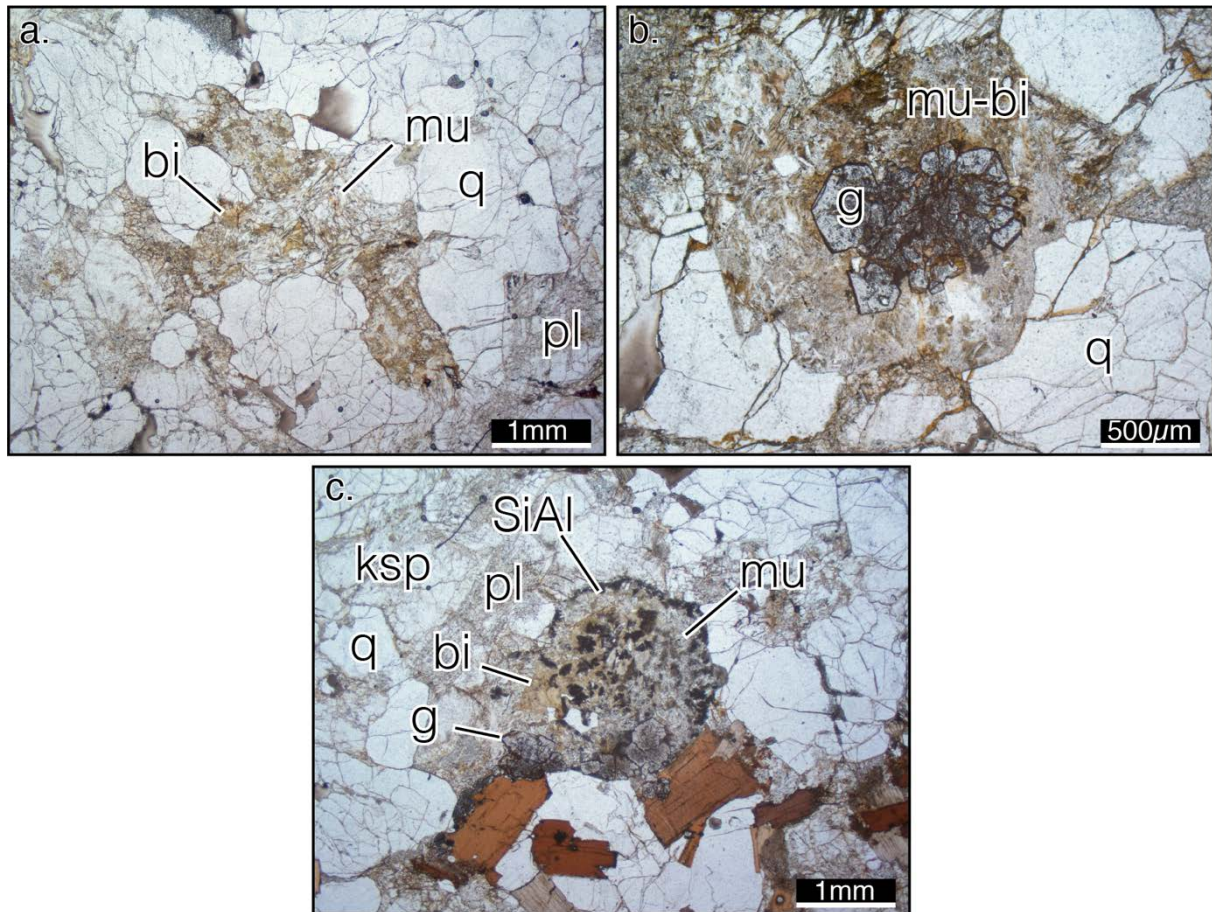


Figure II.11: Fine-grained aggregates of muscovite and biotite (a), with garnet (b) and sillimanite (c).

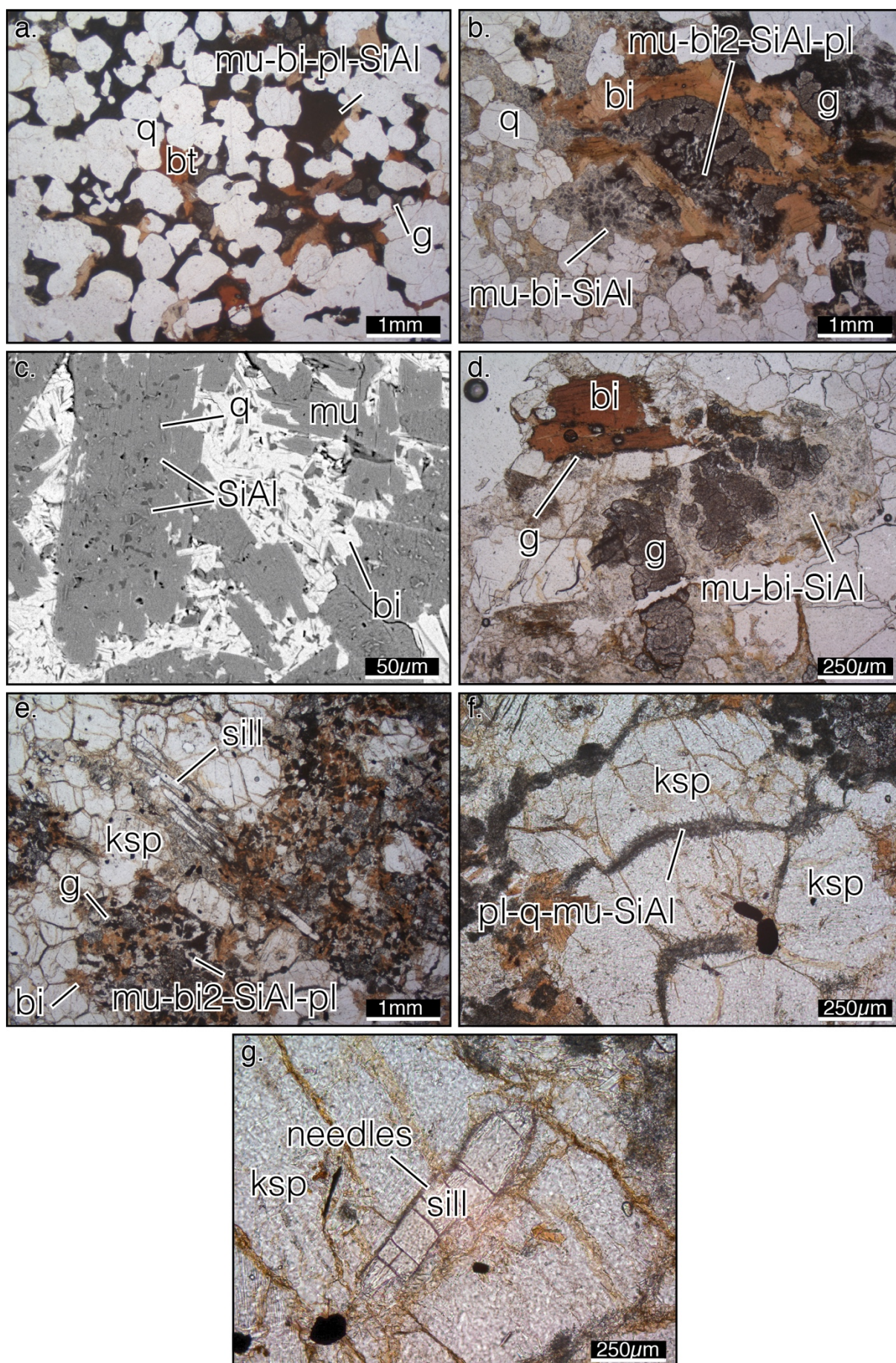
A second type (type B) of aggregate contains abundant quartz and minor brown biotite 1 with interstitial fine-grained (μm) green biotite 2-muscovite-plagioclase-aluminium silicate associated with larger garnet ($100\mu\text{m}$) between quartz crystals (Figure II.12b). Quartz is remarkably rounded and biotite 1 display convex grains boundaries (Fig. II.12a,b). One of these aggregates (Fig. II.12b) is coarser grained, with a large brown xenomorphic crystal of biotite 1 rimmed by garnet aggregates. The inner part of picture in Fig. II.12b composed by biotite 2-muscovite-plagioclase-aluminium silicate. In the quartz rich part, muscovite-biotite 2-aluminium silicate aggregates are interstitial between the rounded quartz. Back scattered electron imaging revealed that the aluminium silicate is included in muscovite that also contains numerous rounded randomly distributed blebs of quartz (Fig.

Chapter II

II.12c). Green biotite 2 is interstitial. A thin corona of garnet around biotite is also present (Fig. II.12d).

A third type (Type C) of aggregate displays strikingly low amounts of quartz and plagioclase and is mostly composed of K feldspar, sillimanite and brown biotite 1 (Fig. II.12e). Biotite 1 is xenomorphic and rimmed by garnet, green biotite 2, muscovite, plagioclase and an aluminium silicate. A fine-grained aggregate of plagioclase, quartz, muscovite and an aluminium silicate is found between K feldspar grains (Fig. II.12f). Sillimanite is rimmed by a fine-grained aggregate of needles with high-relief that could be fibrolitic sillimanite (Fig. II.12g).

Figure II.13 (next page): Photomicrographs of the Barral granite xenoliths. Type B xenolith (a-d) displays rounded quartz with xenomorphic biotite and interstitial muscovite-green biotite-aluminium silicate±plagioclase assemblage (a,b). Muscovite contains numerous inclusions of quartz and aluminium silicate and the green biotite is interstitial (c). These aggregates may contain garnet (d). Type C xenolith (e-f) is composed of K feldspar, sillimanite, and biotite (e). Biotite is replaced by an assemblage of muscovite, green biotite, aluminium silicate and plagioclase. An assemblage of plagioclase, quartz, muscovite and aluminium silicate forms between K feldspar crystals (f). Prismatic sillimanite is rimmed by needles of fibrolitic sillimanite? (g).



Preliminary thoughts

An intriguing feature of the samples is the prominent HT character of the mineral assemblages (commonly sillimanite-bearing) and textures that could result from partial melting.

The type A aggregate (biotite 1-garnet-sillimanite-plagioclase-muscovite) is mostly composed of Al-Fe-Mg bearing minerals. In addition, the angular shape of the aggregate and the significantly finer grain size compared to the matrix suggest that this aggregate is a xenolith.

The type B aggregate is characterized by abundant anhedral quartz and minor brown biotite 1 with convex edges, with an interstitial fine-grained (μm) aggregate of green biotite 2-muscovite-plagioclase-aluminium silicate with cusped shapes at the junction of quartz grains, typical for migmatite textures (e.g. Holness and Sawyer, 2008). Accordingly, the intercrystalline space is expected to have been filled by a melt.

The Type C aggregate is composed of K feldspar, sillimanite and brown biotite 1 associated with garnet and thin-grained aggregates of muscovite, green biotite 2, an aluminium silicate and plagioclase. The later aggregate is mostly composed of K, Al, Fe, Mg and Ti-rich assemblage interpreted as replacing former biotite. Accordingly, the former assemblage would have been K-feldspar, sillimanite and biotite. Such an assemblage can be produced in a quartz-, muscovite-, plagioclase-bearing protolith by the reaction $\text{mu} + \text{q} + \text{pl} = \text{kfs} + \text{als} + \text{bi} + \text{melt}$ (e.g. Clemens and Vielzeuf, 1987). Accordingly, the K feldspar, biotite and aluminium silicate aggregate are interpreted as a melt depleted residuum xenolith.

The host metagranite also displays many replacement textures. One of these textures replaces prismatic crystals and is composed of garnet-muscovite-green biotite 2-aluminium silicate. The prismatic shape points to a pseudomorph. The high Al, Fe, Mg content of the assemblage suggests it could be a pseudomorph after cordierite as proposed by Gueirard (1976).

Chapter II

In my opinion, the key to understand that processes during the replacement are the interstitial assemblage of muscovite, plagioclase and aluminium silicate between quartz and K feldspar. The textures resemble partial melt films between pre-existing crystals. However, incongruent melting is expected to produce a melt and anhydrous minerals products. Accordingly, this texture is best interpreted in terms of hydration in the stability field of muscovite.

In this framework, it is possible to understand the heterogeneous development of garnet corona around biotite. Garnet between plagioclase and biotite is a reactional texture. The heterogeneous development of these textures suggests that a catalyser was needed for the reaction to happen, but not readily available. Such a catalyser could be an aqueous fluid that would be heterogeneously distributed. It remains that garnet corona around biotite suggest a high-grade metamorphism. The question is: did this metamorphism happened at high pressure?

The observation of ilmenite in garnet in contact with biotite suggests that pressure was limited. Rutile, that is expected at high-pressure is observed in two textural positions. Large (150µm) crystals included in biotite, rather than along biotite edge suggest that rutile was already present when biotite crystallized. Rutile also occurs in quartz aggregates associated with ilmenite in biotite. The apparent co-stability of rutile and ilmenite also suggest that pressure was limited.

P–T pseudosection modelling

In order to constrain the equilibration conditions of the widespread muscovite-green biotite 2-aluminium silicate±garnet±plagioclase assemblages, *P–T* pseudosections have been calculated for the SEM-measured bulk composition of two aggregates of muscovite-green biotite 2-aluminium silicate±garnet±plagioclase to constrain the *P–T* conditions of the formation of these fine-grained aggregates. For the *P–T* pseudosection, I used the SEM measured bulk composition of two aggregates without plagioclase but one having garnet and the other without garnet. For the garnet bearing aggregate, the observed assemblage is modelled in the field g-bi-mu-q between 600-675 °C and 4-7

kbar. This field is encompassed in the modelled P – T conditions of the observed assemblage of the garnet-free aggregate (570–750°C and 3–8.5 kbar). Thus, the aggregate records a low to intermediate pressure and moderate-temperature metamorphism rather than a HP metamorphism. The presence of garnet corona may indicate a higher temperature and possible pressure event but these local equilibrium textures are hard to study using P – T pseudosections.

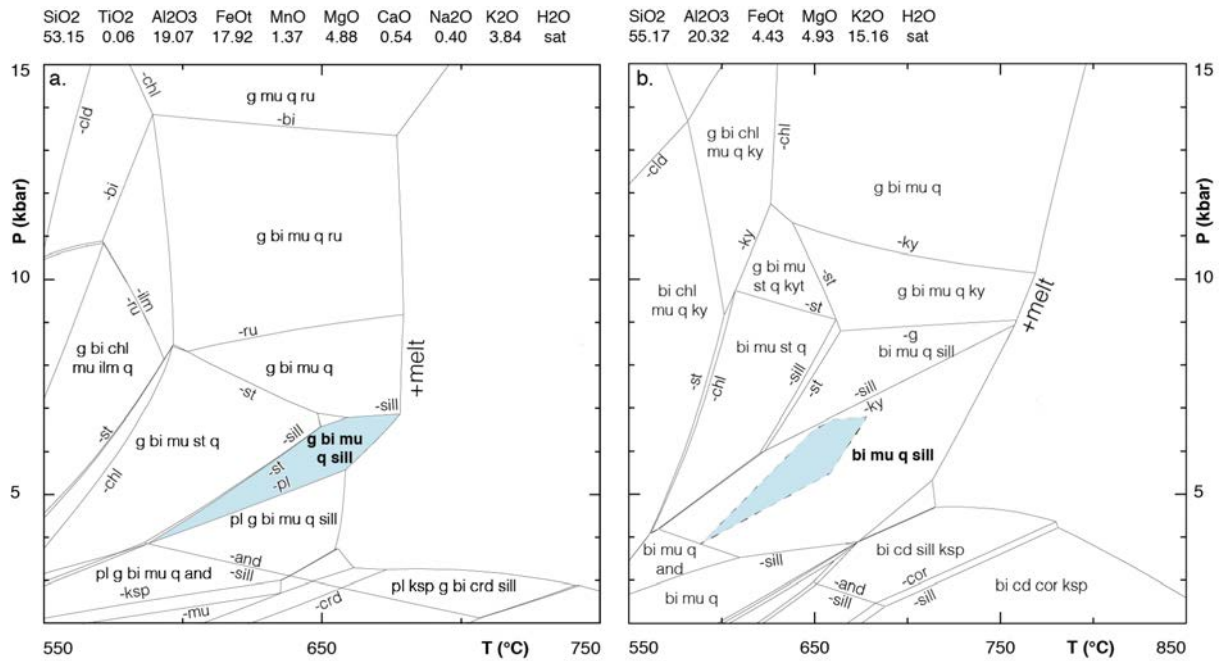


Figure II.14: *P-T pseudosections (H₂O-saturated) for the bulk composition of the muscovite-biotite 2-quartz-aluminium silicate aggregates, with garnet (a) and without garnet (b). Note that the temperature scales are different.*

Petrological investigations of the Notre-Dame de Miramas metagranite

The metagranite was found in the western Maures Massif that display a MP-MT metamorphic gradient. The metagranite outcrops as lenses in a deformed orthogneiss. The metamorphic rocks associated with the orthogneiss lack evidence of HP metamorphism, but the sampled metagranite displays biotite-rich aggregates with a significant amount of kyanite and garnet. Since kyanite and garnet are commonly associated in high-pressure conditions, we studied the metagranite in more detail.

Petrography

In less deformed facies, the magmatic porphyric texture is preserved with numerous angular biotite-rich aggregates. The magmatic assemblage comprises quartz, plagioclase, K-feldspar, and biotite (Fig. II.9).

Under the microscope, quartz and biotite are the largest crystals (up to 1mm) and plagioclase forms 10µm aggregates with a granoblastic texture. A garnet corona is locally observed around biotite. A few kyanite crystals are dispersed in the granoblastic aggregates of plagioclase. The biotite-rich aggregates are the most interesting feature of this rock. They are composed of biotite (~18%), garnet (~19%), kyanite (~30%), plagioclase (~25%) as well as minor quartz (~3%), ilmenite and blue tourmaline, possibly dravite-rich (Fig. II.9). Garnet contains numerous needles of kyanite and minor biotite and quartz (Fig. II.9). All crystals display straight edges suggesting that they are at the equilibrium. Garnet is unzoned and dominantly almandine-pyrope ($X_{Mg} = 0.13$; alm75; prp12; grs3; sps1).

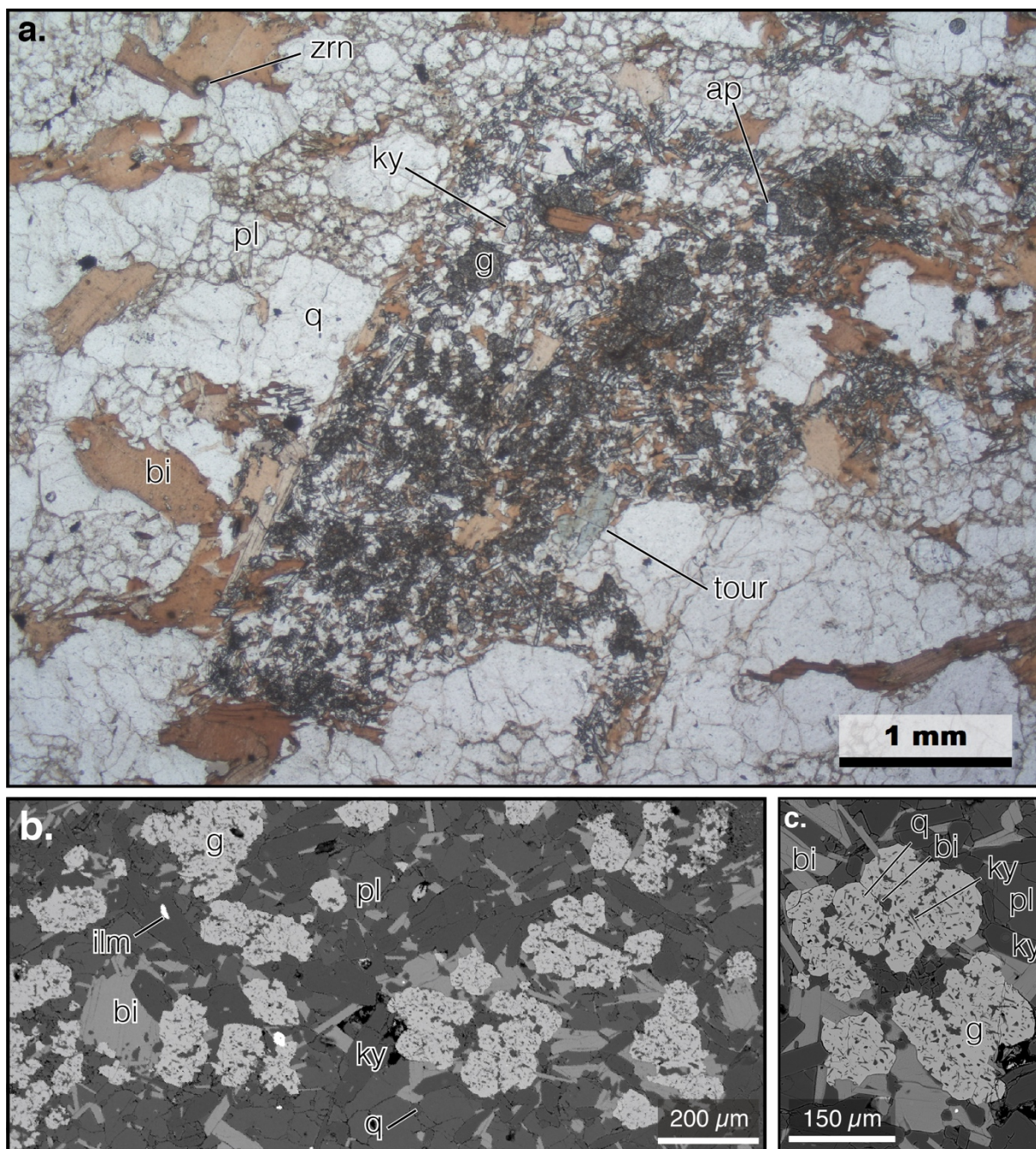
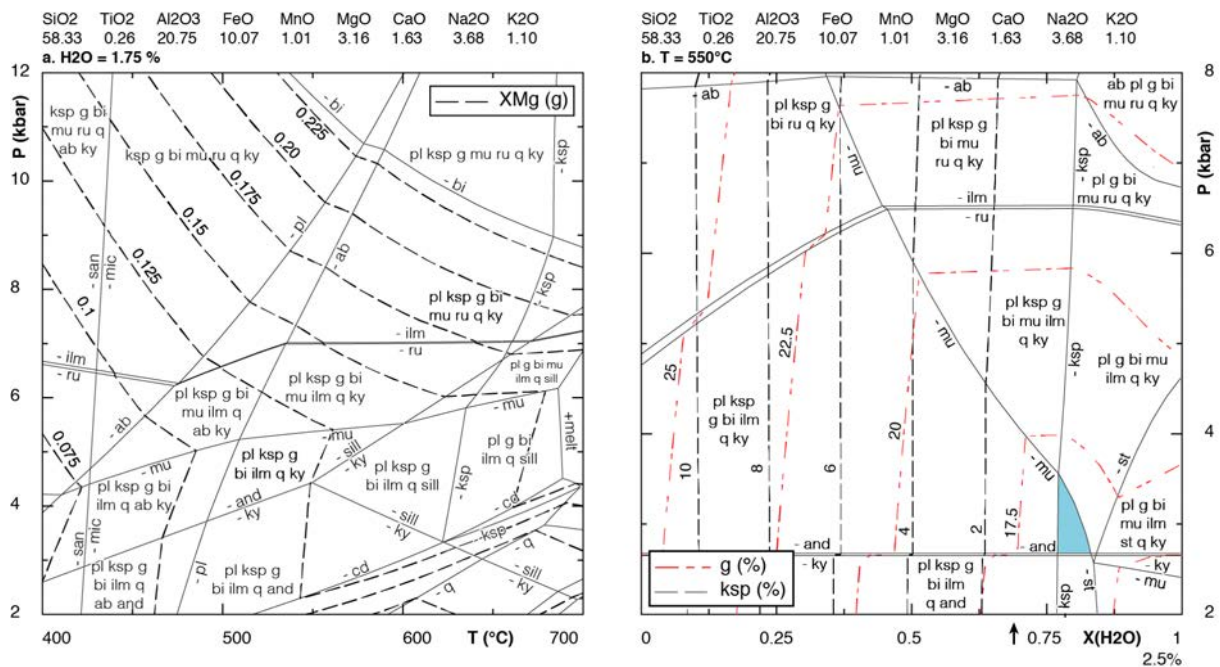


Figure II.15: Photomicrograph (a) and BSE images (b) of a kyanite-garnet bearing xenolith, commonly containing blue dravitic tourmaline (tour). Garnet contains numerous inclusions of kyanite and minor inclusions of quartz and biotite.

P–T pseudosection

A *P–T* pseudosection has been calculated for the bulk composition of the garnet-kyanite-plagioclase-biotite-ilmenite-quartz aggregate (Fig. II.16a). The abundance of Al- and Fe-rich minerals suggests a metapelitic origin. The fine-grained character of the aggregate and the fact that

biotite is the only H₂O-bearing mineral suggest a low H₂O content. Therefore, the P – T pseudosection was calculated with a limited amount of H₂O (arbitrarily set at 1.75 mol%) between 2–12 kbar and 400–700°C and contoured with isopleth for XMg of garnet. In the P – T diagram, the observed assemblage (pl-g-bi-ilms-q-ky) is not modelled but the closest assemblage is modelled by the field labelled pl-ksp-g-bi-ilms-q-ky between 3–5 kbar 500–600°C. The XMg isopleth corresponding to the observed composition of garnet (XMg = 0.13) intersect this field around 550°C. K-feldspar content may be dependent on the H₂O content. Hence, a P – $X(\text{H}_2\text{O})$ pseudosection (Fig. II.16b) was calculated for $T = 550^\circ\text{C}$ and contoured with modal isopleths for garnet and K-feldspar in order to assess the effect of varying H₂O content on mineral assemblages and mode. The mode of K-feldspar but also muscovite is strongly dependent of the H₂O content. The observed ksp- and mu-absent assemblage (pl-g-bi-ilms-q-ky) is modelled the light blue field at a slightly higher water content and pressures of ~3 kbar.



Chapter II

Figure II.16 (previous page): P–T pseudosection (a) and P–X(H₂O) pseudosection for the bulk composition of the xenolith. The P–T pseudosection is contoured with XMg isopleths for garnet. The light blue field in the P–X (H₂O) pseudosection corresponds to the observed assemblage (pl-g-bi-ilm-q-ky).

Interpretation

The angular shape of the biotite-rich aggregate suggests that it could be a xenolith. This interpretation is further supported by the Al- and Fe-rich bulk composition. The abundance of anhydrous minerals indicates that the xenolith was dehydrated. It could represent a “residuum” or a country rock that underwent contact metamorphism and was sampled during the ascent of the pluton. The metamorphic character of the xenolith could result either from the thermal event that led to the granite emplacement only, or could also be affected by a later metamorphic overprint. The granoblastic texture of plagioclase in the granite and the few garnet coronas around biotite suggest that the granite also underwent a metamorphism and better support the second hypothesis. Thus, both the xenolith and the metagranite underwent a low to intermediate pressure and relatively high-temperature metamorphism and indicate that the Notre-Dame de Miramas is not a suitable candidate for our study.

3.3. Haut-Allier

The Saint Didier-sur-Doulon orthogneiss was sampled in the leptyno-amphibolitic complex (Fig. II.3), initially defined by Forestier (1961) as an association of felsic, mafic and ultramafic rocks. Relics of HP metamorphism within this complex were first reported by Marchand (1974) and Lasnier (1977).

Saint Didier-sur-Doulon orthogneiss

The orthogneiss outcrops as a decametric lens in migmatites. A strain gradient is visible across the lens. The inner part is an augen orthogneiss with centimeter sized K feldspar porphyroclasts in a fine-grained matrix (<1 mm) of quartz, plagioclase and biotite. The orthogneiss contains fine-grained

Chapter II

biotite aggregates with diffuse borders. A poorly-defined foliation is marked by the alignment of biotite and elongated polycrystalline aggregates of plagioclase. Toward the outer part of the lens the rock is darker and contains more biotite. The grain size is similar; but the fabric is stronger. The foliation marked by the alternation of biotite and plagioclase-rich layers and wraps around oval-shaped, strongly flattened polycrystalline aggregates of K-feldspar. The foliation is parallel to the fabric in the surrounding migmatites.

Petrography

Under the microscope, the less deformed facies contain garnet, plagioclase, biotite, quartz, K-feldspar and minor zircon and ilmenite. Plagioclase always displays a granoblastic texture with a few disseminated biotite crystals (Fig. II.17a). Quartz forms elongated lenses. Garnet is abundant. Figure II.17a shows a biotite-quartz-plagioclase aggregate surrounded by a discontinuous corona of garnet. The core of the aggregate is composed of fine-grained (20 μ m) aggregate of biotite and quartz with a granoblastic texture. Small biotite crystals display a fabric perpendicular to the elongation of the aggregate. The size of quartz and biotite crystals in the aggregate increases (up to 250 μ m) toward the matrix. Garnet is found between biotite of the aggregate and plagioclase of the matrix. Figure II.17c shows that the garnet corona interrupts when biotite is in contact with quartz. Another peculiar feature of the sample is a biotite rich aggregate with diffuse borders. It is composed of biotite, garnet, plagioclase and quartz. The fabric in the aggregate is marked by the preferential orientation of biotite. The fabric is parallel with the fabric of the host orthogneiss.

The outer part of the lens displays a very small amount of xenomorphic garnet disseminated in the rock. A layering is marked by the alternation of plagioclase, quartz-biotite-plagioclase and microcline-rich layers. Rare xenomorphic crystals of orthoclase are surrounded by a corona of microcline and plagioclase without biotite.

Interpretation

The first order observation is that garnet is found between biotite and plagioclase. The garnet-plagioclase and garnet-biotite contact are straight, suggesting that an equilibrium was achieved. In addition, biotite-quartz and plagioclase aggregates display a granoblastic texture, suggesting an equilibrium recrystallisation. In the biotite-rich aggregate, garnet, plagioclase, biotite and quartz appear homogeneously distributed.

In more detail, the biotite-quartz aggregates surrounded by a corona are intriguing. Though always in contact with biotite the garnet corona does not form around a single crystal of biotite but a polymineral aggregate, therefore, the biotite and quartz aggregate could be a pseudomorph, possibly after orthopyroxene.

The presence of garnet in the inner lens (i.e. less deformed facies) and its scarcity in the outer lens (well deformed orthogneiss) where the deformation is stronger and the fabric parallel with the fabric of the host layering indicates that the fabric overprints the granulitic assemblage. This fabric of the migmatite is marked by high temperature and low-pressure assemblage (sillimanite bearing; Burg, 1977) suggesting that the deformation occurred during a decompression.

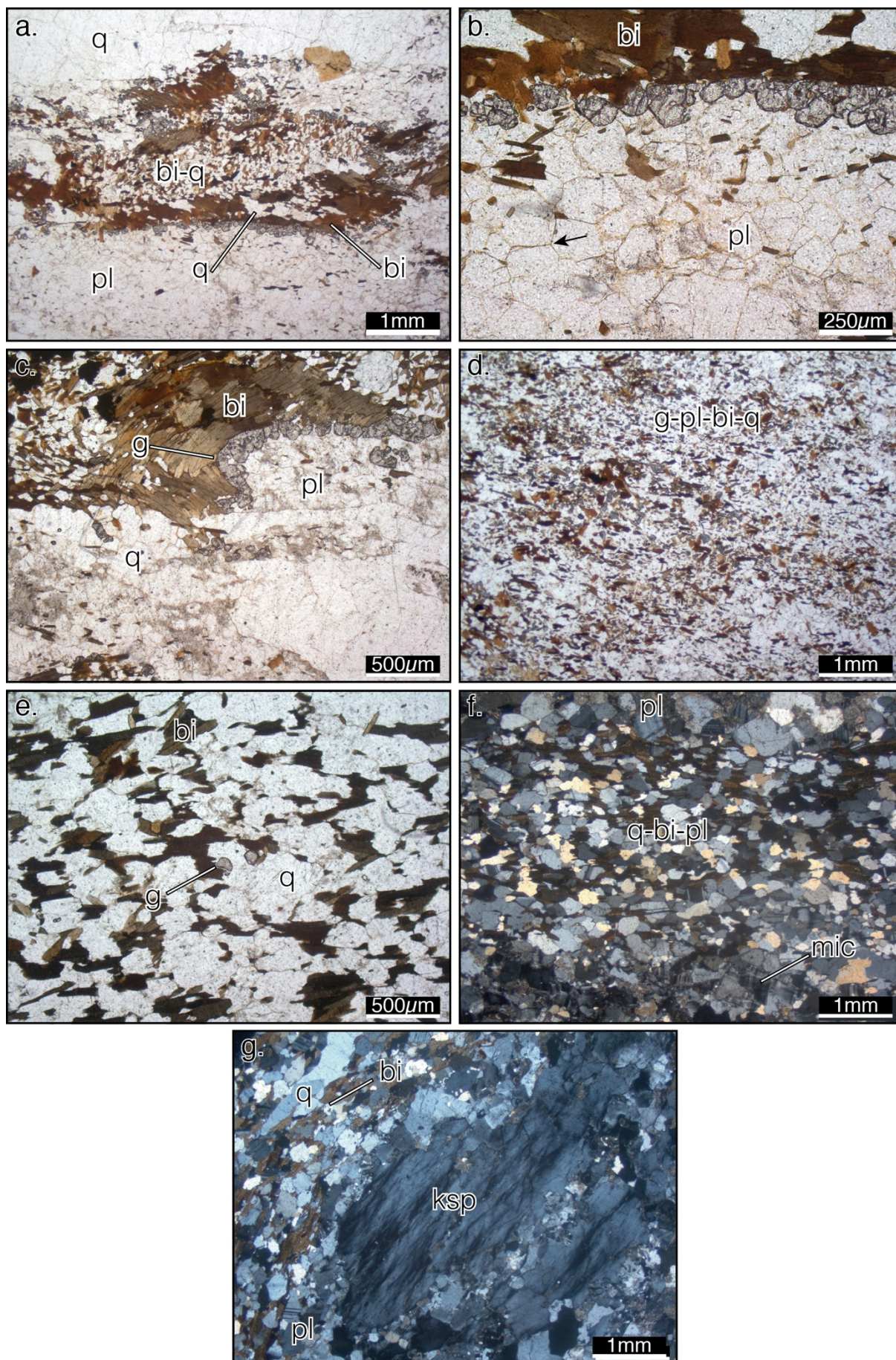


Figure II.17: Photomicrographs of the inner (a-d) and the outer (e-g) part of the lens. (a) Garnet corona forms around biotite-quartz aggregates, commonly at the contact with plagioclase. Garnet displays sharp contacts with both biotite and plagioclase (b). The corona interrupts when biotite is in contact with quartz (c). The biotite-rich aggregate (most likely a xenolith; d). In the outer part of the lens, garnet is anhedral and resorbed (e). A layering is marked by the alternation of plagioclase, biotite-quartz-plagioclase and plagioclase microcline rich layers (f). Orthoclase porphyroclasts are xenomorphic and surrounded by a corona of mostly microcline with minor plagioclase and quartz.

4. Discussion and implications of the petrological study of the metagranites

Among the five metagranites and orthogneiss studied, three are spatially associated with eclogites (Thaurion, Haut-Allier, Tanneron). However, in all studied samples, garnet appears in equilibrium with plagioclase, suggesting that they equilibrated in the granulite facies that encompasses a wide range of pressure conditions. A proper estimation of the P – T conditions has only been possible in the Notre Dame de Miramas metagranite (Maures massif), and pointed to low-pressure recrystallisation. However, as a perspective, the study of the pressure during garnet crystallization could be carried out if quartz is included in garnet by quartz-in-garnet Raman barometry (e.g. Ashley et al., 2014).

In the Thaurion and Barral metagranites, the presence of interstitial green biotite between muscovite crystals suggest that biotite crystallized after muscovite. Similar green biotite has been shown to result from the destabilization of muscovite during decompression from HP granulite (Nahodilová et al., 2014) therefore, the observed assemblage could result from a decompression from HP conditions. This is further suggested in the Limousin (Thaurion) by the presence of kyanite (but not observed in this study) reported by Arène and Autran (1987).

Coronitic textures may be different from one sample to another. In the Tanneron massif, garnet coronas develop around the orthopyroxene. In the Haut-Allier, the contact between biotite and garnet

Chapter II

is straight suggesting that biotite recrystallized during a continuous reaction producing garnet. In the Barral metagranite, biotite is xenomorphic suggesting that biotite did not recrystallized and was out of the equilibrium.

In the Barral, Notre Dame de Miramas and Haut-Allier metagranites, a metamorphism is also recorded by biotite-rich aggregates interpreted as xenoliths. In the Notre Dame de Miramas, and the Haut-Allier metagranite, the xenoliths were probably metamorphosed together with the granite. On the other hand, in the Barral metagranite, the metamorphism recorded by the various xenolith may represent a metamorphism prior to the emplacement of the granite. In the Barral metagranite, and Tanneron Massif, some metamorphic aggregates are arguably pseudomorphs after cordierite. Several authors also inferred that metamorphic assemblages develop preferentially in the vicinity of cordierite. (e.g. Gueirard, 1976; Arène and Autran, 1987; Godard, 2009; Lotout, 2017). Therefore, the initial composition of the magmatic protolith as well as the abundance and composition of its enclaves are key factors for the record of metamorphism in granitoid rocks. Barbarin (1999) suggested that every granite is susceptible to contain some enclaves, independently of its composition and tectonic emplacement setting. Such enclaves are expected to be dehydrated and could be unreactive with respect to a metamorphism after the cooling of the granite. The situation is different in peraluminous granites, which may contain cordierite absent in the other types of granites. As discussed above, cordierite appears much more reactive. Therefore, if I should start a similar study elsewhere, in addition to a synthesis of the mineralogical indicators, I would start by a synthesis of the geochemical data of the orthogneiss in order to identify the peraluminous cordierite-bearing granites.

I figured out that several metagranitoid examples from the literature derive from granodioritic protoliths (e.g. Monte Mucrone, Italian Alps, Compagnoni and Mafféo, 1973; Farinole, Corsican Alps, Lahondere, 1988; Malpica-Tuy, Spanish Variscan belt, Gil Ibarguchi, 1995; Brossasco-Isasca metagranite, Italian Alps, Bruno et al., 2001; Vibal orthogneiss, French Variscan belt, Burg and

Chapter II

Leyreloup, 1989). In these types of rocks, some K and/or Na are fixed by hydrated minerals like amphibole and micas rather than anhydrous K feldspar. An elegant explanation to the notable absence of metamorphism in granite is provided by Proyer (2003) who argues that plagioclase and biotite breakdown into zoisite and phengite bearing assemblage respectively are water consuming reactions. In the absence of water, the metamorphism is not recorded. Because granodiorite may contain more hydrated minerals, a possible explanation would be that the breakdown of these crystals could lead to higher free water content that could help the metamorphic reactions to proceed (Fig. II.18). This requires to be tested.

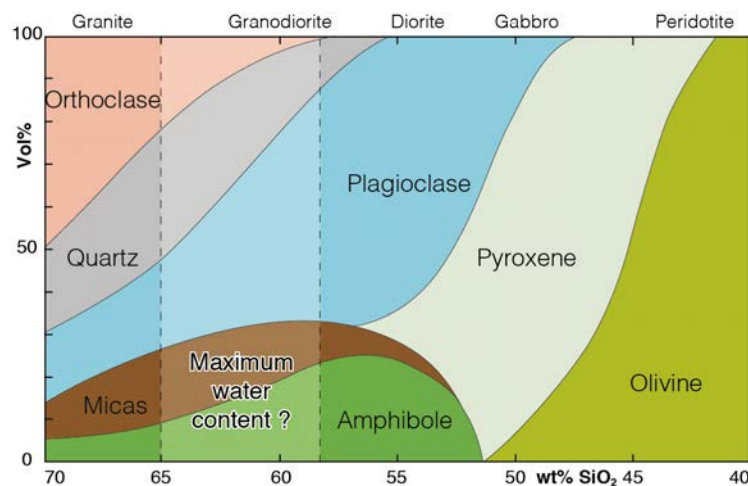


Fig. II.18: Mineralogical classification of igneous rocks as a function of the SiO₂ content.

Finally, it is noteworthy that only the undeformed (or weakly deformed) facies preserve the early metamorphic record. In the Haut-Allier, the transition between the undeformed and the deformed facies is visible, and there is no doubt that the weakly deformed and strongly deformed orthogneiss derive from a similar protolith. The xenomorphic shape of garnets in the most deformed orthogneiss suggest that the deformation postdates the metamorphism and is characterized by lower-grade metamorphic assemblages. This conclusion is consistent with the results of Burg and Leyreloup (1989) in the Vibal metagranite (Lévézou complex, Massif Central), where the granulite facies

Chapter II

orthogneiss, associated with eclogites is surrounded by deformed and migmatitic gneisses characterized by sillimanite assemblage. The best descriptive example is given by Lasnier (1973) in the La Picheraie granulite (Champtoceaux complex, Armorican massif) where garnet coronas around biotite are increasingly dispersed in the matrix with increasing strain, and finally disappear. This means that the orthogneisses always preferentially record retrograde (commonly amphibolite-facies) metamorphism. Only undeformed metagranite septa may preserve traces of the earlier higher-grade, and particularly higher-pressure metamorphic history.

Petrologic study of metapelites from the Variscan Pyrenees

**Two-stage Variscan metamorphism in the Canigou massif: evidence
for crustal thickening in the Pyrenees**

(Published in Journal of Metamorphic Geology)

Luc de Hoÿm de Marien¹, Benjamin Le Bayon², Pavel Pitra^{1,3}, Jean Van Den Driessche¹, Marc
Poujol¹ and Florence Cagnard²

¹Univ Rennes, CNRS, Géosciences Rennes - UMR 6118, F-35000 Rennes, France

²Bureau de Recherches Géologiques et Minières – BRGM – 3 avenue Claude Guillemin, BP 36009,
45060 Orléans cedex 2, France

³Česká geologická služba, CZ-118 21 Prague 1, Czech Republic

Corresponding author: luc.dehoym@gmail.com

Running title: *Variscan two-stage metamorphism, Pyrenees*

Key words: Variscan Pyrenees, Barrovian metamorphism, pseudosections, polyphase *P–T* path,
crustal thickening

Abstract

The Variscan metamorphism in the Pyrenees is dominantly of the low-pressure–high-temperature (LP–HT) type. The relics of an earlier, Barrovian-type, metamorphism that could be related to orogenic crustal thickening are unclear and insufficiently constrained. A microstructural and petrological study of micaschists underlying an Ordovician augen orthogneiss in the core of the Canigou massif (Eastern Pyrenees, France) reveal the presence of two syntectonic metamorphic stages characterized by the crystallization of staurolite (M1) and andalusite (M2), respectively. Garnet is stable during the two metamorphic stages with a period of resorption between M1 and M2. The metamorphic assemblages M1 and M2 record similar peak temperatures of 580 °C at different pressure conditions of 5.5 kbar and 3 kbar, respectively. Using chemical zoning of garnet and calculated P – T pseudosections, a prograde P – T path is constrained with a peak pressure at ~6.5 kbar and 550 °C. This P – T path, syntectonic with respect to the first foliation S1, corresponds to a cold gradient (of ~9 °C/km), suggestive of crustal thickening. Resorption of garnet between M1 and M2 can be interpreted either in terms of a simple clockwise P – T path or a polymetamorphic two stage evolution. We argue in favour of the later, where the medium-pressure (Barrovian) metamorphism is followed by a period of significant erosion and crustal thinning leading to decompression and cooling. Subsequent advection of heat, probably from the mantle, lead to a new increase in temperature, coeval with the development of the main regional fabric S2.

LA-ICP-MS U-Th-Pb dating of monazite yields a well-defined date at c. 300 Ma. Petrological evidence indicates that monazite crystallization took place close to the M1 peak-pressure conditions. However, the similarity between this age and that of the extensive magmatic event well documented in the eastern Pyrenees suggests that it probably corresponds to the age of monazite recrystallization during the M2 LP–HT event.

1. Introduction

Late low-pressure–high-temperature (LP–HT) metamorphism occurs in most orogens resulting from continental convergence, such as the European Variscan belt. This metamorphism is generally preceded by a higher-pressure metamorphic evolution, commonly of the Barrovian type, typically associated with crustal thickening responsible for a higher heat production (e.g. England & Thompson, 1984). The subsequent horizontal ductile flow of the thermally relaxed thickened crust induces thinning and triggers the onset of exhumation processes and the associated LP–HT metamorphism.

The Variscan basement of the so-called Axial Zone of the Pyrenees (Figure 1a), is characterized by such a late pervasive LP–HT metamorphism. This metamorphism develops in gneissic to migmatitic dome-shaped structures that refold an initial flat-lying foliation, whereas a steeply dipping cleavage affects the overlying low-grade metamorphic rocks (De Sitter & Zwart, 1960; Zwart, 1979). This vertical metamorphic and structural zonation led to contrasting interpretations ranging from transpressional to transtensional tectonics, including deformation partitioning between the lower and the upper crust (see Carreras & Capella, 1994; Cochelin, Chardon, Denèle, Gumiaux, & Le Bayon, 2017). Whatever their differences, most of these tectonic models imply an early crustal thickening. Previous petrological studies have documented or invoked an early medium-pressure (MP) metamorphism interpreted as the record of this crustal thickening (Aguilar et al., 2015; Mezger, Passchier, & Régnier, 2004; Vilà, Pin, Liesa, & Enrique, 2007). However, a syntectonic prograde up-pressure P – T path that typifies crustal thickening has not yet been documented.

In the Canigou massif (Figure 1b), a previous petrological study of garnet-staurolite-andalusite bearing micaschists has interpreted garnet prograde growth zoning and andalusite crystallization after staurolite as the results of a prograde LP–HT metamorphism (Gibson, 1992). The subsequent

discovery of kyanite associated with garnet and staurolite suggested that these porphyroblasts belonged to an earlier, higher-pressure, event (Azambre & Guitard, 2001).

In order to document the early metamorphic and structural events that affected the Variscan basement in the Pyrenees, we reinvestigate the garnet-staurolite-andalusite bearing micaschists from the Canigou using a microstructural and pseudosection-based petrological approach. Our results reveal unequivocal evidence of crustal thickening and allow to discuss the subsequent exhumation and thermal evolution of these previously buried rocks.

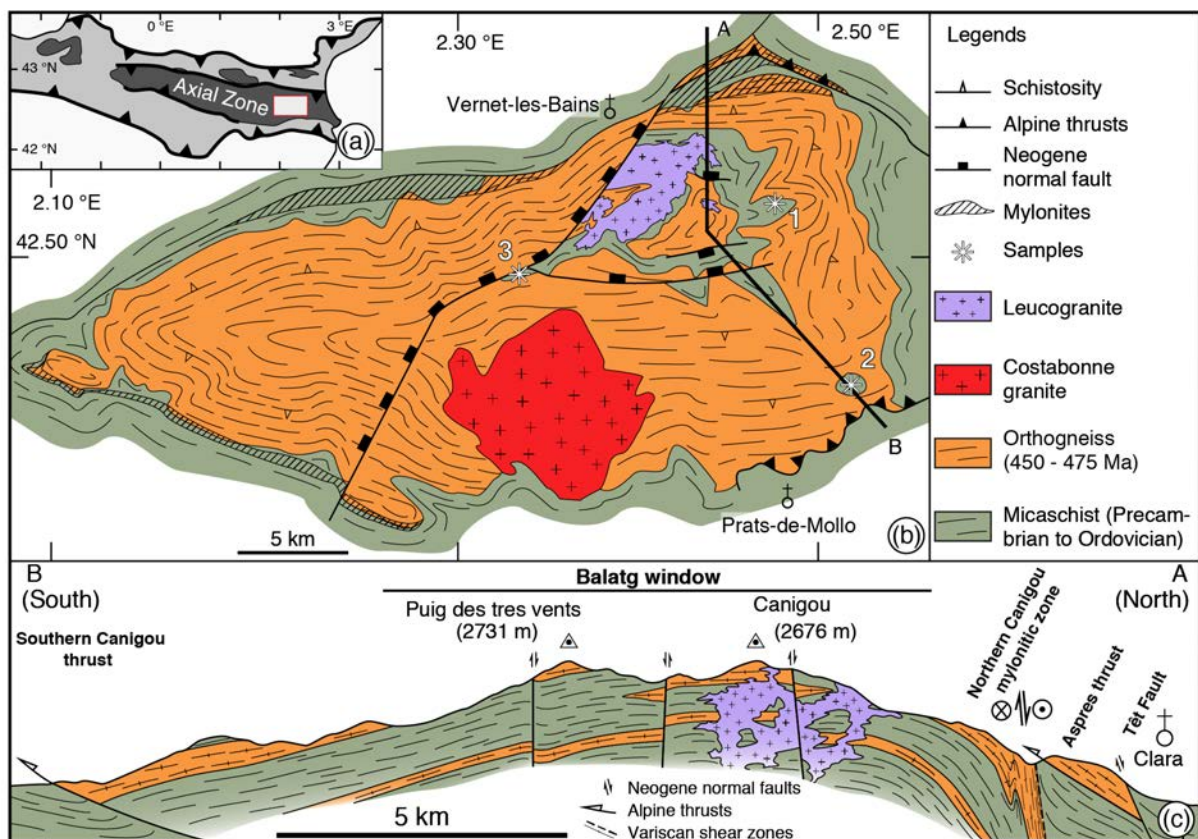


Figure III.1 (a) Location of the study area in the Axial Zone of the Pyrenean belt. Dark grey—pre-Mesozoic, mostly Palaeozoic rocks; light grey—Mesozoic to Cainozoic sedimentary rocks involved in the Alpine age fold and thrust belts. (b) Map of the Canigou massif with location of samples (sampled areas) mentioned in the text (coordinates are given in decimal longitude and latitude in WGS84). Sampled area 1—LH1B (2.4868; 42.5186), LH2 (2.4869; 42.5191), LH3 (2.4881; 42.5210), LH9 (2.4880; 42.5203) and LH16 (2.4847; 42.5229); sampled area 2—BLB1457 (2.3027; 42.4767); sampled area 3—BLB816 (2.5154; 42.4271). (c) Section across the massif

2. Geological setting

2.1. The Variscan Pyrenees: metamorphic and chronological framework

Modern petrological studies on the Axial Zone of the Pyrenees (see Figure S1 for the localisation of the massifs mentioned hereafter) are relatively rare and infer contrasting peak P – T conditions and P – T paths (Figure III.2; Table S1). They agree on the dominance of a LP–HT metamorphism ($P < \sim 4.5$ kbar, $T > \sim 550$ °C) that would be achieved, however, through heating and decompression (Bossòst massif, Mezger & Passchier, 2003; Albères, Vilà et al., 2007), isobaric heating or heating at increasing pressure (Aston-Hospitalet, Mezger & Régnier, 2016), or cooling and decompression (Bossòst, Mezger et al., 2004; Roc de France, Aguilar et al., 2015). Importantly, although medium-pressure (MP) conditions ($P > \sim 5$ kbar) are locally inferred (Aguilar et al., 2015; Mezger et al., 2004), no study documents the prograde P – T path leading to the MP pressure peak.

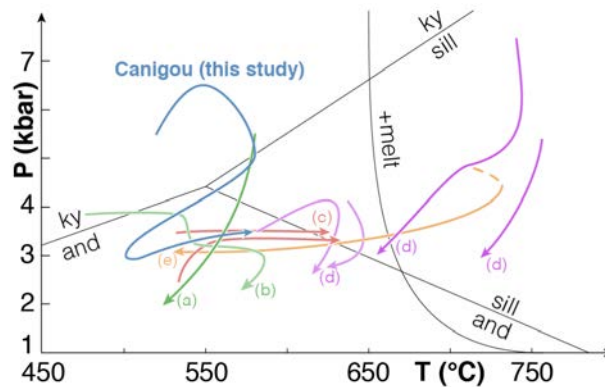


Figure III.2: Recently published P – T paths (mostly phase diagram-based) for the gneissic domes of the Axial Zone. (a)

Bossòst (Mezger et al., 1994), (b) (Mezger & Passchier, 2003), (c) Aston-Hospitalet (Mezger & Régnier, 2017), (d)

Roc de France (Aguilar et al., 1966) and (e) Albères (Vilà et al., 2018)

The timing of the metamorphic events is also a matter of debate. On the one hand, U-Pb dating on zircon and U-Th-Pb on monazite in granitic rocks and a paragneiss in the Bossòst and Aston-

Hospitalet massifs yielded dates around ~340-320 Ma, interpreted as the age of the LP–HT event (Mezger & Gerdes, 2016). On the other hand, in many other studies, the widespread calc-alkaline magmatism emplaced between 310-290 Ma is considered coeval with the LP–HT metamorphism (e.g. Denèle et al., 2014 and references therein; Druguet, Castro, Chichorro, Pereira, & Fernández, 2014). Separate metamorphic events or a single event diachronic across the Axial Zone have been proposed to account for these age populations (Mezger & Régnier, 2016). Other authors argued in favour of an inherited component for the *c.* 340 Ma ages (see discussion in Denèle et al., 2014; Lopez-Sanchez, García-Sansegundo, & Martínez, 2018).

Partial melting in the Roc de France massif is poorly constrained by U-Pb ages on zircon from leucosomes at 320 ± 13 and 313 ± 13 Ma (Aguilar, Liesa, Castiñeiras, & Navidad, 2014). The subsequent exhumation of the migmatites occurred during a later thermal event constrained at 314-307 Ma (Aguilar et al., 2014, 2015). In addition, in the Lys-Caillaouas massif, zircon grains from mafic and granitic magmatic rocks display cores and rims with metamorphic and magmatic affinities, respectively. The cores yield a date of *c.* 307 Ma, interpreted as the age of the thermal peak of the LP–HT metamorphism, while the magmatic overgrowths dated at *c.* 300 Ma are interpreted as the age of the emplacement of the Lys-Caillaouas pluton (Esteban et al., 2015). To sum up, most authors agree that the dominant LP–HT metamorphism was contemporaneous with a widespread magmatic event that occurred 310-290 Ma ago.

2.2. The Canigou Massif

The Canigou is a gneissic dome-shaped massif of the Axial Zone located in the eastern Pyrenees (Figure III.1a). It comprises orthogneiss, micaschists and undeformed granitoids. The massif is bounded to the north and to the south by roughly E-W trending shear zones (Guitard, Laumonier, Autran, Bandet, & Berger, 1998; Laumonier, Le Bayon, & Calvet, 2015). The Northern Canigou mylonitic zone, as well as the southern border of the orthogneiss were reactivated by south-

Chapter III

vergent thrusting during the Alpine orogeny (Auriol & Casteras, 1958; Fontboté & Guitard, 1958). Finally, the Northern Canigou mylonitic zone was reactivated during the Oligocene opening of the Gulf of Lion (Maurel et al., 2008). Several Neogene NNE-SSW to E-W normal faults cut across the massif.

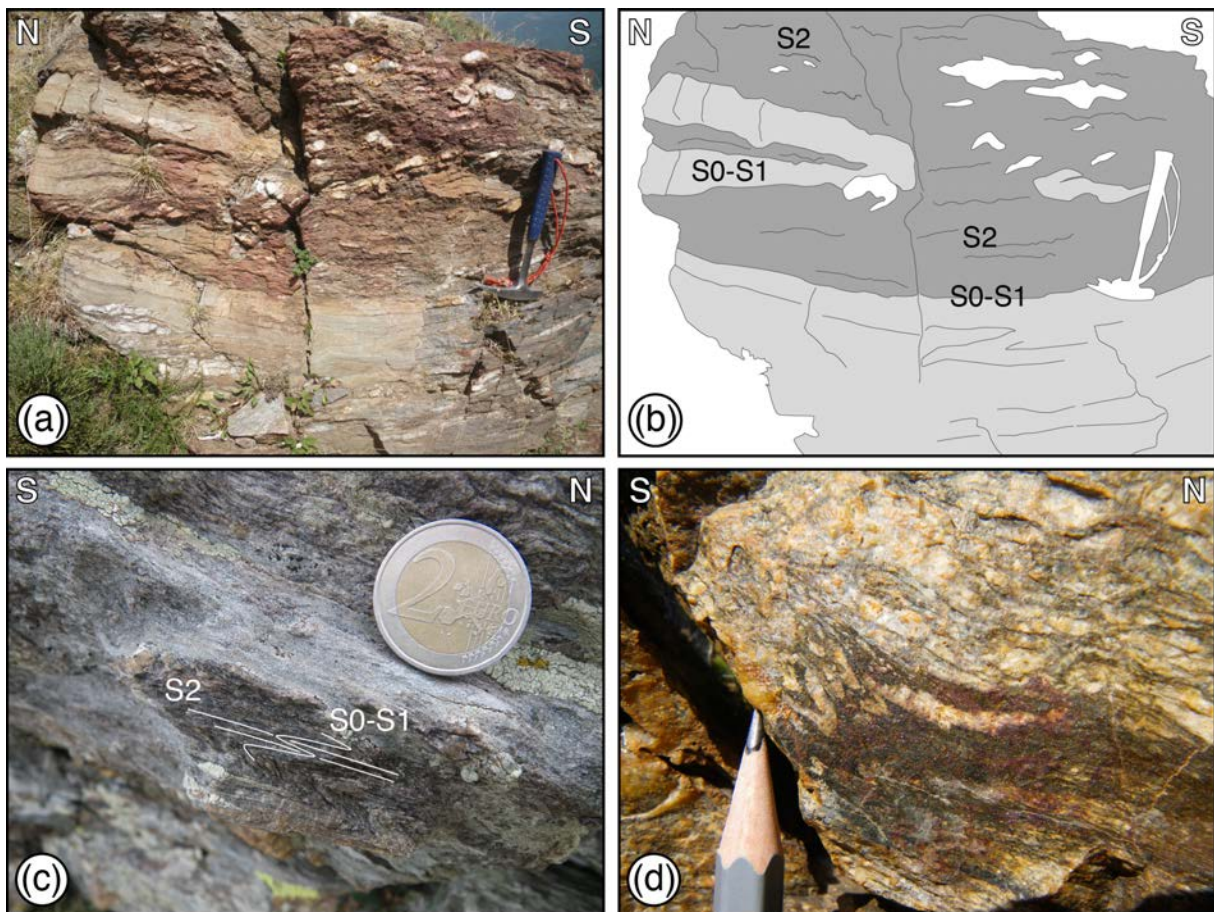
The studied micaschists mostly outcrop in the central part of the dome, in the footwall of the orthogneisses, in the so-called “Balatg window” (Figure III.1c). The main foliation, in both the micaschists and the orthogneisses, is parallel to the lithological contacts and outlines the dome shape of the massif (Figure III.1b,c). The orthogneisses were derived from an Ordovician rapakivi granite (protolith ages at *c.* 475 Ma, Deloule, Alexandrov, Cheilletz, Laumonier, & Barbey, 2002) that intruded Precambrian to Ordovician pelitic rocks (Barbey, Cheilletz, & Laumonier, 2001; Padel et al., 2017). A weakly deformed monzogranite dyke, parallel to the main foliation, from the northern flank of the dome, has been dated at *c.* 305 Ma (Denèle et al., 2014). The undeformed Costabonne granite (Figure III.1b) cuts across the main foliation. Its age is poorly constrained by U-Pb on zircon with two clusters at *c.* 302 Ma (N=2) and *c.* 285 Ma (N=8) (Laumonier et al., 2015).

LP–HT regional metamorphic zoning is defined in the micaschists by the progressive appearance of chlorite, biotite, andalusite \pm cordierite, and sillimanite from the outer to the inner parts of the massif (Guitard, 1970). Increasing temperature during the LP–HT event is revealed by the growth of prismatic sillimanite after andalusite (Gibson, 1992). The peak *P–T* conditions, constrained using conventional thermobarometry, reached 4.5 kbar and ~ 725 °C (Gibson & Bickle, 1994). Andalusite and cordierite locally contain inclusions of resorbed staurolite (Guitard, 1970). Staurolite porphyroblasts contain straight inclusion trails of ilmenite disposed at high angle relative to the external foliation (Gibson, 1991, 1992). Staurolite is associated with kyanite (Azambre & Guitard, 2001) and helicitic or static garnet with prograde growth zoning (Gibson, 1992). The development of the main regional foliation is coeval with the crystallization of andalusite and cordierite. Their growth

at the expense of staurolite was initially interpreted as the result of down-pressure, up-temperature prograde metamorphism in an overall low-pressure setting (Gibson, 1992).

3. Structural data

The dome shape of the Canigou massif results from the refolding of the main regional foliation, S2. The strike of the foliation parallels the map outline of the massif and the dip increases from the core to the rim of the dome (Figure III.1b). In the orthogneiss, this foliation is marked by the flattening of quartz and feldspars and by the preferential orientation of micas. Isoclinal folds, rarely observed in the orthogneiss (Figure III.3d), indicate that the main planar fabric corresponds to a composite S1/S2 foliation.



Chapter III

Figure III.3 (previous page): (a–c) The initial sedimentary layering (S0) in the micaschists, transposed by a first schistosity S1, is folded with S2 parallel to the axial planes of the folds. (b) Schematic drawing of the structures observed in (a). (c) The composite S0–S1 is marked by the alternation of quartz-rich layers (light grey) and pelitic micaschists (dark grey) with quartz lenses (white). S2 is well marked in the micaschists. (d) S2 folding and transposing S1 in the orthogneiss

The schistosity in the micaschists is parallel to the foliation in the orthogneiss. The micaschists display a compositional layering (S0), marked by alternating mica-rich and quartz-feldspar-rich layers, and interpreted as inherited from an original sedimentary structure. A first schistosity, S1, parallel to this layering, is defined by preferential orientation of micas. Both structures are folded (Figure III.3a–c) mostly by isoclinal rootless folds. The main regional schistosity S2 is parallel to the axial plane of these folds and generally transposes S1. Consequently, the D1 structures are erased by D2 in most of the Canigou massif.

A lineation is oriented NE-SW and marked by the stretching of feldspar and quartz lenses in the orthogneiss. In the micaschists, it corresponds to the intersection between S2 and S1 and is parallel to the fold axes.

4. Petrography and mineral chemistry

Mineral analyses have been performed with a Cameca SX100 electron microprobe (Microsonde Ouest, IFREMER, Brest-Plouzané, France). Representative analyses of selected minerals are listed in Table 1. Mineral abbreviations are: all: allanite, and: andalusite, bi: biotite, camp: clinoamphibole, cd: cordierite, ep: epidote, g: garnet, ilm: ilmenite, ksp: potassium feldspar, ky: kyanite, ma: margarite, mt: magnetite, mu: muscovite, pa: paragonite, pl: plagioclase, q: quartz, ru: rutile, sill: sillimanite, sp: spinel, st: staurolite, wm: white mica. Mineral endmembers (expressed in mole %) and compositional variables are: $X_{\text{Fe}} = \text{Fe}/(\text{Fe}+\text{Mg})$, $X_{\text{K}} = \text{K}/(\text{Ca}+\text{Na}+\text{K})$, $X_{\text{Na}} = \text{Na}/(\text{Ca}+\text{Na}+\text{K})$; epidote, $\text{Ep} = \text{Fe}^{3+}/(\text{Fe}^{3+}+\text{Al}-2)$; almandine, $\text{Alm} = \text{Fe}/(\text{Fe}+\text{Mg}+\text{Ca}+\text{Mn})$, pyrope,

Chapter III

Prp = $\text{Mg}/(\text{Fe}+\text{Mg}+\text{Ca}+\text{Mn})$, grossular, Grs = $\text{Ca}/(\text{Fe}+\text{Mg}+\text{Ca}+\text{Mn})$, spessartine, Sps = $\text{Mn}/(\text{Fe}+\text{Mg}+\text{Ca}+\text{Mn})$, ilmenite, Ilm = $\text{Fe}/(\text{Fe}+\text{Mg}+\text{Mn})$; anorthite, An = $\text{Ca}/(\text{Ca}+\text{Na}+\text{K})$; pfu: per formula unit.

Three micaschist samples (LH1B, LH3, LH16) and one sample of a garnet-grunerite-bearing gneiss (LH9) come from a small area (~500m²; star 1 in Figure III.1b) of the “Balatg window”, underlying the orthogneiss. The micaschist samples LH1B, LH3 and LH16 display similar petrographic and microstructural features. Alternating quartz \pm plagioclase- and mica-rich layers are parallel to the preferred orientation of muscovite and biotite and define the first schistosity, S1. This schistosity is folded by tight to isoclinal mostly rootless folds. The main regional schistosity S2 developed in the axial plane of the folds (Figure III.4a) and is marked by the preferred orientation of muscovite and biotite and wraps around porphyroblasts of andalusite and garnet (LH16). Garnet is rare and generally forms small crystals (max. 1 mm), with the exception of sample LH16, where both small and large (up to 7 mm) crystals are present. Biotite ($X_{\text{Fe}} = 0.57\text{-}0.61$, Ti = 0.07-0.17 pfu) and muscovite ($X_{\text{Na}} = 0.10\text{-}0.13$, Si = 3.00-3.09 pfu) have the same composition regardless of the textural position. Matrix plagioclase contains 27-33% anorthite. Accessory minerals include ilmenite (Ilm90-92), apatite, tourmaline, monazite, pyrite (LH1B), zincian spinel (LH3; 64-69% gahnite, 24-29% hercynite), and chlorite ($X_{\text{Fe}} = 0.55\text{-}0.59$) locally replacing biotite. Anhedral porphyroblasts of andalusite (up to 10 mm) are preferentially localized in mica-rich layers. When these layers are folded, andalusite is occasionally S-shaped, but displays only a weak or no undulose extinction. The folded S1 is also preserved in andalusite as curved inclusions of biotite and ilmenite (Figure III.4b). S2 wraps around, but is also preserved in andalusite as inclusions of biotite, the size of which increases from core to rim (0.25→0.75mm; Figure III.4c). Andalusite includes anhedral staurolite (up to 2 mm; $X_{\text{Fe}} = 0.85\text{-}0.89$) and garnet (up to 0.5 mm; Figure III.4b). Staurolite may contain oriented ilmenite inclusions that define an internal fabric (S1) at high angle to the external S2 (Figure III.4d).

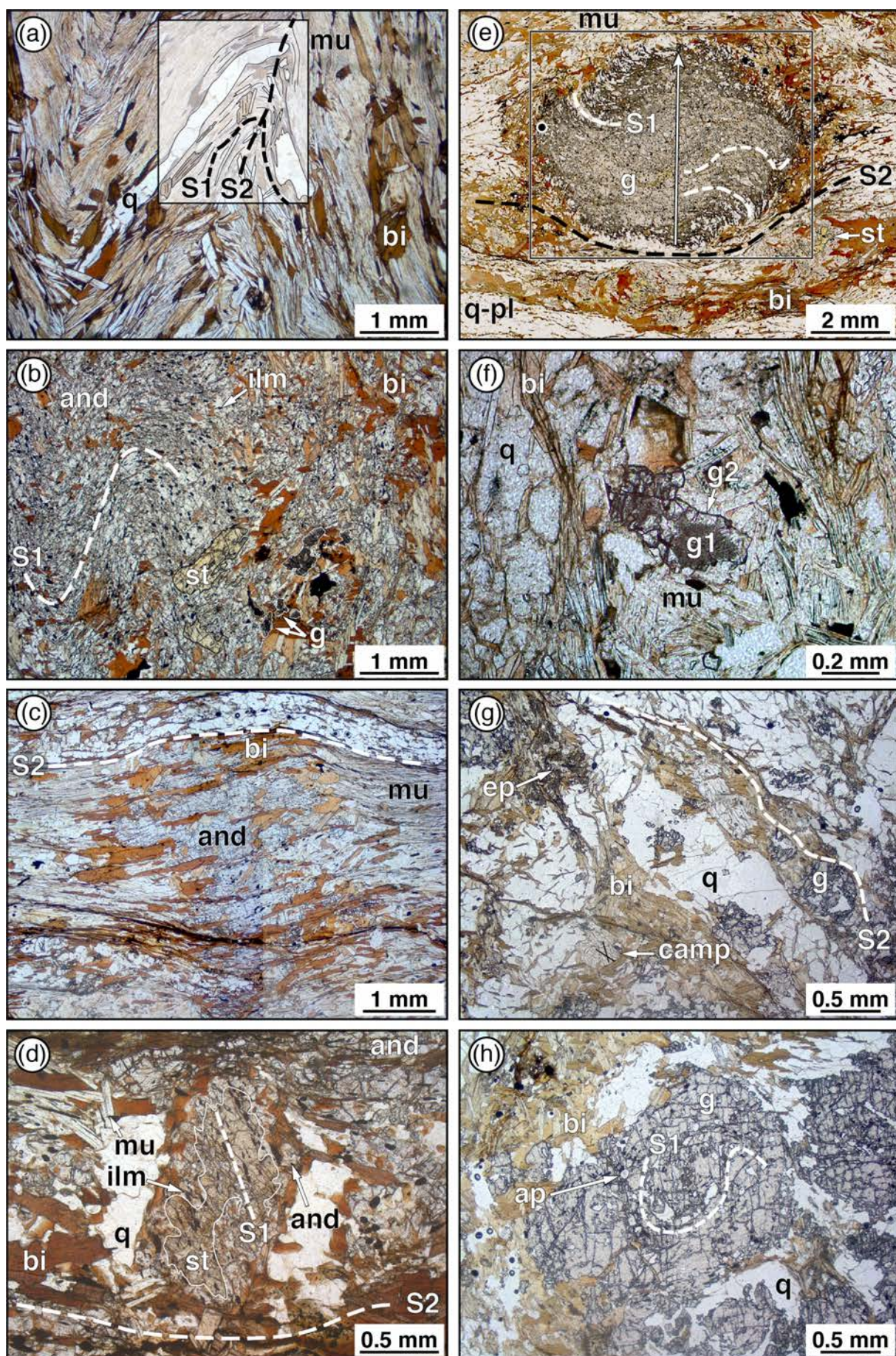
Chapter III

In sample LH16, garnet forms large (up to 7 mm) subhedral porphyroblasts commonly surrounded by biotite (Figure III.4e), and small crystals (0.2 mm) included in staurolite. Large garnet contains numerous unidentified micrometric inclusions and larger inclusions (~0.1 mm) of muscovite ($X_{\text{Na}} = 0.06\text{-}0.18$), quartz, plagioclase (An20-25) and epidote (Ep35-67) that define a sigmoidal internal foliation (S1) oriented at high angle to the matrix S2 (Figure III.4e). Some epidote crystals contain LREE and have the composition of allanite (Ca = 1.51-1.94 pfu). Biotite is absent from the garnet core and appears in its rim. Garnet is chemically zoned (Figure III.5a). A large core (~5 mm) is characterized by a relatively homogeneous grossular content (Grs19-23) and X_{Fe} (0.92-0.94) and a rimward decreasing content of spessartine (Sps14→11). A rim (<1 mm) displays a strong decrease in grossular (Grs19-23→10), and further decrease in spessartine (Sps11→8, the lowermost values were collected manually off the automatic profile presented) and X_{Fe} (0.92→0.90). The outermost rim (~100 μm) displays a sharp increase of spessartine (Sps8→17), accompanied by a continuing decrease of X_{Fe} (0.90→0.87) and grossular (Grs10→7). Small garnets, chemically similar to the rim of the large crystals ($X_{\text{Fe}} = 0.89$; Grs11-12; Sps8), are systematically separated from the staurolite host by a corona of andalusite, which is in optical continuity with andalusite surrounding the staurolite relic. Unlike allanite, only present as inclusions in garnet, monazite is absent from garnet and exclusively present in the rock matrix, or as inclusions in staurolite and andalusite.

In samples LH1B and LH3, garnet forms small (max. 1 mm) crystals in the matrix. They are optically zoned with an anhedral embayed greyish “cloudy” core (g1) and a clear euhedral to anhedral rim (g2; Figures III.4f and III.5b). Chemical zoning is subtle but systematic. Cores display a weak increase of spessartine and X_{Fe} towards the core-rim interface ($X_{\text{Fe}} = 0.89\rightarrow 0.91$, Sps21→22, Grs7-6). Rims are poorer in grossular and also display an increase of spessartine and X_{Fe} towards the outer rim ($X_{\text{Fe}} = 0.90\rightarrow 0.93$, Sps21→24, Grs4; Figure III.5b). Outermost rims locally contain up to 32% spessartine (LH3).

Chapter III

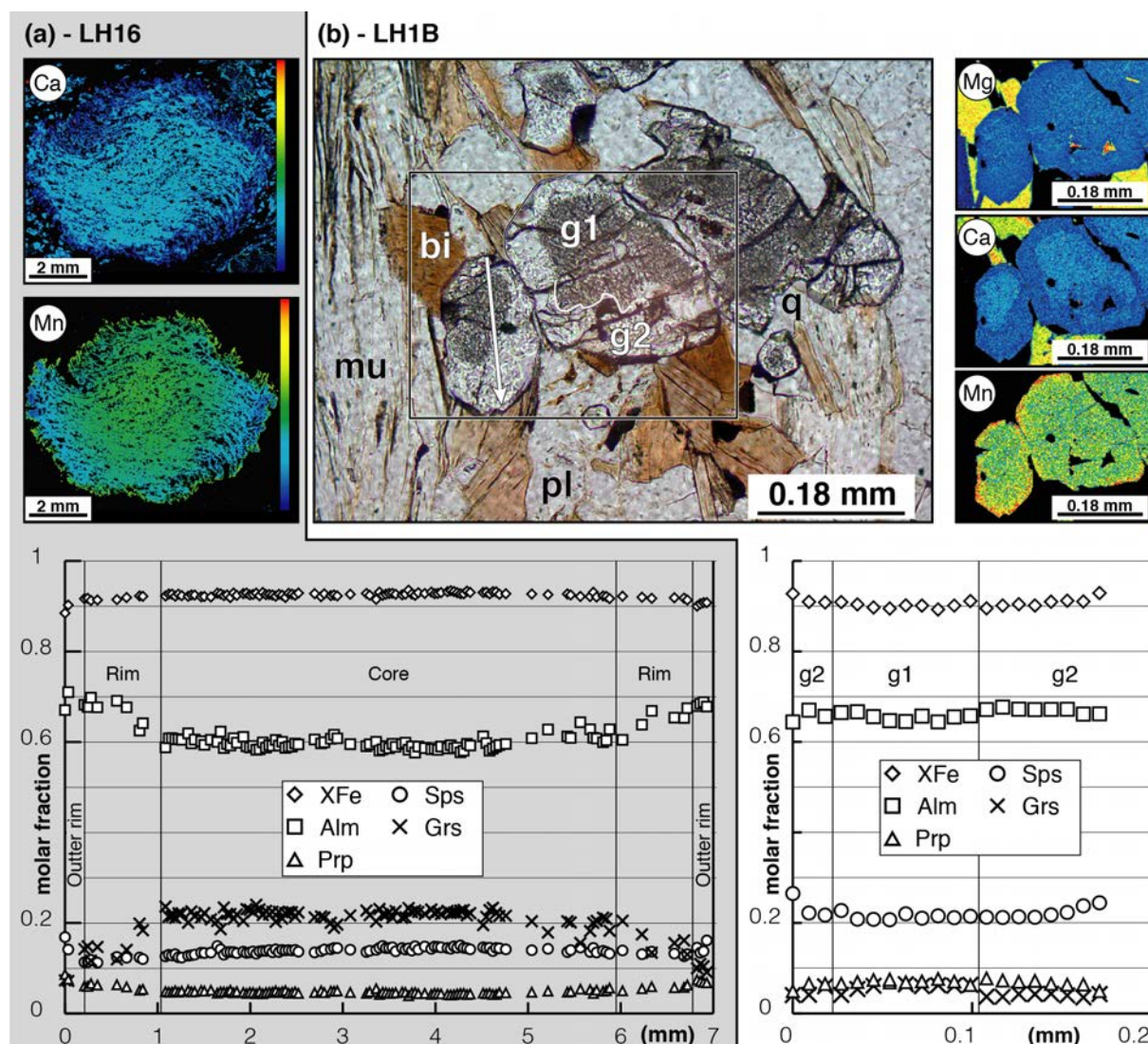
The garnet-grunerite-bearing gneiss sample LH9 displays an irregular poorly developed schistosity marked by the alignment of biotite (up to 0.5 mm; $X_{\text{Fe}} = 0.57\text{-}0.63$, $\text{Ti} = 0.07\text{-}0.09$ pfu). It wraps around abundant large (up to 5 mm) anhedral crystals of garnet, and smaller crystals of polysynthetically twinned grunerite (up to 1 mm; $X_{\text{Fe}} = 0.59\text{-}0.61$, $\text{Ca}+\text{Na}(\text{B}) = 0.1\text{-}0.3$ pfu, $\text{Si} = 7.9$ pfu; Figure III.4g). The sample matrix contains abundant quartz, epidote (Ep03-09), ilmenite, apatite, and minor muscovite ($X_{\text{Na}} = 0.01\text{-}0.06$; $\text{Si} = 3.04\text{-}3.09$ pfu) and chlorite. Garnet is anhedral, poikilitic and contains sigmoidal inclusions of epidote (Ep30-46), quartz, apatite, ilmenite, and minor muscovite ($X_{\text{Na}} = 0.02\text{-}0.03$; $\text{Si} = 3.05\text{-}3.09$ pfu), plagioclase (An01-05) and biotite (Figure III.4h). Epidote is concentrated in garnet core and the mode strongly decreases towards the rim. Chemical zoning of garnet is marked by a rimward decrease of X_{Fe} ($0.96 \rightarrow 0.89$), spessartine (Sps9 \rightarrow 1) and grossular (Grs24 \rightarrow 17). The outermost rim is locally marked by a slight increase in spessartine (Sps5). Both garnet and grunerite are coated by coarse and poorly oriented crystals of biotite (up to 0.5 mm; Figure III.4g,h) and minor chlorite.



Chapter III

Figure III.4 (previous page): Photomicrographs (plane polarized light). (a) S1 foliation, marked by an elongated quartz lens and oriented mica, is folded, and S2 is parallel to the axial planes of folds (sample LH62). (b) Anhedral staurolite and garnet inclusions in andalusite. Ilmenite inclusions mark the folded S1 overgrown by the andalusite poikiloblast (LH1A). (c) The main foliation S2 wraps around an andalusite porphyroblast. Biotite inclusions are parallel with S2 in the matrix and their size increases from core to rim (LH1B). (d) Anhedral crystal of staurolite surrounded by andalusite, biotite, and quartz. Staurolite contains oriented inclusions of ilmenite that define an internal fabric, labelled S1. S1 is at high angle to the external fabric S2 marked by inclusions of biotite and ilmenite in the andalusite porphyroblast surrounding the staurolite crystal (LH2A). (e) Centimetric porphyroblast of garnet with sigmoidal inclusions of S1, at a high angle with the matrix S2 (LH16). Rectangle and arrow show the location of X-ray maps and the chemical profile, respectively (Figure III.5a). (f) Cloudy core of garnet 1 surrounded by clear rims of garnet 2 (LH3). (g) Anhedral garnet and grunerite surrounded by biotite that marks the main fabric S2 (LH9). The cleavage directions are highlighted by two black lines in the grunerite crystal (camp). (h) Anhedral garnet with sigmoidal inclusion trails of S1. Biotite surrounds garnet and crystallizes in fractures (LH9).

Figure III.5 (next page): Grey background (a)—sample LH16, garnet zoning profile, and Ca and Mn X-ray maps (Figure III.3d). The core is relatively homogeneous and most of the zoning occurs in the rim. The core-to-rim Mn decrease is characteristic of prograde growth zoning, whereas the enriched outermost rim indicates limited resorption. White background (b)—sample LH1B, photomicrograph (PPL), garnet zoning profile and X-ray maps for magnesium, calcium, and manganese content. Anhedral cloudy garnet 1 cores are surrounded by clear rims of garnet 2. The optical zoning corresponds to a slight discontinuity in calcium content. Arrow indicates the position of the chemical profile.



These observations can be interpreted in terms of two syntectonic metamorphic events. In the micaschists, the early development of S1 was associated with the crystallization of the large garnet crystals with sigmoidal inclusions. The main characteristic of the garnet is a continuous rimward decrease of X_{Fe} , Sps and Grs, typical of prograde growth zoning. The increase of spessartine in the outermost rim is interpretable in terms of partial resorption of garnet. However, it is associated with a decrease of X_{Fe} , suggesting that resorption occurred along a prograde (heating) P - T path. This prograde growth started in the stability field of epidote, exclusively preserved as inclusions in large garnet, continued during the appearance of biotite included in the garnet rim, and peaked in the

stability field of staurolite (stage M1). The “cloudy” cores of the small garnets (g1) are inferred to also belong to this metamorphic stage. Their anhedral shape and the slight increase of spessartine towards the interface with garnet 2 (i.e. the g1-g2 interface; Figure III.5b) is interpreted in terms of partial resorption of garnet 1 prior to a renewed growth of garnet (g2). The increase of spessartine in the outermost rim of garnet 2 is attributable to a final stage of partial resorption. The second metamorphic stage M2 is associated with the development of the main schistosity S2, marked by the crystallization of andalusite as well as the second generation of garnet (g2). Muscovite, plagioclase, quartz and ilmenite were stable during the whole metamorphic history.

In the garnet-grunerite-bearing gneiss, the first event (M1) is characterized by a syn-S1 crystallization of garnet, grunerite and minor plagioclase. The subsequent event (M2) was coeval with S2 and caused partial resorption, and replacement of garnet and grunerite by biotite. Biotite, ilmenite, quartz and minor muscovite are inferred to be stable during all the metamorphic history of the rock. Epidote seems to crystallize in two episodes, at the beginning of M1 and during M2, whereas the peak-M1 assemblage may be epidote-free. Minor chlorite either belongs to M2, or develops late, at the expense of biotite.

5. *P–T* estimations

5.1. *Methods*

P–T pseudosections were calculated in the model system MnNCKFMASHTO using THERMOCALC (Powell & Holland, 1988) and Theriak/Domino (de Capitani & Brown, 1987; de Capitani & Petrakakis, 2010) and the thermodynamic data set 5.5 (Holland & Powell, 1998); updated November 2003; translation for Theriak/Domino by Tinkham, 2012 – <http://dtinkham.net/peq.html>). The solution phases considered in the calculations, and the activity-composition models used are amphibole (Diener & Powell, 2012), chlorite (Le Bayon, Pitra, Ballèvre, & Bohn, 2006; based on

Holland, Baker, & Powell, 1998), chloritoid, cordierite, epidote, staurolite (Holland & Powell, 1998), garnet, biotite, ilmenite, hematite (White, Pomroy, & Powell, 2005), magnetite (White, Powell, Holland, & Worley, 2000), plagioclase (Holland & Powell, 2003); muscovite, paragonite (Coggon & Holland, 2002) and margarite (margarite-paragonite mixing on sites, neglecting muscovite, $W(\text{ma}, \text{pa}) = 14.5 \text{ kJ}$ (AX notes, Powell & Holland, 2002), DQF for paragonite set to 5 kJ to fit natural data of Höck, 1974 and Feenstra, 1996).

Bulk compositions used for the calculations were obtained by the area-scan method at SEM-EDS (JSM-7100 F scanning electron microscope, CMEBA, University Rennes 1) on parts of thin sections estimated to approach an equilibration volume. Due to the heterogeneous nature of the samples (presence of porphyroblasts or layering) analyses were performed using various area sizes and the results checked for robustness. The bulk compositions used are indicated as insets in the diagrams in mole per cent normalized to 100%. Additionally, although all the samples contain ilmenite and lack magnetite, which suggests relatively low amounts of Fe^{3+} (Connolly & Cesare, 1993), the effects of varying Fe^{3+} were investigated in $P/T-X(\text{Fe}^{3+})$ pseudosections. Three samples contain apatite and one of them pyrite. The bulk compositions were corrected accordingly. The fluid phase was fixed as pure H_2O and considered in excess in the calculations.

5.2. Sample LH16

First, two $P-T$ pseudosections were calculated using both THERMOCALC and Theriak/Domino for a bulk composition measured over an area of 1.5x2 cm that comprises garnet, epidote, andalusite, staurolite as well as the matrix. The proportion of Fe^{3+} was arbitrarily set to 5% of the total Fe. The only significant difference between these diagrams is the appearance of chloritoid at $P < 2 \text{ kbar}$ and $T < 510 \text{ }^\circ\text{C}$ on the pseudosection calculated with Theriak/Domino with respect to the one calculated with THERMOCALC (Figure S2). Otherwise, the two diagrams are virtually identical,

Chapter III

the relative position of the fields being the same, and the differences in the absolute position of the lines being less than 5 °C and 0.1 kbar. Because the computations with Theriak/Domino are significantly less time-consuming than with THERMOCALC, subsequent calculations were carried out using only Theriak/Domino.

In these diagrams, magnetite is stable across a large domain at $P < 7$ kbar, but is lacking in our samples. Consequently, a P – $X(\text{Fe}^{3+})$ pseudosection has been calculated at $T = 580$ °C (Figure S3) in order to estimate the influence of the oxidation state of the sample on the stability of the mineral assemblages (cf. López-Carmona, Pitra, & Abati, 2013; White et al., 2000). In the interval $0\% < X(\text{Fe}^{3+}) < 5\%$, the variation of $X(\text{Fe}^{3+})$ only influences the stability of magnetite, ilmenite and rutile, whereas the other minerals only display negligible variations. Magnetite becomes stable for $X(\text{Fe}^{3+})$ ratios ($= \text{Fe}^{3+}/\text{Fe}_{\text{tot}}$) higher than ~3%, and an arbitrary low value of 1% Fe^{3+} was used for the subsequent calculations.

The resulting P – T pseudosection (Figure III.6) was contoured with compositional isopleths for garnet (X_{Fe} , Grs, Sps) in order to infer the conditions of crystallization of the epidote-bearing garnet core. In the P – T space investigated, epidote is stable at $T < 510$ °C and $P > 3$ kbar. The isopleths corresponding to the composition of the garnet core ($X_{\text{Fe}} = 0.94$, Grs23, Sps14) intersect in the field ma-pl-chl (+ g, mu, q, ilm) around 520 °C, 5.5 kbar, just outside the epidote-bearing domain. This point is discussed later. Subsequent slight rimward decrease of spessartine and sub-constant grossular content suggest a limited prograde up-pressure evolution, parallel to the Grs isopleths, during the growth of the garnet core.

LH16 - MnNCKFMASHTO
 (+ H₂O, g, mu, q, ilm)

SiO ₂	TiO ₂	Al ₂ O ₃	F ₂ O ₃	FeO	MnO	MgO	CaO	Na ₂ O	K ₂ O
62.77	0.78	14.93	0.06	10.93	1.39	3.12	2.62	1.16	2.24

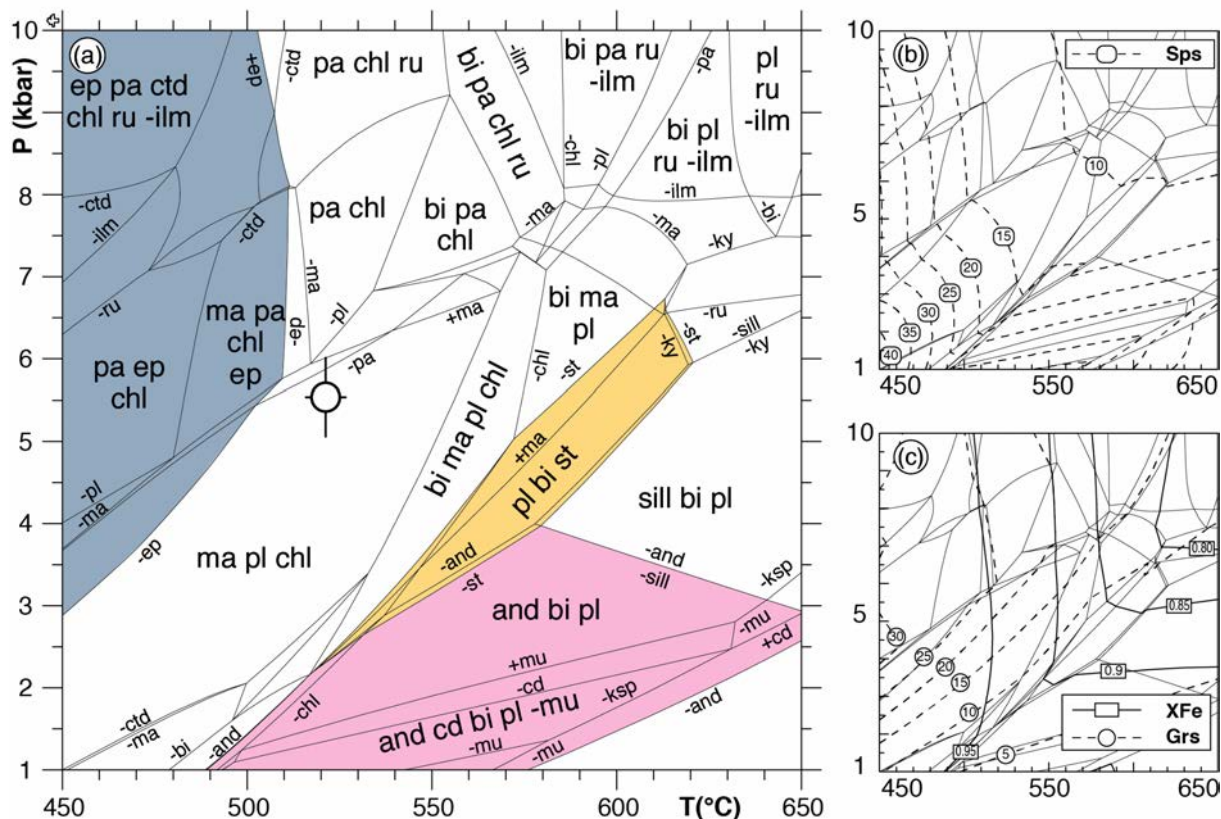


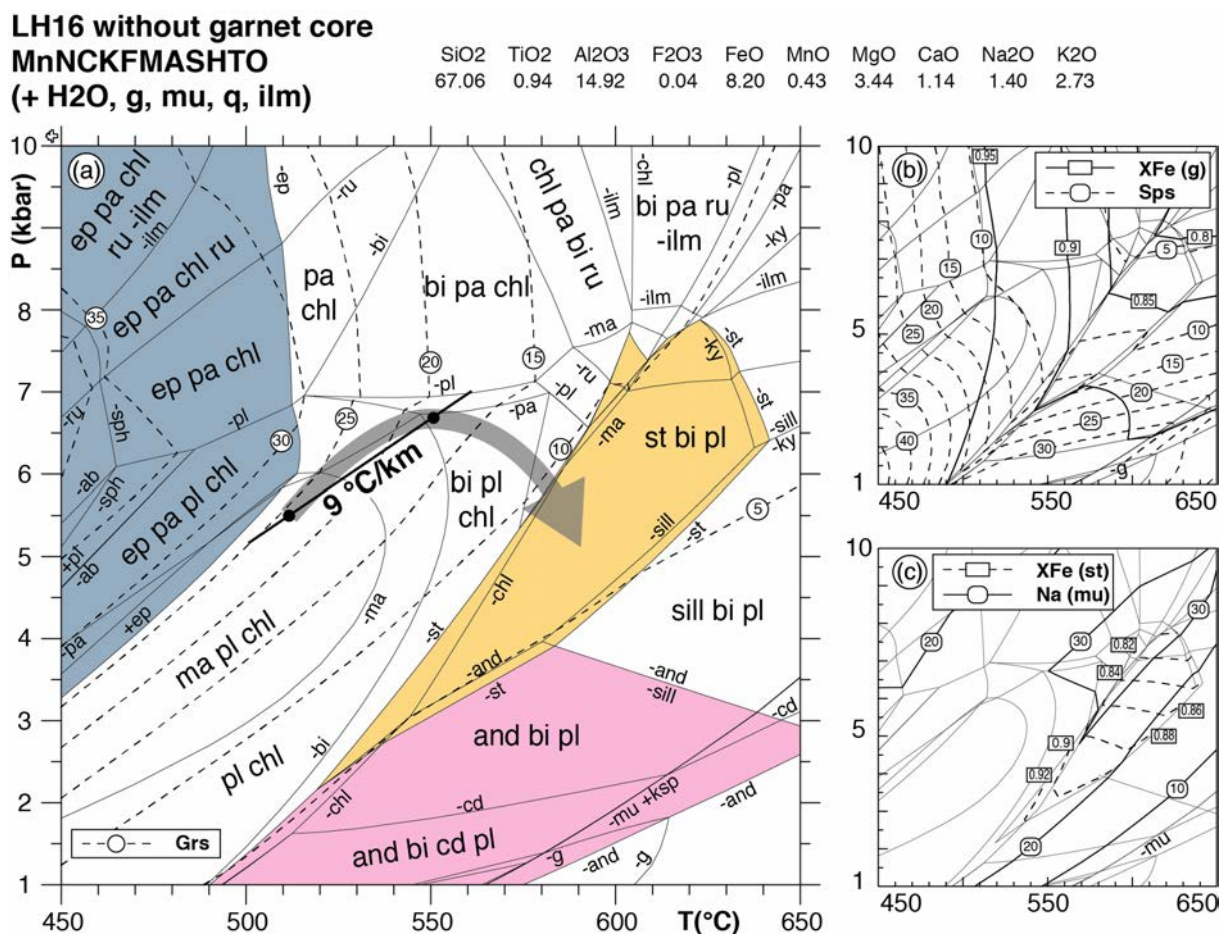
Figure III.6: *P-T* pseudosection for a SEM-measured bulk composition of an area of the sample LH16 (a) and compositional isopleths for garnet–spessartine (b), grossular and X_{Fe} (c). The circle localizes the intersection of the compositional isopleths for garnet core. The whiskers approximate the uncertainty related to the imperfect intersection.

Coloured fields mark the stability of key minerals: epidote (blue), staurolite (yellow), and andalusite (pink)

Garnet represents ~20% of the surface of the domain considered in the previous calculation, and has a large, mostly homogeneous, core and zoned rims (see above). In order to model the crystallization of the assemblage in equilibrium with the garnet rim (M1 peak), the garnet core (~15% of the domain) has been subtracted from the bulk composition of the domain.

With respect to Figure III.6, the pseudosection calculated for this modified bulk-composition (Figure III.7) shows a reduced stability domain of margarite and a larger stability domain for staurolite. The diagram has been contoured with compositional isopleths for garnet (X_{Fe} , Grs, Sps) as well as staurolite (X_{Fe}) and muscovite (X_{Na}). The isopleths corresponding to the core/rim transition

($X_{\text{Fe}} \sim 0.92$, Grs ~ 20 , Sps ~ 11) intersect around 6-7 kbar 550 °C. The rim zoning, characterized by a significant decrease of grossular associated with a slight decrease of X_{Fe} and spessartine, corresponds to decreasing pressure and increasing temperature. The subsequent increase of spessartine in the outermost rim is interpretable in terms of partial resorption and reequilibration of garnet during continuous heating and decreasing pressure in the field of staurolite. The inferred peak M1 association staurolite, garnet, biotite (+ muscovite, plagioclase, ilmenite and quartz) corresponds to the field st-bi-pl (+ g, mu, q, ilm) at 3-7 kbar and 550-640 °C. The observed compositions of staurolite ($X_{\text{Fe}} = 0.88-0.89$) and garnet ($X_{\text{Fe}} = 0.87$, Sps17, Grs7) compared to the position of the corresponding isopleths (Figure III.7) suggest 4-5 kbar and 580 °C for the peak of the M1 stage.



Chapter III

Figure III.7: P – T pseudosection for the sample LH16 after removing the contribution of the garnet core to the measured composition (a) and compositional isopleths for garnet (b), staurolite and muscovite (c). Isopleths for garnet mode (not shown) are roughly parallel with those of the spessartine content. The arrow indicates the evolution of P – T conditions during the M1 prograde metamorphism inferred from garnet zoning.

The association andalusite, garnet, biotite, muscovite, plagioclase and quartz, representative of the M2 stage, corresponds to the field and-bi-pl spanning 1-4 kbar and 510-640 °C. Compositional isopleths indicate that muscovite becomes less paragonitic toward high temperatures in the andalusite field (Figure III.7c). Values in agreement with the measured composition ($X_{\text{Na}} = 0.10\text{-}0.13$) are found in the high temperature part of the andalusite field around 580-620 °C.

5.3. Sample LH1B

The chemical composition used to calculate the first P – T pseudosection for this sample (Figure III.8) has been calculated using a SEM-measured composition of an area of ~1.2 cm² that comprises staurolite, garnet 1 and 2, andalusite and a large proportion of matrix. One of the remarkable features of the diagram is the stability of garnet, reduced to $T > \sim 500$ °C and $P > \sim 3$ kbar. The peak M1 association staurolite, garnet, biotite, muscovite, plagioclase, quartz, ilmenite is modelled in the field g-bi-st-pl (+ mu, q, ilm) between 540-650 °C and 3-7 kbar. The M2 assemblage is interpreted to contain andalusite, biotite and plagioclase (+ mu, q, ilm) in equilibrium with the clear garnet 2 overgrowths on garnet 1 “cloudy” cores. This assemblage is modelled in the narrow field and-g-bi-pl at 530-600 °C, 3-4 kbar, in the uppermost part of the andalusite stability domain.

Given the low mode of garnet in the rock, and the possible dependence of its stability on the choice of the effective bulk composition, another P – T pseudosection has been calculated using the SEM-measured composition of a smaller area (0.15 cm²) included in the previously analysed region, in order to explore the crystallization of garnet 2. This area comprises garnet, andalusite, biotite,

Chapter III

muscovite, plagioclase, quartz and ilmenite, and contains a comparatively larger proportion of garnet. Additionally, the relics of garnet 1 (the anhedral “cloudy” cores) have been removed from the bulk composition. This diagram (Figure III.9) is contoured with compositional isopleths for garnet and muscovite, as well as the mode isopleths for garnet. With respect to Figure III.8, the stability field of garnet is significantly increased and that of staurolite decreased. The paragenesis garnet, andalusite, biotite, muscovite, plagioclase, quartz, ilmenite is modelled in a field between 540-640 °C and 1.5-4 kbar. Isopleths corresponding to the composition of garnet 2 ($X_{\text{Fe}} = 0.90$, Sps21, Grs4) indicate equilibration at ~3 kbar, 570 °C, whereas the observed X_{Na} of muscovite (0.10-0.13) suggests slightly higher temperatures (580-620 °C).

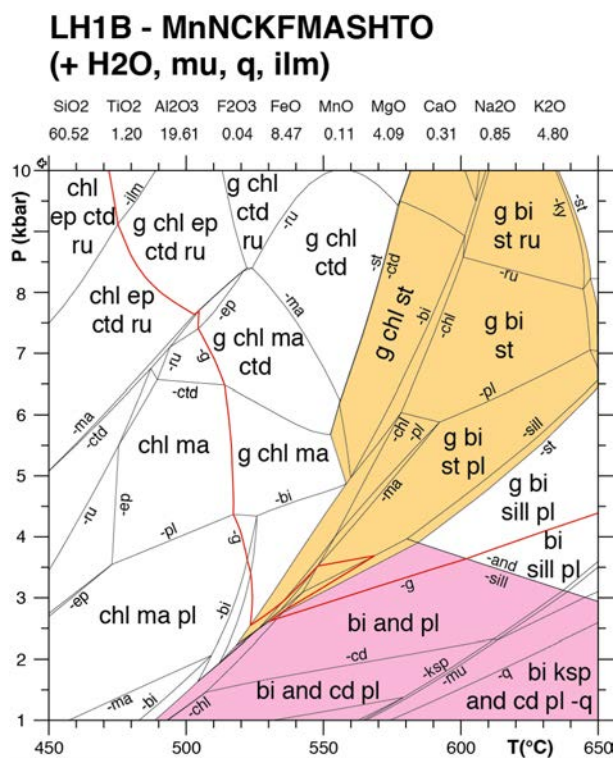


Figure III.8: *P–T pseudosection for a SEM-measured composition of an area of the sample LH1B.*

The isopleths of garnet mode have a steep negative slope at low temperatures, in the chlorite-present fields, and a flat positive slope at low pressures and high temperatures, in the fields with aluminium silicates or staurolite (Figure III.9a). In this framework, the inferred two-stage growth of

garnet, interrupted by a period of garnet resorption (cf. above) can be interpreted. Garnet 1 growth is compatible with a prograde P - T path peaking in the g-st-bi-pl field (M1). Subsequent partial resorption requires an evolution involving cooling and/or decompression. The growth of garnet 2, peaking in the field g-pl-bi-and (M2), might involve renewed heating, possibly associated with moderate pressure increase. Alternatively, garnet 2 could grow during cooling in the g-pl-bi-and field. This point is discussed later.

LH1B-2**MnNCKFMASHTO****(+ H₂O, bi, mu, ilm, q)**

SiO ₂	TiO ₂	Al ₂ O ₃	F ₂ O ₃	FeO	MnO	MgO	CaO	Na ₂ O	K ₂ O
65.90	1.00	14.81	0.04	0.02	0.31	3.78	0.90	1.31	3.93

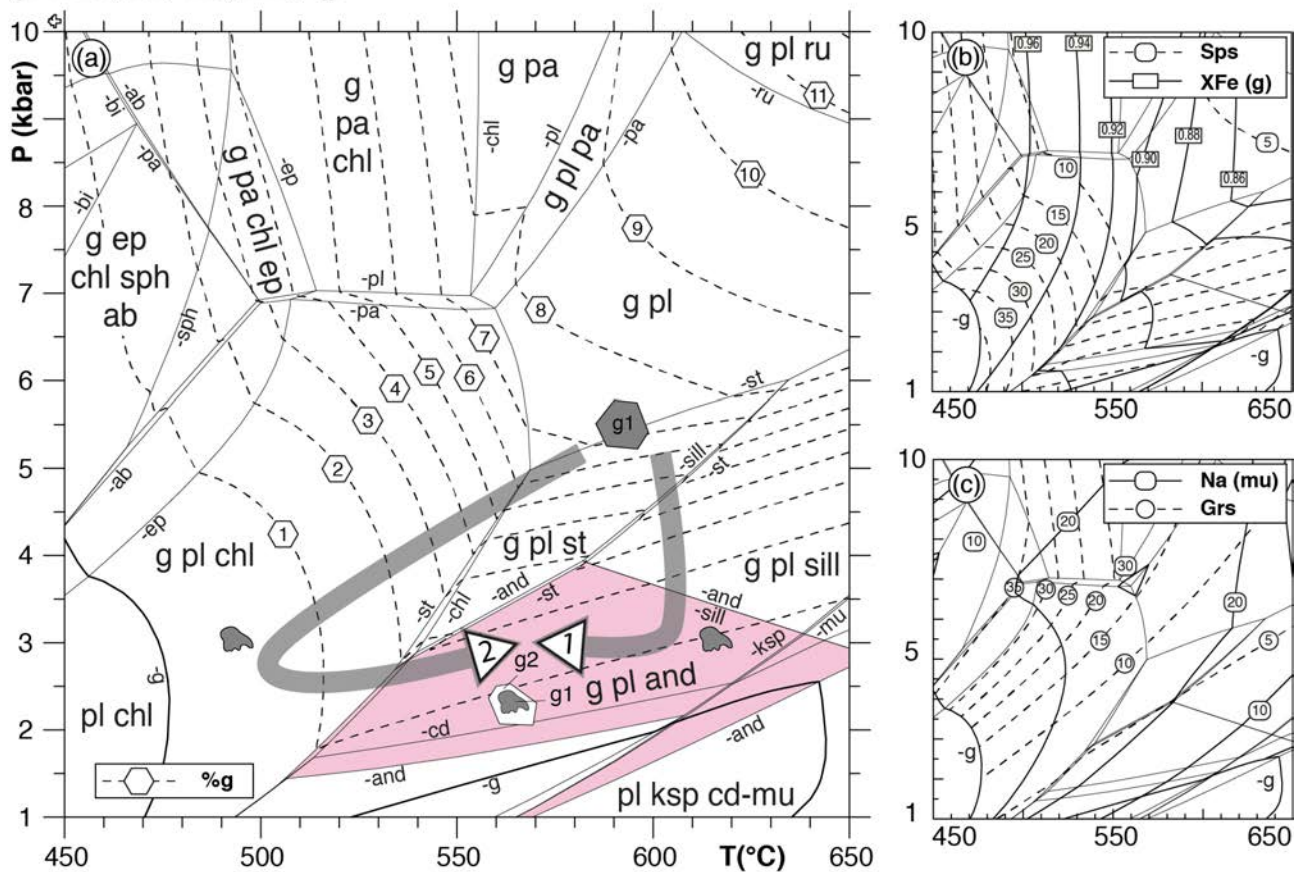


Figure III.9: (a) P - T pseudosection for a local estimated effective composition of the sample LH1B after having removed the contribution of the relictual cores of garnet 1 (see text), calculated to investigate the partial resorption of garnet 1 and subsequent growth of garnet 2. (b, c) Compositional isopleths for garnet and muscovite. Isopleths for garnet mode (a) have a steep negative slope in fields with chlorite and a low positive slope in the fields with andalusite. Arrows 1 and 2 represent two P - T paths that could account for the resorption of garnet 1 followed by the growth of garnet 2.

5.4. *Sample LH3*

P – T pseudosections have been calculated for a bulk composition measured over a small area (0.15 cm²) that includes garnet, staurolite, andalusite, biotite, muscovite, plagioclase, quartz and ilmenite. The diagram has been contoured with compositional isopleths for staurolite and muscovite as well as mode isopleths for garnet (Figure III.10). The peak M1 association staurolite, garnet, biotite, muscovite, plagioclase, quartz, ilmenite is modelled in the field g-st-pl-ilm between 3-7 kbar and 550-650 °C. The measured composition of staurolite ($X_{Fe} = 0.86$ -0.87) indicates equilibration around 5-6 kbar and 590-640 °C. The M2 association garnet 2, andalusite, biotite, muscovite, plagioclase, quartz, ilmenite corresponds to the g-pl-and-ilm field and indicates equilibration at 520-620 °C, 2-4 kbar. Removing garnet core (corresponding to garnet 1) from the measured composition does not introduce major modifications in the pseudosection, except that the garnet-out line is shifted toward higher pressures (~0.5 kbar, dashed line in the g-pl-and-ilm field; Figure III.10).

LH3 - MnNCKFMASHTO
(+ H₂O, bi, mu, q)

SiO ₂	TiO ₂	Al ₂ O ₃	F ₂ O ₃	FeO	MnO	MgO	CaO	Na ₂ O	K ₂ O
63.32	0.80	16.61	0.03	6.01	0.17	3.54	2.77	3.51	3.25

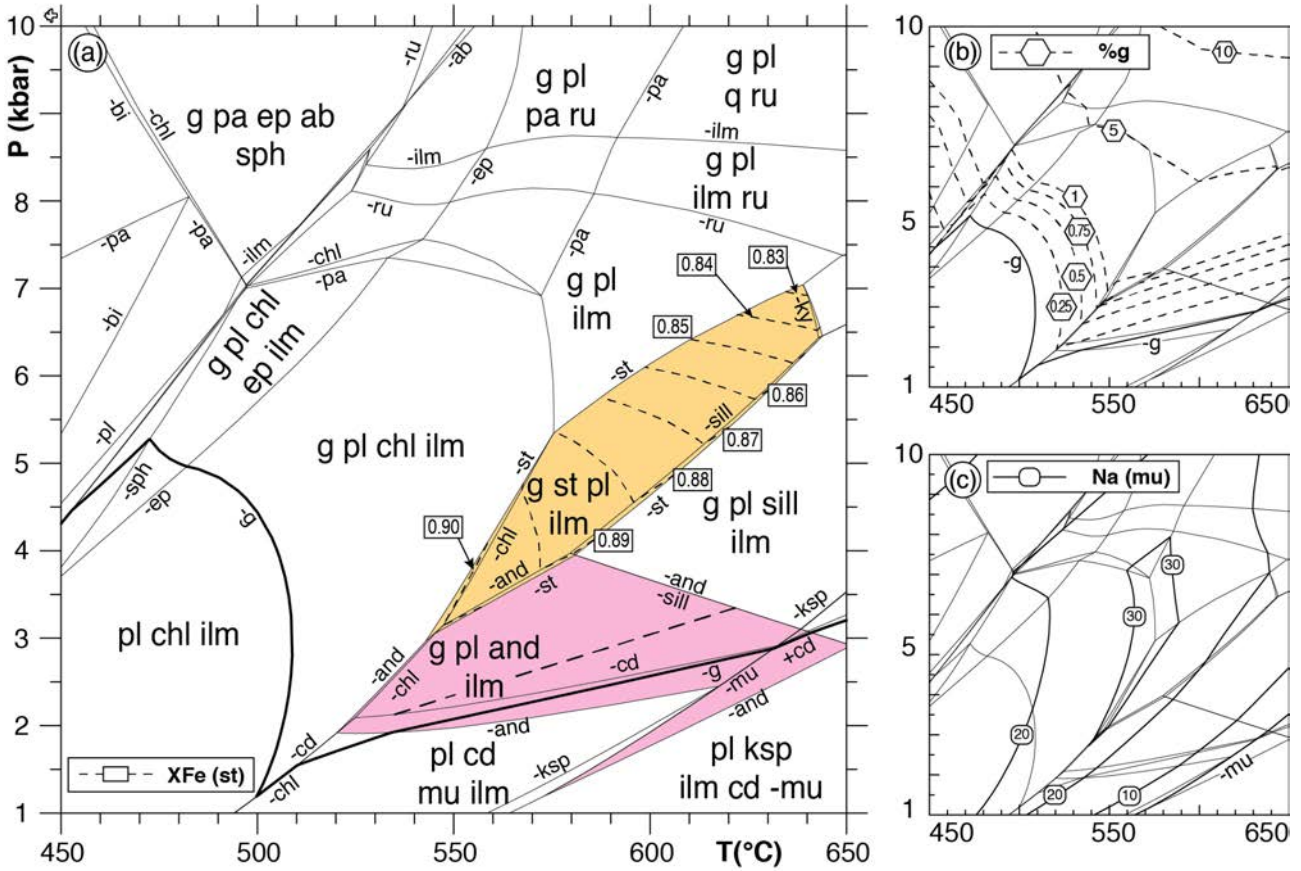


Figure III.10: P - T pseudosection for the sample LH3 contoured with compositional isopleths (X_{Fe}) for staurolite (a), mode isopleths for garnet (b), and compositional isopleths for muscovite (c). Dashed line in (a) indicates the displacement of the garnet-out line when garnet 1 is removed from the bulk composition used

5.5. Sample LH9 – Garnet-grunerite-bearing gneiss

The diagrams for this sample are shown in the supplementary material (Figure S4). They are calculated for the bulk composition measured over a small area (0.9 cm²) of the thin section considered as representative of the mineralogical composition of the sample. This area comprises grunerite, garnet, epidote, biotite, muscovite, ilmenite and quartz. The $X(Fe^{3+})$ ratio was set to 2%, following the exploration of a range of P/T - $X(Fe^{3+})$ pseudosections. In the resulting P - T pseudosection (Figure S4), biotite, quartz and ilmenite are stable over the whole P - T range modelled. Garnet is stable in most fields with the exception of those at $T < 485$ °C at $P < \sim 8$ kbar. Fe-Mg

clinoamphibole (cummingtonite-grunerite) is stable in the HP-LT part of the diagram ($P > 4$ kbar, $T < 560$ °C), epidote and chlorite in the LT ($T < 530$ °C and 550 °C, respectively) and plagioclase in the LP and HT part of the diagram. Orthoamphibole, not present in our samples, is stable in the LP-HT part of the diagram (550 - 650 °C, 1 - 6.5 kbar). Plagioclase and clinoamphibole are stable together only along a chaplet of small fields between 4 - 6 kbar and 490 - 560 °C (Figure S4), but none of them contains the complete inferred M1 paragenesis, comprising garnet, grunerite, epidote, biotite, plagioclase, muscovite, ilmenite and quartz. Despite the ubiquitous presence of chlorite, not observed in the M1 assemblage, it can be tentatively inferred, to first order, that garnet crystallization started in the field pl-chl-mu-ep (+ g, bi, ilm, q) at 480 - 510 °C, 3 - 6 kbar. The P - T evolution followed up pressure, up temperature to the field camp-chl-mu (+ g, bi, ilm, q) at 530 - 550 °C, 5.5 - 6 kbar. The M2 association epidote, biotite, muscovite, ilmenite, quartz (\pm chlorite, garnet) is not successfully modelled in the pseudosection either, since plagioclase (or albite), inferred not to be part of M2, is always present. Varying the $X(\text{Fe}^{3+})$ ratio does not improve the results.

6. Geochronology

Two metamorphic stages, associated with different regional structures, were identified in the Canigou metapelites. In order to set the tectono-metamorphic evolution in a temporal framework, an attempt was made to date some of the allanite and monazite grains found in sample LH16 in distinct textural positions. Unfortunately, the allanite grains were too small and too thin to get any meaningful data.

6.1. Analytical procedure

Suitable minerals for U-Th-Pb dating were identified using a petrological microscope and imaged using backscattered electron microscopy (BSE; CMEBA, Université Rennes 1, France). U-Th-Pb in-situ monazite dating was performed ‘in context’ directly in thin sections at Géosciences

Rennes using an ESI NWR193UC Excimer laser system coupled to an Agilent 7700x Q-ICP-MS, and consisted of 7 μm ablation spots with repetition rates of 2 Hz.

Raw data were corrected for Pb/U and Pb/Th laser-induced elemental fractionation and for instrumental mass discrimination by standard bracketing with repeated measurements of the Moacir monazite standard (Gasquet et al., 2010). With the samples, the Manangoutry monazite standard (*c.* 555 Ma; Paquette & Tiepolo 2007; 556.5 ± 3.9 Ma ($N = 7$), MSWD = 0.99) was measured as unknowns to monitor the precision and accuracy of the analyses. For more information on the procedures, see Ballouard et al. (2015). Operating conditions are given in Table S2.

Data reduction was carried out with the GLITTER® software package developed by the Macquarie Research Ltd. (Van Achterbergh, Ryan, & Griffin, 2001). Concordia ages and diagrams were generated using Isoplot/Ex (Ludwig, 2012). All errors given in Table 2 are listed at one sigma, but where data are combined for regression analysis or to calculate weighted means, the final results are provided with 95 % confidence limits.

6.2. U-Th-Pb dating

Monazite is found as small crystals ($\sim 30 \mu\text{m}$) either in the matrix or as inclusions in biotite, andalusite as well as along cracks in staurolite. These monazite grains show a slight patchy zoning (inset in Figure III.11). Twenty-four analyses were performed on ten monazite crystals in every textural position. The Th/U ratios of these grains vary between 7.1-10.9 in andalusite ($N = 12$), 4.5-6.8 in staurolite ($N = 4$) and 4.3-7.9 in biotite ($N = 8$) except for one inclusion in biotite with a significantly lower value (Th/U = 0.2). Plotted in a $^{206}\text{Pb}/^{238}\text{U}$ versus $^{208}\text{Pb}/^{232}\text{Th}$ Concordia diagram, a cluster of seventeen out of the twenty-four analyses (plain black ellipses, Figure III.11), regardless of their textural position, yields a concordant age of 300.0 ± 1.4 Ma (Figure III.11, MSWD = 0.85). Six other analyses yield older or younger dates (dashed ellipses, Figure III.11). Three older apparent ages plot between *c.* 317-305 Ma, with one having a very concordant apparent age and distinctive

Th/U (c. 317 Ma; Th/U = 0.2). The last and older apparent age plot at c. 330 Ma (long-dashed ellipse, Figure III.11).

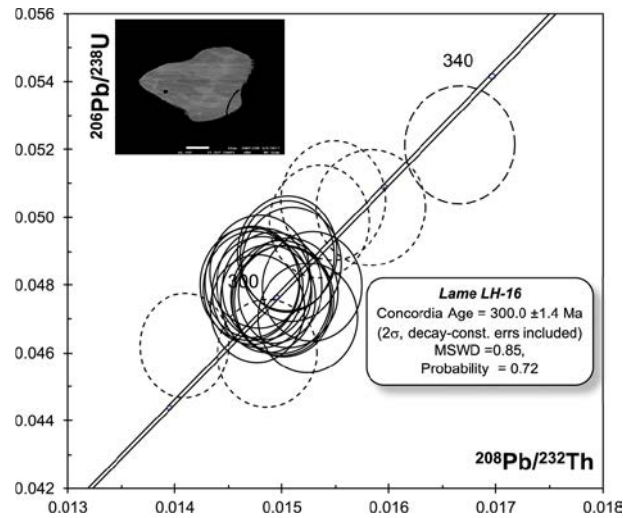


Figure III.11: $^{206}\text{Pb}/^{238}\text{U}$ versus $^{208}\text{Pb}/^{232}\text{Th}$ Concordia diagram for the monazite from sample LH16. Ellipses are plotted at 2 sigma. Inset backscattered electron image of representative monazite crystal from sample LH16.

7. Discussion

7.1. *P–T* conditions

Both the micaschists and the garnet-grunerite gneiss have been gathered in a small area within the same tectonic unit, and must have consequently undergone the same metamorphic history and broadly the same *P–T* conditions. In the micaschists, this is supported by the presence of the same key minerals in identical microstructural positions: staurolite for M1 and andalusite for M2. This can be used to further constrain the *P–T* evolution.

The first metamorphic event (M1) peaks with assemblages containing staurolite, garnet, biotite, muscovite, plagioclase quartz and ilmenite. The *P–T* conditions estimated from the different micaschist samples (LH1B: 3-7 kbar, 540-650 °C; LH3: 5-6 kbar, 590-630 °C; LH16: 4-5 kbar, 580 °C) suggest M1 peak *T* conditions of ~5 kbar, 600 °C. This M1 peak is the thermal culmination of a prograde evolution evidenced by the inclusions of epidote, progressive appearance of biotite and

Chapter III

chemical zoning in garnet (sample LH16), and that passed through a pressure peak at ~6-7 kbar, 550 °C.

The observation that the isopleths corresponding to the composition of the garnet core (LH16) only intersect at slightly higher temperature than the stability domain of epidote (around 520 °C and 5.5 kbar, Figure III.6) can be related to overstepping of the garnet-in reaction and subsequent fast crystallization in a metastable epidote-bearing matrix, or to later partial diffusional reequilibration of the composition of the garnet core, or to modelling uncertainties. These may include uncertainties in the estimation of the effective bulk composition, including, but not limited to, the $X(\text{Fe}^{3+})$ ratio, and also imperfections in the thermodynamic data and activity-composition relations. Textural and chemical evidence suggest subsequent partial resorption of garnet (outermost rim of large garnet and g1/g2 interface in small garnet), prior to the second metamorphic stage M2. This is compatible with a temperature and/or pressure decrease (Figures III.9a and III.10b).

The second metamorphic stage (M2) is characterized by the stability of andalusite. The overlap of the M2 P - T conditions (based on the composition of garnet 2 and muscovite) from the different samples, yields P - T conditions of ~2-3 kbar, 550-600 °C for this metamorphic stage (Figure III.9). The whole metamorphic evolution could then be interpreted in terms of a simple clockwise P - T path (arrow 1, Figure III.9). However, the growth of garnet 2 around partly resorbed garnet 1 possibly suggests a period of heating following decompression and cooling (arrow 2, Figure III.9), pointing to a two-stage evolution.

The results from the micaschists are difficult to reconcile with those for the garnet-grunerite gneiss. In the later, none of the fields modelled correspond to either the M1 or the M2 assemblage. The P - T conditions from the micaschists point to domains in the pseudosection without Fe-Mg clinoamphibole (grunerite) and with orthoamphibole, which was not observed in the sample. Clinoamphibole and epidote are modelled to be stable at temperatures lower by ~75 °C and ~50 °C, respectively. The reasons for this misfit are probably related to the imperfections of the existing

activity-composition relations for Fe-Mg clino- and orthoamphibole.

7.2. *Simple P – T loop or polymetamorphism?*

The key to this crucial question lies in the interpretation of the garnet 2 overgrowths on garnet 1. In order to allow garnet growth, the P – T path has to cross the isopleths of garnet mode in the sense of increasing proportion of garnet. Given the orientation of these isopleths, this can easily be achieved only along a prograde P – T path in the field g-pl-chl (Figure III.9, arrow 2). A continuous heating in the andalusite-bearing fields would lead to only slightly resorbing the newly formed garnet 2, or to keeping its proportion constant if heating was associated with a slight pressure increase.

A retrograde P – T path in the g-pl-and field, following decompression from the M1 stage, could theoretically produce similar features (Figure III.9a, arrow 1). However, retrograde growth of garnet appears to be uncommon, being rarely reported in the literature (e.g. Korhonen, Brown, Clark, & Bhattacharya, 2013). Furthermore, three first-order observations point to the growth of the M2 andalusite-bearing assemblage along a prograde P – T path. (1) The size of biotite inclusions increases from the core to the rim of andalusite (Figure III.4c). (2) In the andalusite stability field, the proportion of andalusite increases at the expense of muscovite with increasing temperature. Consequently, if garnet 2 crystallized during cooling, a concomitant replacement of andalusite by muscovite would be expected, but is not observed. (3) The growth of sillimanite (locally prismatic) at the expense of andalusite was reported in micaschists from the sillimanite zone in the north-western part of the “Balatg window” (Gibson, 1992; Guitard et al., 1998). Similar features are observed in sample BLB1457 collected in the sillimanite zone in the south-westernmost Balatg micaschists (Figure III.1, star 3; Figure III.12a). Consequently, it is suggested that M1 and M2 do not correspond to two stages of a simple clockwise metamorphic P – T loop, but rather to two prograde metamorphic (and deformational) events separated by a period of exhumation and cooling (Figure III.9a, arrow 2). Interestingly, Laumonier, Marignac, & Kister (2010), using general regional considerations, proposed

a similar scenario.

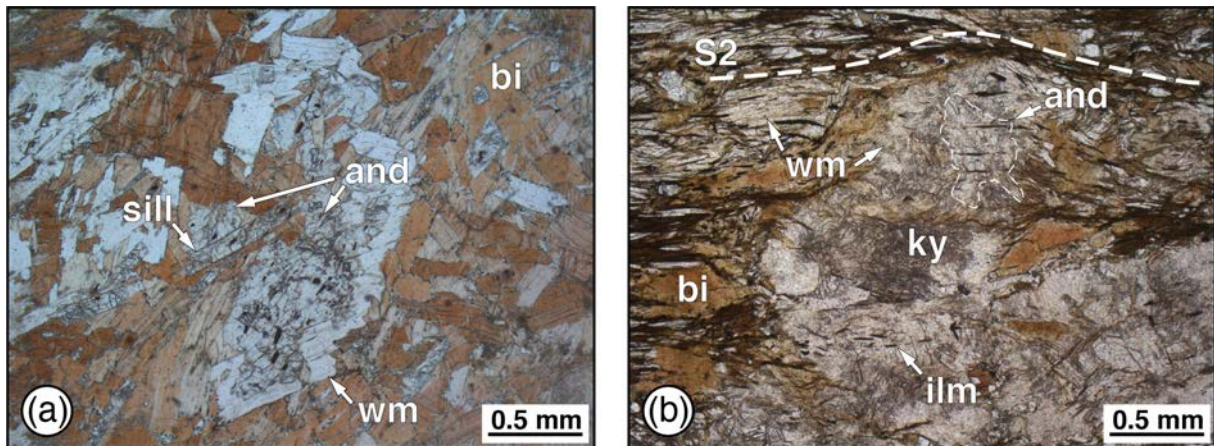


Figure III.12: (a) Photomicrograph of euhedral sillimanite cross-cutting anhedral andalusite (the individual parts are in optical continuity) in sample BLB1457 (located in Figure 1). Andalusite contains tiny anhedral inclusions of garnet and staurolite ($\sim 10 \mu\text{m}$). (b) Anhedral andalusite replaced by decussate aggregates of white mica (rims) and a cluster of small unoriented kyanite crystals (core). Sample BLB816 (Figure III.1).

7.3. Geochronology

In sample LH16, garnet crystallized along a prograde P – T path at temperatures ranging between 520 and 600 °C. It contains inclusions of allanite, the quantity of which strongly decreases in the garnet rims. Monazite is never found in garnet and only occurs as inclusions in either biotite, staurolite or andalusite that crystallized at temperatures reaching up to ~ 600 °C. This suggests metamorphic crystallization of monazite at the expense of allanite close to the peak of the prograde metamorphism M1. This appears to be a common feature in metapelitic rocks with increasing temperature in a similar P – T range. This typically happens near the staurolite (Smith & Barreiro, 1990; Spear & Pyle, 2002) or biotite isograds depending on the whole rock composition, and more particularly on the calcium and aluminium contents (Spear, 2010; Wing, Ferry, & Harrison, 2003). According to empiric determination of the allanite/monazite transition in metapelitic rocks (Wing et al., 2003), the crystallization of monazite in our sample ($\text{Ca}/\text{Ca}_{\text{Shaw}} = 0.90$ and $\text{Al}/\text{Al}_{\text{Shaw}} = 1.20$; calculated with respect to the average pelite composition defined by Shaw, 1956) occurred at a

temperature close to the biotite isograd ($\sim 550^\circ\text{C}$; i.e. close to the peak pressure during the M1 event in Figures III.7 and III.13).

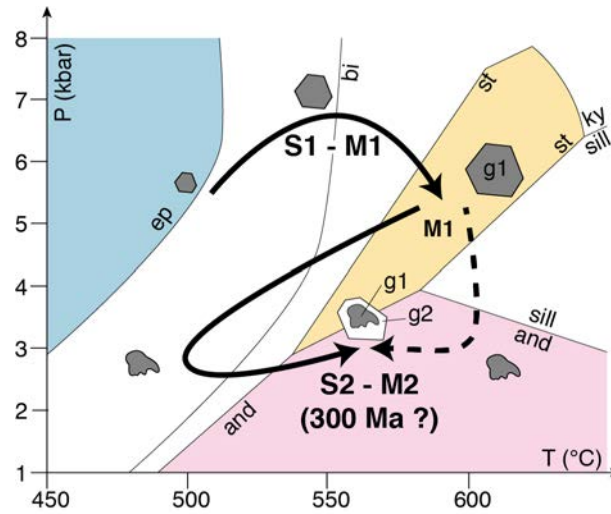


Figure III.13: Synthetic P - T paths with sketches of sequential growth of garnet. The prograde part of the P - T path between 5.5 kbar, 510°C and 6.7 kbar, 550°C corresponds to a gradient of $9^\circ\text{C}/\text{km}$.

Consequently, the easiest interpretation of the geochronological data would be that the *c.* 300 Ma age corresponds to the crystallization of monazite near the pressure peak of the M1 metamorphic event. The two younger dates can then be attributed to a slight lead loss. The four older apparent ages could be the result of either incorporation of external radiogenic lead during or after the initial crystallization of the monazite crystals, or partial resetting of older (detrital) grains.

On the other hand, despite the reputedly high closure temperature of its U-Th-Pb system (at least 700°C ; e.g. Cherniak, Watson, Grove, & Harrison, 2004; Parrish, 1990), monazite is known to recrystallize readily by dissolution/precipitation processes, in particular when fluids are involved (Didier et al., 2013; Tartèse, Ruffet, Poujol, Boulvais, & Ireland, 2011; Williams, Jercinovic, Harlov, Budzyń, & Hetherington, 2011). Consequently, the well-defined *c.* 300 Ma age cluster could correspond to the resetting of the M1 monazite during the dominant M2 LP-HT metamorphism. Inclusions in staurolite and biotite can be easily reset by interaction with fluids along fractures and cleavage planes. The apparent older ages would correspond to partly reset older (detrital) grains, or

represent relicts (possibly also partly reset) of the initial crystallization age of the M1 monazite.

Trace element (in particular Y and Th) zoning of monazite can be used to discriminate different generations of monazite (Kohn, 2016; Kohn, Wieland, Parkinson, & Upreti, 2005). However, this method commonly yields equivocal results (e.g. Štípská et al., 2015). Furthermore, in the present case, both M1 and M2 occur in subsolidus conditions, in assemblages containing garnet, and at similar temperatures. Consequently, they would be expected to bear similar trace element signatures and the detailed mapping of the analysed crystals has not been performed.

On the basis of these considerations, the *c.* 300 Ma age cannot readily be attributed to the M1 or the M2 metamorphic event. However, an extensive magmatic event associated with LP–HT metamorphism is well documented in the eastern Pyrenees at *c.* 305–300 Ma (Denèle et al., 2014). Consequently, the *c.* 300 Ma age most probably corresponds to monazite crystals having crystallized, or recrystallized during the M2 LP–HT event.

7.4. *Kyanite in the Canigou*

Kyanite has been described in several massifs of the Pyrenees in contrasting textural positions. In the Canigou, kyanite epitaxially intergrown with anhedral crystals of staurolite has been found as inclusion in cordierite and interpreted as a primary mineral (Azambre & Guitard, 2001). This association is inferred to represent an early medium-pressure event (that might be correlated with our M1), preceding a regionally lower-pressure high-temperature event. Conversely, in the Cap de Creus and Albères massifs, kyanite was found as pseudomorphs of andalusite and/or sillimanite and attributed to an increase in pressure during late folding, subsequent to the regional low-pressure metamorphic event (Autran, Fonteilles, & Guitard, 1966; Autran & Guitard, 1970; Fonteilles & Guitard, 1971).

In agreement with the results of thermodynamic modelling, no early (M1) kyanite has been found during this study, although M1 *P–T* conditions would lead to kyanite crystallization in rocks

with the appropriate chemical composition. Yet, in the micaschists overlying the orthogneiss (in the south-eastern part of the dome, Figure III.1, star 2), clusters of unoriented kyanite prisms (~10-100 μm) were discovered, surrounded by an undeformed corona of white mica (Figure III.12b). Such coronas were also found around anhedral crystals of andalusite and interpreted as pseudomorphs thereof. Consequently, this kyanite occurrence is interpreted as a pseudomorph after andalusite, subsequent to the M2 metamorphic event, and possibly related to cooling. Further investigation of this phenomenon is beyond the scope of this study.

7.5. Tectonic implications

Three types of tectonic models have been proposed for the Variscan Pyrenees, characterised by gneiss domes, and widespread LP–HT metamorphism and associated magmatism: 1) gravity-driven (diapiric) doming of hot lower crust (e.g. Aguilar et al., 2015; Soula, 1982; Soula, Debat, Deramond, & Pouget, 1986); 2) lithosphere-scale extension, following or not initial crustal thickening (e.g. Gibson, 1991; Vissers, 1992; Wickham & Oxburgh, 1986); 3) regional transpression (e.g. Carreras & Capella, 1994; Cochelin et al., 2017; Denèle, Olivier, Gleizes, & Barbey, 2009; Druguet, 2001; Gleizes, Leblanc, & Bouchez, 1998; Mezger, 2009). The latter have progressively evolved from models invoking pure transpression (e.g. Carreras & Capella, 1994) to those admitting a significant contribution of localised extension (e.g. Cochelin et al., 2017; Mezger & Passchier, 2003).

Our data from the Canigou massif show the existence of a MP–MT Barrovian metamorphism (M1), followed by decompression and cooling, before renewed heating at low pressures (M2). The regionally dominant foliation S2 is associated with the andalusite-bearing M2 assemblages that typify a LP–HT geothermal gradient. The peak pressure (6.5 kbar) recorded by the metasediments during the M1 stage corresponds to a minimum burial of about 25 km, assuming lithostatic pressure and a mean density of 2.7 g.cm⁻³ for the metasediments. Given the sedimentary nature of the protoliths,

Chapter III

such depths imply burial through subduction or crustal thickening. Relics of subduction zones have not been identified in the Variscan Pyrenees contrary to the other parts of the Variscan belt (e.g. Lardeaux, 2014; Paquette, Ballèvre, Peucat, & Cornen, 2017; Pin, 1990). The prograde up-pressure part of the P – T path is characterized by a cold gradient (of ~ 9 °C/km, Figure III.7), which suggests crustal thickening. Although important, this demonstration is not discriminatory, since most tectonic models (with the exception of Wickham & Oxburgh, 1986) implicitly or explicitly involve some initial crustal thickening.

The exhumation of the rocks indicated by the pressure decrease between M1 and M2 requires crustal thinning by extension and/or erosion (although other mechanisms may be important in other geological settings – e.g. diapiric ascent if rocks have a significant density contrast; e.g. Platt, 1993). Rapid extension and thinning of a previously thickened and thermally relaxed crust would lead to an evolution characterised by a nearly isothermal decompression (arrow 1 in Figure III.9; dashed arrow in Figure III.13; e.g. Gardien, Lardeaux, Ledru, Allemand, & Guillot, 1997; Rey, Teyssier, & Whitney, 2009; Sonder, England, Wernicke, & Christiansen, 1987). A similar P – T path is characteristic for models involving diapiric ascent of hot material (Aguilar et al., 2015; Lexa et al., 2011). Consequently, such tectonic models can be rejected for the Canigou massif, because this P – T path is not supported by our observations. The alternative P – T evolution, better supported by petrological data, involves a decrease in both pressure and temperature between stages M1 and M2 (arrow 2 in Figure III.9, solid arrow in Figure III.13; see also Laumonier et al., 2010). Such a P – T path can be attributed to an exhumation driven by significant erosion (albeit possibly combined with some extension) since crustal thickening induces surface elevation and subsequent relief increase (Thompson & England, 1984). It could also be achieved if extension was slow, since P – T paths may be very sensitive to strain rate (Rey et al., 2009).

Tectonic models featuring simple transpression associated with magmatism (Carreras & Capella, 1994; Carreras & Druguet, 2014, Denèle et al., 2009, Denèle et al., 2014) fail to account for,

Chapter III

or even discuss, the inferred decompression. Furthermore, these models, as well as the similar model of Mezger (2009), and the purely compressive model of Soliva, Salel & Brunel (1989) associate the regionally dominant foliation in the domes with early thrusting (and implicitly the medium-pressure metamorphism), which is at variance with our observations. Conversely, other tectonic interpretations invoke lateral flow of the lower crust as well as significant, albeit local, extension during regional transpression to explain the rising of the gneiss domes in the Variscan Pyrenees (Cochelin et al., 2017; Mezger & Passchier, 2003). The decrease of pressure between the M1 and M2 stages may be related to such thickness attenuation of the lower crust after crustal thickening (M1 stage) and depending on the strain rate may be accompanied by cooling.

The subsequent temperature increase (M2) would require an additional heat source. Numerous works have invoked extreme thinning of the lithospheric mantle by either delamination or detachment to explain such additional heat to account for the anomalously hot crust in the Variscan belt in general or specifically in the Pyrenees (Cochelin et al., 2017; Dewey, 1988; Gibson, 1991; Gutiérrez-Alonso et al., 2011; Henk, Blanckenburg, Finger, Schaltegger, & Zulauf, 2000; Ménard & Molnar, 1988; Vissers, 1992). The bimodal character of the abundant late Carboniferous magmatism as well as alkaline volcanism during the Permian in the Pyrenees (e.g. Driouch et al., 1989; Kilzi et al., 2016; Lago, Arranz, Pocoví, Galé, & Gil-Imaz, 2004) support such an interpretation. Although the origin of the mantle thinning remains unclear, it is predicted for and consequently supports tectonic models invoking significant crustal thickening and subsequent extension (e.g. Dewey, 1988; Houseman, McKenzie, & Molnar, 1981; Ménard & Molnar, 1988).

The late Carboniferous - Permian period is also marked by the occurrence of continental sedimentary basins that are considered to develop during transtensional, rather than transpressional, tectonics in the Variscan Pyrenees (Bixel & Lucas, 1983; Speksnijder, 1985). The proposed metamorphic evolution (solid arrow, Figure III.13), involving a slight pressure increase during the prograde LP metamorphism M2, may be explained by the overburden pressure caused by a significant

Chapter III

accumulation of detrital sediments (cf. Martínez, Reche, & Arboleya, 2001; Pitra & Guiraud, 1996), later removed by erosion during the Mesozoic. Alternatively, this slight pressure increase may be related to the late crustal shortening invoked to account for the reactivation of previous extensional shear zones into steeply dipping transpressive shear zones, resulting in the amplification of the gneiss domes (e.g. Cochelin et al., 2017). Nevertheless, the timing of the activity of these shear zones, crucial to all the transpressive models, remains a matter of vigorous argument, and could be to a significant degree Alpine rather than Variscan in age (Monié, Soliva, Brunel, & Maluski, 1994; Vissers, Hinsbergen, Ganerød, & Wilkinson, 2018; Vissers, Hinsbergen, Wilkinson, & Ganerød, 2017).

To sum up, after the crustal thickening, our data require a phase of relatively slow crustal thinning. This can be achieved by erosion and/or slow extension or transtension. Tectonic interpretations involving generalized rapid extension, diapiric ascent of the gneiss domes or those suggesting pure transpression do not account for the P – T evolution inferred for the Canigou massif.

The lack of radiometric data in the Canigou massif does not allow to determine the precise timing for the two metamorphic stages, especially the time gap between crustal thickening and subsequent thinning. However, we tentatively propose the following scenario. As noted above most tectonic interpretations of the Variscan Pyrenees involve a phase of crustal thickening that predates the regional ductile deformation coeval with the pervasive LP–HT metamorphism (M2). The Culm sedimentation in the Variscan Pyrenean foreland basin is considered to mark this phase of thickening (Delvolvé, Vachard, & Souquet, 1998; Engel & Raymond, 1983). The time span of the Culm sedimentation in the eastern Pyrenees has recently been determined at 330–319 Ma (Martín-Closas, Trias, & Casas Tuset, 2018). As discussed previously, the M2 LP–HT metamorphism most probably developed around *c.* 300 Ma. If true, this leaves a time gap of about 20 Ma between the two phases of metamorphism M1 and M2, allowing for the thermal relaxation of the thickened crust and its subsequent lateral flow.

8. Conclusions

Two syntectonic metamorphic stages have been recognized in the metapelites underlying the orthogneiss in the core of the dome-shaped Canigou massif. The first metamorphic stage is characterized by the crystallization of staurolite at 5.5 kbar and 580 °C, following a prograde up-pressure, up-temperature evolution through the peak pressure at ~6.5 kbar, 550 °C, constrained by garnet zoning. It is associated with the S1 foliation, only preserved in the core of the Canigou massif. The second metamorphic stage, characterized by the crystallization of andalusite, implies a pressure decrease of about 2.5 kbar. It is coeval with the development of the main regional fabric S2 that transposes S1 and defines the dome shape of the massif. Resorption of garnet between the two metamorphic stages and its subsequent renewed growth is tentatively attributed to a two-stage P – T path. This involves an exhumation dominated by erosion and/or slow extension followed by heating, probably associated with the delamination of the lithospheric mantle and the regional magmatic event. The *c.* 300 Ma monazite age is tentatively attributed to monazite recrystallization during the M2 LP–HT stage.

Acknowledgements

This work received the support of the Bureau de Recherches Géologiques et Minières (BRGM) through the “Référentiel Géologique de la France” programme (RGF). The newly acquired data compiled into the Geofield database will be available on the RGF website (www.rgf.brgm.fr). X. Le Coz is acknowledged for the efficient production of the numerous thin sections. We are grateful for the assistance in SEM observations and EDS analyses of the staff of the CMEBA facility (ScanMAT, University Rennes 1), which received a financial support from the Région Bretagne and the European Union (CPER-FEDER 2007-2014). The detailed reviews of J. Mezger and an anonymous reviewer, and the helpful editorial handling of M. Brown are gratefully acknowledged.

Conflict of interest

No conflict of interests to declare.

References

- Aguilar, C., Liesa, M., Castiñeiras, P., & Navidad, M. (2014). Late Variscan metamorphic and magmatic evolution in the eastern Pyrenees revealed by U–Pb age zircon dating. *Journal of the Geological Society*, 171(2), 181–192. <https://doi.org/10.1144/jgs2012-086>
- Aguilar, C., Liesa, M., Štípská, P., Schulmann, K., Muñoz, J. A., & Casas, J. M. (2015). P–T–t–d evolution of orogenic middle crust of the Roc de Frausa Massif (Eastern Pyrenees): a result of horizontal crustal flow and Carboniferous doming? *Journal of Metamorphic Geology*, 33(3), 273–294. <https://doi.org/10.1111/jmg.12120>
- Auriol, L., & Casteras, M. (1958). Les témoins de la couverture posthercynienne de la zone axiale à l'E et au SE du Canigou. *Bulletin de La Société Géologique de France*, S6-VIII(8), 871–880. <https://doi.org/10.2113/gssgfbull.S6-VIII.8.871>
- Autran, A., Fontelles, M., & Guitard, G. (1966). Discordance du Paléozoïque inférieur métamorphique sur un socle gneissique antéhercynien dans le massif des Albères (Pyrénées orientales). *Comptes Rendus de l'Académie Des Sciences, Paris*, 263, 317–320.
- Autran, A., & Guitard, G. (1970). Hystero-genic formation of kyanite in mesozonal micaschists with andalusite and sillimanite of Paleozoic series of the Cap de Creus, Eastern Pyrenees. *Comptes Rendus de l'Académie Des Sciences, Paris*, 270(22), 2616.
- Azambre, B., & Guitard, G. (2001). Disthène et staurotide reliques dans les métapelites du Canigou (Pyrénées orientales). Relations avec les épisodes hercyniens de basse et moyenne pressions. *Comptes Rendus de l'Académie des Sciences*, 333(10), 601–609. [https://doi.org/10.1016/S1251-8050\(01\)01670-6](https://doi.org/10.1016/S1251-8050(01)01670-6)
- Ballouard, C., Boulvais, P., Poujol, M., Gapais, D., Yamato, P., Tartèse, R., & Cuney, M. (2015). Tectonic record, magmatic history and hydrothermal alteration in the Hercynian Guérande leucogranite, Armorican Massif, France. *Lithos*, 220, 1–22. <https://doi.org/10.1016/j.lithos.2015.01.027>

- Barbey, P., Cheilletz, A., & Laumonier, B. (2001). The Canigou orthogneisses (Eastern Pyrenees, France, Spain): an Early Ordovician rapakivi granite laccolith and its contact aureole. *Comptes Rendus de l'Académie Des Sciences - Series IIA - Earth and Planetary Science*, 332(2), 129–136. [https://doi.org/10.1016/S1251-8050\(00\)01506-8](https://doi.org/10.1016/S1251-8050(00)01506-8)
- Bixel, F., & Lucas, C. L. (1983). Magmatisme, tectonique et sédimentation dans les fossés stéphanopériens des Pyrénées occidentales. *Revue de Géologie Dynamique et de Géographie Physique*, 24(4), 329–342.
- Carreras, J., & Capella, I. (1994). Structures and Tectonics at Different Lithospheric Levels Tectonic levels in the Palaeozoic basement of the Pyrenees: a review and a new interpretation. *Journal of Structural Geology*, 16(11), 1509–1524. [https://doi.org/10.1016/0191-8141\(94\)90029-9](https://doi.org/10.1016/0191-8141(94)90029-9)
- Cherniak, D. J., Watson, E. B., Grove, M., & Harrison, T. M. (2004). Pb diffusion in monazite: a combined RBS/SIMS. *Geochimica et Cosmochimica Acta*, 68(4), 829–840. <https://doi.org/10.1016/j.gca.2003.07.012>
- Cochelin, B., Chardon, D., Denèle, Y., Gumiaux, C., & le Bayon, B. (2017). Vertical strain partitioning in hot Variscan crust: Syn-convergence escape of the Pyrenees in the Iberian-Armorican syntax. *Bulletin de La Société Géologique de France*, 188(6), 39. <https://doi.org/10.1051/bsgf/2017206>
- Coggon, R., & Holland, T. J. B. (2002). Mixing properties of phengitic micas and revised garnet-phengite thermobarometers. *Journal of Metamorphic Geology*, 20(7), 683–696. <https://doi.org/10.1046/j.1525-1314.2002.00395.x>
- Connolly, J. A. D., & Cesare, B. (1993). C-O-H-S fluid composition and oxygen fugacity in graphitic metapelites. *Journal of Metamorphic Geology*, 11(3), 379–388. <https://doi.org/10.1111/j.1525-1314.1993.tb00155.x>
- de Capitani, C., & Brown, T. H. (1987). The computation of chemical equilibrium in complex systems containing non-ideal solutions. *Geochimica et Cosmochimica Acta*, 51(10), 2639–2652. [https://doi.org/10.1016/0016-7037\(87\)90145-1](https://doi.org/10.1016/0016-7037(87)90145-1)
- de Capitani, C., & Petrakakis, K. (2010). The computation of equilibrium assemblage diagrams with Theriak/Domino software. *American Mineralogist*, 95(7), 1006–1016. <https://doi.org/10.2138/am.2010.3354>
- Deloule, E., Alexandrov, P., Cheilletz, A., Laumonier, B., & Barbey, P. (2002). In-situ U–Pb zircon ages for Early Ordovician magmatism in the eastern Pyrenees, France: the Canigou

Chapter III

- orthogneisses. *International Journal of Earth Sciences*, 91(3), 398–405.
<https://doi.org/10.1007/s00531-001-0232-0>
- Delvolvé, J.-J., Vachard, D., & Souquet, P. (1998). Stratigraphic record of thrust propagation, Carboniferous foreland basin, Pyrenees, with emphasis on Pays-de-Sault (France/Spain). *Geologische Rundschau*, 87(3), 363–372. <https://doi.org/10.1007/s005310050215>
- Denèle, Y., Laumonier, B., Paquette, J.-L., Olivier, P., Gleizes, G., & Barbey, P. (2014). Timing of granite emplacement, crustal flow and gneiss dome formation in the Variscan segment of the Pyrenees. *Geological Society, London, Special Publications*, 405(1), 265–287. <https://doi.org/10.1144/SP405.5>
- Denèle, Y., Olivier, P., Gleizes, G., & Barbey, P. (2009). Decoupling between the middle and upper crust during transpression-related lateral flow: Variscan evolution of the Aston gneiss dome (Pyrenees, France). *Tectonophysics*, 477(3), 244–261. <https://doi.org/10.1016/j.tecto.2009.04.033>
- De Sitter, L.U. & Zwart, H.J. 1960. Tectonic development in supra- and infrastructures of a mountain chain. In: Kale, A. & Metzler, A. (eds) *Structure of the Earth's crust and deformation of rocks, Proceedings 21st International Geological Congress*. Det Berlingske Bogtrykkeri, Copenhagen, 18, 248–256.
- Dewey, J. F. (1988). Extensional collapse of orogens. *Tectonics*, 7(6), 1123–1139. <https://doi.org/10.1029/TC007i006p01123>
- Didier, A., Bosse, V., Boulvais, P., Bouloton, J., Paquette, J.-L., Montel, J.-M., & Devidal, J.-L. (2013). Disturbance versus preservation of U–Th–Pb ages in monazite during fluid–rock interaction: textural, chemical and isotopic in situ study in microgranites (Velay Dome, France). *Contributions to Mineralogy and Petrology*, 165(6), 1051–1072. <https://doi.org/10.1007/s00410-012-0847-0>
- Diener, J. F. A., & Powell, R. (2012). Revised activity–composition models for clinopyroxene and amphibole. *Journal of Metamorphic Geology*, 30(2), 131–142. <https://doi.org/10.1111/j.1525-1314.2011.00959.x>
- Driouch, Y., Dahmani, A., Debat, P., Pouget, P., Seyler, M., & Soula, J. C. (1989). Les formations ultrabasiques et basiques au sein des séries mésocrustales des Pyrénées hercyniennes. *Comptes Rendus de l'Académie Des Sciences.*, 308(14), 1249–1255.

- Druguet, E., 2001. Development of high thermal gradients by coeval transpression and magmatism during the Variscan orogeny: insights from the Cap de Creus (Eastern Pyrenees). *Tectonophysics*, 332, 275-293.
- Druguet, E., Castro, A., Chichorro, M., Pereira, M. F., & Fernández, C. (2014). Zircon geochronology of intrusive rocks from Cap de Creus, Eastern Pyrenees. *Geological Magazine*, 151(6), 1095–1114. <https://doi.org/10.1017/S0016756814000041>
- Engel, W., & Raymond, D. (1983). Phénomènes de resédimentation dans le Carbonifère a faciés Culm du Haut Pays de Sault (E de la zone primaire axiale pyrénéenne, France). Signification géodynamique dans la branche sud de l’orogène varisque. *Bulletin de La Société Géologique de France*, S7-XXV(6), 921–926. <https://doi.org/10.2113/gssgfbull.S7-XXV.6.921>
- England, P. C., & Thompson, A. B. (1984). Pressure—Temperature—Time Paths of Regional Metamorphism I. Heat Transfer during the Evolution of Regions of Thickened Continental Crust. *Journal of Petrology*, 25(4), 894–928. <https://doi.org/10.1093/petrology/25.4.894>
- Esteban, J. J., Aranguren, A., Cuevas, J., Hilario, A., Tubía, J. M., Larionov, A., & Sergeev, S. (2015). Is there a time lag between the metamorphism and emplacement of plutons in the Axial Zone of the Pyrenees? *Geological Magazine*, 152(5), 935–941. <https://doi.org/10.1017/S001675681500014X>
- Feenstra, A. (1996). An EMP and TEM—AEM Study of Margarite, Muscovite and Paragonite in Polymetamorphic Metabauxites of Naxos Cyclades, Greece) and the Implications of Fine-scale Mica Interlayering and Multiple Mica Generations. *Journal of Petrology*, 37(2), 201–233. <https://doi.org/10.1093/petrology/37.2.201>
- Fontboté, J. M., & Guitard, G. (1958). Aperçus sur la tectonique cassante de la zone axiale des Pyrenees orientales entre les bassins de Cerdagne et de l’ Ampurdan-Roussillon. *Bulletin de La Société Géologique de France*, S6-VIII(8), 884–890. <https://doi.org/10.2113/gssgfbull.S6-VIII.8.884>
- Fonteilles, M., & Guitard, G. (1971). Disthène relique et disthène hystérogène dans les terrains métamorphiques hercyniens des Pyrénées orientales franco-espagnoles. *Comptes Rendus de l’Académie Des Sciences, Paris*, 272, 361–363.
- Gardien, V., Lardeaux, J.-M., Ledru, P., Allemand, P., & Guillot, S. (1997). Metamorphism during late orogenic extension; insights from the French Variscan belt. *Bulletin de La Société Géologique de France*, 168(3), 271–286.

- Gasquet, D., Bertrand, J. M., Paquette, J. L., Lehmann, J., Ratzov, G., Guedes, R. D. A., ... Nomade, S. (2010). Miocene to Messinian deformation and hydrothermal activity in a pre-Alpine basement massif of the French western Alps: new U-Th-Pb and argon ages from the Lauzière massif. *Bulletin de La Société Géologique de France*, 181(3), 227–241. <https://doi.org/10.2113/gssgfbull.181.3.227>
- Gibson, R. L. (1991). Hercynian low-pressure-high-temperature regional metamorphism and subhorizontal foliation development in the Canigou massif, Pyrenees, France—Evidence for crustal extension. *Geology*, 19(4), 380–383. [https://doi.org/10.1130/0091-7613\(1991\)019<0380:HLPHTR>2.3.CO;2](https://doi.org/10.1130/0091-7613(1991)019<0380:HLPHTR>2.3.CO;2)
- Gibson, R. L. (1992). Sequential, syndeformational porphyroblast growth during Hercynian low-pressure/high-temperature metamorphism in the Canigou massif, Pyrenees. *Journal of Metamorphic Geology*, 10(5), 637–650. <https://doi.org/10.1111/j.1525-1314.1992.tb00112.x>
- Gibson, R. L., & Bickle, M. J. (1994). Thermobarometric constraints on the conditions of metamorphism in the Canigou massif, Pyrenees: implications for Hercynian geothermal gradients. *Journal of the Geological Society*, 151(6), 987–997. <https://doi.org/10.1144/gsjgs.151.6.0987>
- Gleizes, G., Leblanc, D., & Bouchez, J. L. (1998). The main phase of the Hercynian orogeny in the Pyrenees is a dextral transpression. *Geological Society, London, Special Publications*, 135(1), 267–273. <https://doi.org/10.1144/GSL.SP.1998.135.01.17>
- Guitard, G. (1970). Le métamorphisme hercynien mésozonal et les gneiss oeillés du massif du Canigou:(Pyrénées-Orientales). *Mémoires du BRGM*, 63, 353 pp.
- Guitard, G., Laumonier, B., Autran, A., Bandet, Y., & Berger, G. M. (1998). Notice explicative, Carte géol. France (1/50 000), feuille Prades (1095). Orléans : BRGM, 198 p. Carte géologique par G. Guitard et al. (1992).
- Gutiérrez-Alonso, G., Murphy, J. B., Fernández-Suárez, J., Weil, A. B., Franco, M. P., & Gonzalo, J. C. (2011). Lithospheric delamination in the core of Pangea: Sm-Nd insights from the Iberian mantle. *Geology*, 39(2), 155–158. <https://doi.org/10.1130/G31468.1>
- Henk, A., Blanckenburg, F. von, Finger, F., Schaltegger, U., & Zulauf, G. (2000). Syn-convergent high-temperature metamorphism and magmatism in the Variscides: a discussion of potential

- heat sources. *Geological Society, London, Special Publications*, 179(1), 387–399. <https://doi.org/10.1144/GSL.SP.2000.179.01.23>
- Höck, V. (1974). Coexisting phengite, paragonite and margarite in metasediments of the mittlere Hohe Tauern, Austria. *Contributions to Mineralogy and Petrology*, 43(4), 261–273. <https://doi.org/10.1007/BF00373483>
- Holland, T., & Blundy, J. (1994). Non-ideal interactions in calcic amphiboles and their bearing on amphibole-plagioclase thermometry. *Contributions to Mineralogy and Petrology*, 116(4), 433–447. <https://doi.org/10.1007/BF00310910>
- Holland, T., & Powell, R. (1998). An internally consistent thermodynamic data set for phases of petrological interest. *Journal of Metamorphic Geology*, 16(3), 309–343. <https://doi.org/10.1111/j.1525-1314.1998.00140.x>
- Holland, T., & Powell, R. (2003). Activity–composition relations for phases in petrological calculations: an asymmetric multicomponent formulation. *Contributions to Mineralogy and Petrology*, 145(4), 492–501. <https://doi.org/10.1007/s00410-003-0464-z>
- Holland, T., Baker, J., & Powell, R. (1998). Mixing properties and activity-composition relationships of chlorites in the system MgO-FeO-Al₂O₃-SiO₂-H₂O. *European Journal of Mineralogy*, 395–406. <https://doi.org/10.1127/ejm/10/3/0395>
- Houseman, G. A., McKenzie, D. P., & Molnar, P. (1981). Convective instability of a thickened boundary layer and its relevance for the thermal evolution of continental convergent belts. *Journal of Geophysical Research: Solid Earth*, 86(B7), 6115–6132. <https://doi.org/10.1029/JB086iB07p06115>
- Kilzi, M. A., Grégoire, M., Bosse, V., Benoît, M., Driouch, Y., de Saint Blanquat, M. & Debat, P., 2016. Geochemistry and zircon U–Pb geochronology of the ultramafic and mafic rocks emplaced within the anatectic series of the Variscan Pyrenees: The example of the Gavarnie–Heas dome (France). *Comptes Rendus Geoscience*, 348, 107–115.
- Kohn, M. J. (2016). Metamorphic chronology—a tool for all ages: Past achievements and future prospects. *American Mineralogist*, 101(1), 25–42. <https://doi.org/10.2138/am-2016-5146>
- Kohn, M. J., Wieland, M. S., Parkinson, C. D., & Upreti, B. N. (2005). Five generations of monazite in Langtang gneisses: implications for chronology of the Himalayan metamorphic core. *Journal of Metamorphic Geology*, 23(5), 399–406. <https://doi.org/10.1111/j.1525-1314.2005.00584.x>

- Korhonen, F. J., Brown, M., Clark, C. & Bhattacharya, S., 2013. Osumilite–melt interactions in ultrahigh temperature granulites: phase equilibria modelling and implications for the P–T–t evolution of the Eastern Ghats Province, India. *Journal of Metamorphic Geology*, 31, 881–907. <https://doi.org/10.1111/jmg.12049>
- Lago, M., Arranz, E., Pocoví, A., Galé, C., & Gil-Imaz, A. (2004). Permian magmatism and basin dynamics in the southern Pyrenees: a record of the transition from late Variscan transtension to early Alpine extension. *Geological Society, London, Special Publications*, 223(1), 439–464. <https://doi.org/10.1144/GSL.SP.2004.223.01.19>
- Lardeaux, J. M. (2014). Deciphering orogeny: a metamorphic perspective Examples from European Alpine and Variscan belts. *Bulletin de La Société Géologique de France*, 185(5), 281–310. <https://doi.org/10.2113/gssgfbull.185.5.281>
- Laumonier, B., Le Bayon, B., & Calvet, M. (2015). Carte géologique France (1/50 000), feuille Prats-de-Mollo-La-Prete (1099). Orléans : BRGM. Notice explicative par Laumonier, B., Calvet, M., Le Bayon, B., Barbey, P., Lenoble, J.-L., 2015, 189p. Orléans.
- Laumonier, B., Marignac, C., & Kister, P. (2010). Polymétamorphisme et évolution crustale dans les Pyrénées orientales pendant l’orogénèse varisque au Carbonifère supérieur. *Bulletin de la Société géologique de France*, 181(5), 411–428.
- Le Bayon, B., Pitra, P., Ballevre, M., & Bohn, M. (2006). Reconstructing P–T paths during continental collision using multi-stage garnet (Gran Paradiso nappe, Western Alps). *Journal of Metamorphic Geology*, 24(6), 477–496. <https://doi.org/10.1111/j.1525-1314.2006.00649.x>
- Lexa, O., Schulmann, K., Janoušek, V., Štípská, P., Guy, A., & Racek, M. (2011). Heat sources and trigger mechanisms of exhumation of HP granulites in Variscan orogenic root. *Journal of Metamorphic Geology*, 29(1), 79–102. <https://doi.org/10.1111/j.1525-1314.2010.00906.x>
- López-Carmona, A., Pitra, P., & Abati, J. (2013). Blueschist-facies metapelites from the Malpica–Tui Unit (NW Iberian Massif): phase equilibria modelling and H₂O and Fe₂O₃ influence in high-pressure assemblages. *Journal of Metamorphic Geology*, 31(3), 263–280. <https://doi.org/10.1111/jmg.12018>
- Lopez-Sanchez, M. A., García-Sansegundo, J., & Martínez, F. J. (2018). The significance of early Permian and early Carboniferous U–Pb zircon ages in the Bossòst and Lys-Caillaouas granitoids (Pyrenean Axial Zone). *Geological Journal*, 0(0). <https://doi.org/10.1002/gj.3283>

- Ludwig, K. R. (2012). Isoplot/Ex, v. 3.75. Berkeley Geochronology Center Special Publication, 5.
- Martín-Closas, C., Trias, S., & Casas Tuset, J. M. (2018). New palaeobotanical data from Carboniferous Culm deposits constrain the age of the Variscan deformation in the eastern Pyrenees. *Geologica acta*, 16(2), 0107–0123. <https://doi.org/10.1344/GeologicaActa2018.16.2.1>
- Martínez, F. J., Reche, J., & Arboleya, M. L. (2001). P–T modelling of the andalusite–kyanite–andalusite sequence and related assemblages in high-Al graphitic pelites. Prograde and retrograde paths in a late kyanite belt in the Variscan Iberia. *Journal of Metamorphic Geology*, 19(6), 661–677. <https://doi.org/10.1046/j.0263-4929.2001.00335.x>
- Maurel, O., Monié, P., Pik, R., Arnaud, N., Brunel, M., & Jolivet, M. (2008). The Meso-Cenozoic thermo-tectonic evolution of the Eastern Pyrenees: an ⁴⁰Ar/³⁹Ar fission track and (U–Th)/He thermochronological study of the Canigou and Mont-Louis massifs. *International Journal of Earth Sciences*, 97(3), 565–584.
- Ménard, G., & Molnar, P. (1988). Collapse of a Hercynian Tibetan Plateau into a late Palaeozoic European Basin and Range province. *Nature*, 334(6179), 235. <https://doi.org/10.1038/334235a0>
- Mezger, J. E. (2009). Transpressional tectonic setting during the main Variscan deformation: evidence from four structural levels in the Bossòst and Aston-Hospitalet mantled gneiss domes, central Axial Zone, Pyrenees. *Bulletin de La Société Géologique de France*, 180(3), 199–207. <https://doi.org/10.2113/gssgfbull.180.3.199>
- Mezger, J. E., & Gerdes, A. (2016). Early Variscan (Visean) granites in the core of central Pyrenean gneiss domes: implications from laser ablation U–Pb and Th–Pb studies. *Gondwana Research*, 29(1), 181–198. <https://doi.org/10.1016/j.gr.2014.11.010>
- Mezger, J. E., & Passchier, C. W. (2003). Polymetamorphism and ductile deformation of staurolite–cordierite schist of the Bossòst dome: indication for Variscan extension in the Axial Zone of the central Pyrenees. *Geological Magazine*, 140(5), 595–612. <https://doi.org/10.1017/S0016756803008112>
- Mezger, J. E., Passchier, C. W., & Régnier, J. L. (2004). Metastable staurolite–cordierite assemblage of the Bossòst dome: Late Variscan decompression and polyphase metamorphism in the Axial Zone of the central Pyrenees. *Comptes Rendus Geoscience*, 336(9), 827–837. <https://doi.org/10.1016/j.crte.2003.12.024>

- Mezger, J. E., & Régnier, J.-L. (2016). Stable staurolite–cordierite assemblages in K-poor metapelitic schists in Aston and Hospitalet gneiss domes of the central Pyrenees (France, Andorra). *Journal of Metamorphic Geology*, 34(2), 167–190. <https://doi.org/10.1111/jmg.12177>
- Monié, P., Soliva, J., Brunel, M., & Maluski, H. (1994). Les cisaillements mylonitiques du granite de Millas (Pyrénées, France). Age Crétacé 40 Ar/ 39 Ar et interprétation tectonique. *Bulletin de La Société Géologique de France*, 165(6), 559–571.
- Padel, M., Álvaro, J. J., Casas, J. M., Clausen, S., Pujol, M., & Sánchez-García, T. (2017). Cadomian volcanosedimentary complexes across the Ediacaran–Cambrian transition of the Eastern Pyrenees, southwestern Europe. *International Journal of Earth Sciences*, 1–23. <https://doi.org/10.1007/s00531-017-1559-5>
- Paquette, J. L., Ballèvre, M., Peucat, J. J., & Cornen, G. (2017). From opening to subduction of an oceanic domain constrained by LA-ICP-MS U-Pb zircon dating (Variscan belt, Southern Armorican Massif, France). *Lithos*, 294–295(Supplement C), 418–437. <https://doi.org/10.1016/j.lithos.2017.10.005>
- Paquette, J. L., & Tiepolo, M. (2007). High resolution (5 µm) U–Th–Pb isotope dating of monazite with excimer laser ablation (ELA)-ICPMS. *Chemical Geology*, 240(3), 222–237. <https://doi.org/10.1016/j.chemgeo.2007.02.014>
- Parrish, R. R. (1990). U–Pb dating of monazite and its application to geological problems. *Canadian Journal of Earth Sciences*, 27(11), 1431–1450. <https://doi.org/10.1139/e90-152>
- Pin, C. (1990). Variscan oceans: ages, origins and geodynamic implications inferred from geochemical and radiometric data. *Tectonophysics*, 177(1), 215–227.
- Pitra, P., & Guiraud, M. (1996). Probable anticlockwise P–T evolution in extending crust: Hlinsko region, Bohemian Massif. *Journal of Metamorphic Geology*, 14(1), 49–60. <https://doi.org/10.1111/j.1525-1314.1996.t01-1-00049.x>
- Platt, J. P. (1993). Exhumation of high-pressure rocks: a review of concepts and processes. *Terra Nova*, 5(2), 119–133. <https://doi.org/10.1111/j.1365-3121.1993.tb00237.x>
- Powell, R., & Holland, T. J. B. (1988). An internally consistent dataset with uncertainties and correlations: 3. Applications to geobarometry, worked examples and a computer program. *Journal of Metamorphic Geology*, 6(2), 173–204. <https://doi.org/10.1111/j.1525-1314.1988.tb00415.x>

Chapter III

- Powell, R. & Holland, T. J. B., (2002). Course Notes for "THERMOCALC Workshop 2002: Calculating Metamorphic Phase Equilibria"(Barcelona). CD-ROM.
- Rey, P. F., Teyssier, C., & Whitney, D. L. (2009). Extension rates, crustal melting, and core complex dynamics. *Geology*, 37(5), 391–394. <https://doi.org/10.1130/G25460A.1>
- Shaw, D. M. (1956). Geochemistry of pelitic rocks. Part III: Major element and general geochemistry. *GSA Bulletin*, 67(7), 919–934. [https://doi.org/10.1130/0016-7606\(1956\)67\[919:GOPRPI\]2.0.CO;2](https://doi.org/10.1130/0016-7606(1956)67[919:GOPRPI]2.0.CO;2)
- Smith, H. A., & Barreiro, B. (1990). Monazite U-Pb dating of staurolite grade metamorphism in pelitic schists. *Contributions to Mineralogy and Petrology*, 105(5), 602–615. <https://doi.org/10.1007/BF00302498>
- Soliva, J., Salel, J. F., & Brunel, M. (1989). Shear deformation and emplacement of the gneissic Canigou thrust nappe (Eastern Pyrenees). *Geologie En Mijnbouw*, 68(3), 357–366.
- Sonder, L. J., England, P. C., Wernicke, B. P., & Christiansen, R. L. (1987). A physical model for Cenozoic extension of western North America. *Geological Society, London, Special Publications*, 28(1), 187–201. <https://doi.org/10.1144/GSL.SP.1987.028.01.14>
- Soula, J. C. (1982). Characteristics and mode of emplacement of gneiss domes and plutonic domes in central-eastern Pyrenees. *Journal of Structural Geology*, 4(3), 313–342. [https://doi.org/10.1016/0191-8141\(82\)90017-7](https://doi.org/10.1016/0191-8141(82)90017-7)
- Soula, J. C., Debat, P., Deramond, J., & Pouget, P. (1986). A dynamic model of the structural evolution of the Hercynian Pyrenees. *Tectonophysics*, 129(1), 29–51. [https://doi.org/10.1016/0040-1951\(86\)90244-1](https://doi.org/10.1016/0040-1951(86)90244-1)
- Spear, F. S. (2010). Monazite–allanite phase relations in metapelites. *Chemical Geology*, 279(1), 55–62. <https://doi.org/10.1016/j.chemgeo.2010.10.004>
- Spear, F. S., & Pyle, J. M. (2002). Apatite, Monazite, and Xenotime in Metamorphic Rocks. *Reviews in Mineralogy and Geochemistry*, 48(1), 293–335. <https://doi.org/10.2138/rmg.2002.48.7>
- Speksnijder, A. (1985). Anatomy of a strike-slip fault controlled sedimentary basin, Permian of the Southern Pyrenees, Spain. *Sedimentary Geology*, 44(3), 179–223. [https://doi.org/10.1016/0037-0738\(85\)90014-4](https://doi.org/10.1016/0037-0738(85)90014-4)
- Štípská, P., Hacker, B. R., Racek, M., Holder, R., Kylander-Clark, A. R. C., Schulmann, K., & Hasalová, P. (2015). Monazite Dating of Prograde and Retrograde P–T–d paths in the

Chapter III

- Barrovian terrane of the Thaya window, Bohemian Massif. *Journal of Petrology*, 56(5), 1007–1035. <https://doi.org/10.1093/petrology/egv026>
- Tartèse, R., Ruffet, G., Poujol, M., Boulvais, P., & Ireland, T. R. (2011). Simultaneous resetting of the muscovite K-Ar and monazite U-Pb geochronometers: a story of fluids. *Terra Nova*, 23(6), 390–398. <https://doi.org/10.1111/j.1365-3121.2011.01024.x>
- Thompson, A. B., & England, P. C. (1984). Pressure—temperature—time paths of regional metamorphism II. Their inference and interpretation using mineral assemblages in metamorphic rocks. *Journal of Petrology*, 25(4), 929–955.
- Van Achterbergh, E., Ryan, C. G., & Griffin, W. L. (2001). GLITTER on-line interactive data reduction for the LA-ICPMS microprobe. Macquarie Research Ltd., Sydney.
- Vilà, M., Pin, C., Liesa, M., & Enrique, P. (2007). LPHT metamorphism in a late orogenic transpressional setting, Albera Massif, NE Iberia: implications for the geodynamic evolution of the Variscan Pyrenees. *Journal of Metamorphic Geology*, 25(3), 321–347. <https://doi.org/10.1111/j.1525-1314.2007.00698.x>
- Vissers, R. L. M. (1992). Variscan extension in the Pyrenees. *Tectonics*, 11(6), 1369–1384. <https://doi.org/10.1029/92TC00823>
- Vissers, R. L. M., Hinsbergen, D. J. J. van, Ganerød, M., & Wilkinson, C. M. (2018). Reply to discussion on ‘Middle Jurassic shear zones at Cap de Creus (eastern Pyrenees, Spain): a record of pre-drift extension of the Piemonte–Ligurian Ocean?’ *Journal of the Geological Society*, London, 174, 289–300. *Journal of the Geological Society*, 175(1), 189–191. <https://doi.org/10.1144/jgs2017-115>
- Vissers, R. L. M., Hinsbergen, D. J. J. van, Wilkinson, C. M., & Ganerød, M. (2017). Middle Jurassic shear zones at Cap de Creus (eastern Pyrenees, Spain): a record of pre-drift extension of the Piemonte–Ligurian Ocean? *Journal of the Geological Society*, 174(2), 289–300. <https://doi.org/10.1144/jgs2016-014>
- White, R. W., Pomroy, N. E., & Powell, R. (2005). An in situ metatexite–diatexite transition in upper amphibolite facies rocks from Broken Hill, Australia. *Journal of Metamorphic Geology*, 23(7), 579–602. <https://doi.org/10.1111/j.1525-1314.2005.00597.x>
- White, R. W., Powell, R., Holland, T. J. B., & Worley, B. A. (2000). The effect of TiO₂ and Fe₂O₃ on metapelitic assemblages at greenschist and amphibolite facies conditions: mineral equilibria calculations in the system K₂O–FeO–MgO–Al₂O₃–SiO₂–H₂O–TiO₂–Fe₂O₃.

Chapter III

Journal of Metamorphic Geology, 18(5), 497–511. <https://doi.org/10.1046/j.1525-1314.2000.00269.x>

- Wickham, S. M., & Oxburgh, E. R. (1986). A rifted tectonic setting for hercynian high-thermal gradient metamorphism in the pyrenees. *Tectonophysics*, 129(1), 53–69. [https://doi.org/10.1016/0040-1951\(86\)90245-3](https://doi.org/10.1016/0040-1951(86)90245-3)
- Williams, M. L., Jercinovic, M. J., Harlov, D. E., Budzyń, B., & Hetherington, C. J. (2011). Resetting monazite ages during fluid-related alteration. *Chemical Geology*, 283(3), 218–225. <https://doi.org/10.1016/j.chemgeo.2011.01.019>
- Wing, B. A., Ferry, J. M., & Harrison, T. M. (2003). Prograde destruction and formation of monazite and allanite during contact and regional metamorphism of pelites: petrology and geochronology. *Contributions to Mineralogy and Petrology*, 145(2), 228–250. <https://doi.org/10.1007/s00410-003-0446-1>
- Zwart, H. J. (1979). The geology of the central Pyrenees. *Leidse Geologische Mededelingen*, 50, 1–74.

Table III.1: Table of representative microprobe analyses.

Litho.	Micaschist										LH16								
Sample	LH1B																		
Anal#	p011	p020	401	113	206	311	112	307	p106	MEB1	p001	107	306	013	022	021	425	035	111
Mx.	g	g	mu	bi	bi	chl	pl	ilm	g	g	g	st	mu	bi	bi	chl	pl	ep	ilm
Pos.	g1	g2	matrix	in g	in and	matrix	in and	matrix	core	rim	outer rim	in and	matrix	matrix	in and	matrix	in g	in st.	
SiO ₂	36.18	36.60	46.01	33.77	34.24	28.03	60.68	0.06	36.65	36.63	35.90	27.25	45.22	33.36	33.81	23.36	59.78	38.42	0.04
TiO ₂	0.05	0.04	0.51	2.89	1.56	0.31	0.05	53.33	0.14	0.00	0.05	0.75	0.51	1.93	2.25	0.11	0.00	0.14	52.91
Al ₂ O ₃	20.94	21.25	35.99	19.18	20.88	20.44	24.55	0.03	20.99	20.98	21.11	56.42	37.22	19.63	21.59	23.68	25.53	29.73	0.02
MgO	1.74	1.24	0.70	7.61	7.56	10.64	0.00	0.03	1.17	1.37	2.09	0.87	0.50	8.25	7.61	12.03	0.03	0.03	0.05
FeO	30.49	29.26	1.31	21.99	20.49	26.94	0.35	40.65	27.08	30.14	30.86	12.67	0.82	21.22	19.67	27.65	0.06	5.73	44.42
MnO	9.05	10.55	0.00	0.42	0.18	0.22	0.03	4.28	6.14	5.77	7.09	0.49	0.00	0.09	0.19	0.32	0.00	0.29	2.25
ZnO	0.00	0.00	0.00	0.00	0.00	0.10	0.00	0.00	0.00	0.00	0.03	0.34	0.00	0.00	0.00	0.00	0.00	0.00	0.00
CaO	2.08	1.46	0.02	0.07	0.03	0.15	5.58	0.04	7.30	5.12	2.42	0.01	0.03	0.00	0.00	0.05	6.74	23.12	0.01
P ₂ O ₅	0.00	0.00	0.03	0.05	0.00	0.00	0.11	0.00	0.00	0.00	0.00	0.00	0.00	0.00	0.00	0.01	0.04	0.06	0.00
Na ₂ O	0.00	0.00	0.78	0.16	0.20	0.02	8.31	0.00	0.00	0.00	0.00	0.00	0.95	0.10	0.14	0.00	7.53	0.00	0.00
K ₂ O	0.00	0.04	10.11	9.01	9.13	0.86	0.05	0.02	0.00	0.00	0.16	0.01	10.19	9.56	8.98	0.01	0.05	0.06	0.00
Sum	100.54	100.43	95.45	95.15	94.27	87.71	99.69	98.43	99.46	100.00	99.68	98.81	95.43	94.15	94.23	87.22	99.75	97.57	99.70
Si	2.93	2.97	3.05	2.62	2.65	2.97	2.71	0.00	2.96	2.94	2.91	7.79	3.00	2.61	2.60	2.51	2.67	2.96	0.00
Ti	0.00	0.00	0.03	0.17	0.09	0.03	0.00	1.02	0.01	0.00	0.00	0.16	0.03	0.11	0.13	0.01	0.00	0.01	1.00
Al	2.00	2.03	2.81	1.75	1.90	2.55	1.29	0.00	2.00	1.98	2.02	19.01	2.91	1.81	1.96	3.00	1.34	2.70	0.00
Fe ³⁺	0.14	0.02	0.00	0.00	0.00	0.00	0.00	0.00	0.05	0.00	0.16	0.00	0.00	0.00	0.00	0.00	0.00	0.37	0.00
Mg	0.21	0.15	0.07	0.88	0.87	1.68	0.00	0.00	0.14	0.19	0.25	0.37	0.05	0.96	0.87	1.93	0.00	0.00	0.00
Fe ²⁺	1.92	1.96	0.07	1.43	1.32	2.39	0.01	0.86	1.78	2.09	1.93	3.03	0.05	1.39	1.27	2.49	0.00	0.00	0.94
Mn	0.62	0.73	0.00	0.03	0.01	0.02	0.00	0.09	0.42	0.26	0.49	0.12	0.00	0.01	0.01	0.03	0.00	0.00	0.05
Zn	0.00	0.00	0.00	0.00	0.00	0.01	0.00	0.00	0.00	0.00	0.00	0.07	0.00	0.00	0.00	0.00	0.00	0.00	0.00
Ca	0.18	0.13	0.00	0.01	0.00	0.02	0.27	0.00	0.63	0.55	0.21	0.00	0.00	0.00	0.00	0.01	0.32	1.91	0.00
P	0.00	0.00	0.00	0.00	0.00	0.00	0.00	0.00	0.00	0.00	0.00	0.00	0.00	0.00	0.00	0.00	0.00	0.00	0.00
Na	0.00	0.00	0.10	0.02	0.03	0.01	0.72	0.00	0.00	0.00	0.00	0.00	0.12	0.02	0.02	0.00	0.65	0.00	0.00
K	0.00	0.00	0.86	0.89	0.90	0.12	0.00	0.00	0.00	0.00	0.02	0.00	0.86	0.95	0.88	0.00	0.00	0.01	0.00
OH	0.00	0.00	2.00	2.00	2.00	8.00	0.00	0.00	0.00	0.00	0.00	0.00	2.00	2.00	2.00	8.00	0.00	1.00	0.00
Sum	8.00	8.00	8.99	9.79	9.78	17.79	5.00	1.98	8.00	8.00	8.00	30.55	9.01	9.86	9.74	17.98	4.99	8.98	1.99
X _{Fe} /X _{Na}	0.90	0.93	0.10	0.62	0.60	0.59			0.93	0.92	0.88	0.89	0.12	0.59	0.59	0.56	Ep	0.14	
Alm/An	0.66	0.66					0.27		0.60	0.68	0.67						0.33		
Prp/Ab	0.07	0.05					0.73		0.05	0.06	0.09						0.67		
Grs/Or	0.06	0.04					0.00		0.21	0.18	0.07						0.00		
Sps	0.21	0.24							0.14	0.08	0.17								

Litho.	Micaschist									Garnet-grunerite gneiss										
Sample	LH3									LH9										
Anal#	280	285	304	203	204	206	201	209	212	037	041	209	025	018	019	023	013	006	009	106
Mx.	g		g	st	mu	bi	chl	pl	ilm	sp	g	g	camp	mu	bi	bi	chl	pl	ep	ep
Pos.	g1	g2	in and	matrix	matrix	matrix	matrix	matrix	matrix	core	rim	matrix	matrix	matrix	in g	matrix	in g	matrix	in g	in g
SiO ₂	36.88	35.50	26.30	45.40	34.40	24.26	59.54	0.01	0.05	36.59	36.87	51.89	45.76	34.88	35.19	23.95	67.86	40.92	37.32	0.04
TiO ₂	0.00	0.00	0.57	0.37	1.49	0.20	0.01	52.69	0.05	0.15	0.06	0.02	0.03	1.20	1.39	0.08	0.01	0.00	0.13	51.42
Al ₂ O ₃	21.31	20.67	55.36	37.54	19.59	23.19	25.58	0.04	57.84	21.23	21.40	0.60	36.28	18.63	17.36	21.77	20.55	32.85	27.59	0.02
MgO	1.61	0.81	0.98	0.40	8.53	12.06	0.02	0.03	1.51	0.65	1.50	12.11	0.36	9.04	8.48	12.33	0.00	0.01	0.02	0.11
FeO	29.21	26.02	10.24	0.68	21.33	27.85	0.04	43.39	13.15	29.96	34.54	32.06	1.91	21.68	22.72	29.30	0.26	1.40	7.59	46.26
MnO	9.34	13.29	0.52	0.00	0.19	0.39	0.00	3.54	0.22	3.67	0.40	0.05	0.00	0.00	0.00	0.03	0.00	0.04	0.11	0.18
ZnO	0.00	0.00	4.61	0.00	0.00	0.02	0.00	0.00	28.60	0.00	0.05	0.00	0.00	0.00	0.00	0.03	0.01	0.00	0.00	0.00
CaO	1.65	1.19	0.04	0.00	0.00	0.03	7.01	0.02	0.03	8.02	5.84	0.35	0.04	0.06	0.06	0.03	1.00	23.66	22.48	0.13
P ₂ O ₅	0.00	0.00	0.00	0.04	0.00	0.00	0.07	0.00	0.00	0.01	0.00	0.00	0.00	0.02	0.00	0.00	0.00	0.00	0.01	0.00
Na ₂ O	0.00	0.00	0.08	0.88	0.07	0.00	7.48	0.03	0.35	0.00	0.00	0.09	0.19	0.08	0.06	0.00	10.74	0.49	0.00	0.00
K ₂ O	0.00	0.00	0.00	10.13	9.65	0.26	0.05	0.03	0.00	0.01	0.00	0.02	11.04	7.99	9.13	0.00	0.04	0.01	0.00	0.00
Sum	100.00	100.29	98.70	95.44	95.25	88.28	99.80	99.77	101.80	100.27	100.66	97.18	95.62	93.57	94.39	87.52	100.46	99.36	95.23	98.15
Si	2.99	2.91	7.64	3.00	2.65	2.58	2.66	0.00	0.00	2.94	2.95	7.94	3.05	2.71	2.75	2.59	2.95	3.05	2.96	0.00
Ti	0.00	0.00	0.12	0.02	0.09	0.02	0.00	1.00	0.00	0.01	0.00	0.00	0.00	0.07	0.08	0.01	0.00	0.00	0.01	0.99
Al	2.04	2.00	18.95	2.93	1.78	2.91	1.35	0.00	1.98	2.01	2.02	0.11	2.85	1.71	1.60	2.78	1.05	2.89	2.58	0.00
Fe ³⁺	0.00	0.17	0.00	0.00	0.00	0.00	0.00	0.00	0.04	0.08	0.07	0.02	0.00	0.00	0.00	0.00	0.00	0.09	0.50	0.01
Mg	0.20	0.10	0.42	0.04	0.98	1.91	0.00	0.00	0.07	0.08	0.18	2.76	0.04	1.05	0.99	1.99	0.00	0.00	0.00	0.00
Fe ²⁺	1.98	1.79	2.49	0.04	1.38	2.48	0.00	0.92	0.28	1.93	2.25	4.08	0.11	1.41	1.49	2.65	0.01	0.00	0.00	0.98
Mn	0.64	0.92	0.13	0.00	0.01	0.04	0.00	0.08	0.01	0.25	0.03	0.01	0.00	0.00	0.00	0.00	0.00	0.00	0.00	0.00
Zn	0.00	0.00	0.99	0.00	0.00	0.00	0.00	0.00	0.61	0.00	0.00	0.00	0.00	0.00	0.00	0.00	0.00	0.00	0.00	0.00
Ca	0.14	0.11	0.01	0.00	0.00	0.00	0.34	0.00	0.00	0.69	0.50	0.06	0.00	0.01	0.01	0.00	0.05	1.89	1.91	0.00
P	0.00	0.00	0.00	0.00	0.00	0.00	0.00	0.00	0.00	0.00	0.00	0.00	0.00	0.00	0.00	0.00	0.00	0.00	0.00	0.00
Na	0.00	0.00	0.05	0.11	0.01	0.00	0.65	0.00	0.02	0.00	0.00	0.03	0.03	0.01	0.01	0.00	0.91	0.07	0.00	0.00
K	0.00	0.00	0.00	0.86	0.95	0.04	0.00	0.00	0.00	0.00	0.00	0.00	0.94	0.79	0.91	0.00	0.00	0.00	0.00	0.00
OH	0.00	0.00	0.00	2.00	2.00	8.00	0.00	0.00	0.00	0.00	0.00	0.00	2.00	2.00	2.00	8.00	0.00	1.00	1.00	0.00
Sum	7.99	8.00	30.79	9.00	9.85	17.97	4.99	2.00	3.00	8.00	8.00	15.01	9.01	9.76	9.83	18.02	4.97	8.99	8.98	2.00
X _{Mg} /X _{Na}	0.91	0.95	0.85	0.12	0.58	0.56				0.96	0.93	0.60	0.03	0.57	0.60	0.57	Ep	0.09	0.46	
Alm/An	0.67	0.61					0.34			0.65	0.76						0.05			
Prp/Ab	0.07	0.03					0.66			0.03	0.06						0.95			
Grs/Or	0.05	0.04					0.00			0.23	0.17						0.00			
Sps	0.22	0.32								0.08	0.01									

ilm

Table III.2: U–Th–Pb LA-ICP-MS data for the monazite grains in sample LH16.

# Analysis	Grain	[Pb] (ppm)	[U] (ppm)	[Th] (ppm)	Th/U	238U/232Th $\pm 1\sigma$		206Pb/238U $\pm 1\sigma$		Ages (Ma)			
										206Pb/238U $\pm 1\sigma$	Pb208/232Th $\pm 1\sigma$		
5100317b	Mz1	658	3919	35930	9.2	0.0151	0.0002	0.0489	0.0007	307.5	4.1	302.0	3.7
6100317b	Mz1	499	3179	23612	7.4	0.0167	0.0002	0.0521	0.0007	327.7	4.4	334.0	4.1
7100317b	Mz1	628	4096	32565	8.0	0.0154	0.0002	0.0499	0.0007	313.7	4.2	308.0	3.8
8100317b	Mz2	730	5124	41280	8.1	0.0141	0.0002	0.0462	0.0006	291.3	3.9	282.8	3.5
9100317b	Mz2	711	4993	37805	7.6	0.0149	0.0002	0.0476	0.0007	299.8	4.0	298.4	3.7
13100317b	Mz2	760	5648	40266	7.1	0.0148	0.0002	0.0473	0.0007	298.0	4.0	296.3	3.6
14100317b	Mz2	762	5108	40338	7.9	0.0153	0.0002	0.0480	0.0007	302.0	4.1	306.6	3.8
15100317b	Mz2	859	6478	44899	6.9	0.0148	0.0002	0.0480	0.0007	302.4	4.1	297.6	3.7
16100317b	Mz2	663	4919	35128	7.1	0.0147	0.0002	0.0481	0.0007	302.8	4.1	295.4	3.7
18100317b	Mz3	377	3785	17002	4.5	0.0151	0.0002	0.0478	0.0007	300.8	4.1	302.2	3.8
22100317b	Mz3	756	7620	34540	4.5	0.0150	0.0002	0.0475	0.0007	299.4	4.1	301.0	3.8
23100317b	Mz4	715	5638	36727	6.5	0.0152	0.0002	0.0470	0.0007	296.3	4.1	305.7	3.8
26100317b	Mz4	881	6789	46472	6.8	0.0149	0.0002	0.0479	0.0007	301.7	4.2	299.1	3.8
27100317b	Mz5	613	3979	34046	8.6	0.0151	0.0002	0.0489	0.0007	308.0	4.3	301.9	3.8
31100317b	Mz5	810	4360	47466	10.9	0.0151	0.0002	0.0486	0.0007	306.0	4.3	302.7	3.8
32100317b	Mz5	465	3142	24584	7.8	0.0155	0.0002	0.0505	0.0007	317.6	4.4	310.4	3.9
33100317b	Mz7	351	8382	1641	0.2	0.0158	0.0002	0.0503	0.0007	316.3	4.3	317.5	4.1
34100317b	Mz9	969	10421	44908	4.3	0.0149	0.0002	0.0460	0.0007	289.8	4.0	298.1	3.8
35100317b	Mz9	924	9095	43862	4.8	0.0150	0.0002	0.0477	0.0007	300.1	4.2	300.7	3.8
4100317c	Mz9	662	5115	34698	6.8	0.0147	0.0002	0.0479	0.0007	301.7	4.2	295.5	3.7
5100317c	Mz10	779	7514	36612	4.9	0.0148	0.0002	0.0484	0.0007	304.6	4.2	296.7	3.7
7100317c	Mz11	705	5752	36189	6.3	0.0147	0.0002	0.0480	0.0007	302.4	4.2	294.9	3.7
13100317c	Mz16	711	4921	38637	7.9	0.0148	0.0002	0.0478	0.0007	300.9	4.2	297.2	3.7
14100317c	Mz16	928	8021	45333	5.7	0.0150	0.0002	0.0475	0.0007	299.4	4.1	301.3	3.8

General discussion and conclusions

Variscan eclogite-to granulite-facies metamorphism in the Haut-Allier

A robust P – T path has been determined for the La Borie eclogites. The prograde P – T path is dominated by an initial pressure increase ($\sim 650^{\circ}\text{C}$, 20 kbar to 750°C , 22.5 kbar) and then a roughly isobaric heating up to the field of partial melting ($\sim 875^{\circ}\text{C}$, 22.5 kbar). The prograde P – T path thus indicates the burial of an oceanic crust followed by an input of external heat, likely from the asthenosphere.

Garnet-plagioclase co-stability after limited isothermal decompression ($\sim 875^{\circ}\text{C}$, 19 kbar), subsequent to, or during partial melting, typifies the eclogite-granulite facies transition. Therefore, the P – T path preclude thermal equilibration on the way up to the surface in an orogenic root.

Subsequent stronger and steep decompression (750 – 820°C , <7 kbar) is marked by the widespread retrogression during a HT amphibolite to LP granulite facies similar to the regional metamorphic grade (Forestier et al. 1973; Marchand, 1974). A fast exhumation is suggested by the steep P – T path.

The similarity of this P – T path with the one of the pelitic granulites (Marchand, 1974) points to a common tectonic history during the exhumation. Therefore, the retrograde (i.e. decompression) and regionally homogeneous (i.e. without gradient) character of the HT (sillimanite zone) amphibolite overprint of the HP units is not comparable to Barrovian metamorphism and may not be readily related with crustal thickening during continental collision.

Garnet-rich layers in eclogites: evidence of eclogites partial melting?

Garnet-rich layers may form in response to the metamorphism of a primary feature of the rock (e.g. magmatic layering) or to secondary processes during the metamorphism (e.g. metasomatism or partial melting at subsolidus or suprasolidus conditions respectively). Similar mineralogy of inclusions, chemical composition and trend of garnet zoning from the garnet-rich layer and their host eclogites, suggest a primary homogeneous composition of the protoliths. Major element composition of the garnet-rich layers and their host support a significant deviation during metamorphism explained by partial melting and melt extraction.

Variable degrees of partial melting evidence various hydration states and focused partial melting caused by localized water influx under partial hydration conditions. Rutile and zircon enrichment is interpreted in terms of external influx of Zr and Ti transported in an aqueous fluid and subsequent precipitation from a peraluminous melt at the onset of partial melting.

Partial melting of the subducted oceanic crust has been reported either during decompression of UHP eclogites (Cao et al., 2019; Wang et al., 2014) or during granulitic metamorphism of hot and young oceanic crust (i.e. subducted ridge; e.g. Rosetti et al., 2010; Angiboust et al., 2017; García-Casco et al., 2008) or Archean oceanic crust (i.e. high thermal gradient; e.g. Mints et al., 2014; Balagansky et al., 2015) or metasomatized lens in a subduction channel (Sorensen and Barton, 1987). Partial melting resulting from a strong heating of the subducted crust at peak pressure conditions may typify the juxtaposition of hot material from the asthenosphere with the subducted crust.

Partial melting is likely to change the rheological behaviour of the subducted portion of the oceanic crust. Accordingly, it may facilitate the lithospheric mantle to detach from the subducted crust and therefore facilitate the subsequent exhumation of the crust.

Petrologically constrained U-Pb dating of the “La Borie” eclogites

The petrological constraints of the U/Pb geochronology of rutiles, apatites and zircons constrain the P–T evolution of the eclogites in time.

Magmatic zircons indicates a crystallization of the protolith at c. 485 Ma. A second generation is inferred to have crystallized by ilmenite breakdown, during prograde metamorphism. This second generation, observed as μm -sized cluster around rutiles in garnets were too small to be analysed, however, heritage in larger metamorphic crystals could correlate to this event. The third zircon generation formed close to the P–T peak conditions reached by c. 363 Ma. Rutile and apatite ages yield similar results interpreted as cooling ages around c. 353 Ma. Most of the decompression of the eclogites was achieved before the onset of cooling, therefore, it is inferred that they were exhumed by that time and confirms the suspected fast exhumation.

The wide scatter of the metamorphic zircons $^{206}\text{Pb}/^{238}\text{U}$ apparent ages (~365 to 290 Ma), points to a limited but widespread lead loss subsequent to apatite U/Pb closure. The widespread lead loss suggests a thermal event younger than 353 Ma that has however, not affected the apatites. A petrological record of this thermal event is however still to be confirmed.

The observation of zircons both in garnet, rutile and the matrix suggest that the rock was saturated with respect to zircon. Accordingly, if the protolith contains enough zircon to saturate garnet and rutile at peak P–T conditions, the redistribution of Zr by dissolution-recrystallization and/or solid-state recrystallization of former zircon is expected to be the most efficient process to produce an eclogitic zircon.

Petrological investigation of the metagranites

Many orthogneisses massifs are spatially associated with eclogites, however, none of the studied metagranites display a typical eclogitic assemblage. Yet, granulite facies metamorphism seems widespread. Metamorphic textures suggest that the granulite facies metamorphism occurred toward the “HP” conditions.

Garnet coronae reflect local equilibrium difficult to model using P – T pseudosection and further investigations of the crystallization of garnet coronas around biotite require the use of thermometers and barometers independent from the bulk composition. Raman barometry in quartz included in garnet may be – in some cases – a suitable method to overcome this issue.

The metagranites may contain xenoliths or pseudomorphs after cordierite. On the one hand, xenoliths may be dehydrated during the emplacement of their host and may not record the metamorphism underwent by the metagranite; pseudomorphs after cordierite, on the other one, crystallized from the granitic melt and necessarily record the metamorphism underwent by their host. These pseudomorphs are suitable for P – T pseudosection investigations. Therefore, looking after these metagranites by a geochemical study/synthesis may indicate the best targets for a petrological study.

In the internal zones of the French Variscan belt the granulitic metamorphism is mostly recorded in undeformed lenses (e.g. Burg and Leyreloup, 1989; Lasnier et al., 1973). The regional the syn-metamorphic regional foliation appears to have formed at lower pressure conditions, most likely during the decompression. This observation is repeated in Picheraie, Vibal, Lévézou, Thaurion and Saint Didier-sur-Doulon metagranites. The hosts orthogneisses bear an E-W to NW-SE trending lineation in the Massif Central and Armorican Massif suggesting a similar direction of the main shear during the exhumation. This shear direction is not well understood yet since the metamorphic zoning of the orogeny is rather N-S trending.

Two-stage Variscan metamorphism in the Canigou massif: Evidence for crustal thickening in the Pyrenees

The P – T path of the metapelites of the core of the Canigou massif in the Pyrenees is interpreted in terms of two metamorphic prograde events separated by a period of cooling. The first metamorphic event is characterized by a cold prograde P – T path ($\sim 9^{\circ}\text{C}/\text{km}$; assuming lithostatic pressure) with a peak pressure of 6.5 kbar (at 550°C) and a subsequent peak of temperature at 580°C (at 5.5 kbar). The prograde character of this MP (i.e. amphibolite facies) metamorphic event attests for a period of crustal thickening that may be attributed to Barrovian type metamorphism. Subsequent decompression and cooling are interpreted in terms of significant erosion and crustal thinning. Renewed heating associated with limited pressure increase may be explained by the overburden pressure caused by a significant accumulation of detrital sediments (e.g. Martínez et al., 2001; Pitra & Guiraud, 1996).

The heating, associated with the resetting of monazites at ~ 300 Ma (most likely through fluids) indicates a thermal event that coincide with the emplacement of numerous plutons in the Variscan Pyrenees. This result suggests that the thermal regime of the orogen was mostly controlled by the advection of heat by the magmatism (e.g. Dewey, 2005; Viete et al., 2011; Viete and Lister, 2017; Ague and Baxter, 2007). Several authors have proposed a mantellic origin for the thermal perturbation (e.g. Cochelin et al., 2017; Dewey, 1988; Gibson, 1991; Gutiérrez-Alonso et al., 2011; Henk et al., 2000).

A proposition of tectonic model for the exhumation the HP units of the Massif Central

The eclogites were buried in a subduction zone as indicated by the up-pressure, up-temperature portion of the P–T path. Subsequent resorption of the oceanic domain and subduction of small pieces of continental crust such as recorded by the Lévézou massif (Lotout, 2017, Lotout et al. 2017) would result in the steepening of the slab. Consequently, to slab retreat, the overriding plate suffered extension resulting in the onset of magmatism in the Brévenne back-arc basin (c. 365–360 Ma; Pin and Paquette, 1997) and a coeval flow of the hot asthenosphere next to the subducted crust accounting for the roughly isobaric heating of the eclogites. Subsequent crust mantle delamination, most likely facilitated by the widespread partial melting of eclogites (Haut-Allier: this study, Marvejol and Lévézou: Nicollet and Leyreloup: 1978) led to the retreat of the trench and thrust zones towards external areas of the orogeny. Such migration induced a dramatic exhumation of the previously subducted crust, accounting for the similar age of the HP metamorphism of the Lévézou (Lotout et al., submitted), Montagne-Noire (Faure et al., 2014; Bretagne et al., submitted) and the studied eclogites. The exhumation resulted in the HT overprint of the eclogites and orthogneisses, as well as the widespread syntectonic migmatisation of their host country rocks. Continuous underthrusting led to the progressive isoclinal and subsequent map scale folding of the migmatitic foliation in the internal zones of the orogen and to a Barrovian type metamorphism in the external zones of the orogen. This evolution is shown in Fig. V.1.

Discussion and conclusions

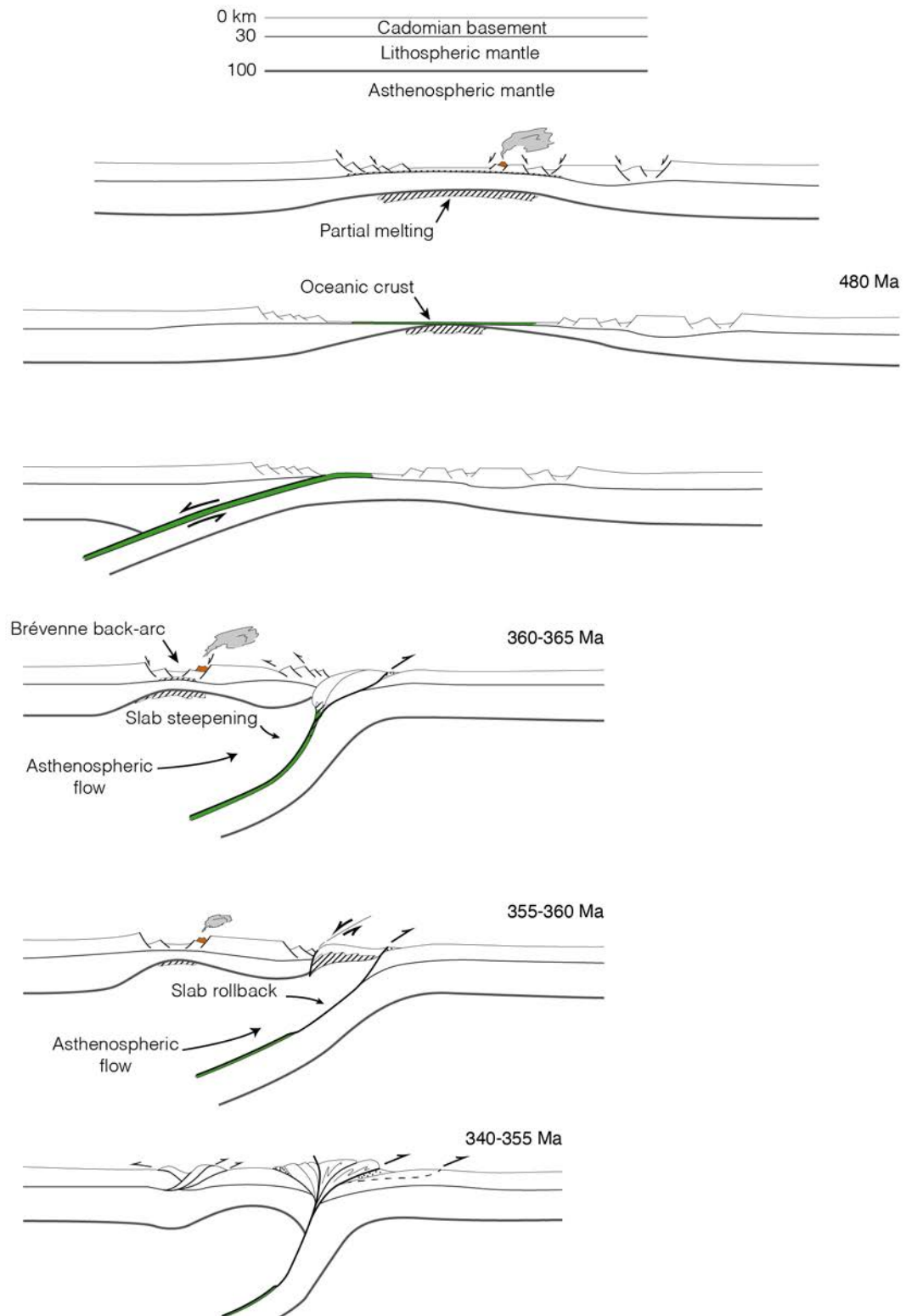


Figure IV.1: Preliminary proposition of tectonic model for the exhumation of the eclogites based on observations in the eastern Massif Central.

Conclusions

This petrologic and geochronologic study is dedicated to the understanding of the first stages of the tectonometamorphic evolution of the Variscan orogeny. The main result is a re-evaluation of the P – T – t path of a previously inferred Silurian eclogites to (i) determine whether the HT overprint on the eclogitic assemblage result from the subduction or later thermal relaxation in an orogenic root; (ii) re-evaluate the age of the eclogite metamorphism; (iii) constrain the timing of the exhumation. The secondary study was dedicated to the petrology of Variscan metagranites (i.e. Cambrian and Ordovician protolith) in order to (i) produce a map of the Variscan HP metamorphism of the continental crust and (ii) reveal the deformations respectively associated with the burial and the exhumation of the HP units. A side study was dedicated to the study of the elusive Barrovian metamorphism of the Pyrenees in order to better understand the subsequent widespread HT metamorphism. These objectives were addressed by the study of eclogites from the Massif Central, metagranites from the Massif Central and the Maures-Tanneron and metapelites from the Variscan basement of the Pyrenees.

The study of the metapelites of the Variscan basement of the Pyrenees reveal two syntectonic metamorphic stages. The first metamorphic stage records a prograde P – T path with an initial peak of pressure (6.5 kbar – 550°C) and a subsequent peak of temperature (5.5 kbar – 580°C) interpreted as a Barrovian type metamorphism resulting from crustal nappe stacking. The later LP–HT pressure metamorphism (3 kbar – 580°C) may be accounted for by two P – T paths: (i) isothermal decompression and cooling or (ii) decompression and cooling before a renewed period of heating. The latter is favoured because of the regional observation of sillimanite growing after andalusite suggesting a period of heating. This event was dated at 300 Ma by monazite geochronology and may be related to a widespread magmatic event in the Pyrenees the origin of which may be found in the mantle. These results point to a time lag

Discussion and conclusions

between crustal thickening and magmatism and emphasize the role of crust-mantle relationships in the thermal evolution continental collisions zones.

The petrologic study of metagranites emplaced in Cambrian or Ordovician times and metamorphosed during the Variscan orogeny points out that several massifs underwent a high-grade metamorphism, most likely at HP granulite facies conditions. However, this metamorphism has not been quantified. The metamorphism is evidenced by garnet-bearing coronitic textures, pelitic enclaves or pseudomorphs after magmatic cordierite. Several orthogneiss massifs are spatially associated with eclogites (Thaurion, Tanneron, Haut-Allier, La Picheraie, Lévézou and Vibal) suggesting a common metamorphic history. Most of the time, evidences of metamorphism (e.g. garnet coronas) is best preserved in lenses of undeformed metagranites wrapped in a host orthogneiss where the relicts of metamorphism are xenomorphic and dispersed in the foliation. This observation indicates that the foliation developed during a lower grade metamorphism overprinting the high-grade metamorphism. Accordingly, it is inferred that most of the deformation developed during a retrograde metamorphism and possibly during the exhumation of the high-grade units.

The main results of this study concern the re-evaluation of the P – T – t path of the La Borie eclogites in the Haut-Allier. The protolith of the eclogite represent a stage of opening of an oceanic or back-arc domain during the Ordovician (c. 485 Ma). The different steps of the oceanic domain closure during the Variscan orogeny can be reconstructed from the clockwise P – T path recorded in the eclogites metamorphism. Burial of the eclogite in a subduction zone is recorded by metamorphic zircons nucleated at the onset of the eclogite facies metamorphism and an up-pressure, up-temperature P – T path (from 20 kbar-650°C to 22.5 kbar-750°C). Localized partial melting during isobaric heating (up to ~875°C) evidence heat and localized fluid influx to the subducted crust. Melt extraction melting yielded the formation of garnet-rich residuum enriched in zircon at the peak P – T conditions reached by c. 363 Ma. This second

Discussion and conclusions

generation of zircon formed by dissolution-precipitation and solid-state recrystallization of the previous magmatic and metamorphic zircons as well as precipitation of Zr transported in an aqueous fluid at the onset of partial melting. Fast exhumation is evidenced by the pervasive replacement of clinopyroxene at HT and subsequent cooling by the closure U/Pb system of the apatites at c. 353 Ma. Isobaric heating and subsequent fast exhumation points to a modification of the dynamic of the subduction. Slab steepening at the onset of subduction of continental ribbons and consecutive asthenospheric flow account for the isobaric heating. Resulting partial melting might have facilitated slab detachment and induced slab roll back resulting in the exhumation of the subducted crust during a period of extension.

References

- Arène J, Autran A. 1978. Notice explicative de la carte géologique de Bourgneuf au 1/50 000°
- Ashley KT, Caddick MJ, Steele-MacInnis MJ, Bodnar RJ, Dragovic B. 2014. Geothermobarometric history of subduction recorded by quartz inclusions in garnet. *Geochem. Geophys. Geosyst.* 15(2):350–60
- Axelsson E, Pape J, Berndt J, Corfu F, Mezger K, Raith MM. 2018. Rutile R632 – A New Natural Reference Material for U-Pb and Zr Determination. *Geostandards and Geoanalytical Research.* 42(3):319–38
- Balagansky V, Shchipansky A, Slabunov AI, Gorbunov I, Mudruk S, et al. 2015. Archaean Kuru-Vaara eclogites in the northern Belomorian Province, Fennoscandian Shield: crustal architecture, timing, and tectonic implications. *International Geology Review.* 57(11–12):1543–65
- Ballèvre M, Capdevila R, Guerrot C, Peucat J-J. 2002. Discovery of an alkaline orthogneiss in the eclogite-bearing Cellier Unit (Champtoceaux Complex, Armorican Massif): a new witness of the Ordovician rifting. *Comptes Rendus Geoscience.* 334(5):303–11
- Ballèvre M, Fourcade S, Capdevila R, Peucat J-J, Cocherie A, Fanning CM. 2012. Geochronology and geochemistry of Ordovician felsic volcanism in the Southern Armorican Massif (Variscan belt, France): Implications for the breakup of Gondwana. *Gondwana Research.* 21(4):1019–36
- Ballouard C, Boulvais P, Poujol M, Gapais D, Yamato P, et al. 2015. Tectonic record, magmatic history and hydrothermal alteration in the Hercynian Guérande leucogranite, Armorican Massif, France. *Lithos.* 220:1–22
- Barbarin B. 1999. A review of the relationships between granitoid types, their origins and their geodynamic environments. *Lithos.* 46(3):605–26
- Barrat JA, Zanda B, Moynier F, Bollinger C, Liorzou C, Bayon G. 2012. Geochemistry of CI chondrites: Major and trace elements, and Cu and Zn Isotopes. *Geochimica et Cosmochimica Acta.* 83:79–92
- Beckman V, Möller C. 2018. Prograde metamorphic zircon formation in gabbroic rocks: The tale of microtextures. *Journal of Metamorphic Geology.* 36(9):1221–36

- Berger J, Féménias O, Ohnenstetter D, Plissart G, Mercier J-CC. 2010. Origin and tectonic significance of corundum–kyanite–sapphirine amphibolites from the Variscan French Massif Central. *Journal of Metamorphic Geology*. 28(3):341–60
- Biino GG, Compagnoni R. 1992. Very-high pressure metamorphism of the Brossasco coronite metagranite, southern Dora Maira Massif, Western Alps. *Schweizerische Mineralogische und Petrographische Mitteilungen*. 72(3):347–63
- Bingen B, Austrheim H, Whitehouse M. 2001. Ilmenite as a Source for Zirconium during High-grade Metamorphism? Textural Evidence from the Caledonides of Western Norway and Implications for Zircon Geochronology. *J Petrology*. 42(2):355–75
- Boehnke P, Watson EB, Trail D, Harrison TM, Schmitt AK. 2013. Zircon saturation re-revisited. *Chemical Geology*. 351:324–34
- Bosse V, Féraud G, Ballèvre M, Peucat J-J, Corsini M. 2005. Rb–Sr and $^{40}\text{Ar}/^{39}\text{Ar}$ ages in blueschists from the Ile de Groix (Armorican Massif, France): Implications for closure mechanisms in isotopic systems. *Chemical Geology*. 220(1–2):21–45
- Bosse V, Féraud G, Ruffet G, Ballèvre M, Peucat J-J, De Jong K. 2000. Late Devonian subduction and early-orogenic exhumation of eclogite-facies rocks from the Champtoceaux Complex (Variscan belt, France). *Geol. J.* 35(3–4):297–325
- Briand B, Piboule M, Santallier D, Bouchardon JL. 1991. Geochemistry and tectonic implications of two Ordovician bimodal igneous complexes, southern French Massif Central. *Journal of the Geological Society*. 148(6):959–71
- Brun J-P, Burg J-P. 1982. Combined thrusting and wrenching in the Ibero-Armorican arc: A corner effect during continental collision. *Earth and Planetary Science Letters*. 61(2):319–32
- Brun J-P, Faccenna C. 2008. Exhumation of high-pressure rocks driven by slab rollback. *Earth and Planetary Science Letters*. 272(1–2):1–7
- Bruno M, Compagnoni R, Rubbo M. 2001. The ultra-high pressure coronitic and pseudomorphous reactions in a metagranodiorite from the Brossasco-Isasca Unit, Dora-Maira Massif, western Italian Alps: a petrographic study and equilibrium thermodynamic modelling. *Journal of Metamorphic Geology*. 19(1):33–43
- Bundy FP. 1980. The P, T phase and reaction diagram for elemental carbon, 1979. *Journal of Geophysical Research: Solid Earth*. 6930–36
- Burg JP. 1977. *Tectonique et microtectonique des séries cristallophylliennes du Haut-Allier et de la vallée de la Truyère : contribution du microscope électronique à transmission à*

- l'étude de la déformation des minéraux dans les zones profondes*. phdthesis thesis.
Université des Sciences et Techniques du Languedoc
- Burg JP. 1987. Regional shear variation in relation to diapirism and folding. *Journal of Structural Geology*. 9(8):925–34
- Burg J-P, Leyreloup A. 1989. Métamorphisme granulitique de roches granitiques en Rouergue (Massif Central). *Comptes rendus de l'Académie des sciences. Série 2, Mécanique, Physique, Chimie, Sciences de l'univers, Sciences de la Terre*. 309(7):719–725
- Burg JP, Leyreloup A, Marchand J, Matte P. 1984. Inverted metamorphic zonation and large-scale thrusting in the Variscan Belt: an example in the French Massif Central. *Geological Society, London, Special Publications*. 14(1):47–61
- Burg JP, Matte PJ. 1978. A Cross Section through the French Massif Central and the Scope of its Variscan Geodynamic Evolution. *Zeitschrift der Deutschen Geologischen Gesellschaft*. 429–60
- Cao W, Gilotti JA, Massonne H-J, Ferrando S, Foster Jr. CT. 2019. Partial melting due to breakdown of an epidote-group mineral during exhumation of ultrahigh-pressure eclogite: An example from the North-East Greenland Caledonides. *Journal of Metamorphic Geology*. 37(1):15–39
- Chamberlain KR, Bowring SA. 2001. Apatite–feldspar U–Pb thermochronometer: a reliable, mid-range (~450°C), diffusion-controlled system. *Chemical Geology*. 172(1):173–200
- Cherniak DJ. 2000. Pb diffusion in rutile. *Contrib Mineral Petrol*. 139(2):198–207
- Cherniak DJ, Lanford WA, Ryerson FJ. 1991. Lead diffusion in apatite and zircon using ion implantation and Rutherford Backscattering techniques. *Geochimica et Cosmochimica Acta*. 55(6):1663–73
- Cherniak DJ, Watson EB. 2001. Pb diffusion in zircon. *Chemical Geology*. 172(1):5–24
- Chopin C. 1984. Coesite and pure pyrope in high-grade blueschists of the Western Alps: a first record and some consequences. *Contr. Mineral. and Petrol*. 86(2):107–18
- Chopin F, Schulmann K, Štípská P, Martelat JE, Pitra P, et al. 2012. Microstructural and metamorphic evolution of a high-pressure granitic orthogneiss during continental subduction (Orlica–Śnieżnik dome, Bohemian Massif). *Journal of Metamorphic Geology*. 30(4):347–76
- Clemens JD, Vielzeuf D. 1987. Constraints on melting and magma production in the crust. *Earth and Planetary Science Letters*. 86(2):287–306

- Cochelin B, Chardon D, Denèle Y, Gumiaux C, le Bayon B. 2017. Vertical strain partitioning in hot Variscan crust: Syn-convergence escape of the Pyrenees in the Iberian-Armorican syntax. *Bull. Soc. géol. Fr.* 188(6):39
- Cochrane R, Spikings RA, Chew D, Wotzlaw J-F, Chiaradia M, et al. 2014. High temperature (>350°C) thermochronology and mechanisms of Pb loss in apatite. *Geochimica et Cosmochimica Acta*. 127:39–56
- Coggon R, Holland TJB. 2002. Mixing properties of phengitic micas and revised garnet-phengite thermobarometers. *Journal of Metamorphic Geology*. 20(7):683–96
- Compagnoni R, Mafféo B. 1973. Jadeite-Bearing metagranites l.s. and related rocks in the Mount Mucrone Area (Sesia-Lanzo Zone, Western Italian Alps). *Schweizerische mineralogische und petrographische Mitteilungen*. (53):355–78
- Corfu F, Hanchar JM, Hoskin PWO, Kinny P. 2003. Atlas of Zircon Textures. *Reviews in Mineralogy and Geochemistry*. 53(1):469–500
- Couzinié S, Laurent O, Poujol M, Mintrone M, Chelle-Michou C, et al. 2017. Cadomian S-type granites as basement rocks of the Variscan belt (Massif Central, France): Implications for the crustal evolution of the north Gondwana margin. *Lithos*. 286(Supplement C):16–34
- Crévola G. 1977. *Étude pétrographique et structurale de la partie orientale du massif de Tanneron (Provence cristalline)*. Thèse de doctorat thesis. Université de Nice-Sophia Antipolis. Faculté des sciences
- Crowley QG, Floyd PA, Winchester JA, Franke W, Holland JG. 2000. Early Palaeozoic rift-related magmatism in Variscan Europe: fragmentation of the Armorican Terrane Assemblage. *Terra Nova*. 12(4):171–80
- Daczko NR, Clarke GL, Klepeis KA. 2001. Transformation of two-pyroxene hornblende granulite to garnet granulite involving simultaneous melting and fracturing of the lower crust, Fiordland, New Zealand. *Journal of Metamorphic Geology*. 19(5):549–62
- de Capitani C, Brown TH. 1987. The computation of chemical equilibrium in complex systems containing non-ideal solutions. *Geochimica et Cosmochimica Acta*. 51(10):2639–52
- de Capitani C, Petrakakis K. 2010. The computation of equilibrium assemblage diagrams with Theriak/Domino software. *American Mineralogist*. 95(7):1006–16
- Dewey JF. 1988. Extensional collapse of orogens. *Tectonics*. 7(6):1123–39
- Dewey JF. 2005. Orogeny can be very short. *Proc Natl Acad Sci USA*. 102(43):15286

- Dickinson JE, Hess PC. 1982. Zircon saturation in lunar basalts and granites. *Earth and Planetary Science Letters*. 57(2):336–44
- Diener JFA, Powell R. 2012. Revised activity–composition models for clinopyroxene and amphibole. *Journal of Metamorphic Geology*. 30(2):131–42
- Ducrot J, Lancelot JR, Marchand J. 1983. Datation U-Pb sur zircons de l'éclogite de La Borie (Haut-Allier, France) et conséquences sur l'évolution ante-hercynienne de l'Europe occidentale. *Earth and Planetary Science Letters*. 62(3):385–94
- Ducrot J, Lancelot JR, Reille JL. 1979. Datation en Montagne Noire d'un témoin d'une phase majeure d'amincissement crustal caractéristique de l'Europe prévarisque. *Bulletin de la Société Géologique de France*. S7-XXI(4):501–5
- Duthou JL. 1977. *Chronologie Rb-Sr et géochimie des granitoïdes d'un segment de la chaîne varisque, relations avec le métamorphisme: Le nord Limousin*. Univ. Clermont-Ferrand 2
- Echtler H, Malavieille J. 1990. Extensional tectonics, basement uplift and Stephano-Permian collapse basin in a late Variscan metamorphic core complex (Montagne Noire, Southern Massif Central). *Tectonophysics*. 177(1):125–38
- Faure M, Bé Mézème E, Cocherie A, Rossi P, Chemenda A, Boutelier D. 2008. Devonian geodynamic evolution of the Variscan Belt, insights from the French Massif Central and Massif Armoricain. *Tectonics*. 27(2):
- Faure M, Cocherie A, Gaché J, Esnault C, Guerrot C, et al. 2014. Middle Carboniferous intracontinental subduction in the Outer Zone of the Variscan Belt (Montagne Noire Axial Zone, French Massif Central): multimethod geochronological approach of polyphase metamorphism. *Geological Society, London, Special Publications*. 405(1):289–311
- Faure M, Couterau N. 1988. Données cinématiques sur la mise en place du dôme migmatique carbonifère moyen de la zone axiale, de la Montagne Noire (Massif Central, France). *Comptes Rendus de l'Académie des Sciences*. 307:1787–94
- Faure M, Leloix C, Roig JY. 1997. L'Evolution polycyclique de la chaîne hercynienne. *Bulletin de la Société Géologique de France*. 168(6):695–705
- Faure M, Prost AE, Lasne E. 1990. Deformation ductile extensive d'âge namuro-westphalien dans le plateau d'Aigurande, Massif central français. *Bulletin de la Société Géologique de France*. VI(1):189–97

- Feenstra A. 1996. An EMP and TEM—AEM Study of Margarite, Muscovite and Paragonite in Polymetamorphic Metabauxites of Naxos Cyclades, Greece) and the Implications of Fine-scale Mica Interlayering and Multiple Mica Generations. *J Petrology*. 37(2):201–33
- Feybesse JL, Lardeaux JM, Johan V, Teygey M, Dufour E, et al. 1988. La série de la Brévenne (Massif central français) : une unité dévonienne charriée sur le complexe métamorphique des Monts du Lyonnais à la fin de la collision varisque. *C. R. Acad. Sc. Paris*. 307:991–96
- Forestier F-H. 1961. *Métamorphisme hercynien et antéhercynien dans le bassin du haut-Allier (Massif Central français)*
- Forestier FH, Lasnier B. 1969. Découverte de niveaux d’amphibolites à pargasite, anorthite, corindon et saphirine dans les schistes cristallins de la vallée du Haut-Allier. *Contr. Mineral. and Petrol*. 23(3):194–235
- Forestier FH, Lasnier B, Leyreloup A, Marchand J. 1973. Vues nouvelles sur la catazone dans le Massif Central français et le Massif Armoricain, de l’affleurement au Moho. *Bulletin de la Société Géologique de France*. S7-XV(5–6):562–78
- Gapais D. 1987. *Les Orthogneiss : Structures, mécanismes de déformation et analyse cinématique*. phdthesis thesis. Université Rennes 1
- García-Casco A, Lázaro C, Rojas-Agramonte Y, Kröner A, Torres-Roldán RL, et al. 2008. Partial Melting and Counterclockwise P–T Path of Subducted Oceanic Crust (Sierra del Convento Mélange, Cuba). *J Petrology*. 49(1):129–61
- Gebauer D, Bernard-Griffiths J, Grünenfelder M. 1981. U-Pb zircon and monazite dating of a mafic-ultramafic complex and its country rocks. *Contr. Mineral. and Petrol*. 76(3):292–300
- Gebauer D, Schertl H-P, Brix M, Schreyer W. 1997. 35 Ma old ultrahigh-pressure metamorphism and evidence for very rapid exhumation in the Dora Maira Massif, Western Alps. *Lithos*. 41(1):5–24
- Geisler T, Schaltegger U, Tomaschek F. 2007. Re-equilibration of Zircon in Aqueous Fluids and Melts. *Elements*. 3(1):43–50
- Gibson RL. 1991. Hercynian low-pressure-high-temperature regional metamorphism and subhorizontal foliation development in the Canigou massif, Pyrenees, France—Evidence for crustal extension. *Geology*. 19(4):380–83

- Girardeau J, Dubuisson G, Mercier JC. 1986. Cinématique de mise en place des ophiolites et nappes crystallophiliennes du Limousin, Ouest du Massif Central français. *Bulletin de la Société Géologique de France*. II(5):849–60
- Giraud A, Marchand J, Dupuy C, Dostal J. 1984. Geochemistry of leptyno-amphibolite complex from Haut Allier (French Massif Central). *Lithos*. 17:203–14
- Gueirard S. 1976. Le “Granite de Barral”. Un nouveau témoin des conditions sévères de métamorphisme qui ont affecté la région occidentale du Massif des Maures (Var, France). *CR Acad Sci Paris, D*. 283:455–457
- Gutiérrez-Alonso G, Murphy JB, Fernández-Suárez J, Weil AB, Franco MP, Gonzalo JC. 2011. Lithospheric delamination in the core of Pangea: Sm-Nd insights from the Iberian mantle. *Geology*. 39(2):155–58
- Gwinn R, Hess PC. 1989. Iron and titanium solution properties in peraluminous and peralkaline rhyolitic liquids. *Contr. Mineral. and Petrol*. 101(3):326–38
- Harlov DE. 2015. Apatite: A Fingerprint for Metasomatic Processes. *Elements*. 11(3):171–76
- Harrison TM, Catlos EJ, Montel J-M. 2002. U-Th-Pb Dating of Phosphate Minerals. *Reviews in Mineralogy and Geochemistry*. 48(1):524–58
- Henk A, Blanckenburg F von, Finger F, Schaltegger U, Zulauf G. 2000. Syn-convergent high-temperature metamorphism and magmatism in the Variscides: a discussion of potential heat sources. *Geological Society, London, Special Publications*. 179(1):387–99
- Höck V. 1974. Coexisting phengite, paragonite and margarite in metasediments of the mittlere Hohe Tauern, Austria. *Contr. Mineral. and Petrol*. 43(4):261–73
- Hofmann AE, Baker MB, Eiler JM. 2014. Sub-micron-scale trace-element distributions in natural zircons of known provenance: implications for Ti-in-zircon thermometry. *Contrib Mineral Petrol*. 168(3):1057
- Holland T, Baker J, Powell R. 1998. Mixing properties and activity-composition relationships of chlorites in the system MgO-FeO-Al₂O₃-SiO₂-H₂O. *European Journal of Mineralogy*. 395–406
- Holland TJB. 1980. The reaction albite = jadeite+quartz determined experimentally in the range 600-1200 degrees C. *American Mineralogist*. 65(1–2):129–34
- Hollocher K, Ruiz J. 1995. Major and Trace Element Determinations on Nist Glass Standard Reference Materials 611, 612, 614 and 1834 by Inductively Coupled Plasma-Mass Spectrometry. *Geostandards Newsletter*. 19(1):27–34

- Holness MB, Sawyer EW. 2008. On the Pseudomorphing of Melt-filled Pores During the Crystallization of Migmatites. *J Petrology*. 49(7):1343–63
- Horstwood MSA, Košler J, Gehrels G, Jackson SE, McLean NM, et al. 2016. Community-Derived Standards for LA-ICP-MS U-(Th-)Pb Geochronology – Uncertainty Propagation, Age Interpretation and Data Reporting. *Geostandards and Geoanalytical Research*. 40(3):311–32
- Ibarguchi JIG, Gironés EO. 1985. Petrology, structure and geotectonic implications of glaucophane-bearing eclogites and related rocks from the Malpica—Tuy (MT) Unit, Galicia, northwest Spain. *Chemical Geology*. 50(1):145–62
- Jackson SE, Pearson NJ, Griffin WL, Belousova EA. 2004. The application of laser ablation-inductively coupled plasma-mass spectrometry to in situ U–Pb zircon geochronology. *Chemical Geology*. 211(1):47–69
- Kent AJR, Jacobsen B, Peate DW, Waight TE, Baker JA. 2004. Isotope Dilution MC-ICP-MS Rare Earth Element Analysis of Geochemical Reference Materials NIST SRM 610, NIST SRM 612, NIST SRM 614, BHVO-2G, BHVO-2, BCR-2G, JB-2, WS-E, W-2, AGV-1 and AGV-2. *Geostandards and Geoanalytical Research*. 28(3):417–29
- Kohn MJ. 2016. Metamorphic chronology—a tool for all ages: Past achievements and future prospects. *American Mineralogist*. 101(1):25–42
- Kohn MJ, Corrie SL, Markley C. 2015. The fall and rise of metamorphic zircon. *American Mineralogist*. 100(4):897–908
- Konilov AN, Shchipansky AA, Mints MV, Dokukina KA, Kaulina TV, et al. 2011. 19 - The Salma Eclogites of the Belomorian Province, Russia: HP/UHP Metamorphism Through the Subduction of Mesoarchean Oceanic Crust. In *Ultrahigh-Pressure Metamorphism*, eds. LF Dobrzhinetskaya, SW Faryad, S Wallis, S Cuthbert, pp. 623–70. London: Elsevier
- Konzett J, Miller C, Armstrong R, Thöni M. 2005. Metamorphic Evolution of Iron-rich Mafic Cumulates from the Ötztal–Stubai Crystalline Complex, Eastern Alps, Austria. *J Petrology*. 46(4):717–47
- Labrousse L, Duret T, Gerya T. 2015. H₂O-fluid-saturated melting of subducted continental crust facilitates exhumation of ultrahigh-pressure rocks in continental subduction zones. *Earth and Planetary Science Letters*. 428:151–61
- Labrousse L, Prouteau G, Ganzhorn A-C. 2011. Continental exhumation triggered by partial melting at ultrahigh pressure. *Geology*. 39(12):1171–74

- Lagarde JL. 1978. *La Deformation des roches dans les domaines à schistosité subhorizontale: applications à la nappe du Canigou-Roc de France (Pyrénées Orientales) et au complexe cristallophyllien de Champtoceaux (Massif Armoricain)*. Université de Rennes
- Lahondere D. 1988. Le Metamorphisme eclogitique dans les orthogneiss et les metabasites ophiolitiques de la region de Farinole (Corse). *Bulletin de la Société Géologique de France*. IV(4):579–85
- Lambert IB, Wyllie PJ. 1972. Melting of Gabbro (Quartz Eclogite) with Excess Water to 35 Kilobars, with Geological Applications. *The Journal of Geology*. 80(6):693–708
- Lardeaux JM. 2014. Deciphering orogeny: a metamorphic perspective Examples from European Alpine and Variscan belts. *Bulletin de la Société Géologique de France*. 185(5):281–310
- Lardeaux J-M, Dufour E. 1987. Champs de déformation superposés dans la chaîne varisque. Exemple de la zone nord des Monts du Lyonnais (Massif central français). *Comptes rendus de l'Académie des sciences. Série 2, Mécanique, Physique, Chimie, Sciences de l'univers, Sciences de la Terre*. 305(1):61–64
- Lardeaux JM, Ledru P, Daniel I, Duchene S. 2001. The Variscan French Massif Central—a new addition to the ultra-high pressure metamorphic ‘club’: exhumation processes and geodynamic consequences. *Tectonophysics*. 332(1–2):143–67
- Lasnier B. 1968. Découverte d’une granulite à disthène et almandin associée à la péridotite à grenat du massif de Courtilles (Haute-Loire). *Bulletin de Minéralogie*. 91(5):490–94
- Lasnier B. 1977. *Persistance d’une série granulitique au coeur du Massif Central français, Haut-Allier: les termes basiques, ultrabasiques et carbonatés*. phdthesis thesis. Université de Nantes ; laboratoire de pétrologie et de minéralogie
- Lasnier B, Leyreloup A, Marchand J. 1973. Découverte d’un granite « charnockitique » au sein de « gneiss œillés » Perspectives nouvelles sur l’origine de certaines leptynites du Massif Armoricain Méridional (France). *Contr. Mineral. and Petrol*. 41(2):131–44
- Laurent O, Couzinié S, Zeh A, Vanderhaeghe O, Moyen JF, et al. 2017. Protracted, coeval crust and mantle melting during Variscan late-orogenic evolution: U–Pb dating in the eastern French Massif Central. *Int J Earth Sci (Geol Rundsch)*. 106(2):421–51
- Le Bayon B, Pitra P, Ballevre M, Bohn M. 2006. Reconstructing P–T paths during continental collision using multi-stage garnet (Gran Paradiso nappe, Western Alps). *Journal of Metamorphic Geology*. 24(6):477–96

- Ledru P, Lardeaux JM, Santallier D, Autran A, Quenardel JM, et al. 1989. Où sont les nappes dans le Massif central français ? *Bulletin de la Société géologique de France*. 8(3):605–618
- Leloix C, Faure M, Feybesse J-L. 1999. Hercynian polyphase tectonics in the northeast French Massif Central: the closure of the Brévenne Devonian–Dinantian rift. *Int Journ Earth Sciences*. 88(3):409–21
- Liermann H-P, Isachsen C, Altenberger U, Oberhänsli R. 2002. Behavior of zircon during high-pressure, low-temperature metamorphism Case study from the Internal Unit of the Sesia Zone (Western Italian Alps). *European Journal of Mineralogy*. 14(1):61–71
- Lotout C. 2017. *Âge, durée et enregistrement du métamorphisme de haute pression dans le massif Central*. thesis thesis. Rennes 1
- Lotout C, Pitra P, Poujol M, Anczkiewicz R, Van Den Driessche J. 2018. Timing and duration of Variscan high-pressure metamorphism in the French Massif Central: A multimethod geochronological study from the Najac Massif. *Lithos*. 308–309:381–94
- Lotout C, Pitra P, Poujol M, Driessche JVD. 2017. Ordovician magmatism in the Lévézou massif (French Massif Central): tectonic and geodynamic implications. *Int J Earth Sci (Geol Rundsch)*. 106(2):501–15
- Luvizotto GL, Zack T, Meyer HP, Ludwig T, Triebold S, et al. 2009. Rutile crystals as potential trace element and isotope mineral standards for microanalysis. *Chemical Geology*. 261(3):346–69
- Malavieille J. 1993. Late Orogenic extension in mountain belts: Insights from the basin and range and the Late Paleozoic Variscan Belt. *Tectonics*. 12(5):1115–30
- Marchand J. 1974. *Persistance d'une série granulitique au coeur du Massif Central français, Haut-Allier: les termes acides*. Université de Nantes
- Marco R, Alessandro B, Roberto C. 1999. Thermodynamic analysis of garnet growth zoning in eclogite facies granodiorite from M. Mucrone, Sesia Zone, Western Italian Alps. *Contrib Mineral Petrol*. 137(4):289–303
- Martínez FJ, Reche J, Arboleya ML. 2001. P–T modelling of the andalusite–kyanite–andalusite sequence and related assemblages in high-Al graphitic pelites. Prograde and retrograde paths in a late kyanite belt in the Variscan Iberia. *Journal of Metamorphic Geology*. 19(6):661–77
- Matte P. 1986. Tectonics and plate tectonics model for the Variscan belt of Europe. *Tectonophysics*. 126(2):329–374

- Matte P. 1991. Accretionary history and crustal evolution of the Variscan belt in Western Europe. *Tectonophysics*. 196(3):309–37
- Matte P, Burg JP. 1981. Sutures, thrusts and nappes in the Variscan Arc of western Europe: plate tectonic implications. *Geological Society, London, Special Publications*. 9(1):353–58
- McDowell FW, McIntosh WC, Farley KA. 2005. A precise ^{40}Ar – ^{39}Ar reference age for the Durango apatite (U–Th)/He and fission-track dating standard. *Chemical Geology*. 214(3):249–63
- Melleton J, Cocherie A, Faure M, Rossi P. 2010. Precambrian protoliths and Early Paleozoic magmatism in the French Massif Central: U–Pb data and the North Gondwana connection in the west European Variscan belt. *Gondwana Research*. 17(1):13–25
- Mints MV, Belousova EA, Konilov AN, Natapov LM, Shchipansky AA, et al. 2010. Mesoarchean subduction processes: 2.87 Ga eclogites from the Kola Peninsula, Russia. *Geology*. 38(8):739–42
- Moussavou M. 1998. Contribution à l’histoire thermo-tectonique varisque du massif des Maures, par la typologie du zircon et la géochronologie U/Pb sur minéraux accessoires (Var, France). Thèse de doctorat de Montpellier.
- Nahodilová R, Štípská P, Powell R, Košler J, Racek M. 2014. High-Ti muscovite as a prograde relict in high pressure granulites with metamorphic Devonian zircon ages (Běstvína granulite body, Bohemian Massif): Consequences for the relamination model of subducted crust. *Gondwana Research*. 25(2):630–48
- Nasdala L, Zhang M, Kempe U, Panczer G, Gaft M, et al. 2003. Spectroscopic methods applied to zircon. *Reviews in Mineralogy and Geochemistry*. 53(1):427–67
- Nicollet C, Lahlafi M, Lasnier B. 1993. Occurrence of a late Hercynian metamorphic event, of low pressure granulitic conditions, in the Haut-Allier (French Massif Central): geodynamic implications. *Comptes Rendus de l’Académie des Sciences*. 317:1609–15
- Nicollet C, Leyreloup A. 1978. Pétrologie des niveaux trondhjémiques de haute pression associés aux éclogites et amphibolites des complexes leptyno-amphiboliques du Massif Central français. *Canadian Journal of Earth Sciences*. 15(5):696–707
- Oberhänsli R, Hunziker JC, Martinotti G, Stern WB. 1985. Geochemistry, geochronology and petrology of Monte Mucrone: An example of EO-alpine eclogitization of Permian granitoids in the Sesia-Lanzo Zone, Western Alps, Italy. *Chemical Geology: Isotope Geoscience section*. 52(2):165–84

- Palin RM, Sayed AB, White RW, Mertz-Kraus R. 2018. Origin, age, and significance of deep-seated granulite-facies migmatites in the Barrow zones of Scotland, Cairn Leuchan, Glen Muick area. *Journal of Metamorphic Geology*. 36(8):1071–96
- Paquette JL, Ballèvre M, Peucat JJ, Cornen G. 2017. From opening to subduction of an oceanic domain constrained by LA-ICP-MS U-Pb zircon dating (Variscan belt, Southern Armorican Massif, France). *Lithos*. 294–295:418–37
- Paquette JL, Monchoux P, Couturier M. 1995. Geochemical and isotopic study of a norite-eclogite transition in the European Variscan belt: Implications for U/Pb zircon systematics in metabasic rocks. *Geochimica et Cosmochimica Acta*. 59(8):1611–22
- Paquette JL, Peucat J-J, Bernard-Griffiths J, Marchand J. 1985. Evidence for old Precambrian relics shown by U–Pd zircon dating of eclogites and associated rocks in the Hercynian belt of South Brittany, France. *Chemical Geology: Isotope Geoscience section*. 52(2):203–16
- Paton C, Hellstrom J, Paul B, Woodhead J, Hergt J. 2011. Iolite: Freeware for the visualisation and processing of mass spectrometric data. *Journal of Analytical Atomic Spectrometry*. 26(12):2508–18
- Peacock. 1991. Numerical simulation of subduction zone pressure-temperature-time paths: constraints on fluid production and arc magmatism. *Philosophical Transactions of the Royal Society of London. Series A: Physical and Engineering Sciences*
- Peacock SM, Rushmer T, Thompson AB. 1994. Partial melting of subducting oceanic crust. *Earth and Planetary Science Letters*. 121(1):227–44
- Peterman EM, Hacker BR, Baxter EF. 2009. Phase transformations of continental crust during subduction and exhumation: Western Gneiss Region, Norway. *European Journal of Mineralogy*. 21(6):1097–1118
- Peucat JJ, Vidal Ph, Godard G, Postaire B. 1982. Precambrian U-Pb zircon ages in eclogites and garnet pyroxenites from South Brittany (France): an old oceanic crust in the West European Hercynian belt? *Earth and Planetary Science Letters*. 60(1):70–78
- Philippot P, Selverstone J. 1991. Trace-element-rich brines in eclogitic veins: implications for fluid composition and transport during subduction. *Contr. Mineral. and Petrol*. 106(4):417–30
- Pin C. 1990. Variscan oceans: ages, origins and geodynamic implications inferred from geochemical and radiometric data. *Tectonophysics*. 177(1):215–227

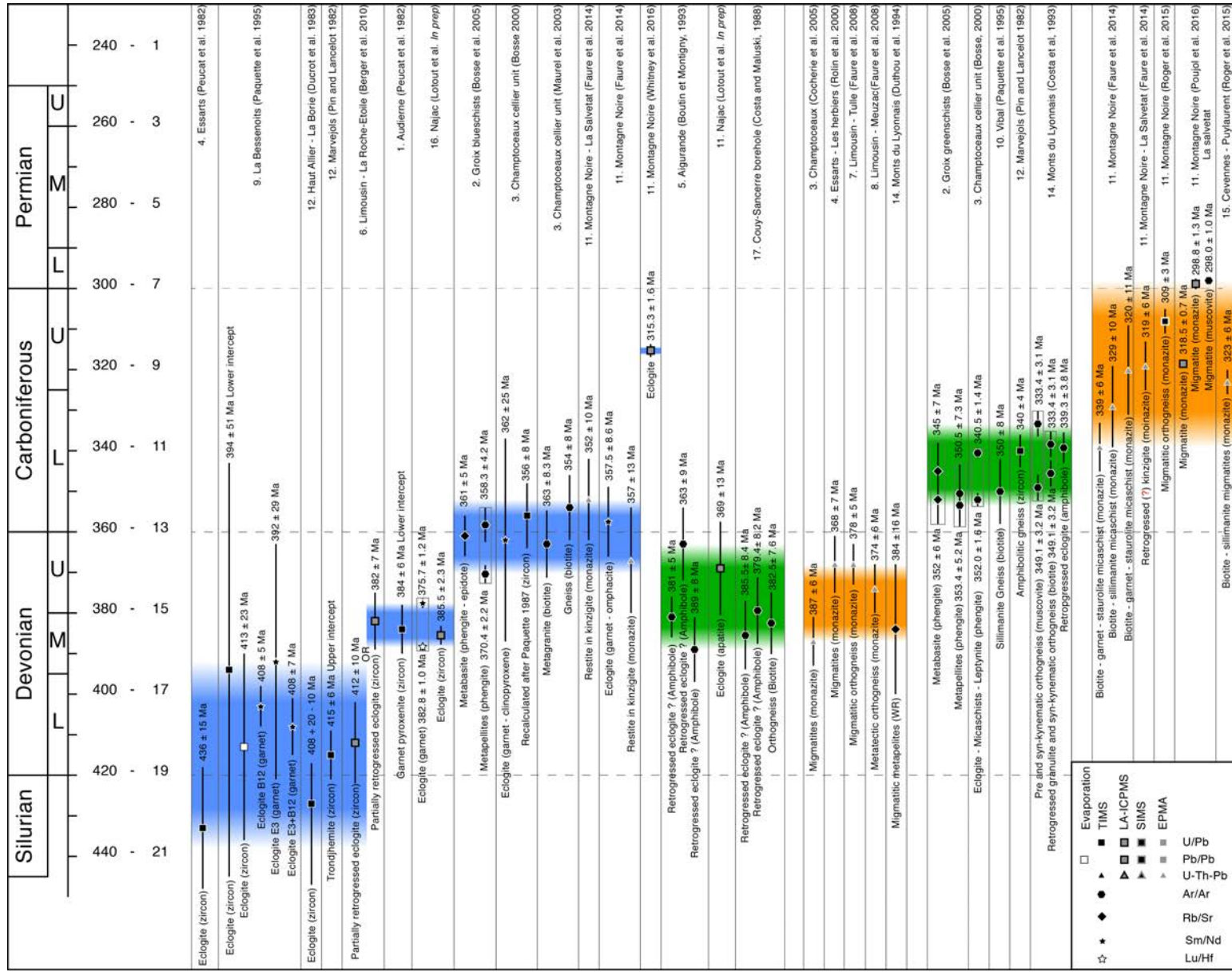
- Pin C, Lancelot J. 1982. U-Pb dating of an early paleozoic bimodal magmatism in the french Massif Central and of its further metamorphic evolution. *Contr. Mineral. and Petrol.* 79(1):1–12
- Pin C, Paquette JL. 1997. A mantle-derived bimodal suite in the Hercynian Belt: Nd isotope and trace element evidence for a subduction-related rift origin of the Late Devonian Brévenne metavolcanics, Massif Central (France). *Contrib Mineral Petrol.* 129(2–3):222–38
- Pin C, Vielzeuf D. 1988. Les granulites de haute-pressure d'Europe moyenne temoins d'une subduction eo-hercynienne; implications sur l'origine des groupes leptyno-amphiboliques. *Bulletin de la Société Géologique de France.* IV(1):13–20
- Pitra P, Poujol M, Van Den Driessche J, Poilvet JC, Paquette JL. 2012. Early Permian extensional shearing of an Ordovician granite: The Saint-Eutrope “C/S-like” orthogneiss (Montagne Noire, French Massif Central). *Comptes Rendus Geoscience.* 344(8):377–84
- Pochon A, Poujol M, Gloaguen E, Branquet Y, Cagnard F, et al. 2016. U-Pb LA-ICP-MS dating of apatite in mafic rocks: Evidence for a major magmatic event at the Devonian-Carboniferous boundary in the Armorican Massif (France). *American Mineralogist.* 101(11):2430–42
- Proyer A. 2003. The preservation of high-pressure rocks during exhumation: metagranites and metapelites. *Lithos.* 70(3):183–94
- Roig JY, Faure M. 2000. La tectonique cisailante polyphasée du Sud Limousin (Massif central français) et son interprétation dans un modèle d'évolution polycyclique de la chaîne hercynienne. *Bulletin de la Société Géologique de France.* 171(3):295–307
- Rolland Y, Corsini M, Demoux A. 2009. Metamorphic and structural evolution of the Maures-Tanneron massif (SE Variscan chain): evidence of doming along a transpressional margin. *Bulletin de la Société Géologique de France.* 180(3):217–30
- Rossetti F, Nasrabady M, Vignaroli G, Theye T, Gerdes A, et al. 2010. Early Cretaceous migmatitic mafic granulites from the Sabzevar range (NE Iran): implications for the closure of the Mesozoic peri-Tethyan oceans in central Iran. *Terra Nova.* 22(1):26–34
- Rubatto D, Hermann J. 2003. Zircon formation during fluid circulation in eclogites (Monviso, Western Alps): implications for Zr and Hf budget in subduction zones. *Geochimica et Cosmochimica Acta.* 67(12):2173–87

- Santallier D, Briand B, Menot RP, Piboule M. 1988. Les complexes leptyno-amphiboliques (CLA): revue critique et suggestions pour un meilleur emploi de ce terme. *Bull Soc Géol Fr.* 1:3–12
- Santallier D, Floc'h JP. 1989. Tectonique tangentielle et décrochements ductiles dévono-carbonifères superposés dans la région de Bellac (nord-ouest du Massif Central français). *Comptes Rendus de l'Académie des Sciences.* 309:1419–24
- Schaltegger U, Fanning CM, Günther D, Maurin JC, Schulmann K, Gebauer D. 1999. Growth, annealing and recrystallization of zircon and preservation of monazite in high-grade metamorphism: conventional and in-situ U-Pb isotope, cathodoluminescence and microchemical evidence. *Contrib Mineral Petrol.* 134(2):186–201
- Schertl H-P, O'Brien PJ. 2013. Continental Crust at Mantle Depths: Key Minerals and Microstructures. *Elements.* 9(4):261–66
- Schmidt MW, Vielzeuf D, Auzanneau E. 2004. Melting and dissolution of subducting crust at high pressures: the key role of white mica. *Earth and Planetary Science Letters.* 228(1):65–84
- Schneider J, Corsini M, Reverso-Peila A, Lardeaux J-M. 2014. Thermal and mechanical evolution of an orogenic wedge during Variscan collision: an example in the Maures–Tanneron Massif (SE France). *Geological Society, London, Special Publications.* 405(1):313–31
- Schoene B, Bowring SA. 2006. Determining accurate temperature–time paths from U–Pb thermochronology: An example from the Kaapvaal craton, southern Africa. *Geochimica et Cosmochimica Acta.* 71(1):165–85
- Schulz B. 2014. Early Carboniferous P-T path from the Upper Gneiss Unit of Haut-Allier (French Massif Central) - reconstructed by geothermobarometry and EMP-Th-U-Pb monazite dating. *J Geosci.* 59(4):327–49
- Sen C, Dunn T. 1994. Dehydration melting of a basaltic composition amphibolite at 1.5 and 2.0 GPa: implications for the origin of adakites. *Contr. Mineral. and Petrol.* 117(4):394–409
- Shchipansky AA, Khodorevskaya LI, Konilov AN, Slabunov AI. 2012. Eclogites from the Belomorian Mobile Belt (Kola Peninsula): geology and petrology. *Russian Geology and Geophysics.* 53(1):1–21

- Sláma J, Košler J, Condon DJ, Crowley JL, Gerdes A, et al. 2008. Plešovice zircon — A new natural reference material for U–Pb and Hf isotopic microanalysis. *Chemical Geology*. 249(1):1–35
- Solá AR, Pereira MF, Williams IS, Ribeiro ML, Neiva AMR, et al. 2008. New insights from U–Pb zircon dating of Early Ordovician magmatism on the northern Gondwana margin: The Urro Formation (SW Iberian Massif, Portugal). *Tectonophysics*. 461(1):114–29
- Sorensen SS, Barton MD. 1987. Metasomatism and partial melting in a subduction complex Catalina Schist, southern California. *Geology*. 15(2):115–18
- Stacey JS, Kramers JD. 1975. Approximation of terrestrial lead isotope evolution by a two-stage model. *Earth and Planetary Science Letters*. 26(2):207–21
- Taylor-Jones K, Powell R. 2015. Interpreting zirconium-in-rutile thermometric results. *Journal of Metamorphic Geology*. 33(2):115–22
- Thomson SN, Gehrels GE, Ruiz J, Buchwaldt R. 2018. Routine low-damage apatite U–Pb dating using laser ablation–multicollector–ICPMS. *Geochemistry, Geophysics, Geosystems*
- Tirel C, Brun J-P, Burov E, Wortel MJR, Lebedev S. 2013. A plate tectonics oddity: Caterpillar-walk exhumation of subducted continental crust. *Geology*. 41(5):555–58
- Tomkins HS, Powell R, Ellis DJ. 2007. The pressure dependence of the zirconium-in-rutile thermometer. *Journal of Metamorphic Geology*. 25(6):703–13
- Vaucher A, Bufalo M. 1985. La limite Maures occidentales-Maures orientales (Var, France): un décrochement ductile senestre majeur entre deux provinces structurales très contrastées. *Comptes rendus de l'Académie des sciences. Série 2, Mécanique, Physique, Chimie, Sciences de l'univers, Sciences de la Terre*. 301(14):1059–1062
- Vaucher A, Maillet D, Sougy J. 1987. Strain and deformation mechanisms in the Variscan nappes of Vendée, South Brittany, France. *Journal of Structural Geology*. 9(1):31–40
- Vavra G, Gebauer D, Schmid R, Compston W. 1996. Multiple zircon growth and recrystallization during polyphase Late Carboniferous to Triassic metamorphism in granulites of the Ivrea Zone (Southern Alps): an ion microprobe (SHRIMP) study. *Contrib Mineral Petrol*. 122(4):337–58
- Vermeesch P. 2018. IsoplotR: A free and open toolbox for geochronology. *Geoscience Frontiers*. 9(5):1479–93

- Vidal Ph, Peucat JJ, Lasnier B. 1980. Dating of granulites involved in the hercynian fold-belt of Europe: An example taken from the granulite-facies orthogneisses at La Picherais, Southern Armorican Massif, France. *Contr. Mineral. and Petrol.* 72(3):283–89
- Viete DR, Hermann J, Lister GS, Stenhouse IR. 2011. The nature and origin of the Barrovian metamorphism, Scotland: diffusion length scales in garnet and inferred thermal time scales. *Journal of the Geological Society.* 168(1):115–32
- Viete DR, Lister GS. 2017. On the significance of short-duration regional metamorphism. *Journal of the Geological Society.* 174(3):377–92
- Villa. 1998. Isotopic closure. *Terra Nova.* 10(1):42–47
- Villa IM. 2010. Disequilibrium textures versus equilibrium modelling: geochronology at the crossroads. *Geological Society, London, Special Publications.* 332(1):1–15
- Wang L, Kusky TM, Polat A, Wang S, Jiang X, et al. 2014. Partial melting of deeply subducted eclogite from the Sulu orogen in China. *Nature Communications.* 5:5604
- Watson EB. 1979. Zircon saturation in felsic liquids: Experimental results and applications to trace element geochemistry. *Contr. Mineral. and Petrol.* 70(4):407–19
- Watson EB, Harrison TM. 2005. Zircon Thermometer Reveals Minimum Melting Conditions on Earliest Earth. *Science.* 308(5723):841–44
- White RW, Pomroy NE, Powell R. 2005. An in situ metatexite–diatexite transition in upper amphibolite facies rocks from Broken Hill, Australia. *Journal of Metamorphic Geology.* 23(7):579–602
- White RW, Powell R, Holland TJB, Worley BA. 2000. The effect of TiO₂ and Fe₂O₃ on metapelitic assemblages at greenschist and amphibolite facies conditions: mineral equilibria calculations in the system K₂O–FeO–MgO–Al₂O₃–SiO₂–H₂O–TiO₂–Fe₂O₃. *Journal of Metamorphic Geology.* 18(5):497–511
- Whitney DL, Roger F, Teyssier C, Rey PF, Respaut J-P. 2015. Syn-collapse eclogite metamorphism and exhumation of deep crust in a migmatite dome: The –t record of the youngest Variscan eclogite (Montagne Noire, French Massif Central). *Earth and Planetary Science Letters.* 430:224–34
- Wiedenbeck M, Hanchar JM, Peck WH, Sylvester P, Valley J, et al. 2004. Further Characterisation of the 91500 Zircon Crystal. *Geostandards and Geoanalytical Research.* 28(1):9–39
- Wyns R, Godard G, Lablanche G, Biron R, Bresson G. 1989. Notice explicative de la carte géologique de La Roche Sur Yon au 1/50 000°.

- Yamamoto H, Yoshino T. 1998. Superposition of replacements in the mafic granulites of the Jijal complex of the Kohistan arc, northern Pakistan: dehydration and rehydration within deep arc crust. *Lithos*. 43(4):219–34
- Yang TN, Zeng L, Zhao ZR, Liou JG. 2008. Retrograde Reactions of an Ultrahigh-Pressure Metamorphic Spinel Pyroxenite Lens, Northeast Sulu UHP Terrane, Eastern China. *International Geology Review*. 50(1):32–47



Titre : Évolution pression-température-temps des unités varisques de haute pression de l'est du Massif Central : implications géodynamiques

Mots clés : Massif Central, orogène varisque, subduction, exhumation, éclogite, pétrochronologie

Résumé : La chaîne varisque en France a été interprétée comme une chaîne de collision paléozoïque où l'essentiel des déformations et du métamorphisme résultent de l'épaississement crustal et de la relaxation thermique qui s'ensuit.

L'analyse des relations entre métamorphisme et déformation au sein des massifs d'orthogneiss (principalement du Massif Central) et la datation du métamorphisme de haute pression d'éclogites mafiques démontrent :

(i) le caractère précoce du métamorphisme de haute température reflété par la fusion partielle des éclogites au pic de pression à ~363 Ma ;

(ii) l'exhumation et le refroidissement rapide des roches après le pic de pression datés à ~353 Ma ;

(iii) le caractère rétrograde de l'essentiel des déformations des orthogneiss.

Le métamorphisme et les déformations sont finalement interprétés dans le cadre d'un changement de dynamique de la zone de subduction suite à l'entrée en subduction de lambeaux de croûte continentale plutôt que dans celui d'une collision continentale succédant à la subduction océanique initiale.

Title: Pressure-temperature-time evolution of the Variscan high-pressure units of the eastern Massif-Central: geodynamic implications

Keywords: Massif Central, Variscan orogen, subduction, exhumation, eclogite, petrochronology

Abstract: The Variscan belt in France is interpreted as a collisional orogen where crustal thickening and subsequent thermal relaxation account for most of the metamorphic and structural record.

Detailed analysis of the relationships between metamorphism and deformation of orthogneisses, as well as petrologically constrained geochronology of mafic eclogites reveal:

(i) an early high-temperature metamorphism demonstrated by partial melting of the eclogites close the peak P–T conditions at ~363 Ma;

(ii) subsequent fast decompression followed by cooling dated at ~353 Ma;

(iii) the retrograde metamorphic character of the deformation of most orthogneisses.

The metamorphic and structural record are inferred to result from a switch of the dynamics of the subduction zone at the onset of subduction of small continental ribbons rather than from continental collision after the initial oceanic subduction.